ROMA TRE
UNIVERSITÀ DEGLI STUDI

SCUOLA DOTTORALE IN SCIENZE MATEMATICHE E FISICHE

XXVI CICLO

Dynamics of two-electron photoemission: a study of electronic correlations in solids

Dottorando: Gianluca Di Filippo

Docente guida: Prof. Giovanni Stefani

Coordinatore: Prof. Roberto Raimondi

Contents

Introduction

Electron-electron interaction plays a crucial role in the determination of the electronic and physical properties in a wide class of materials. The study of the behaviour of those many-body interacting systems has been a very important topic since the first days of modern physics. This is because most of the properties of interest for technological development, for example ferro- or antiferromagnetism, giant and colossal magneto-resistance, superconductivity and half-metallic behaviour, are driven by the correlated behaviour of the system's constituents.
Unfortunately, the terms describing the electron-electron interaction in Schrödinger equation make impossible to find an exact solution for the system eigenstates. Thus, the commonly considered Hamiltonians are those deriving from a single-particle approximation in which one describes the interaction among electrons through a mean field and completely neglects correlations between the motions of different electrons. Despite very appealing, these models fails in the description of strongly correlated systems. This could be, for example, the case of the developing of a localised magnetic moment in transition metals. Taking into consideration the latter case, in a single particle picture, the d electrons of the metal valence band are free to hop from atom to atom with a characteristic time of the order of $\hbar/W$ (W is the d band width). Each electron carries its own spin and consequently the atom spin, given by the sum of all the electronic spins on it, fluctuates randomly in magnitude and direction and no local magnetic moment is observed. This scenario is inverted if one takes into account electron-electron interactions. Indeed, Hund's first rule for atoms affirms that, due to intra-atomic interactions, the energetically favourable state is the one with the electronic spins aligned. In this case, a spin-up atom will tend to attract electrons with spin-up and repel those with spin-down. This leads to the spin of the atom not to fluctuate and to persist for a time period longer than the electron hopping time, thus giving rise to a localised magnetic moment. We must pay attention, this does not mean that the electrons are stuck on one atom but they "continue" to move following band motion, and the magnetic moment of the atom persists due to the correlations between the motion of the electrons. Even in this very simple example we can see the importance of considering electronic correlations when describing the motion of valence band electrons in solids.

The description of physical properties of strongly correlated materials has represented, in the past few decades, one of the major intellectual challenge of modern physics and has led to the development of many theories trying to go beyond the independent particle picture, e.g. Hubbard theory [1], LDA (local density approximation) + U [2, 3, 4], DMFT (Dynamical mean field theory) [5, 6], etc. The understanding of Coulomb interactions in many-electron systems is made even more difficult if one consider that most of the spectroscopic techniques commonly used to investigate matter in its various states of aggregation are based on reactions involving one electron at a time and whose results, thus, can be described within a single-particle theory where the electronic correlations are only considered as a perturbation to the central field effects. Hence the effort, in the past thirty years, in developing a new class of experiments whose spectral response is

directly influenced by the electron-electron interaction. The common feature of this experimental techniques is that they are all based on reactions involving two (or more) electrons simultaneously and whose final states are characterised by two (or more) holes in target's valence band combined to two (or more) electrons in the continuum. The interaction between the holes in the sample and between the emitted electrons are the forces driving these processes and directly shaping their cross sections.
Experimental "correlation spectroscopy" techniques involve the momentum- and energy-resolved detection of pairs of time correlated electrons, which emerge from an atom, molecule or solid following the collision/absorption of a probe particle (e.g. electron, positron, photon).
Two prototypical processes that create hole-pairs in the valence band of a considered system are the direct and core-resonant Double Photoemission (DPE). In direct DPE the absorption of one photon leads to the simultaneous emission of two correlated electrons, according to the reaction,

$$h\nu + A \longrightarrow A^{++}(v^{-1}v^{-1}) + e^- + e^-,$$

where $h\nu$ represents the photon, A is the neutral sample in its ground state and $A^{++}(v^{-1}v^{-1})$ is the doubly ionised sample with two holes in the valence levels. In core-resonant DPE (also termed as APECS) the double-ionisation takes place through the decay of a core-hole with the emission of an Auger electron that is coupled to the photoelectron of the primary ionisation,

$$h\nu + A \longrightarrow A^{+}(c^{-1}) + e^- \longrightarrow A^{++}(v^{-1}v^{-1}) + e^- + e^-.$$

Because of the single-particle nature of the dipole interaction, the electric field of the photon directly interacts with only one electron of the system. This means that in order to have the simultaneous emission of two electrons a non vanishing electronic interaction must be present [7, 8, 9].
These 1 photon-IN 2 electrons-OUT $(\gamma, 2e)$ experiments are the ideal candidates for the study of two-particle quantities, essential for the understanding of important phenomena such as the optical conductivity [10], superconductivity [11], generation of entangled states of two electrons [12, 13]. Two-particle properties can be classified into those associated to

- particle-hole interaction
- hole-hole interaction
- particle-particle interaction.

The first channel is probably the most studied of them, definitely because it can be highlighted by the use of single-particle techniques, e.g. (single) photoemission spectroscopy, PES. Further informations can be achieved with the help of $(\gamma, 2e)$ spectroscopies, in particular by studying the nature of core-resonant DPE processes. The emission of electron-pairs by core-resonant DPE proceeds through the formation of an intermediate core-hole state and for this reason it is often treated within a two-step model, where the Auger decay is treated independently from the initial photoionisation. This two-step approach fails in describing the properties of Auger spectra in some cases, e.g. Cu(001) $M_{23}VV$ Auger transition [14, 15], where the core-resonant DPE processes have a one-step nature. In those cases the system, excited by photon absorption, decays to a two-hole final state by the emission of electrons in an interacting two-particle state. The one- or two-step nature of the core-resonant DPE is dictated by the behaviour of the intermediate state. If the lifetime of the core-hole state is long enough to allow the decay of all the additional excitations, then it can be described in a quasi-particle picture as a well defined stationary state. The Auger decay

takes place from this stationary state and can be treated independently from the initial photoemission. If this condition is not satisfied the quasi-particle picture breaks down and the core-hole can be described as a virtual intermediate state given by the superposition of all the possible excited single-electron states. Therefore the photoionisation and Auger decay are no more independent and the core-resonant DPE takes place in one single step. In the one-step picture the core-hole experiences the effects of dynamic electron-screening processes. These electron-hole interactions, acting on a few fs (or even attosecond) timescale [16, 17], cannot be accessed in single photoemission. On the contrary, they can be probed by the emitted Auger electron and be observable in the core-resonant DPE spectrum. Due to its nature the DPE represents a good method to investigate these very fast particle-hole interactions.

Particle-particle and hole-hole channels, requiring the presence of two holes (electrons) in the final state, can be exclusively studied with the help of two-particle spectroscopies In this sense the dynamics of the emitted electron-pairs strongly depends on the properties of 2-electron and 2-hole wavefunctions of the pair in the continuum and of the residual ion, respectively.

Since the $(\gamma, 2e)$ technique can be viewed as the extension of PES to two particles, from a conceptional point of view, the energy distribution of correlated electron-pairs can be directly associated to the 2-particle density of state (2p-DOS) of the studied system. Several theoretical works have been put forward for the evaluation of two-particle spectral functions [18, 19, 20, 21, 22], most of them based on the Hubbard model [1]. The results obtained by Cini and Sawatzky (C-S) in their pioneering works [18, 19] connect the 2p-DOS to the on-site Coulomb interaction between the holes generated in the DPE process. This allows, by comparing the DPE energy distributions with the predictions of C-S theory, the direct determination of the 2-particle interaction energy in the final state.

The angular dependence of the DPE cross-section gives the opportunity to get informations on the correlations among the electrons in the valence band of the considered material. For example, direct DPE was able to reveal and completely map out the exchange-correlation hole, i.e. a zone of reduced electronic charge surrounding each electron of a system ascribable to the tendency of the electrons to stay away from each other as a consequence of Coulomb and exchange interactions [23, 24].

Additional informations on the two-particle wave functions properties are obtained by using circularly polarised light as excitation source. In this case the exchange interaction between the electrons, i.e. the fact that the two emitted electrons cannot be distinguished, and parity conservation in the whole 2-electron emission process are responsible for the DPE cross section to depend on the helicity of the light polarisation. Indeed, the dipole matrix elements calculated between two-electron wavefunctions give rise to a DPE cross section with an antisymmetric part with respect to the exchange of the two particles. This part is the source of circular dichroism, i.e. differences between the cross section for left and right circularly polarised light, in those cases where the electrons can be distinguished according to their kinetic energy and emission angle [25, 26]. Circular dichroism, oppositely to single photoemission [27], enters in a non-trivial way in the dynamics of the DPE processes and represents a footprint of the correlated behaviour of the emitted electron-pairs.

Despite the ability of $(\gamma, 2e)$ spectroscopy to determine how the interactions among the electrons of a systems affect its microscopic and macroscopic properties has been widely proved, the understanding of double ionisation processes from systems more complicated than simple atomic targets is far from being completely achieved.
This thesis is devoted to the study of double ionisation processes from solid surfaces and inter-

faces. We measured direct and core-resonant DPE spectra of different materials and observed how the two-electron dynamics is influenced by the correlated motion of the electrons in both the initial and final states of the reaction.

- In chapter 1 we mainly review the topic of direct and indirect double-photoionisation in atoms and solids. The evolution of the DPE technique, from the very beginning to the present days, is illustrated paying particular attention to the role of electron-electron correlations in determining two-electron dynamics.

- In chapter 2, 3 and 4 the theory of two-electron emission is discussed. In chapter 2 we describe the theory of direct DPE from solids surfaces, showing that the simultaneous emission of two electrons from a system corresponds to the absorption of a photon in the center-of-mass of the electron-pair. Therefore it can be considered as the photoemission of a quasi-particle whose energy and momentum are given by the sum of the electrons energies and momenta, respectively. Chapter 3 is devoted to the description of core-resonant DPE processes, paying particular attention to highlighting the differences between one- or two-step model for the description of indirect double-photoionisation. In chapter 4 the case of DPE from circularly polarised photons is outlined. We work out the conditions under which the spectrum of correlated electron-pairs shows a chiral character, i.e. depends on the helicity of the incident photon. It is also discussed how the presence of a well-defined core-hole state is expected to influence the chirality of the core-resonant DPE spectra.

- In chapter 5 we introduce electron-electron coincidence spectroscopy paying particular attention to the description of the experimental apparatus used in this thesis. The optimisation of the experimental conditions is also discussed.

- In chapter 6 we present the direct and core-resonant DPE spectra from the valence band of Cu(001). By the use of linearly and circularly polarised light we study how the presence of a preferred direction in the experimental set-up (the light polarisation vector and the light incident direction in first and second case, respectively) affects the energy and angular distribution of the emitted electron-pairs. In the case of linearly polarised light, the core-resonant DPE spectrum is determined by the alignment of the core-hole with respect to the quantization axis. Thus, a selection in the emission angles of the two emitted electrons is expected to give informations about the magnetic sub-levels of both Auger and photoelectrons wavefunctions.
  In the case of circularly polarised light interesting informations can be obtained by studying the chiral or achiral behaviour of the DPE pairs. For a paramagnetic system, in which the initial system has no preferred orientation, the chirality in the initial state is carried by the incident photon. After the photon is absorbed its chirality is transferred either to the emitted electron-pair or to the two-hole pair in the residual ion. In the first case, the detected electron-pair wavefunction is chiral and the DPE intensity changes when the helicity of the light is inverted, leading to the appearance of circular dichroism (CD). The chiral/achiral behaviour of the correlated pairs depends on the spatial symmetry of the two-hole final state so that CD in DPE can be regarded as a powerful tool to study the symmetry properties of the two-particle wavefunctions in matter.

- In chapter 7 we present the direct and core-resonant DPE spectrum of sulphur adsorbed on clean Cu(001) upon the absorption of circularly polarised photons. In this particular case, in which the lifetime of the core-hole excited in the resonant transition is much longer than the

Cu(001) case, we can observe the energy distribution and chirality of the DPE pairs when a two-step description of the core-resonant process is valid. Complementary informations about how hole-hole correlations affects the electronic properties in the valence band of the system can also be obtained by studying the line shape of the DPE transitions.

- In chapter 8 we present and discuss DPE spectra from Ag(001) surface. This part of the work is devoted to the study of electron-hole interactions following the initial ionisation in core-resonant DPE processes. Core-resonant DPE represents an interesting way to probe the electron-dynamics around a core-hole in the attosecond time-scale. In this sense DPE experiments can be considered as "pump" and "probe" experiments, in which the pump signal is provided by the photoelectron and the probe corresponds to the correlated Auger electron. In order to get informations on the early stages of the photoemission process we take into consideration the case in which the two-step description of the indirect double-photoionisation breaks down. Indeed, in this case the high rate of the decay does not allow the singly-ionised state to relax and all the excitations due to fast electron-screening can be absorbed and carried away by the probe (Auger electron). With this experiment we expect to identify the effects of electron-hole interaction in the line shape of core-resonant DPE spectra.
- In the conclusions we summarize the results obtained and outline future works and developments.

Chapter 1

Study of electron-electron correlations by DPE

In this chapter we will present a short review on the state of the art of Double-Photoemission. The evolution of DPE spectroscopy, on both theoretical and experimental grounds, will be presented from the very beginning to the present days paying particular attention to the role of electron-electron correlations in the determination of two-electron emission dynamics.

1.1 The beginning

The first experiment pointing out the importance of the electronic correlations to describe the simultaneous emission of electron-pairs was carried by Carlson in 1967 [28]. In his work the author investigated the probability of ejecting two or more electrons by the interaction of a photon with the outermost shell of gaseous He, Ne and Ar by means of single photoemission and mass charge spectroscopy.
It was observed that the line shape of photoemitted electrons energy distribution shows considerable contributions in its low kinetic energy side. These contributions add to the characteristic photo-line associated to the emission of one electron from the outermost *s* or *p* levels of the rare gases. The extra emissions in the electron distribution were ascribed to satellite processes, accompanying the principal ionisation, in which a second electron is excited to a less bound level (electron shake-up) or to the continuum (electron shake-off). Energy conservation in these type of processes implies that the first electron must leave some of its energy to the second according to the relation,

$$h\nu = E_1 + E_2 + I_1 + I_2, \tag{1.1}$$

where $h\nu$ is the photon energy, E_1 and E_2 are the electrons' kinetic energies, and I_1, I_2 are the energy needed to the ionisation and excitation of first and second electron, respectively. The probability of these kind of processes was initially described, in a single-particle approximation, by the product of a matrix element for a dipole transition, describing the photoemission, and a monopole matrix element for the electron shake-up (shake-off). For example, the matrix element for the simultaneous emission of two *s* electrons from atomic He can be written as,

$$M_d = \langle 1s\,|\mathbf{d}|\,\varepsilon_p\rangle\,\langle 1s|\,(E-\varepsilon_p)s\rangle\,, \tag{1.2}$$

where the first electron, due to dipole selection rules, is emitted as a p-wave of energy ε_p. The second electron is emitted as an s-wave whose energy is given by the difference of the energy

above the double ionisation threshold, $E = h\nu - I_1 - I_2$, and the energy of the first electron ε_p. Additional measurements, by means of charge spectroscopy, were carried on in order to measure the relative abundances of doubly to singly charged ions resulting from the photo-ionisation of the rare gases. The author observed that multiple emission intensity follows the behaviour observed for electron shake-off [29]. Despite that, the calculated probability of electron shake-off as the result of a sudden change in the effective electronic charge was in each considered system considerably lower than the experimental data obtained with charge spectroscopy. On the contrary, the data were very well described by the calculations by Salpeter and Zaidi [30] in which the transition probability, proportional to the dipole matrix element,

$$M_d = \int \psi_f(\mathbf{r}_1, \mathbf{r_2})(\mathbf{d}_1 + \mathbf{d}_2)\psi_i(\mathbf{r}_1, \mathbf{r}_2) d\mathbf{r}_1 d\mathbf{r}_2, \tag{1.3}$$

is calculated by means of two-particle wavefunctions for the initial, ψ_i, and final, ψ_f, state, respectively, with electron correlation included in the initial state.

This suggested the need of a many-body approach which includes electron correlation for the description of processes in which two electrons are removed from a system after the absorption of a single photon.

1.2 The He atom

The small cross section of the DPE processes and the need to detect both the emitted electrons to determine the complete two-particle emission dynamics set huge challenges to the experimentalists. These challenges have been overcome in the latest years by the birth of electron-electron coincidence spectroscopy [31, 32], as well as the advent of high brilliance third generation synchrotron radiation sources [33] and the development of new electron spectrometers which allow the simultaneous detection of electrons with several energies over a large solid angle. This explains why, despite Carlson's experiment dates back to 1967, the first experiment studying direct DPE from atomic targets was only performed 25 years later [34].

The archetypal system to study direct DPE is the Helium atom, the most simple two-electron system. In this system the absorption of a photon of energy larger than 79.004 eV, i.e. the He double ionisation potential I^{2+}, may lead to a bare nucleus and two free electrons according to the process,

$$h\nu + \mathrm{He} \rightarrow He^{2+} + e^- + e^-. \tag{1.4}$$

The final state is fully characterised by the momenta $\mathbf{k}_1$ and $\mathbf{k}_2$ or alternatively by the kinetic energies E_1 and E_2 and the spherical angles Ω_1, Ω_2 of the two electrons. The excess energy of the process $E = h\nu - I^{2+}$ is shared between the emitted particles according to $E = E_1 + E_2$.
The process in (1.4) is fully described by a triple differential cross section (TDCS $= \frac{d^3\sigma}{dE d\Omega_1 d\Omega_2}$), which describes the correlated motion of the electron-pair for a fixed energy sharing $R = \frac{E_1}{E_2}$. It was firstly calculated by Huetz *et al.* (1991) [35] following Wannier formalism [36]. Taking into account the symmetries of the two-electron final state wavefunction the authors showed that the TDCS for the emission of two interacting electrons is given exactly by,

$$\frac{d^3\sigma}{dE d\Omega_1 d\Omega_2} = \left| a_g(E_1, E_2, \theta_{12})(\cos\theta_1 + \cos\theta_2) + a_u(E_1, E_2, \theta_{12})(\cos\theta_1 - \cos\theta_2) \right|^2, \tag{1.5}$$

where $a_g(E_1, E_2, \theta_{12})$ and $a_u(E_1, E_2, \theta_{12})$ are two complex amplitudes, respectively symmetric and antisymmetric with respect to the exchange $E_1 \leftrightarrow E_2$, which describe the dynamics of the pair.

For this reason these amplitudes only depend on the energies and on the mutual angle θ_{12} of the emitted electrons. The factors containing the emission angles $(\cos\theta_1 \pm \cos\theta_2)$ result from the selection rules of photon-atom interaction, i.e. from the character of the final state which, in the He case, is described by the quantum numbers $L = 1$ and $M = 0$ ($^1P^0$).

In the case of equal sharing, $E_1 = E_2$, the antisymmetric amplitude vanishes and the TDCS reduces to:

$$\frac{d^3\sigma}{dEd\Omega_1 d\Omega_2} = |a_g(E_1, E_2, \theta_{12})|^2 (\cos\theta_1 + \cos\theta_2)^2. \tag{1.6}$$

This expression clearly shows that back-to-back emission in equal sharing is forbidden because $\mathbf{k}_1 = -\mathbf{k}_2$ implies $\theta_1 = \pi - \theta_2$, and therefore $\frac{d^3\sigma}{dEd\Omega_1 d\Omega_2} = 0$. It has also to be noticed that the amplitudes $a_{g,u}$ alone must have their maxima for back-to-back configuration ($\theta_{12} = \pi$) because the Coulomb repulsion between the negatively charged particles tend to drive the electrons in opposite directions. From this very simple ideas Huetz et al. predicted that the DPE cross section for the He atom, due to the competitive behaviour of the two factors, should have a "butterfly" shape in polar coordinates, as the one depicted in Fig. 1.1.
This theoretical prediction was firstly experimentally verified by Schwarzkopf *et al.* [37] in 1993. In their work the authors measured the TDCS for double photoemission from atomic He by means of electron-electron coincidence spectroscopy in the simple case of equal energy sharing and of a geometry in which one electron spectrometer was aligned to the major axis of the light polarisation ellipse and the other one was turned around the photon beam incident direction. The obtained data, acquired at an excess energy $E = 20$ eV, were compared to an approximated version of (1.6) in which the complex amplitude is replaced by a Gaussian function, having the property to be maximum at $\theta_{12} = \pi$,

$$|a_g(E/2, E/2, \theta_{12})| = a(E) \exp[-4\ln 2(\theta_{12} - \pi)^2/\theta_{1/2}^2]. \tag{1.7}$$

Here $a(E)$ is a scaling factor and the width of the Gaussian at half maximum $\theta_{1/2}$ gives the strength of angular electron correlations between the two electrons at equal sharing: these correlations are the highest when $\theta_{1/2}$ is small, the lowest when $\theta_{1/2}$ is large. The Wannier theory [36] predicts values of the Gaussian width which increases with the excess energy as $\theta_{1/2} = 91 \cdot E^{0.25}$ ($\theta_{1/2}$ in degrees units and E in eV).
The results, represented by the dots with the error bars in Fig. 1.1, were not reproduced by the model calculated at $\theta_{1/2} = 91 \cdot 10^{0.25} = 161.8^\circ$ represented by the dotted line. On the contrary, good agreement between experiment and theory was obtained by a least-squares fit of the TDCS to the experimental data performed using $\theta_{1/2}$ and the amplitude of the TDCS as free parameters, the dashed curve in Fig. 1.1. From the fit the authors got $\theta_{1/2} = 76.5 \pm 5.3^\circ$, a value well below the predicted value of 161.8°.

Since the pioneering experiment of Schwarzkopf *et al.*, plenty of similar experiments have been performed taking into consideration different excess energies E, sharing ratios $R = E_2/E_1$ and types of polarisation. All these experiments, reviewed in [38, 39], show that the Wannier predictions are consistent with the experiments only for excess energies near the double ionisation threshold $E = 0.1, 0.2$ eV, but overestimate the strength of angular correlations already at $E = 1$ eV. These results allowed a direct observation of the fact that the correlations repelling the electrons into different directions are very intense at threshold, where the kinetic energies are very small, and they become negligible as long as the kinetic energies increase.

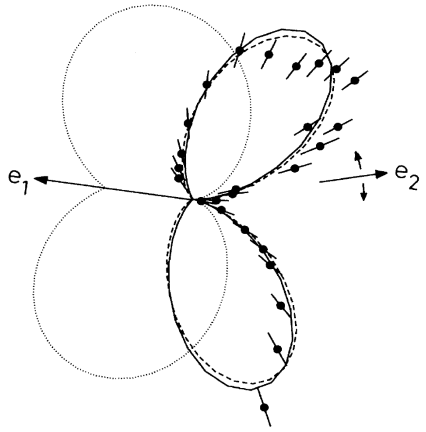

Figure 1.1: Experimental (dots) and theoretical TDCS for the double-photoionisation of He at $h\nu = 99$ eV ($E = 20$ eV) in the plane perpendicular to the photon beam. The direction of the electron e_1 is fixed along the major axis of the polarisation ellipse, while the direction of the electron e_2 is rotated within the plane. The solid line shows the predictions of three body calculations. The dashed curve is a fit using (1.5) and(1.7). The dotted curve, which does not reproduce the data, uses the same expression but with the value of the angular correlations strength deduced from the Wannier law. See [35] for further details.

1.3 Circular dichroism in He DPE

Berakdar and Klar in 1992 [25] and Berakdar *et al.* in 1993 [26] predicted that He TDCS for double photoionisation measured by circularly polarised light should display a dependence on the helicity of incident radiation, i.e. a non vanishing circular dichroism, CD. The details of the theory will be given in section 4.1 but, qualitatively speaking, this effect is due to the fact that, according to parity conservation, the helicity of the photon is transferred to the He atom and the spectrum of this excited system depends on the handedness of the photon polarisation. Indeed, theoretical studies demonstrated that the dipole matrix elements calculated on the two-particle wavefunctions produce TDCS with a part being antisymmetric with respect to the angular and energy exchange of the two electrons. This portion being the source of dichroism. The properties of the antisymmetric part implies necessary conditions to observe circular dichroism that can be summarized as follows:

(i) The two electrons unevenly share the excess energy, $E_1 \neq E_2$.

(ii) The direction of the incident photon, and the directions of the two ejected electrons do not lie on the same plane.

(iii) Both electrons must be detected.

The size and sign of the circular dichroism, being effects of the electron correlations, depend sensitively on the two-electron wavefunctions used in the calculations. In particular CD can be very useful to the study of the electronic interactions in the final state of the DPE process.

First observations of CD in the double photoionisation of helium atoms were achieved by Viefhaus *et al.* [40]. In their experiments the authors made use of coincidence spectrometer made up by three electron analysers to detect the DPE pairs with three different relative emission angles between the electrons, $\theta_{12} = 85°, 125°, 150°$. In order to satisfy condition (ii) the analysers were lying in the plane perpendicular to the incident photon direction.

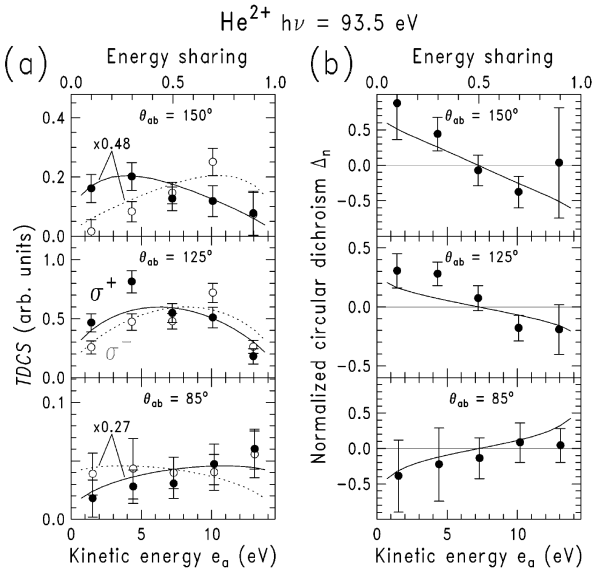

Figure 1.2: (a) The helium DPE cross section versus kinetic energy sharing at $h\nu = 93.5$ eV measured at different relative emission angles θ_{ab} of the electrons. The circles represents the measurements with right (full) and left (open) helicity of the circularly polarised light. The continuous and dotted lines are results of theoretical calculations. (b) Normalised circular dichroism for the three relative emission angles. The lines represent the theoretical predictions. Image from [40].

The TDCS with positive (σ^+) and negative (σ^-) helicity of the circularly polarised radiation were measured (at different θ_{12}) as a function of the energy sharing $R = E_2/E_1$, Fig. 1.2(a). The authors observed that a change in the light helicity corresponds, for the TDCS, in a mirror image with respect to a reflection at the equal energy sharing line $E_1 = E_2 = 7.25$ eV. This is because changing the helicity of the radiation, as well as changing the labels ("fast" or "slow") of the electrons leads to the same geometry of the experiment. In addition, the relative degree of circular dichroism,

$$\mathrm{CD} = \frac{\mathrm{TDCS}(\sigma^+) - \mathrm{TDCS}(\sigma^-)}{\mathrm{TDCS}(\sigma^+) + \mathrm{TDCS}(\sigma^-)}, \tag{1.8}$$

shown in Fig. 1.2(b), vanishes for equal energy sharing according to condition (i). In fact, there is no chirality in the set-up when it is not possible to distinguish between the two emitted electrons. The experimental results [dots in Fig. 1.2(b)] were compared to numerical calculations using Hylleraas-type wave functions [40] [continuous lines in Fig. 1.2(b)] and showed good qualitative agreement with the theoretical predictions. The first observation of CD in a DPE experiment demonstrated the unquestionable importance of two-electron processes to get informations about the correlated behaviour of the particles composing a system.

1.4 Direct DPE on solids

In the latest years, a general theory to describe the direct DPE from solids was developed by J. Berakdar [7]. The DPE cross section was obtained by the calculation of the dipole transition matrix elements between two-electron wavefunctions describing the initial and final states. Two extreme

cases were considered: the emission from localised electronic states, e.g. the valence levels of transition metals, and from delocalised ones, i.e. the valence band of s-p metals. In both cases it was demonstrated that the DPE transition probability vanishes if one neglects electron-electron correlations. Indeed, because of the single-particle nature of the dipole interaction, the electric field of the photon directly interacts with only one electron. However, a photon can be absorbed by the centre-of-mass of two interacting electrons leading to their simultaneous emission. The spectra of emitted electron-pairs follows propensity rules given by the scalar product of the centre-of-mass vector momentum of the pairs and the light polarisation vector. Furthermore, it was shown that diffraction from the crystal lattice occurs when the centre-of-mass wave vector of the pairs changes by a reciprocal lattice vector. Berakdar's work pointed out that, to some extent, the DPE process can be regarded as the single photoemission of a "quasi-particle" formed by two correlated electrons.

The first attempt to perform DPE on condensed matter was made on van der Waals solids of rare gases using a photon energy range $20 - 56$ eV [41]. The used spectrometer permitted the measurement of electron-electron coincidences without energy or angular discrimination. The coincidence yield was surprisingly high when compared with theoretical DPE cross sections. The authors invoked a two-step process, i.e. single photoemission followed by cascade electron-impact ionisation, to explain the high coincidence rate, rather than direct valence DPE.

This pioneering work was followed, a few years later, by the first experiment on clean metal surfaces performed by Hermann *et al.* [42]. This experiment, whose details will be given in section 2.4, represents the first experimental evidence of direct DPE from the valence band of solids. The authors made use of a time-of-flight coincidence spectrometer to measure the kinetic energy distribution of correlated electron-pairs emitted from Cu(001) and Ni(001) surfaces. The photon energy was chosen to measure the energy sharing probability of electron-pairs emitted from electronic states located near the Fermi level. The obtained data were in good agreement with the predictions of Berakdar's theory. Both the theoretical and experimental energy sharing distributions display a minimum for equal energy sharing and symmetric conditions, which is a signature of the prevalence of direct DPE events. This is because, the dipole transition matrix elements for direct DPE depends on the scalar product of the light polarisation vector and the sum of the momenta of the emitted electrons. In the adopted geometry this product vanishes at equal energy sharing. On the contrary, two-step mechanisms are characterised by a maximum in the cross section at equal energy sharing [43]. Although one- and two-step mechanisms are indistinguishable on the basis of energy balance, direct DPE can be made the dominant process by suitably choosing the kinematics under which the electron-pairs are collected.

1.5 DPE reveals the exchange-correlation hole

One of the most relevant achievements obtained by direct DPE on solids is represented by the detection of the exchange-correlation (xc) hole. The correlated motion of electron-pairs is a consequence of the Pauli principle and of the Coulomb interaction. This leads to the tendency of the electrons to stay away from each other and to the well-known concept of exchange-correlation hole, i.e. a zone of reduced electronic charge which surrounds each electron of a system. This concept, introduced for the first time by Weigner and Seitz [44] and Slater [45] about 80 years ago, represents an integral part in many theories of modern solid state physics. It is for example currently used in the definition of the exchange-correlation energy functional of local density approximation (LDA) in density functional theory (DFT).
Despite its wide use in many field of solid state physics no experimental proof of the xc hole was

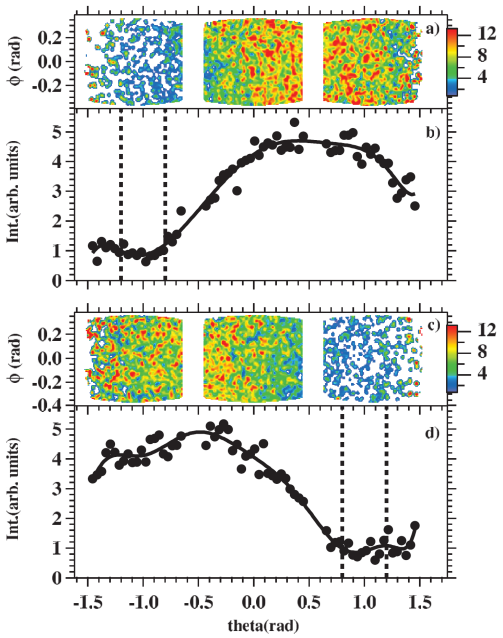

Figure 1.3: False color maps of 2D angular distributions (upper panels) and resulting electron yield profiles (lower panels) for pairs of electrons with energy $E_{fast} = 23$ eV and $E_{slow} = 12$ eV. The direction of the fixed position electron is at either $\theta = -1.0$ rad, for panel (a) and (b) or $\theta = 1$ rad, for panel (c) and (d). The dashed vertical bands indicate the boundaries of the angular region accepted by the fast electron detector. The depletion in the coincidence signal around the position of the fixed electron is interpreted as a direct evidence of the xc hole [24].

available until the advent of DPE. Theoretical studies demonstrated that the presence of the xc hole manifests as a depletion zone of the DPE cross section around the emission direction of one of the two electrons [46, 47, 48]. These predictions were verified by Schumann *et al.* [23, 24]. In one of their experiments the authors made use of three micro-channel plate detectors and time-of-flight technique to measure the energy and angular distribution of electron-pairs emitted from a Cu(111) surface upon the absorption of 50 eV linearly polarised photons. Emission from Cu 3*d* bands was considered, with an excess energy $E = 35$ eV, and unequal energy sharing corresponding to $E_{fast} = 23$ eV and $E_{slow} = 12$ eV, for the "fast" and "slow" electron, respectively. The angular distribution of the DPE intensity obtained by fixing the emission direction of the fast electron, Fig. 1.3, shows that the fast electron is always surrounded by a reduced slow electrons intensity. The angular extension of the depletion zone (~ 1.2 rad) does not depend on the position of the fast electron and on the energy of the electrons, cfr. Fig. 1.3(b) and (d), and can be considered the experimental manifestation of the xc hole.
The experiments performed by Schumann *et al.* proved once more the incredible potentiality of the DPE technique to get an insight into the role of electron-electron correlation in determining the electronic properties of solids.

1.6 Indirect double-photoemission

In targets with a more complicated structure than He, double ionisation may also proceed by an indirect process. In this case the absorption of a photon results in the formation of a singly ionised state which is embedded into the double-ionisation continuum. This excited single-hole state may decay into the continuum through an auto-ionisation process, in which the rearrangement of the electrons of the singly-ionised system may lead to a double ionisation via the emission of an (Auger) electron.
When the lifetime of the intermediate state is long enough to consider it as a well-defined isolated state in the double ionisation continuum then the indirect process can be regarded as a sequential process, consisting of two incoherent steps. In this picture the two ejected electrons, i.e. the photoelectron and the Auger electron, can be distinguished according to their kinetic energy and the long-lived intermediate state can be considered a discrete state. On the contrary, when the lifetime of the intermediate state is shorter than the relaxing time of the singly-ionised system the Auger decay takes place from a non-stationary state spanning on all the possible single-hole states. In this case the indirect DPE acts as a coherent single-step process that can be considered a resonance in the direct DPE continuum. The distinction between photo- and Auger electron does not hold any more and the emitted particles can share the available energy in the same way of direct DPE.

The distinction between one- and two-step model for indirect DPE was first proposed by Gunnarson & Schönhammer [8] and Ohno & Wendin [49] in 1980; details will be given in chapter 3. A striking evidence of the appropriateness of the core-resonant double photoemission model was obtained by van Riessen *et al.* in 2010 [15], by measuring the two-particle emission spectrum from clean Cu(001) surface. The authors made use of linearly polarised light of energy far above the Cu $3p$ ionisation threshold to observe both direct and core-resonant (Auger decay of Cu $3p$ holes leaving the system with two valence band holes, $M_{23}VV$) DPE pairs emitted from Cu valence band. They observed that the energy distribution of the DPE pairs, measured over a wide energy range ($\sim$ 30 eV for each electron), is the same in both direct and core-resonant processes. The pairs are shown to share their sum energy continuously while jointly conserving the available energy of the process. In the energy sharing curves obtained by reporting the coincidence yield as a function of the differences of the two electrons kinetic energies (Fig. 1.4), they observed that the almost constant DPE signal resonantly increases in the vicinity of the Auger and photoelectron characteristic energies, thus confirming the validity of the models in which the Auger decay of a core-hole is described as a coherent single-step process with the emitted electrons representing a correlated two-particle state.

1.7 Auger-photoelectron coincidence spectroscopy (APECS)

The most complete way to study two-hole final states created via indirect double-emission processes is to detect the photoelectron of the primary ionisation and the Auger electron which are correlated in time, and by analysing the two partners in energy and ejection angle.
The schematic diagram of an APECS experiment is reported in Fig. 1.5. It can be used to elucidate the usefulness of the coincidence technique to understand the properties of inhomogeneous systems, e.g. a solid composed by two different types of atoms, indicated by A and B in Fig. 1.5. This is a suitable model to represent any kind of energy-splitting in the core-levels of a system, e.g. different species of atoms, atom of the same species in different sites and chemical environment or even the spin-orbit interaction within the same atom. In conventional photoemission the

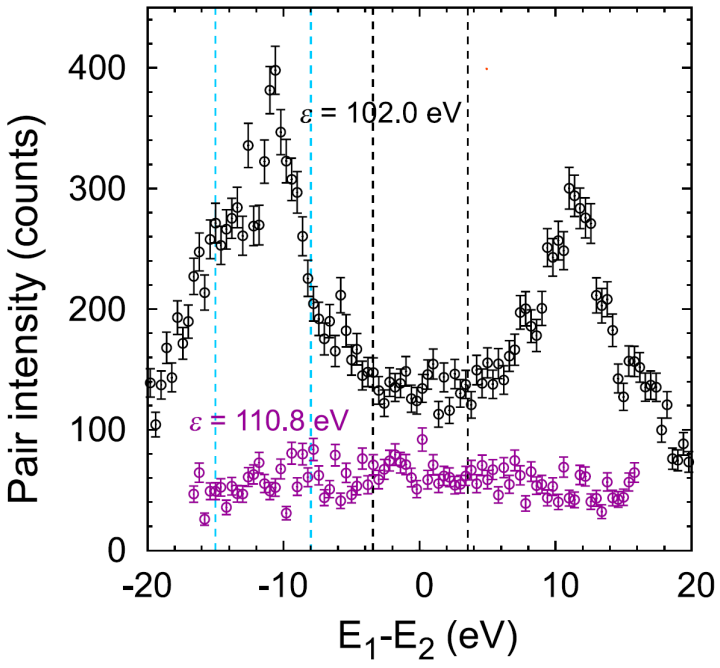

Figure 1.4: The energy sharing curve corresponding to electron-pairs emitted by the core-resonant DPE resulting in ^1G $M_{45}M_{45}$ final state (black circles) and by direct DPE from the top of the Cu *d* valence bands (magenta circles) [15].

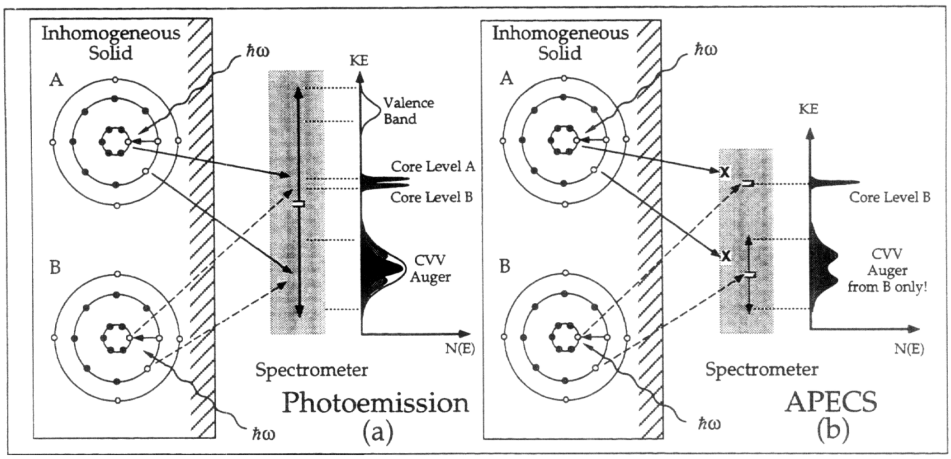

Figure 1.5: Schematic diagram of the acquisition of hypothetical photoemission (a) and APECS (b) spectra from an inhomogeneous solid. In this case the inhomogeneity is given by the presence of two different atoms, A and B, that give rise to two energy-split photoemission peaks. The ability of APECS to isolate overlapping structures is illustrated. Image from [50].

entire kinetic energy distribution of the emitted electrons is analysed, Fig. 1.5(a). It contains the two energy-split core-level peaks, as well as the valence and Auger bands. As the band parts of the spectrum integrate over many sites, they give an average of the contributions from both atoms which are difficult to disentangle. Fig. 1.5(b) shows how APECS can be used to resolve the different contributions to the Auger spectrum and to obtain informations about the local electronic structure in each site. In these measurements two (or more) electron analysers are used; one is set to detect the photoelectrons and the other to detect the Auger electrons. In the illustrated example, Fig. 1.5(b), one analyser detects the photoelectrons from core-level associated with site B, hence only the Auger electrons associated with the decay of this particular site are accepted by the other analyser. The resulting coincidence spectrum is characteristic of the local density of states associated to the selected site. The APECS technique merges the unique elemental sensitivity of photoemission and the sensitivity to valence band electronic structure and 2-particle properties of Auger spectroscopy.

In the pioneering experiment performed in the late 70's by Haak *et al.* [31], the two electrons emitted by the copper L shell ionisation process were detected and correlated in time. This experiment demonstrated the feasibility of the APECS technique and its capability to disentangle the overlapping contributions due to different decays. In this case a selection was applied to the $2p$ spin-orbit doublet by measuring the $L_{23}VV$ Auger spectrum in coincidence with $2p_{1/2}$ and $2p_{3/2}$ photoelectrons. The authors succeeded in unambiguously determining the L_3VV and L_2VV Auger lines and in separating the Coster-Kronig-preceded transitions from the main Auger lines. This experiment also showed a drastic suppression of the background due to multiple inelastic scattering with respect to conventional Auger and photoelectron spectra.

In the same work it was also proposed the possibility to use APECS to perform core photoemission with an energy resolution which is not limited by the lifetime broadening of the core-hole state [31, 51]. This effect arises from the single-step nature of the Auger decay, i.e. to the fact that energy conservation must be applied to the emitted electron-pair rather than to the single particles separately. In this picture the uncertainty affecting the kinetic energies of photo- and Auger-electron correlated in time only depends on the lifetime broadening of the two-hole final state which is much more narrow than the single-hole broadening. These predictions suggested the exciting possibility of studying interesting structures associated with chemical shifts, surface shifts, many-body structures, etc., that are obscured by the broadening due to the short Auger decay lifetime of the core-holes. The first experimental evidence of the line narrowing was obtained by Jensen *et al.* [52] by measuring the Cu(001) $3p$ photoemission lines in coincidence with the M_3VV Auger line. The authors observed a consisting narrowing of the core lines from their 2.2 eV core-lifetime-broadened width to 1.0 eV, which represents the intrinsic width of the two-hole Auger final state.

1.8 Hole-hole correlation energy determination by APECS

One of the major achievements of the APECS technique is represented by the possibility to determine the hole-hole correlation energy in the valence band of solids by studying the Auger electrons energy distribution. The Auger line shape is strongly influenced by electronic correlations and the case which involves valence band holes in the final state can be predicted by the Cini-Sawatzky theory [18, 19]. In their works, independently developed in 1977, the authors derived the core-valence-valence (CVV) Auger line shape by calculating the two-particle Green function within the framework of the Hubbard model [1]. The line shape, proportional to the 2-particle density of states (2p-DOS), depends on the competitive contributions of the kinetic energies and repulsion

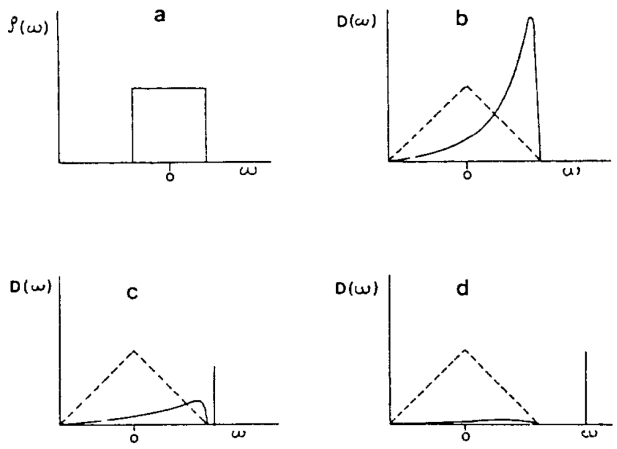

Figure 1.6: Effects of the 2-hole interaction on the 2-particle density of states $D(\omega)$ for a system described by a constant single-particle density of state $\rho(\omega)$. In (a) the model DOS is shown. The corresponding non-interacting 2p-DOS is represented by the triangular dotted line. The interacting $D(\omega)$ for $U/W = 0.5$, 0.9 and 1.5 are reported in (b), (c) and (d), respectively. The vertical bars represents the split-off bound states. Image from [18].

energy of the holes in the final state. The first is determined by the valence band width W, the second by the Hubbard hole-hole correlation energy U. When the kinetic energy of the holes is dominant, $U/W \ll 1$, the two holes can be considered free to move within the valence band, thus they do not interact with each other and the Auger line shape is proportional to the self convolution of the single particle density of states. On the contrary, when the repulsion energy of the holes is comparable or larger than their kinetic energy, $U/W \gtrsim 1$, singularities appear in the low kinetic energy portion of the Auger spectrum, similar to a quasi atomic structure, which are called two-hole resonances and are due to two-hole states localised on a single atomic site. The prediction of the Cini-Sawatzky theory, as presented in [18], are illustrated in Fig. 1.6 in the simplest case of a system described by a constant single-particle density of states $\rho(\omega)$. The non-interacting 2p-DOS, described by the self-convolution of $\rho(\omega)$, is shown as the dotted line in Fig. 1.6 and corresponds to a triangular shaped function whose width is twice the valence band width. The evolution of the interacting 2p-DOS, $D(\omega)$, as a function of the dimensionless quantity U/W is shown in panels (b) - (d). For $0 \leq U/W \leq (2\ln 2)^{-1} \sim 0.72$, solid line in Fig. 1.6(b), the non-interacting line shape is deformed and the maximum at $\omega = 0$ moves towards higher ω values. It has to be noted that in this notation, the independent variable ω corresponds to the difference between the energy available in the process $(E_i - E_f)$ and the Auger electron kinetic energy (E_k), $\omega = E_i - E_f - E_k$. Thus, as long as the hole-hole interaction increases the spectral weight of the Auger spectrum is progressively transferred to more bound states.
When $U/W > (2\ln 2)^{-1}$, panel (c) of Fig. 1.6, a sharp bond state appears outside of the band region and once this happens the intensity of the Auger spectrum is progressively concentrated inside this split-off state. When $U/W > 1$, panel (d), 90% of the intensity is contained inside the sharp state while the band part of the spectrum contributes only for 10%.

A case of study is represented by the $L_{23}M_{45}M_{45}$ Auger spectrum of metallic Cu [51]. This spectrum, shown in Fig. 1.7, is an example of a quasi-atomic spectrum due to the large $d-d$

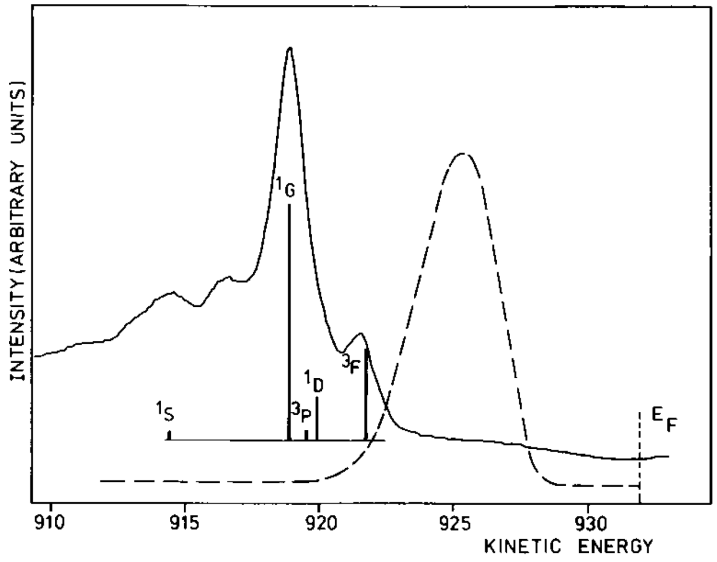

Figure 1.7: The $L_3M_{45}M_{45}$ Auger spectrum of Cu (solid line) [51]. The vertical bars represent the energies and relative intensities of the d^8-like final state multiplets. The dashed line represents the self convolution of the 3d bands density of states.

Coulomb interaction ($U_{dd} \sim 8$ eV) with respect to the d-band width ($W \sim 3.5$ eV) in Cu. The LVV Auger line shape is dominated by sharp peaks that can be associated to the atomic d^8-like multiplets. Since the Coulomb interaction is dominant in the final state, it can be described in the L-S representation leading to the atomic multiplet terms ^1S, ^1D, ^1G, ^3P and ^3F indicated by the vertical bars in Fig. 1.7. The different energy positions of the multiplet terms correspond to different values of the hole-hole correlation energy U, which appears to be maximum (~ 12 eV) for the ^1S and minimum (~ 5 eV) for the ^3F final-state, respectively. The dashed line represents the self convolution of the single particle density of states which would represent the spectral distribution if $U = 0$. In this case, where $U/W > 1$, the intensity of the band-like part of the Auger spectrum is almost negligible and is extremely difficult to distinguish it from the background.

In recent years Cini-Sawatzky theory used in conjunction with APECS measurements has proved to be a very powerful tool to determine the hole-hole correlation energy in solids. Very good results have been obtained by Arena *et al.* [53] and Butterfield *et al.* [54] in the case of silver and palladium, respectively. In both cases the authors determined the intrinsic line shapes of the overlapping M_4VV and M_5VV Auger spectra by measuring them in coincidence with $3d_{3/2}$ and $3d_{5/2}$ photoelectrons, respectively. Due to the fact that for both the transition metals $U/W \gtrsim 1$, they observed that neither band-like nor atomic-like line shapes, used separately or in combination, give a satisfactorily description of the measured Auger spectra. Instead, they can be perfectly described by the Cini-Sawatzky theory when it is applied separately to each component of the multiplet structure of the d^8 Auger final state. Fits to the APECS data using the sum of a CS distortion of the final-state multiplet splittings for the M_4VV and M_5VV Auger transitions allowed the determination of the correlation energies of all the multiplet terms in the two-hole final state of both Ag and Pd.

1.9 Angle-Resolved APECS

The final-state discrimination power of APECS is made more incisive if one performs angle-resolved measurements, i.e. by selecting the photoelectron and Auger electron emission angles. The changes in the APECS line shape, within an atomic framework, are ascribed to a different degree of the alignment of the intermediate state which is given by the imbalance in the population of its magnetic sub-levels.
In a simple closed shell model the intermediate state is fully described by the quantum numbers of the core-hole. At different detection angles of the emitted electrons, the sub-levels m_l contributions related to the inner core-hole are weighted in a different manner. This means that the photoelectron partial waves, having different magnetic quantum number m_l values, have different angular distributions. For example, in the case of linearly polarised light, whenever the photoelectron is collected in the direction of the light polarisation axis only photoelectrons with $m_l = 0$ are detected [55, 56]. The same is for the Auger electron, whose quantum numbers are related to the core-hole ones by the selection rules for the Auger process [57]. Hence, a moderate angular resolution allows to observe decays originating from core-hole states whose alignment can be controlled by varying the mutual directions of light polarisation and momentum vectors of the two electrons, as pointed out by Gotter *et al.* [58, 14] and Stefani *et al.* [59, 60]. In one of these works [58] the authors measured the Auger coincidence spectrum associated to $M_5N_{45}N_{45}$ decay from $(\sqrt{3}\times\sqrt{3})R30^\circ$ -Sn/Ge(111) at different detection angles of the photoelectron. It was observed that the portion of the spectrum associated to triplet two-hole final states is suppressed with respect to the one ascribable to singlet ones when the photoelectron is detected in the direction parallel to the light polarisation vector $\hat{\varepsilon}$. This effect is not observable in other kinematic conditions, i.e. when the photoelectron forms a 55° angle with $\hat{\varepsilon}$. Since the multiplet terms that give rise to the peaks in the Auger spectrum are given by the combinations of the magnetic sub-levels of the two final-holes, the different geometries allow to weight in a different way the multiplet terms, and thus the coincidence Auger spectrum changes depending on the detection angle of the photoelectron. In the mentioned case, in which the emitting atoms are part of a crystal, diffraction of the Auger and photoelectron wavefunctions by the surrounding atoms was also taken into account. It was observed, by means of multiple scattering simulations, that diffraction for the crystal lattice do not forbid to interpret the Auger photoelectron angular distribution as the angular distribution of Auger electrons emitted after the decay of a polarised core-hole, where the polarisation of the hole is determined by the angular selection of the photoelectron [14].

The spin-selectivity in angle-resolved (AR)-APECS has been used in recent papers to probe the electronic structure in magnetic materials [62, 63, 61]. Indeed, in magnetic systems, where exchange and correlation effects are dominant, the Auger line shape is often broad and featureless, does not change when crossing the temperatures of magnetic transitions and does not furnish any information about electronic correlations which are potentially contained in the Auger spectra. On the contrary, angle-resolved APECS is able to resolve the contributions due to the different multiplet components of the final state, in particular high-spin and low-spin components, and to study the Auger line shape even in complex magnetic materials. In one of the aforementioned works [61] AR-APECS has been used to investigate the local magnetic properties of anti-ferromagnetic NiO/Ag(001) films. The authors measured the Ni MVV Auger spectra in coincidence with Ni $3p$ photoelectrons at different angles (Fig. 1.8), below (upper panel) and above (lower panel) the paramagnetic/anti-ferromagnetic transition (Néel) temperature, T_N, of the system. A sharp multiplet structure is observed in the Auger line shape when the sample is in its anti-ferromagnetic phase ($T < T_N$). By comparing the experimental data and the calculated spin-resolved Auger spectrum

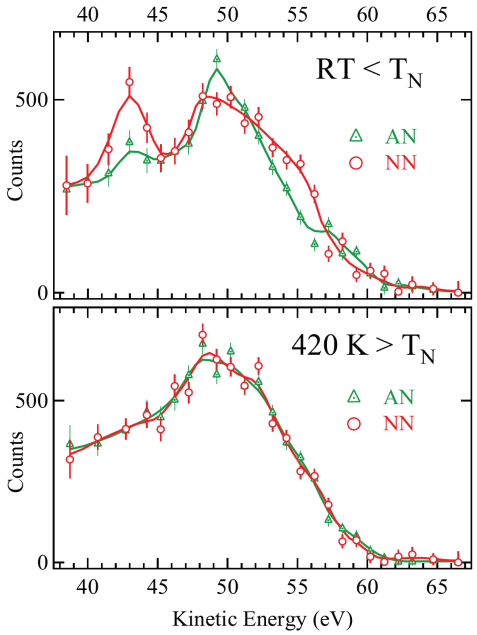

Figure 1.8: AR-APECS spectra of NiO/Ag(001) in its anti-ferromagnetic state at room temperature (upper panel) and its paramagnetic state at 420 K (lower panel) as measured in [61]. Green triangles and red circles with error bars show data collected in AN and NN geometry, respectively. The solid lines joining the experimental points are sp-line fit acting as guides to the eyes.

the authors were able to describe the curve obtained when the photoelectron is emitted parallel to the light polarisation (AN) as the combination of triplet and quintet multiplet terms. In a different kinematic condition, i.e. when the photoelectron is not aligned to the polarisation vector (NN), the main contributions to the coincidence spectrum arise from singlet and triplet terms. Below T_N AR-APECS allows to disentangle the high-spin and low-spin multiplet terms contributing to the total Auger spectrum. On the contrary, when the sample is in its paramagnetic phase ($T > T_N$) spin-selectivity is lost and more featureless and identical spectra are obtained in both the considered geometries. The loss of spin-selectivity, observed also in CoO [62], is characteristic of transition metals oxides and according to the authors indicates a collapse of the surface short-range magnetic order, presumably due to a strongly reduced exchange field in the surface compared to that in the bulk.

All the results presented in this chapter show the evolution of 1-photon in 2-electrons out $(\gamma, 2e)$ experiments during the last fifty years. This class of experiments represents an unique tool that provides an insight into the role of 2-particle properties in both the initial and final state of the double-ionisation process.
Double-Photoemission from atomic targets has been proved to be strongly determined by the long range Coulomb interactions between the three charged final-state particles, i.e. the two electrons in the presence of the residual doubly-charged ion, and by the interplay of electron-electron correlations and photon-atom interaction in the initial state. At low kinetic energies, near the DPE threshold, the former are dominant and double escape of the electrons is very unlikely, as each of

them tends to be attracted by the residual ion. At high kinetic energies the Coulomb interaction can be considered negligible and the electron-electron interaction in the initial state dominates the process, thus making DPE experiments suitable for the investigation of electronic correlations in the bound states of the investigated sample.
The aforementioned capability of the DPE technique is also valid in the case of solid targets. Indeed, the angular distribution of direct DPE is able to give access to the exchange-correlation hole, which is a consequence of the Coulomb and exchange interactions between the two electrons in the final state. In the case of core-resonant DPE, in which the double-photoionisation takes place through the excitation of a core-hole, the line shape is influenced by hole-hole correlations in the valence band of the system. In addition, the angular distribution of the core-resonant DPE pairs is selective in the spin of the two-particle final state and gives informations on the local magnetic moment of the system.
However, while considerable progress has been made in the understanding of double-ionisation processes in simple atomic targets (e.g. He), the complementary process at surfaces is still far to be perfectly understood. This, from the theoretical side, is due to the fact that the treatment of electronic systems with a large number of electrons rapidly becomes more complex than the atomic case. In this sense a complete characterisation of the two-electron dynamics in the case of double escape from a solid surface has not been achieved jet. Objective of this thesis is to give a contribution to this topic from an experimental point view. To this end, we measured direct and core-resonant DPE spectra from different systems in order to observe how the two-electron dynamics is influenced by the correlated motion of the electrons in both initial and final state of the reaction. Our hope is to bring an increasing interest in the development of $(\gamma, 2e)$ spectroscopy and to stimulate a close collaboration between experimental and theoretical groups.

Chapter 2

Direct Double-Photoemission

In this chapter a detailed theoretical description of direct Double Photoemission is given. We will consider the simultaneous emission of two electrons from both localised and delocalised electronic states of a solid after the absorption of a linearly polarised photon.
It will be shown that the DPE cross section is non-vanishing only if the electron-electron interaction is taken into account. In order to give an exact description of the process interactions among the electrons must be included in both the initial and final state of the reaction. This results in very complex calculations which can be simplified by means of approximated methods in which electron-electron interaction is considered either in the initial, e.g. for DPE from localised levels, or in the final state, e.g. for initial delocalised levels.
Calculations show that the emission of the electron pairs must follow propensity rules expressed by the scalar product of the photon's polarisation vector and the momentum in the centre-of-mass of the electron couple. Furthermore, diffraction occurs when the pair's momentum changes by a reciprocal lattice vector. This means that the simultaneous emission of two electrons can be associated to the photoemission of a quasi-particle whose momentum and energy are given by the sum of the single particle momenta and energies, respectively.
All the results shown in this chapter are taken from [7] and references therein.

2.1 Theoretical framework

In this part we derive the transition amplitude for simultaneous electron ejection. We start by assuming the unperturbed system in the initial state to be described by the Hamiltonian H and to be in a stationary state, $|i\rangle$:

$$H|i\rangle = \varepsilon_i |i\rangle \tag{2.1}$$

The effect of the time-dependent action of the incident photon field on the system is to induce a transition into vacuum states $|f\rangle$, whose probability dw_{if} can be derived from the Fermi golden rule:

$$dw_{if} = \frac{2\pi}{\hbar} |\langle f|H_{int}|i\rangle|^2 \rho(E_f), \tag{2.2}$$

where $\rho(E_f)$ is the density of final states and H_{int} is the interaction Hamiltonian between the incident photon field and the system. In the most general case this operator is given by [64, p. 41]

$$H_{int} = \sum_{j=1}^{N} \left[\frac{e}{2mc}(\mathbf{A}\cdot\mathbf{p}_j + \mathbf{p}_j\cdot\mathbf{A}) + \frac{e^2}{2mc^2}A^2 p_j^2 \right] - e\phi. \tag{2.3}$$

Here $\mathbf{A}$ and ϕ are the vector and scalar potentials of the electromagnetic radiation and $\mathbf{p}_j$ are the one-electron momentum operators $\mathbf{p}_j = -i\hbar\nabla_j$.
Using the relation $\mathbf{A}\cdot\mathbf{p} + \mathbf{p}\cdot\mathbf{A} = 2\mathbf{A}\cdot\mathbf{p} - i\hbar(\nabla\cdot\mathbf{A})$ we can rewrite the interaction Hamiltonian as follows:

$$H_{int} = \sum_{j=1}^{N}\left[\frac{e}{2mc}(2\mathbf{A}\cdot\mathbf{p}_j - i\hbar\nabla\cdot\mathbf{A}) + \frac{e^2}{2mc^2}A^2p_j^2\right] - e\phi. \tag{2.4}$$

If we operate in the Coulomb gauge where $\nabla\cdot\mathbf{A} = 0$ and $\phi = 0$ and consider a low-intensity field, hence we neglect the A^2 terms, equation (2.4) reduces to:

$$H_{int} = \frac{e}{mc}\sum_{j=1}^{N}\mathbf{A}\cdot\mathbf{p}_j. \tag{2.5}$$

A general wave can always be expressed as the superposition of plane-waves, so we can assume for the potential vector $\mathbf{A}$ a monochromatic, plane-wave solution with a wave-vector $\mathbf{k}$ related to the photon frequency via $k = \omega/c$:

$$\mathbf{A}(\mathbf{r},t) = \hat{\mathbf{e}}A\exp(i\mathbf{k}\cdot\mathbf{r} - i\omega t), \tag{2.6}$$

where $\hat{\mathbf{e}}$ indicates the polarisation vector and A is the vector potential's amplitude. As long as the superposition principle holds, the behaviour of the system for a general light wave can be expressed as the superposition of all the plane-wave contributions. Substituting (2.6) into (2.5) leads to:

$$H_{int} = \frac{eA}{mc}\sum_{j=1}^{N}e^{i(\mathbf{k}\cdot\mathbf{r}-\omega t)}\hat{\mathbf{e}}\cdot\mathbf{p}_j. \tag{2.7}$$

Inserting (2.7) into the expression for the transition probability (2.2) and recalling that the cross section of the process $d\sigma$ is related dw_{if} via the relation:

$$d\sigma = \frac{\omega}{I}\,dw_{if}, \tag{2.8}$$

where

$$I = \frac{\omega^2}{2\pi c}A^2$$

is the intensity of a plane wave, we obtain:

$$d\sigma = \frac{4\pi^2e^2}{m^2c\hbar\omega}\sum_{j=1}^{N}\left|\left\langle f\left|e^{i\mathbf{k}\cdot\mathbf{r}}\hat{\mathbf{e}}\cdot\mathbf{p}_j\right|i\right\rangle\right|^2\delta(E_f - E_i)\rho(E_f). \tag{2.9}$$

Here the delta function accounts for energy conservation between the initial and final state. The above expression can be further simplified if we consider moderate photon energies (< 500 eV). In this case we can expand the exponential in the potential vector definition in Taylor series:

$$e^{i\mathbf{k}\cdot\mathbf{r}} \simeq 1 + i\mathbf{k}\cdot\mathbf{r} + \frac{1}{2!}(i\mathbf{k}\cdot\mathbf{r})^2 + \dots$$

and stop it to the first term. This can be done because the atomic wave functions extension is of the order of the Bohr radius (few Å) and the wave vector of low-energy radiation is around 10^{-5}

Å^{-1}, so that their scalar product can be considered negligible. In this case we operate in the dipole approximation where the cross section becomes:

$$d\sigma = \frac{4\pi^2 e^2}{m^2 c\hbar\omega} \sum_{j=1}^{N} \left| \left\langle f \left| \hat{\mathbf{e}} \cdot \mathbf{p}_j \right| i \right\rangle \right|^2 \delta(E_f - E_i)\rho(E_f) \tag{2.10}$$

and the interaction operator between the incident radiation and the electrons of the system,

$$H_{int} = \frac{eA}{mc} \sum_{j=1}^{N} \hat{\mathbf{e}} \cdot \mathbf{p}_j, \tag{2.11}$$

is given by the scalar product of the photon polarisation vector and the electron momentum. Notice that the interaction Hamiltonian in equation (2.11) is the sum of single-particle operators, i.e. one photon interacts with one electron at a time. If we assume the initial and final many-electron states, $|i\rangle$ and $|f\rangle$, to be written in terms of the anti-symmetric product of single particle wave functions, than the matrix element in (2.10) is non-zero only if the emission of a single particle at a time, e.g., single photoemission, is considered.
This can be easily verified if we consider the simple case in which we write the many-electron wave functions of initial and final states, Ψ_i and Ψ_f, as the direct product of single particle orbitals $\phi_{i,j}(\mathbf{r}_j)$ and $\phi_{f,j}(\mathbf{r}_j)$:

$$\Psi_{i/f} = \prod_{j=1}^{N} \phi_{i/f,j}(\mathbf{r}_j) \tag{2.12}$$

and we excite two electrons from the two different orbitals ϕ_l and ϕ_k.
Under these assumptions the only terms surviving in the matrix element between the initial and final state,

$$M_{if} = \sum_{j=1}^{N} \left\langle f \left| \hat{\mathbf{e}} \cdot \mathbf{p}_j \right| i \right\rangle, \tag{2.13}$$

are

$$M_{if} = \left\langle \phi_{i,k}\phi_{i,l} \left| \hat{\mathbf{e}} \cdot \mathbf{p}_k \right| \phi_{f,k}\phi_{f,l} \right\rangle + \left\langle \phi_{i,k}\phi_{i,l} \left| \hat{\mathbf{e}} \cdot \mathbf{p}_l \right| \phi_{f,k}\phi_{f,l} \right\rangle, \tag{2.14}$$

where we assumed that the electrons not taking part to the transition, $j \neq k, l$, remain in the same eigenstate of the initial Hamiltonian.
If we now consider that the one-particle operator $\hat{\mathbf{e}} \cdot \mathbf{p}_{l(k)}$ only acts on $\phi_{l(k)}$, equation (2.14) can be rewritten as

$$\begin{aligned} M_{if} &= \left\langle \phi_{i,l} \,|\, \phi_{f,l} \right\rangle \left\langle \phi_{i,k} \left| \hat{\mathbf{e}} \cdot \mathbf{p}_k \right| \phi_{f,k} \right\rangle + \left\langle \phi_{i,k} \,|\, \phi_{f,k} \right\rangle \left\langle \phi_{i,l} \left| \hat{\mathbf{e}} \cdot \mathbf{p}_l \right| \phi_{f,l} \right\rangle \\ &= \delta_{i,f}[\left\langle \phi_{i,k} \left| \hat{\mathbf{e}} \cdot \mathbf{p}_k \right| \phi_{f,k} \right\rangle + \left\langle \phi_{i,l} \left| \hat{\mathbf{e}} \cdot \mathbf{p}_l \right| \phi_{f,l} \right\rangle], \end{aligned} \tag{2.15}$$

where in the last step we made use of the orthogonality of the single particle orbitals in initial and final state, $\left\langle \phi_{i,l} \,|\, \phi_{f,l} \right\rangle = \delta_{if}$. In this simple example the matrix element results in the incoherent sum of two matrix elements in which one of the two electrons is excited while the other remains in its initial state, hence in two single photoemission events. The same result is also achieved if we consider the antisymmetric product between spatially independent single-particle functions. This means that in order for the DPE process to take place the interaction between the electrons making up the sample must be not negligible. This property makes the DPE an ideal candidate to the study of many-particle interactions in solids.
We need to stress that a DPE process is completely different to a process in which the photon is

absorbed by a single electron and a second electron is emitted after the initial ionisation. This can be seen if we rewrite the reaction matrix element taking into consideration two particle function for the initial (final) state, $\psi_i(\mathbf{r}_k,\mathbf{r}_l)$ ($\psi_f(\mathbf{r}_k,\mathbf{r}_l)$). In this case we can always transform to the coordinate system of the two particles' center of mass,

$$\mathbf{r}^+ = \frac{\mathbf{r}_k+\mathbf{r}_l}{2}, \quad \mathbf{r}^- = \frac{\mathbf{r}_k-\mathbf{r}_l}{2},$$

and in this reference frame the transition matrix element in (2.13) and (2.14) becomes, in the length form,

$$M_{if} = \frac{1}{2}\left\langle \psi_i(\mathbf{r}_k,\mathbf{r}_l)\left|\hat{\mathbf{e}}\cdot\mathbf{r}^+\right|\psi_f(\mathbf{r}_k,\mathbf{r}_l)\right\rangle, \tag{2.16}$$

which means that the photon is absorbed in the center of mass of the emitted electron-pair. This process in which the electrons are simultaneously excited, consistently differs from processes that can be described in a two-step framework, in which one electron is excited by the absorption of one photon and then a secondary electron is emitted into vacuum. The latter processes include reactions in which the initial photo-ionisation is followed by cascade electron-impact ionisations and shake-off excitations (accompanying the photoemission process) in which the charge redistribution within the singly-ionised system leads to the emission of a second electron. The just mentioned processes consists of two incoherent steps, thus the theoretical models adopted for these mechanisms are described by the matrix element for the initial single photoemission multiplied by the matrix element for the secondary ionisation, which is described by electron-impact and monopole operator in the two considered cases, respectively. On the other hand, in direct DPE the electron-electron interaction is responsible for the formation of electron-pairs within the system that can be considered as a single quantum state. In this case the energy of the photon is absorbed in the center of mass of the quasi-particle and DPE takes place. When interactions among the electrons are negligible no electron-pair is formed in the valence band of the system and the DPE probability vanishes.

2.2 DPE from localised electronic states

The first case we are going to consider is the DPE from localised electronic states. These could be the case of core-levels of a solid, the d or f levels of a transition metal or the valence levels of a narrow band insulator. In what follows, we take into consideration electron-electron interaction in the initial state by describing it by means of a two-particle wave function in the tight-binding approximation [65, p. 167]

$$\psi_i(\mathbf{r}_a,\mathbf{r}_b) = C\sum_l e^{i(\mathbf{k}'_a+\mathbf{k}'_b)\cdot\mathbf{R}_l}\phi_i(\mathbf{r}_a-\mathbf{R}_l,\mathbf{r}_b-\mathbf{R}_l), \tag{2.17}$$

where C is a normalization coefficient, $\mathbf{R}_l$ represents the atomic positions and ϕ_i is the two-electron initial state with Bloch wave vectors $\mathbf{k}'_a$ and $\mathbf{k}'_b$. The vacuum motion of the electrons is assumed to be free and is described by two plane-waves of momenta $\mathbf{k}_a$ and $\mathbf{k}_b$ as measured by the electron analysers,

$$\psi_f(\mathbf{r}_a,\mathbf{r}_b) = C' e^{i\mathbf{k}_a\cdot\mathbf{r}_a} e^{i\mathbf{k}_b\cdot\mathbf{r}_b}. \tag{2.18}$$

Under these assumptions, the matrix element in (2.13) can be expressed as:

$$M_{if} = K\sum_l \int\int d^3\mathbf{r}_a d^3\mathbf{r}_b e^{-i\mathbf{k}_a\cdot\mathbf{r}_a - i\mathbf{k}_b\cdot\mathbf{r}_b} e^{i(\mathbf{k}'_a+\mathbf{k}'_b)\cdot\mathbf{R}_l}\hat{\mathbf{e}}\cdot(\mathbf{p}_a+\mathbf{p}_b)\phi_i(\mathbf{r}_a-\mathbf{R}_l,\mathbf{r}_b-\mathbf{R}_l). \tag{2.19}$$

If we perform a change of variable:

$$\mathbf{r} = \mathbf{r}_a - \mathbf{R}_l, \qquad \mathbf{r}' = \mathbf{r}_b - \mathbf{R}_l, \tag{2.20}$$

the above expression becomes:

$$M_{if} = K \sum_l e^{i[(\mathbf{k}'_a + \mathbf{k}'_b) - (\mathbf{k}_a + \mathbf{k}_b)]\cdot \mathbf{R}_l} \int\int d^3\mathbf{r} d^3\mathbf{r}' e^{-i\mathbf{k}_a\cdot\mathbf{r} - i\mathbf{k}_b\cdot\mathbf{r}'} \hat{\mathbf{e}}\cdot(\mathbf{p}_a + \mathbf{p}_b)\phi_i(\mathbf{r},\mathbf{r}'). \tag{2.21}$$

The matrix element in (2.21) results in an atomic matrix element (the double integral), describing the DPE process independently from the atomic site in which it takes place, multiplied by a term (sum over the atomic sites) that describes the dynamics of the excited electron-pair within the crystal lattice and includes diffraction effects. The square modulus of (2.21) reduces to:

$$\left|M_{if}\right|^2 = |K|^2 \, \delta^{(3)}_{(\mathbf{q}_i - \mathbf{q}_f, \mathbf{G})} |\widetilde{M}_{if}|^2, \tag{2.22}$$

where $\mathbf{q}_i = \mathbf{k}'_a + \mathbf{k}'_b$, $\mathbf{q}_f = \mathbf{k}_a + \mathbf{k}_b$ are the initial and final wave vectors in the centre of mass of the electron-pair. To get (2.22) we used the definition of reciprocal lattice vector in a periodic structure [65, p. 58]. $\widetilde{M}_{if}$ represents the atomic matrix element,

$$\widetilde{M}_{if}(\mathbf{k}_a, \mathbf{k}_b) = \int\int d^3\mathbf{r} d^3\mathbf{r}' e^{-i\mathbf{k}_a\cdot\mathbf{r} - i\mathbf{k}_b\cdot\mathbf{r}'} \hat{\mathbf{e}}\cdot(\mathbf{p}_a + \mathbf{p}_b)\phi_i(\mathbf{r},\mathbf{r}'), \tag{2.23}$$

which can be expressed, in the momentum-space representation, as

$$\begin{aligned} \widetilde{M}_{if}(\mathbf{k}_a, \mathbf{k}_b) &= \int\int d^3\mathbf{p} d^3\mathbf{p}' \left\langle \mathbf{k}_a, \mathbf{k}_b \right| \hat{\mathbf{e}}\cdot(\mathbf{p}_a + \mathbf{p}_b) \left| \mathbf{p}, \mathbf{p}' \right\rangle \left\langle \mathbf{p}, \mathbf{p}' \right| \phi_i \rangle \\ &= \hat{\mathbf{e}}\cdot(\mathbf{k}_a + \mathbf{k}_b)\widetilde{\phi}_i(\mathbf{k}_a, \mathbf{k}_b). \end{aligned} \tag{2.24}$$

In order to obtain (2.24) we used the closure relation for the complete set of plane waves $|\mathbf{p}, \mathbf{p}'\rangle$ and denoted with $\widetilde{\phi}_i(\mathbf{k}_a, \mathbf{k}_b)$ the double Fourier transform of the initial state.
It is meaningful to notice that both (2.23) and (2.24) do not factorize into independent particle contributions due to the presence of the two-particle initial state ϕ_i. This confirms what we observed in the first part of this chapter; if the electron-electron interactions are neglected, i.e. if the two-particle wavefunctions are written as the product of single-particle wavefunctions, then the DPE cross section results in the incoherent sum of two independent contributions corresponding to the emission of one of the two electrons. In this case the presence of the two-particle wavefunction, $\phi_i(\mathbf{r}_a - \mathbf{R}_l, \mathbf{r}_b - \mathbf{R}_l)$, in the initial state of the process prevents this to happen and is essential for the DPE cross-section to be non-vanishing.
Taking into consideration eqs. (2.22), (2.23) and (2.24) we can draw important conclusions.

(i) The delta function in the square modulus of the DPE matrix element, eq. (2.22), expresses the Laue condition for the diffraction of the emitted electrons. Diffraction occurs when the difference between the final and initial wave vectors in the center of mass of the electron-pair, $\mathbf{q}_f - \mathbf{q}_i$, equals one reciprocal lattice vector $\mathbf{G}$. An analogous expression can be found in the single photoemission cross section [66]; in analogy to the DPE case, diffraction occurs when the emitted electron wave-vector is exchanged by a reciprocal lattice vector.

(ii) The selection rules for DPE are expressed in the scalar product, $\hat{\mathbf{e}}\cdot(\mathbf{k}_a + \mathbf{k}_b)$, of the absorbed photon's polarisation vector and the wave vector in the center of mass of the excited electron-pair. In particular DPE from linearly polarised light is forbidden when $\hat{\mathbf{e}}\cdot(\mathbf{k}_a + \mathbf{k}_b) = 0$, i.e. when the wave vector in the center of mass of the emitted electron-pair is perpendicular to the polarisation

direction. In this case also an analogous term, given by the scalar product of the polarisation and the wave vector of the photoemitted electron, appears in single photoemission's transition probability [66].

Consequently, the emission of correlated electron-pairs after the absorption of a photon can be treated as the photoemission of one quasi-particle composed by the two emitted electrons and whose wave vector corresponds to the wave vector in the centre of mass of the pair.

2.3 DPE from delocalised electronic states

In what follows we will treat the DPE of one electron-pair from delocalised electronic states, e.g. the valence band of s-p metals. The external states of these metals can be described in a free-electron approximation, so we can neglect electron-electron interaction in the solid and construct many electrons wave functions in the initial states from single particle orbitals. Since DPE is prohibited in a single particle approximation, we will include electronic interactions in the final state, where the emitted electrons propagates into vacuum within a screened Coulomb potentials. In free electron metals we can consider a jellium model to describe the initial electronic states of the system. The atomic nuclei are supposed to be uniformly distributed and form a positive background neutralising the electronic charge. The valence electrons are free to move inside the solid and are forced to stay in its half-space ($z < 0$) by a step-like potential

$$V_0 = E_F + \phi, \tag{2.25}$$

where E_F is the Fermi energy and ϕ is the sample work function. In this scenario the single-particle wave functions for the jellium can be written in terms of the reflection, R, and transmission, T, coefficients:

$$\phi_{\varepsilon_j(\mathbf{k}'_j),\mathbf{k}'_j} = \frac{1}{\sqrt{V}} \exp(i\mathbf{k}'_{j,\parallel} \cdot \mathbf{r}_{j,\parallel}) \begin{cases} e^{i\mathbf{k}'_{j,z} z_j} + Re^{-i\mathbf{k}'_{j,z} z_j} & z < 0 \\ Te^{-\gamma z_j} & z > 0 \end{cases}, \tag{2.26}$$

where $\mathbf{k}'_{j,z}$ ($\mathbf{k}'_{j,\parallel}$) and z'_j ($\mathbf{r}'_{j,\parallel}$) are the components of the wave vector $\mathbf{k}'_j$ and position $\mathbf{r}'_j$ normal (parallel) to the surface, respectively. The wave function inside the metal ($z < 0$) is made up by the sum of an incident wave travelling towards the surface ($z = 0$) and a reflected wave travelling in the opposite direction. Outside the sample ($z > 0$) the electronic wave functions is given by a transmitted exponentially decaying wave. Indeed, the electrons in the initial state do not possess enough energy to overcome the surface potential barrier and are spatially localised within the solid. The boundary conditions for the electronic wavefunctions imply that the probability to find electrons outside the metal decays exponentially when moving from the surface position. The coefficients of reflected and transmitted waves are [67],

$$R = \frac{\mathbf{k}'_{j,z} - i\gamma}{\mathbf{k}'_{j,z} + i\gamma} \qquad T = \frac{2\mathbf{k}'_{j,z}}{\mathbf{k}'_{j,z} + i\gamma} \tag{2.27}$$

with $\gamma = \sqrt{2V_0 - \mathbf{k}'^2_j}$. Having defined the single particle states we can construct the two-particle function by the product of single particle ones. For sake of simplicity we define a singlet two-particle state by taking the symmetrized product of two jellium single-particle functions,

$$\left|\psi_{\varepsilon_i,\mathbf{k}'_a,\mathbf{k}'_b}(\mathbf{r}_a,\mathbf{r}_b)\right\rangle = \frac{1}{2}\left[\left|\phi_{\varepsilon_a,\mathbf{k}'_a}(\mathbf{r}_a)\right\rangle\left|\phi_{\varepsilon_b,\mathbf{k}'_b}(\mathbf{r}_b)\right\rangle + \left|\phi_{\varepsilon_b,\mathbf{k}'_b}(\mathbf{r}_a)\right\rangle\left|\phi_{\varepsilon_a,\mathbf{k}'_a}(\mathbf{r}_b)\right\rangle\right]. \tag{2.28}$$

The total binding energy of this state is given by the sum of the single-particle binding energies

$$\varepsilon_i = \varepsilon_a(\mathbf{k}'_a) + \varepsilon_b(\mathbf{k}'_b) \tag{2.29}$$

where the single-particle states $\varepsilon_{a,b}(\mathbf{k}'_{\mathbf{a},\mathbf{b}})$ follow a free-electron parabolic dispersion. Since we did not consider electronic correlations in the initial state we must include them in the final state. In the final state the two emitted electrons travel in the vacuum and are detected by the analysers with momenta $\mathbf{k}_a$ and $\mathbf{k}_b$, respectively. The two-electron function at the detectors (far away from the interaction point) is described by the measured momenta $|\mathbf{k}_a, \mathbf{k}_b\rangle$ and by the sum energy,

$$E_{sum} = E_a + E_b = \frac{\hbar^2 k_a^2}{2m} + \frac{\hbar^2 k_b^2}{2m}.$$

This asymptotic state is an eigenstate of the two-electron kinetic energy operator, H_0,

$$H_0 |\mathbf{k}_a, \mathbf{k}_b\rangle = \frac{1}{2m}(\mathbf{p}_a^2 + \mathbf{p}_b^2) |\mathbf{k}_a, \mathbf{k}_b\rangle = E_{sum} |\mathbf{k}_a, \mathbf{k}_b\rangle . \tag{2.30}$$

After being excited the electron-pair can interact with all the degrees of freedom of the system, which are described by the total Hamiltonian H. For example, it can suffer lattice diffraction, elastic or inelastic scattering with other electrons or collective modes before emerging from the sample with momentum $\mathbf{q_f} = \mathbf{k}_a + \mathbf{k}_b$. If we write the total Hamiltonian as the sum of the two-particle kinetic energy operator and a potential, V, describing those interactions:

$$H = H_0 + V, \tag{2.31}$$

we can determine the final wave function at the time of absorption by applying the Møller operator [68, p. 30] to its asymptotic expression $|\mathbf{k}_a, \mathbf{k}_b\rangle$. The Møller operator

$$\Omega^- = \lim_{t \to +\infty} e^{iHt} e^{-iH_0 t} \tag{2.32}$$

applied to a free particle state, $|f\rangle = \Omega^- |\mathbf{k}_a, \mathbf{k}_b\rangle$, describes the wave function of particles that at $t \to +\infty$ move freely with momenta $\mathbf{k}_a$ and $\mathbf{k}_b$. In addition, it can be demonstrated that such a constructed state is an eigenstate of the scattering Hamiltonian H with eigenvalue $E_{sum}(\mathbf{k}_a, \mathbf{k}_b)$.
The Møller operator can be written in terms of the Green function of H and of the interaction potential V (see [68, p. 135] for further details):

$$\Omega^- = 1 + G^-(H - H_0) = 1 - G^- V. \tag{2.33}$$

The interaction potential V in eq. (2.33) contains all the interactions that the electron-pair can experience after being excited. Since it is practically impossible to deal with the full potential, in what follows we will consider the interaction between electrons, which cannot be neglected in describing the DPE process, as the strong potential with respect to the surface-photoelectron coupling. In practice we neglect all the effects of the interactions that the electrons experience when travelling towards the sample surface, e.g. plasmon excitations, atomic scattering, surface diffraction, etc., and we only take into consideration the effects of the interaction between the electrons of the emitted pair. This means that we can employ the approximation $V \simeq V_{ee}$. We assume for V_{ee} a screened Coulomb potential with screening constant λ

$$V_{ee}(\mathbf{r}_a, \mathbf{r_b}) = \frac{e^{-\lambda |\mathbf{r}_a - \mathbf{r}_b|}}{|\mathbf{r}_a - \mathbf{r}_b|}. \tag{2.34}$$

Under these assumptions the final state of the DPE process can be written as

$$|f\rangle \approx (1 + G_{ee}^- V_{ee}) |\mathbf{k}_a, \mathbf{k}_b\rangle , \tag{2.35}$$

where G_{ee}^{-} is the Green propagator within the approximate potential.
The transition amplitude in (2.13) can be written as

$$M_{if}(\mathbf{k}_a,\mathbf{k}_b) = \left\langle \mathbf{k}_a,\mathbf{k}_b \left| (1+V_{ee}G_{ee}^{+})[\hat{\mathbf{e}}\cdot(\mathbf{p}_a+\mathbf{p}_b)] \right| \psi_{\varepsilon_i} \right\rangle . \tag{2.36}$$

The evaluation of the above expression is very demanding and it is only possible if we approximate the Green propagator G_{ee}^{+} with its value to the zero order in the potential G_0^{+}, which corresponds to consider the propagator of two free particles and work within the kinematical approximation. In this case,

$$M_{if}(\mathbf{k}_a,\mathbf{k}_b) = \left\langle \mathbf{k}_a,\mathbf{k}_b \left| (1+V_{ee}G_{0}^{+})[\hat{\mathbf{e}}\cdot(\mathbf{p}_a+\mathbf{p}_b)] \right| \psi_{\varepsilon_i} \right\rangle = T_{spe}+T_{dpe}, \tag{2.37}$$

can be written as the sum of two contributions

$$\begin{aligned} T_{spe} &= \langle \mathbf{k}_a,\mathbf{k}_b \left| [\hat{\mathbf{e}}\cdot(\mathbf{p}_a+\mathbf{p}_b)] \right| \psi_{\varepsilon_i} \rangle \\ &= -(\hat{\mathbf{e}}\cdot\mathbf{k}_a+\hat{\mathbf{e}}\cdot\mathbf{k}_b)\delta(\mathbf{k}'_{a,\parallel}-\mathbf{k}_{a,\parallel})\delta(\mathbf{k}'_{b,\parallel}-\mathbf{k}_{b,\parallel}) \\ &\times \frac{\pi\sqrt{2}}{V}\left[L_{\mathbf{k}'_a}(\mathbf{k}_a)L_{\mathbf{k}'_b}(\mathbf{k}_b)+L_{\mathbf{k}'_b}(\mathbf{k}_a)L_{\mathbf{k}'_a}(\mathbf{k}_b) \right] \end{aligned} \tag{2.38}$$

and

$$\begin{aligned} T_{dpe} &= \left\langle \mathbf{k}_a,\mathbf{k}_b \left| V_{ee}G_0^{+}[\hat{\mathbf{e}}\cdot(\mathbf{p}_a+\mathbf{p}_b)] \right| \psi_{\varepsilon_i} \right\rangle \\ &= \hat{\mathbf{e}}\cdot(\mathbf{k}_a+\mathbf{k}_b)\delta[(\mathbf{k}'_{a,\parallel}+\mathbf{k}'_{b,\parallel})-(\mathbf{k}_{a,\parallel}+\mathbf{k}_{b,\parallel})]\times \\ &\times \frac{1}{\sqrt{8}\pi V}\left[I(\varepsilon_a,\mathbf{k}'_a,\varepsilon_b,\mathbf{k}'_b;\mathbf{k}_a,\mathbf{k}_b)+I(\varepsilon_a,\mathbf{k}'_a,\varepsilon_b,\mathbf{k}'_b;\mathbf{k}_a,\mathbf{k}_b) \right], \end{aligned} \tag{2.39}$$

where the functions $L_{\mathbf{k}'_j}(\mathbf{k}_j)$ and $I(\varepsilon_a,\mathbf{k}'_a,\varepsilon_b,\mathbf{k}'_b;\mathbf{k}_a,\mathbf{k}_b)$ are constructed from the Fourier transforms of the single-particle jellium functions $\tilde{\phi}(\mathbf{k}_j)$ ($j=a,b$) and from the definition of G_0 (see [7] for further details).
The two terms in (2.38) and (2.39) explain the differences between single and double photoemission. The first term [eq. (2.38)], in which the electronic interaction in the final state does not appear, is given by the product of terms in which selection rules apply separately to the two emitted particles and the same is for surface wave-vector conservation. This means that the DPE process, in absence of electronic interactions, can be regarded as two independent photoemission processes.
The second term [eq. (2.39)], describes DPE when electronic interactions are included. In this case selection rules apply to the wave vector of the electron-pair in its center of mass, whose surface component is conserved in the emission process. In these conditions the surface momenta of the individual electrons might not be conserved, i.e the electrons can exchange momenta under the constraint that $(\mathbf{k}'_{a,\parallel}+\mathbf{k}'_{b,\parallel})=(\mathbf{k}_{a,\parallel}+\mathbf{k}_{b,\parallel})$.
Analogous considerations can be drawn for the electrons kinetic energies. Let's consider first the photoemission of one electron with kinetic energy E. If $\hbar\omega$ is the photon energy, $E_0(N)$ is the energy of the initial N-electron system in its ground state and $E_j(N-1)$ the energy of the system in its final state with one hole left in the j-th level, then energy conservation between the initial and final state is given by:

$$\hbar\omega+E_0(N)=E+E_j(N-1). \tag{2.40}$$

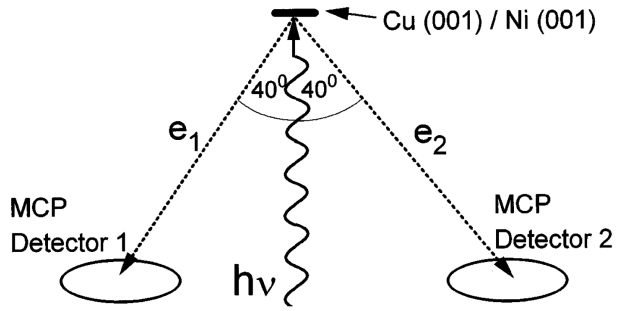

Figure 2.1: Experimental setup for the DPE experiment considered in [7, 42].

In single photoemission (SPE) the kinetic energy of the emitted electron

$$E = \hbar\omega - [E_j(N-1) - E_0(N)] \tag{2.41}$$

is constant and determined by the photon energy and the difference between the final and initial energy of the sample.
In DPE two electrons are emitted and detected with kinetic energies E_a and E_b, respectively. The solid is left with one hole in the i and one hole in the j level with energy $E_{i,j}(N-2)$. In this case energy conservation,

$$\hbar\omega + E_0(N) = E_a + E_b + E_{i,j}(N-2), \tag{2.42}$$

can be read as,

$$E_a + E_b = \hbar\omega - [E_{i,j}(N-2) - E_0(N)], \tag{2.43}$$

indicating that the sum energy $E_{sum} = E_a + E_b$ is conserved in the process. As in the case of surface wave vector, the kinetic energies of the individual particles might not be constant, because the emitted electrons can share their energies conserving the excess energy of the process.

2.4 Two examples: Cu(001) and Ni(001)

In this section we will show results obtained for the direct DPE from the valence band of Cu(001) and Ni(001). The case of Cu will be treated both theoretically and experimentally while, for Ni we will only show some experimental results. In what follows we will refer to [7] for theoretical predictions and to [42] for the experimental part.

In the considered DPE experiments the number of ejected electron-pairs is recorded as a function of the single particle momenta ($\mathbf{k}_a$, $\mathbf{k}_b$). In these conditions the DPE cross section in eq. (2.10) can be written as

$$\frac{d^2\sigma}{d\mathbf{k}_a d\mathbf{k}_b} = \frac{4\pi^2 e^2}{m^2 \hbar c \omega} \int\int d^3\mathbf{k}'_a d^3\mathbf{k}'_b \rho(\mathbf{k}'_a) F(\mathbf{k}'_a, T) \rho(\mathbf{k}'_b) F(\mathbf{k}'_b, T) \left|M_{if}\right|^2 \delta(E_f - E_i). \tag{2.44}$$

To obtain (2.44) we substituted the sum over the possible initial states with the integral over the single particle Bloch wave vectors, $\mathbf{k}'_j$ ($j = a, b$), of the density of states $\rho(\mathbf{k}'_j)$ multiplied by the Fermi distribution at temperature T, $F(\mathbf{k}'_j, T)$. Using for M_{if} the expression (2.37) derived from

the initial wave function presented in eq. (2.28) and considering the system at $T = 0$, the equation above simplifies to

$$\frac{d^2\sigma}{d\mathbf{k}_a, d\mathbf{k}_b} = \frac{e^2V^2}{4\pi^4 m^2 c\hbar\omega} \int_{\mathbf{k}'_a \leq \mathbf{k}_F} \int_{\mathbf{k}'_b \leq \mathbf{k}_F} d^3\mathbf{k}'_a d^3\mathbf{k}'_b \left|M_{if}\right|^2 \delta(E_f - E_i), \tag{2.45}$$

where $\mathbf{k}_F$ is the Fermi momentum for single-particle bands. The above integrals can be resolved numerically to calculate the DPE cross section as a function of the single particles momenta (kinetic energies). Fig. 2.1 depicts the considered experimental set-up. Linearly polarised radiation of energy $\hbar\omega = 45$ eV impinges with normal incidence on the sample surface. The polarisation vector lies parallel to the surface. Emitted electrons are detected by two analysers located in a plane defined by the normal to the surface and the axis of both the analysers, which define an angle with the light direction of $\pm 40^o$, respectively. Using eq. (2.45) we can evaluate the DPE cross section for this particular geometry and construct a so called energy sharing curve in which the DPE cross section for a well defined energy balance is plotted as a function of the energy difference between the two detected electrons. Fig. 2.2(a) shows the energy sharing curve for Cu(001) at

$$E_{sum} = E_a + E_b = 34 \text{ eV}. \tag{2.46}$$

If we assume that the conduction band of the sample is formed of independent single particle bands, energy conservation in (2.43) can be expressed in a very simple way by considering that the total energy of the neutral system,

$$E_0(N) = -\sum_{j=1}^{N} \varepsilon_j(\mathbf{k}'_j),$$

is equal to minus the sum of the single-particle binding energies of the occupied states, $\varepsilon_j(\mathbf{k}'_j)$, defined with respect to the Fermi level. The same is for the doubly ionised state energy,

$$E_{a,b}(N-2) = -\sum_{j \neq a,b} \varepsilon_j(\mathbf{k}'_j).$$

Under these assumptions (2.43) can be written as,

$$E_{sum} = \hbar\omega - \varepsilon_a(\mathbf{k}'_a) - \varepsilon_b(\mathbf{k}'_b) - 2\phi, \tag{2.47}$$

where $\phi = 4.6$ eV is the Cu(001) work function [69]. If we consider the case in which two electrons are simultaneously emitted from the top of the valence band, i.e. from the Fermi level, then $\varepsilon_a(\mathbf{k}'_a) = \varepsilon_b(\mathbf{k}'_b) = 0$ and eq. (2.47) gives: $E_{sum} = 45 - 9.2 = 35.8$ eV. This means that the energy balance in (2.46) describes the DPE of electrons just below the Fermi level.
The detected electrons escape from the sample with the same relative angle with respect to the normal to the surface. The wave vector of the electron-pair in its center of mass is perpendicular to the polarisation vector, when $k_a = k_b$, i.e. when the two electrons have the same kinetic energy. In this condition the DPE cross section vanishes due to the selection rules illustrated in eq. (2.39) as illustrated in Fig.2.2(a). The corresponding experimental sharing curve acquired by Hermann and co-workers [42] is shown in Fig.2.2(b). The spectrum shows the same general trend as the calculations with maxima at $|E_a - E_b| \approx 25$ eV and a minimum reached at equal sharing $E_a = E_b$. Differently from the theoretical case the intensity of the DPE signal does not vanish at equal energies. This is a consequence of the high angular acceptance of the analysers so that symmetric and asymmetric contributions are always measured in the experiment. In addition, one must also

consider the contribution of two-step photoionisation processes in which the photoemission of a single electron from the valence band and the subsequent collision between the photoelectron and a second band electron leads to the emission of both electrons. In this scenario conservation rules stated in (2.24) and (2.39) do not apply and the coincidence signal might be non-vanishing also in the symmetric contributions.
Fig.2.2(c) shows the sharing curve at $E_{sum} = 34 \pm 1$ eV acquired for Ni(001). The general trend of the coincidence spectrum is analogous to the one measured for Cu(001). Ni(001) curve shows maxima around $|E_a - E_b| \approx 13$ eV and a minimum for equal energies. In this case the minimum at $E_a - E_b = 0$ eV is much less pronounced than in the Cu case. Since the experimental setup is identical in the two cases this difference can be considered as a footprint of the different contributions of one-step and two-step processes in the two systems. The deeper valley in Cu(001) spectrum indicates a higher contribution of two-step photoionisation processes in Ni than in Cu.

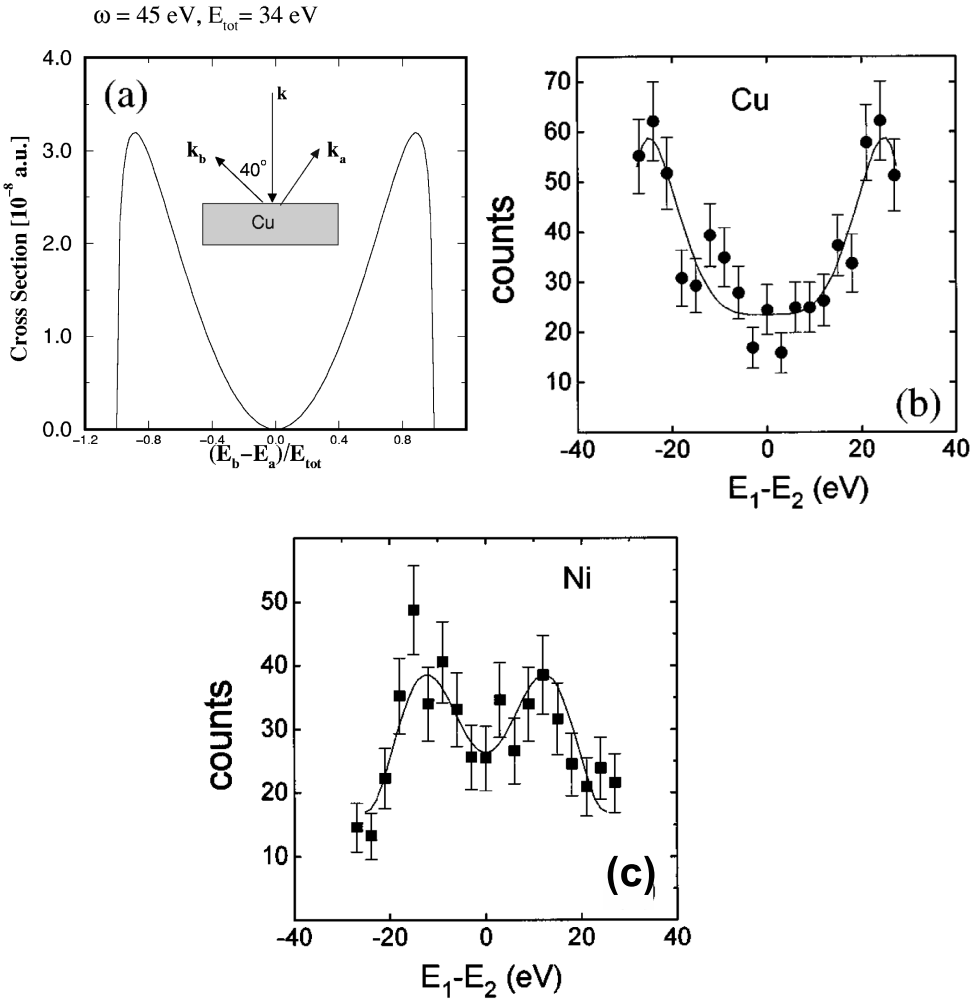

Figure 2.2: (a) Energy sharing distribution of correlated electron-pairs with sum energy $E_a + E_b =$ 34 eV calculated for Cu(001) [7]. The inset represents the considered geometry which is the same of Fig. 2.1. (b) Measured energy sharing distribution of correlated electron-pairs with sum energy 34 ± 1 eV from Cu(001) at 45 eV photon energy. The straight line is a fit to the data points to guide the eye. (c) The same as (b) for Ni(001). Details can be found in [42]

Chapter 3

Core-resonant Double-Photoemission

In this chapter the case of core-resonant DPE will be treated. When the energy of the incident photon exceeds the binding energy of a core-level electron, the electron might be emitted leaving a core-hole in the sample. In addition a further emission can occur via an auto-ionisation process (Auger process) in which the core-hole is filled by a lower binding energy electron and the exceeding energy is transferred to a second electron which might be emitted in the vacuum.
Since its discovery in 1925, the Auger effect has found many applications in the characterisation and chemical analysis of surfaces. This is because the kinetic energies of the emitted Auger electrons strongly depend on the electronic structure of the target and uniquely identify the element from which the electron is ejected. To this aim the Auger decay is commonly treated in a two-step picture in which the emission of the core-electron and the subsequent ejection of the Auger electron are considered as independent events. This approximation is correct if the lifetime of the single core-hole state in the intermediate state is long compared to the time that the system takes to relax to a new ground state. In this case the Auger decay takes place from a stationary single core-hole state and the ejected electron energy only depends on the binding energies of the single-particle levels involved in the process.
If the core-hole lifetime is shorter than the relaxation time, then photoemission and Auger decay act as a coherent single-step process. In this case the singly-ionised state, whose total energy is degenerate with the double ionisation continuum, cannot be described as a single resonance but it can be represented as a virtual state spanning all the possible single-hole states. Thus, all the excitations made together with the primary ionisation can be reabsorbed in the Auger emission process and the distinction between Auger and photoelectron does not hold any more. The emitted electrons are allowed to share the available energy of the process in the same way of direct DPE.

3.1 One-step model

In this section we will derive a general formulation for the Auger electrons current using a single-step approach, following the work by O. Gunnarson and K. Schönhammer [8, 9, 70]. Since in the core-resonant process we are dealing with many interacting particles it is more simple to treat the problem using the second quantization formalism.
We start by writing the total Hamiltonian of the system in which, for sake of simplicity, we neglect the terms due to the radiative decay of the core-hole state,

$$H_T = H_A + T + f(t)V \ . \tag{3.1}$$

The Hamiltonian H_A contains the terms describing the decay of the core level, $|c\rangle$:

$$H_A = H + V_A, \tag{3.2}$$

with

$$V_A = \sum_{kij} v_{kcij} \psi_k^\dagger \psi_c^\dagger \psi_j \psi_i + H.c. \tag{3.3}$$

describing the Auger transition starting with one hole in $|c\rangle$ and ending with two holes in the i and j levels and one free electron with momentum k. $\psi^\dagger_{c(k)}$ is the creation operator for one electron in c (in the continuum), $\psi_{i(j)}$ the annihilation operator for an electron in $i(j)$. The Coulomb matrix elements between initial and final state are denoted with v_{kcij}.
T is the kinetic energy for the states to which photo- and Auger electrons are excited,

$$T = \sum_k E_k n_k, \tag{3.4}$$

where n_k is the number operator associated to electrons in the continuum with kinetic energy E_k. Finally, the term $f(t)V$ describes the coupling between the system and the incident electromagnetic field, with,

$$f(t) = f e^{\eta t} \left(e^{i\omega t} + e^{-i\omega t} \right) \qquad \eta \to 0, \tag{3.5}$$

describing the time dependence of the field, and

$$V = \sum_k \tau_{kc} \psi_k^\dagger \psi_c + H.c., \tag{3.6}$$

characterising the process in which the photon absorption leads to the emission of one electron in the core-level c, described by the dipole one-particle matrix element τ_{kc}, analogous to the one in (2.13).
We assume that the unperturbed Hamiltonian H does not contain any decay channel for the hole in $|c\rangle$ so that,

$$[n_c, H] = 0. \tag{3.7}$$

In what follows the high-energy approximation for both photo- and Auger electron will be considered. In this way we can assume that emissions are not expected in the absence of the perturbation and that there are no terms in H containing the creation or annihilation operators of the final states, $\psi_k^\dagger$ and ψ_k, i.e.

$$[n_k, H] = 0. \tag{3.8}$$

We can also make use of the sudden approximation so that the interaction between the outgoing photoelectrons and the rest of the system can be neglected:

$$[n_p, H_A + T] = 0 \tag{3.9}$$

where n_p is the number operator associated to photoelectrons. In these picture the final-state interactions for the Auger electrons are included only via V_A.
The assumptions expressed in (3.7), (3.8) and (3.9) have the consequence that in the initial ground state, $|E_0\rangle$, the occupancy of both photo- and Auger electron final states is zero,

$$n_k |E_0\rangle = 0. \tag{3.10}$$

Applying the time-dependent perturbation theory to the system we can calculate the time evolution of the initial state wave function under the perturbation $f(t)V$. To the first order in V we obtain that the change of the wave function $\phi(t)$,

$$|\phi_1(t)\rangle = |\phi(t)\rangle - |E_0\rangle = f e^{\eta t} \frac{1}{E_0 + \hbar\omega - T + i\eta} V |E_0\rangle . \tag{3.11}$$

The total emission current, j_k, is given by the time derivative of the final-state occupancy mean value, calculated on $|\phi(t)\rangle$;

$$\begin{aligned} j_k &= \frac{d}{dt} \langle \phi(t) | n_k | \phi(t) \rangle \\ &= 2\eta f^2 \left\langle E_0 \left| V \frac{1}{E_0 + \hbar\omega - H_A - T - i\eta} n_k \frac{1}{E_0 + \hbar\omega - H_A - T + i\eta} V \right| E_0 \right\rangle . \end{aligned} \tag{3.12}$$

If we now want to obtain the photoemission current j_p we must replace n_k with the occupancy of the photoelectron final states n_p and, using the commutation relation in (3.9), we obtain

$$\begin{aligned} j_p &= \frac{d}{dt} \langle \phi(t) | n_p | \phi(t) \rangle \\ &= 2\pi f^2 |\tau_{cp}|^2 \left\langle E_0 \left| \psi_c^\dagger \delta(E_0 + \hbar\omega - E_p - H_A) \psi_c \right| E_0 \right\rangle . \end{aligned} \tag{3.13}$$

If we completely neglect the the Auger decay, we can substitute the Hamiltonian H_A with the non-interacting one, H, and obtain

$$\begin{aligned} j_p^{XPS} &= 2\pi f^2 |\tau_{cp}|^2 \langle E_0 | \psi_c^\dagger \delta(E_0 + \hbar\omega - E_p - H) \psi_c | E_0 \rangle \\ &= 2\pi f^2 |\tau_{cp}|^2 \sum_i \left| \left\langle E_i^{N-1} | \psi_c | E_0 \right\rangle \right|^2 \delta(E_0 + \hbar\omega - E_p - E_i^{N-1}), \end{aligned} \tag{3.14}$$

where to obtain the equation above we inserted a complete set of $(N-1)$-electron eigenstates of the system having energy E_i^{N-1} and applied the delta function to them, i.e. $\delta(E_0 + \hbar\omega - E_p - H) \left| E_i^{N-1} \right\rangle = \left| E_i^{N-1} \right\rangle \delta(E_0 + \hbar\omega - E_p - E_i^{N-1})$.
We can easily see that the expression in (3.14) is the Fermi golden-rule for the photoemission already presented in the previous chapter [see eq. (2.2)].
The Auger-electron current can be obtained taking into consideration the decay term in (3.3). For convenience we define the state,

$$|\phi_k\rangle = \psi_k \frac{1}{E_0 + \hbar\omega - H_A - T + i\eta} V |E_0\rangle , \tag{3.15}$$

so that the electron current (3.13) can be written as

$$\frac{d}{dt} \langle \phi(t) | n_k | \phi(t) \rangle = 2\eta f^2 \langle \phi_k | \phi_k \rangle . \tag{3.16}$$

With some mathematical considerations (see [8] for further details) we can write:

$$|\phi_k\rangle = \sum_p \tau_{cp} \psi_p^\dagger \psi_k^\dagger \frac{1}{E_0 + \hbar\omega - E_p - E_k - H(1)} A_k \psi_c^\dagger \frac{1}{E_0 + \hbar\omega - E_p - H(0) + i\widetilde{\Gamma}} \psi_c |E_0\rangle . \tag{3.17}$$

The state $|\phi_k\rangle$ completely describes the Auger decay process. Firstly, a core-hole is created by the operator ψ_c in the unperturbed ground state $|E_0\rangle$ of the system. The evolution of the ground state

after the ionisation process is described by the Hamiltonian $H(0)+i\widetilde{\Gamma}$, where $H(0)$ contains the screening of the core-hole by the other electrons of the system, and

$$\widetilde{\Gamma}=\sum_{ij,i'j'}\pi\rho_0 v_{ijkc}v_{kci'j'}\psi_i^\dagger\psi_j^\dagger\psi_{j'}\psi_{i'}, \tag{3.18}$$

is the optical potential describing the Auger decay of the $(N-1)$-electron states. Here ρ_0 represents the density of final states. In the absence of other sources of decay the lifetime of the core-hole is completely defined by $\widetilde{\Gamma}$. At this point the core-hole is filled ($\psi_c^\dagger$) by another electron and this process is mediated by the Auger operators,

$$A_k=\sum_{ijc}v_{kcij}\psi_i\psi_j, \tag{3.19}$$

which depend on the Coulomb matrix elements calculated among the levels involved in the transition, v_{kcij}. In the final state two electrons are emitted in the continuum ($\psi_p^\dagger\psi_k^\dagger$) and the evolution of doubly ionised system is described by $H(1)$ which contains the screening of the two holes in the final state. In this case no subsequent cascade Auger processes have been taken into consideration as it can be seen from the fact that no optical potential is associated to the Hamiltonian $H(1)$.
To obtain the Auger current we need to calculate the scalar product $\langle\phi_k|\,\phi_k\rangle$. We can write the ground state putting in evidence the presence of a core-electron in the initial state so that: $|E_0\rangle=\psi_c^\dagger|\tilde{\phi}_0>$. In this way we obtain for the Auger current,

$$\begin{aligned} j_k^A &= 2\pi f^2\sum_p|\tau_{cp}|^2\left\langle\tilde{\phi}_0\left|\frac{1}{E_0+\hbar\omega-E_p-H(0)-i\widetilde{\Gamma}}A_k^\dagger\delta(E_0+\omega-E_p-E_k-H(1))\right.\right. \\ &\quad\left.\left.\times A_k\frac{1}{E_0+\hbar\omega-E_p-H(0)+i\widetilde{\Gamma}}\right|\tilde{\phi}_0\right\rangle. \end{aligned} \tag{3.20}$$

The obtained result provides a "one-step" description of the Auger process. To find an exact solution for the Auger current is not simple because of the presence of the optical potential $\widetilde{\Gamma}$ that does not allow to express it in the occupied set of eigenstates of the Hamiltonian $H(0)$, $|E_0\rangle$. This problem can be overcome if we make the assumption that the major contribution to the Auger spectrum is given by the emission of electrons from completely filled shells. Then $\widetilde{\Gamma}$ can be replaced by a complex number and the insertion of complete sets of $(N-1)$ and $(N-2)$ states in (3.20), together with the integration over the possible photoemission final states lead to (see [8, 9, 70] for further details),

$$j_k^A=\rho_0(E_k)\sum_m\left|\sum_n\frac{\left\langle E_m^{N-2}\left|A_k\psi_c^\dagger\right|E_n^{N-1}\right\rangle\left\langle E_n^{N-1}\left|\psi_c\right|E_0\right\rangle}{E_0+\hbar\omega-E_p-E_n^{N-1}+i\Gamma}\right|^2. \tag{3.21}$$

Applying energy conservation to (3.21) we can derive the probability that photo- and Auger electrons are emitted with kinetic energy E_p and E_k, respectively:

$$\begin{aligned} P(E_p,E_k) &\sim \rho_0(E_k)\sum_m\left|\sum_n\frac{\left\langle E_m^{N-2}\left|A_k\psi_c^\dagger\right|E_n^{N-1}\right\rangle\left\langle E_n^{N-1}\left|\psi_c\right|E_0\right\rangle}{E_0+\hbar\omega-E_p-E_n^{N-1}+i\Gamma}\right|^2 \\ &\quad\times\ \delta(E_0+\hbar\omega-E_p-E_k-E_m^{N-2}). \end{aligned} \tag{3.22}$$

The summation running over the complete set of $(N-1)$-electron states in (3.22) implies that in the one-step picture the Auger decay can take place from all the possible single-hole states. This

means that the decay might occur from any excited $(N-1)$-electron state and the excitations made together with the primary ionisation can be absorbed in the emission of the Auger electron. In the Auger spectrum this corresponds to the appearance of satellite lines on the high kinetic energy side of the main line, also called "shake-down" satellites. In addition, in eq. (3.22) the sum over the intermediate states inside the square modulus can give rise to interference terms which become not negligible if the energy spacing between two intermediate states,

$$\left|E_{n_1}^{N-1} - E_{n_2}^{N-1}\right|,$$

is comparable to the core-hole lifetime $\hbar/\Gamma$.
The delta function in eq.(3.22) represents energy conservation between the initial (photon + neutral system) and final (two free electrons + doubly ionised system) state,

$$E_0 + \hbar\omega = E_p + E_k + E_m^{N-2}. \tag{3.23}$$

As for direct DPE [see eq.(2.42) in chapter 1], energy conservation does not apply to the emitted electrons separately, but the sum energy of the electron couple $E_{sum} = E_p + E_k$ must be constant for the same initial and final states. This means that individual energies of photo- and Auger electron can reach any value and the emitted particles can continuously share the excess energy of the process, $\hbar\omega + E_0 - E_n^{N-2}$.
The probability of the process is maximum when the denominator in the matrix element in (3.22) vanishes, i.e. when the photoelectron's energy equals the one expected in a single-emission process:

$$E_p = E_0 + \hbar\omega - E_n^{N-1}. \tag{3.24}$$

All this clearly shows that the simultaneous emission of a photo- and Auger electron-pair can be considered as a resonance in the DPE continuum.

3.2 Two-step model

If the lifetime of the initial core-hole is long compared to the time that the residual $N-1$ system takes to relax, then the emission of an Auger electron happens from a stationary state and can be considered independent from the initial ionisation.
Under this assumption the sum over all the possible intermediate states in the probability to emit one photo- and one Auger electron in eq. (3.22) disappears and only the emission from the $N-1$-electron ground state $\left|E_0^{N-1}\right\rangle$ must be taken into consideration,

$$\begin{aligned} P(E_p,E_k) &\sim \rho_0(E_k)\sum_m \left| \frac{\left\langle E_m^{N-2}\left|A_k\psi_c^\dagger\right|E_0^{N-1}\right\rangle \left\langle E_0^{N-1}\left|\psi_c\right|E_0\right\rangle}{E_0+\hbar\omega-E_p-E_0^{N-1}+i\Gamma}\right|^2 \\ &\quad \times\delta(E_0+\hbar\omega-E_p-E_k-E_m^{N-2}). \end{aligned} \tag{3.25}$$

In the limit of infinite core-hole lifetime, $\Gamma\to 0^+$, eq. (3.25) can be rewritten as:

$$\begin{aligned} P(E_p,E_k) &\sim \rho_0(E_k)\sum_m \left|\left\langle E_m^{N-2}\left|A_k\psi_c^\dagger\right|E_0^{N-1}\right\rangle \left\langle E_0^{N-1}\left|\psi_c\right|E_0\right\rangle\right|^2 \\ &\quad \times\delta(E_0+\hbar\omega-E_p-E_0^{N-1})\delta(E_0^{N-1}-E_k-E_0^{N-2}). \end{aligned} \tag{3.26}$$

The terms in the square modulus,

$$T_m = \underbrace{\left\langle E_m^{N-2}\left|A_k\psi_c^\dagger\right|E_0^{N-1}\right\rangle}_{A}\ \underbrace{\left\langle E_0^{N-1}\left|\psi_c\right|E_0\right\rangle}_{P} \tag{3.27}$$

in (3.26) can be made more clear considering that the Auger operator $A_k\psi_c^\dagger$ in "A" creates two holes and annihilates the core-hole through the Coulomb interaction and that the annihilation operator in the term "P" creates a core-hole in $|c\rangle$ through the emission of one electron. If we consider a transition leaving the system with two holes in i and j , we can write the matrix elements of the process as,

$$M_{ijck} = \left\langle \phi_{i,j}^{(N-2)} e^{i\mathbf{k}_A\cdot\mathbf{r}_A}\left|\sum_{l\neq k}\frac{e^2}{|\mathbf{r}_l-\mathbf{r}_k|}\right|\phi_c^{(N-1)}\right\rangle \left\langle \phi_c^{(N-1)} e^{i\mathbf{k}_p\cdot\mathbf{r}_p}\left|\hat{\mathbf{e}}\cdot\mathbf{p}_p\right|\phi^{(N)}\right\rangle, \tag{3.28}$$

where $\phi_{i,j}^{(N-2)}$ ($\phi_c^{(n-1)}$) represents the $N-2$-electron ($N-1$-electron) wave function with two (one) holes in the i,j (c) levels. $\mathbf{k}_A$ ($\mathbf{k}_p$) and $\mathbf{r}_A$ ($\mathbf{r}_p$) are the wave-vector and position of the outgoing Auger- (photo-) electron, respectively. The matrix element results in the product of two independent terms representing the initial photoemission of a core electron described by the dipole operator $\hat{\mathbf{e}}\cdot\mathbf{p_p}$ and the subsequent Auger decay driven by the Coulomb interaction between electrons. The delta functions in (3.26) express energy conservation in the two independent steps, photoexcitation,

$$E_p = \hbar\omega + E_0 - E_0^{N-1}, \tag{3.29}$$

and Auger ionisation,

$$E_k = \hbar\omega + E_0 - E_p - E_m^{N-2}. \tag{3.30}$$

The substitution of (3.29) in (3.30) leads to,

$$E_k = E_0^{N-1} - E_m^{N-2}. \tag{3.31}$$

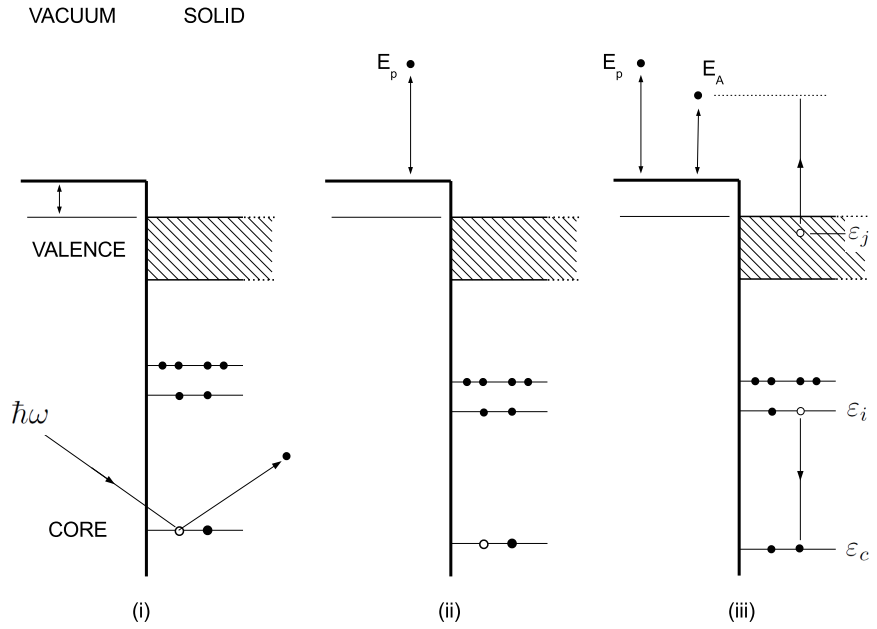

Figure 3.1: A schematic illustration of the Auger transition process. Panel (i) represents the creation of an excited core-hole state by an incident photon of energy $\hbar\omega$. The core-hole state relaxes in panel (ii) and decays by capturing one electron of binding energy ε_i with the excess energy transferred to a valence-band electron which is the detected Auger electron, panel (iii).

Thus, the kinetic energy of the Auger electron is defined as the energy difference of one- and two-hole states involved in the process and it is independent from the photon energy. Differently from the one-step picture, the kinetic energies of the emitted particles are fixed and no energy sharing occurs between photo- and Auger electron. This is because the long-lived core-hole state is responsible for the large delay time of Auger electron emission with respect to the photoemission. This destroys all the interactions between the two particles that, in principle, can be distinguished with fs-time-resolved spectroscopy [71, 72].
In the simplest case of independent particle approximation in which the N-electron wave function can be expressed as a Slater determinant of single-particle orbitals and if the Auger electron interacts only with the electrons involved in the transition, then the matrix element characterizing the Auger distribution is,

$$M^A = \left\langle \phi_i(\mathbf{r})\phi_j(\mathbf{r}') \left| \frac{e^2}{|\mathbf{r}-\mathbf{r}'|} \right| e^{i\mathbf{k}\cdot\mathbf{r}}\phi_c(\mathbf{r}') \right\rangle, \tag{3.32}$$

where ϕ_c is the core wave function, ϕ_i, ϕ_j are the wave functions of the higher-lying electrons and the emitted Auger electron is described by a plane wave of momentum $\mathbf{p} = \hbar\mathbf{k}$. The Coulomb interaction potential acts between two electrons located at sites $\mathbf{r}$ and $\mathbf{r}'$. Since the core-state wave function is very localised in space, the integral in (3.32) has negligible contributions outside the immediate vicinity of the emitting atom [73, 74]. This is the reason why Auger spectroscopy is largely used in the determination of the local properties of materials.
In the considered picture, under the assumption that the states of the system not involved in the transition are not affected by the creation of the core-hole and by the presence of the two holes in the final states, energy conservation in (3.30) reads:

$$E_k = \varepsilon_c - \varepsilon_i - \varepsilon_j - U_{eff}, \tag{3.33}$$

where ε_c, ε_i and ε_j are the binding energies of the intermediate core state and of the levels involved in the transition, respectively. The correction term U_{eff} contains the interaction of the two final-state holes and describes the increase of the i-electron binding energy when a hole is created in the j-state and viceversa.
Fig. 3.1 shows a schematic illustration of the Auger transition process in the two-step picture. First, the excited core-hole state is generated by an incident photon of energy $\hbar\omega$. The excited electron is emitted with a kinetic energy E_p given by (3.29). The core-hole state, that can be created in any of its possible configurations, relaxes to the $(N-1)$-electron ground state. At this point the Auger decay takes place. The core-hole decays by capturing one electron from the electronic level i with the excess energy $(\varepsilon_c - \varepsilon_i)$ transferred to a valence-band electron which is emitted as an Auger electron. Of course the aforementioned transition is not distinguishable from the analogous one in which the valence band electron fills the intermediate hole and the electron with binding energy ε_i is emitted.

Two major differences arise between one- or two-step picture. In the two-step case the Auger decay takes place from a totally relaxed state, the excitations made together with the primary ionisation are not re-absorbed in the Auger transition and no high-energy shake-down peak is observable in the line shape. In addition, only the core-hole ground state takes part in the transition, and this destroys all the possible interferences observable in a single-step Auger transition.

Chapter 4

Circular dichroism in Double-Photoemission

In this chapter we will introduce the case of direct and core-resonant DPE by circularly polarised light from atomic unpolarised targets.
It is well established that single photoionisation of unpolarised atoms is insensitive to the helicity of the incident photon [27] and no difference is observed between photoemission spectra obtained with left or right circular polarisation. This is because the initial atom and the final ion have no preferred orientation and no chirality is introduced in the experimental set-up. Nonetheless, it is possible to observe chiral effects in single photoemission by constructing an asymmetric experimental set-up. This can be done, e.g., by resolving the spin of the emitted electrons [75, 76, 77]. Here the oriented reference system is determined by the wave-vector of the photon, the photoelectron's momentum and spin projection. Analogous effects can be observed for naturally polarised targets, e.g. magnetised samples, for which dichroism in the photoemission spectrum can be achieved reversing the magnetisation of the sample [78].
In what follows we will show that in the case of the two electrons emission after the absorption of one photon the light polarisation, and in particular the helicity of circular polarisation, enters in a non-trivial way in the definition of the cross section of the process. Since the photon is absorbed by the electron-pair and the target initial state is achiral one can think that the photon chirality in the final state is carried by the two interacting electrons. This means that, due to the electron correlation, the electron-pair possesses a chirality as an internal degree of freedom that can be probed by varying the helicity of the photon.

4.1 Circular dichroism in direct DPE

In this section we will focus on the circular dichroism in direct DPE. All the reported results have been taken from the work of Berakdar *et al.* [26] and Berakdar & Klar [25]. The starting point of the calculation is the triple differential cross section (TDCS) for the emission of two electrons, i.e. the differential intensity of the electron-pairs with respect to the electrons' solid angles (Ω_a, Ω_b) and sum energy $E_{sum} = E_a + E_b$. In the atomic case the TDCS can be obtained from (2.10), by considering that the emission takes place from the atomic shell, J_i, with $2J_i + 1$ magnetic sub-levels, M_i, and that the final doubly-ionised state has angular momentum J_f with sub-levels M_j:

$$\frac{d^3\sigma}{d\Omega_a d\Omega_b dE_{sum}} = C \sum_{Mf} \frac{1}{2J_i+1} \sum_{M_i} \left| \langle \psi_{\mathbf{k}_a \mathbf{k}_b} \left| \hat{\varepsilon} \cdot \mathbf{D} \right| \Phi_i \rangle \right|^2 \delta(E_f - E_i). \tag{4.1}$$

To obtain (4.1) we substituted the final state density of states in (2.10), with the sum over all the possible final state magnetic sub-levels, M_f, and the average over all the possible initial magnetic levels, M_i. We included the sum over all the electrons of the system into the length form of the dipole operator $\mathbf{D} = \sum_n \mathbf{r}_n$ [79, p. 198]. It is possible to rewrite the term in (4.1) as the mean value of a scalar operator over the two-electron final state wavefunction $|\psi_{\mathbf{k}_a\mathbf{k}_b}\rangle$,

$$\begin{aligned}\frac{1}{2J_i+1}\sum_{M_i}|\langle\psi_{\mathbf{k}_a\mathbf{k}_b}|\hat{\varepsilon}\cdot\mathbf{D}|\Phi_i\rangle|^2 &= \frac{1}{2J_i+1}\sum_{M_i}\langle\psi_{\mathbf{k}_a\mathbf{k}_b}|\hat{\varepsilon}\cdot\mathbf{D}|\Phi_i\rangle\langle\Phi_i|\hat{\varepsilon}^*\cdot\mathbf{D}|\psi_{\mathbf{k}_a\mathbf{k}_b}\rangle \\ &= \langle\psi_{\mathbf{k}_a\mathbf{k}_b}|(\hat{\varepsilon}\cdot\mathbf{D})(\hat{\varepsilon}\cdot\mathbf{D}')|\psi_{\mathbf{k}_a\mathbf{k}_b}\rangle. \end{aligned} \tag{4.2}$$

Here the informations on the initial state are contained in the operator $\mathbf{D}' = S\mathbf{D}$, where

$$S = \frac{1}{2J_i+1}\sum_{M_i}|\Phi_i\rangle\langle\Phi_i|\,\delta(\hbar\omega-\varepsilon_a-\varepsilon_b-E_{sum}), \tag{4.3}$$

quantifies the density of occupied states. Here we indicated with ε_i, $(i=a,b)$, the binding energy of the emitted electrons with respect to the vacuum level.
In order to have chiral electron-pairs in the final-state we assume that the atom prior to the absorption process is randomly oriented. This means that the chirality is carried by the photon field and that the operator S, containing the average on the magnetic levels of the atom, is invariant under rotation, i.e. is a scalar operator. As a consequence the operator $\mathbf{D}'$ is a polar vector operator.
The expression in (4.2) can be further factorised into a geometrical part, containing the polarisation unit vectors $\hat{\varepsilon}$ and $\hat{\varepsilon}^*$, and a dynamical part with the vectors $\mathbf{D}$ and $\mathbf{D}'$. This can be done using the angular momentum formalism described by Brink and Klar [80, p. 149]. The vector operator in (4.2) can be expressed as,

$$(\hat{\varepsilon}\cdot\mathbf{D})(\hat{\varepsilon}^*\cdot\mathbf{D}') = \frac{1}{3}(\mathbf{D}\cdot\mathbf{D}') + \frac{1}{2}(\hat{\varepsilon}\times\hat{\varepsilon}^*)\cdot(\mathbf{D}\times\mathbf{D}') + T^{(2)}(\hat{\varepsilon},\hat{\varepsilon}^*)T^{(2)}(\mathbf{D},\mathbf{D}'), \tag{4.4}$$

where $T^{(2)}(\mathbf{a},\mathbf{b})$ is a tensor of rank 2 formed by the product of two vectors $\mathbf{a}$ and $\mathbf{b}$,

$$T^{(2)}(\mathbf{a},\mathbf{b})_{kq} = \sum_{m,n} a_m b_n \langle 1m1n\,|\,kq\rangle. \tag{4.5}$$

Here $k = 0,1,2$ and $\langle\cdots|\cdots\rangle$ denotes Clebsch-Gordan coefficient.
To change the helicity of the incident light corresponds to replace the light polarisation vector $\hat{\varepsilon}$ with its complex conjugate $\hat{\varepsilon}^*$. Since the first term in (4.4) does not depend on the polarisation and $T^{(2)}(\hat{\varepsilon},\hat{\varepsilon}^*) = T^{(2)}(\hat{\varepsilon}^*,\hat{\varepsilon})$, the only term giving rise to circular dichroism is the one containing the vectorial product. If we take the $\hat{z}$-axis to be the direction $\hat{\mathbf{k}}$ of the incident light and $\hat{\varepsilon} = \frac{1}{\sqrt{2}}(1,i,0)$ for left circularly polarised light, then we find

$$(\hat{\varepsilon}\times\hat{\varepsilon}^*) = -(\hat{\varepsilon^*}\times\hat{\varepsilon}) = -i\hat{\mathbf{k}}. \tag{4.6}$$

In those conditions, we can write the difference, Δ, between the TDCS for left (σ^-) and right (σ^+) circular polarisation as:

$$\Delta = \left.\frac{d^3\sigma}{d\Omega_a d\Omega_b dE}\right|_{\sigma^-} - \left.\frac{d^3\sigma}{d\Omega_a d\Omega_b dE}\right|_{\sigma^+} = -iC\sum_{M_f}\langle\psi_{\mathbf{k}_a,\mathbf{k}_b}|[\mathbf{D}\times\mathbf{D}']_z|\psi_{\mathbf{k}_a,\mathbf{k}_b}\rangle. \tag{4.7}$$

The same procedure can be applied also in the case of single photoemission, in this case eq. (4.7) reads:

$$\delta = \left.\frac{d^2\sigma}{d\Omega dE}\right|_{\sigma^-} - \left.\frac{d^2\sigma}{d\Omega dE}\right|_{\sigma^+} \propto \langle\psi_p|[\mathbf{D}\times\mathbf{D}']_z]|\psi_p\rangle, \tag{4.8}$$

where δ is the same as Δ but for single photoemission. This expression is equal to zero due to parity conservation. This can be demonstrated using the partial wave expansion of the photoelectron wavefunction,

$$\psi_p = \sum_{lm} C_{lm}(\hat{\mathbf{p}}) \left|\psi_{lm}\right\rangle, \tag{4.9}$$

where $C_{lm}(\hat{\mathbf{p}})$ is related to the spherical harmonic $Y_{lm}(\hat{\mathbf{p}})$ by

$$C_{lm}(\hat{\mathbf{p}}) = \left(\frac{4\pi}{2l+1}\right)^{1/2} Y_{lm}(\hat{\mathbf{p}}).$$

We can apply the Wigner-Eckart theorem [80, p. 56] to express the matrix element $\left\langle \psi_{l'm'} \left| [\mathbf{D}\times\mathbf{D}']_z \right| \psi_{lm} \right\rangle$ as the product of a term independent on the angular momentum projection (m,m') and a Clebsch-Gordan coefficient. Then replacing (4.9) into (4.8), we get:

$$\delta \propto \sum_{ll'}\sum_{mm'} (-1)^{l'+m'} \begin{pmatrix} l' & l & 1 \\ -m' & m & 0 \end{pmatrix} C^*_{l'm'}(\hat{\mathbf{p}}) C_{lm}(\hat{\mathbf{p}}) \left\langle \psi_{l'} \left|\left| \mathbf{D}\times\mathbf{D}' \right|\right| \psi_l \right\rangle. \tag{4.10}$$

Here the Wigner $3-j$ symbol $\begin{pmatrix} l_1 & l_2 & L \\ m_1 & m_2 & -M \end{pmatrix}$ is proportional to the Clebsch-Gordan coefficient $\langle l_1 m_1 l_2 m_2 \,|\, LM\rangle$.
Finally, performing the sum over m and m' we obtain

$$\delta \propto \sum_{ll'} (-1)^{l'} \begin{pmatrix} l' & l & 1 \\ 0 & 0 & 0 \end{pmatrix} C_{10}(\hat{\mathbf{p}}) \left\langle \psi_{l'} \left|\left| \mathbf{D}\times\mathbf{D}' \right|\right| \psi_l \right\rangle \tag{4.11}$$

where to obtain (4.11) we used the spherical harmonic addition properties [80, p. 146]. The $3-j$ symbol in (4.11) is non-vanishing if and only if the quantity $l'+l+1$ is even. Due to parity conservation between l and l' state, the only terms contributing to the sum are the ones in which l and l' are both even or both odd. This means that $l'+l+1$ is always odd and $\delta = 0$ in single photoemission. This result is not unexpected from a qualitative point of view. The initial state of the photoemission process possesses a chirality that, since we are dealing with unpolarised targets, is given by the circularly polarised photon helicity. Once the photon is absorbed, its chirality must be carried away by either the emitted electrons or the residual singly-ionised state. In the case of the emission of a single particle the symmetry axis of the process is defined by the wavevector of the electron in the continuum. In this geometry an inversion of the light helicity corresponds to a parity transformation and, according to parity conservation in the process, no difference is observed in the intensity of emitted electrons. This means that no circular dichroism is observed and the photon chirality is carried away by the electrons in the residual ion.

The above procedure can be generalised to demonstrate that parity conservation does not forbid circular dichroism in the case of DPE [25, 26]. As we did for single photoemission we can expand the two-electron final state in partial waves,

$$\left|\psi_{\mathbf{k}_a\mathbf{k}_b}\right\rangle = \sum_{l_a l_b lm} \left|\psi_{l_a l_b lm}\right\rangle B^{l_a l_b}_{lm}(\hat{\mathbf{k}}_a, \hat{\mathbf{k}}_b). \tag{4.12}$$

Here two-particle (bipolar) spherical harmonics [80, p. 55] are constructed using spherical harmonics with different directions $\hat{\mathbf{k}}_a$ and $\hat{\mathbf{k}}_b$;

$$B^{l_a l_b}_{lm}(\hat{\mathbf{k}}_a, \hat{\mathbf{k}}_b) = \sum_{m_a m_b} \langle l_a m_a l_b m_b \,|\, lm\rangle C_{l_a m_a}(\hat{\mathbf{k}}_a) C_{l_b m_b}(\hat{\mathbf{k}}_b). \tag{4.13}$$

Acting as in the previous case, we can insert the wave functions as defined in eq. (4.12) in the dichroism expression (4.7) and use bipolar harmonics properties and the Wigner-Eckart theorem to write (see [26] for further details):

$$\Delta = -i \sum_{L_a L_b} \gamma_{L_a L_b} B_{10}^{L_a L_b}(\hat{\mathbf{k}}_a, \hat{\mathbf{k}}_b) \tag{4.14}$$

with

$$\begin{aligned}
\gamma_{L_a L_b} &= C \sum_{l_a l_b l} \sum_{l'_a l'_b l'} \sum_{JJ'} (-1)^{l_a+l_b+l'+J'+J_f+1} (2J'+1)(2L_a+1)(2L_b+1) \\
&\times \left[\frac{(2l+1)(2l'+1)}{3}\right]^{1/2} \begin{pmatrix} l_a & l'_a & L_a \\ 0 & 0 & 0 \end{pmatrix} \begin{pmatrix} l_b & l'_b & L_b \\ 0 & 0 & 0 \end{pmatrix} \begin{Bmatrix} l' & J_f & J' \\ J & 1 & L \end{Bmatrix} \\
&\times \begin{Bmatrix} l & l' & 1 \\ l_a & l'_a & L_a \\ l_b & l'_b & L_b \end{Bmatrix} \left\langle J_f(l'_a l'_b) l'; J' \,\middle|\middle|\, \mathbf{D} \times \mathbf{D}' \,\middle|\middle|\, J_f(l_a l_b) l; J \right\rangle .
\end{aligned} \tag{4.15}$$

The terms between graph parenthesis are Wigner 6-j [80, p. 140] and 9-j [80, p. 143] symbols, respectively. To obtain (4.14) and (4.15) we have coupled the angular momentum, J_f (J'_f), of the final ion with the angular momentum of the electron-pair, $l = l_a + l_b$ ($l' = l'_a + l'_b$), to obtain the total angular momentum, J, $\left|J_f(l_a l_b) l; J\right\rangle$ ($|J'_f(l'_a l'_b) l'; J'\rangle$). The properties of 6- and 9-j symbols [80] allows to simplify these expressions. First of all, we must remember that in a photoemission experiment the initial target and the final ion are in parity eigenstates, this means that the emitted electron-pair wave-function must be a parity eigenstate of parity $\Pi = (-1)^{l_a+l_b}$ as well. Parity conservation implies that the two electrons in the continuum can, in principle, possess any angular momenta that satisfy the condition that $l_a + l_b$ is either even or odd. Furthermore, the 3-j symbols in (4.15) imply that the only term contributing to the dichroism are the ones with

$$\begin{aligned}
l_a + l'_a + L_a &= \text{even} \\
l_b + l'_b + L_b &= \text{even}.
\end{aligned} \tag{4.16}$$

The two equations in (4.16) can be added to obtain,

$$\underbrace{l_a + l_b}_{\text{even(odd)}} + \underbrace{l'_a + l'_b}_{\text{even (odd)}} + L_a + L_b = \text{even}, \tag{4.17}$$

through which we can conclude that in order to have non-vanishing circular dichroism it must be $L_a + L_b = $ even. The 9-j symbol implies that the three momenta 1, L_a, L_b satisfy the triangular relation $|L_a - 1| \leq L_b \leq L_a + 1$. The extremal cases, $L_b = L_a \pm 1$, lead to $L_a + L_b = $ odd, so the only possibility is $L_a = L_b$. Therefore eq. (4.14) simplifies to

$$\Delta = -i \sum_{L} \gamma_{LL} B_{10}^{LL}(\hat{\mathbf{k}}_a, \hat{\mathbf{k}}_b). \tag{4.18}$$

The above formula allows to analyse the circular dichroism as a function of the electrons' emission directions $(\hat{\mathbf{k}}_a, \hat{\mathbf{k}}_b)$ and energies (E_a, E_b). These informations are included in the properties of the bipolar spherical harmonics (BSH),

$$B_{10}^{LL}(\hat{\mathbf{k}}_a, \hat{\mathbf{k}}_b) = \sum_{M} \langle LML - M \mid 10 \rangle \, C_{LM}(\hat{\mathbf{k}}_a) C_{L-M}(\hat{\mathbf{k}}_b). \tag{4.19}$$

(i) $B_{10}^{LL}(\hat{\mathbf{k}}_a, \hat{\mathbf{k}}_b)$ are purely imaginary. This can be seen using the properties of spherical harmonics [80, p. 145] $C_{L-M}(\theta,\phi) = (-1)^M C^*_{LM}(\theta,\phi)$ and the symmetry formula for Clebsch-Gordan coefficients $|L-MLM\,|\,10\rangle = -\,|LML-M\,|\,10\rangle$. Since the dichroism is a real quantity property (i) implies that the coefficients $\gamma_{LL}(k_a,k_b)$ are real.

(ii) $B_{10}^{LL}(-\hat{\mathbf{k}}_a, -\hat{\mathbf{k}}_b) = B_{10}^{LL}(\hat{\mathbf{k}}_a, \hat{\mathbf{k}}_b)$; the BSH are even in the momentum space of the two photoelectrons. This is a consequence of spherical harmonics parity $C_{LM}(-\hat{\mathbf{x}}) = (-1)^L C_{LM}(\hat{\mathbf{x}})$.

$$B_{10}^{LL}(-\hat{\mathbf{k}}_a, -\hat{\mathbf{k}}_b) = \sum_M \langle LML-M\,|\,10\rangle\,(-1)^L C_{LM}(\hat{\mathbf{k}}_a)(-1)^L C_{L-M}(\hat{\mathbf{k}}_b) = B_{10}^{LL}(\hat{\mathbf{k}}_a, \hat{\mathbf{k}}_b)$$

(iii) BSH are odd with respect to the exchange of the electrons $B_{10}^{LL}(\hat{\mathbf{k}}_a, \hat{\mathbf{k}}_b) = -B_{10}^{LL}(\hat{\mathbf{k}}_b, \hat{\mathbf{k}}_a)$

(iv) $B_{10}^{LL}(\hat{\mathbf{k}}_a, \hat{\mathbf{k}}_b)$ vanishes when the electrons are emitted in the same direction $\hat{\mathbf{k}}_a = \hat{\mathbf{k}}_b$ or in back-to-back configuration $\hat{\mathbf{k}}_a = -\hat{\mathbf{k}}_b$. See [26, 81] for the demonstration.

(v) The dichroism vanishes if the direction of the incident light, $\hat{\mathbf{k}} \equiv \hat{\mathbf{z}}$, and the electrons' momenta are linearly dependent. Indeed, if $\hat{\mathbf{k}}_a = (\theta_a, \phi_a)$ and the three vectors are dependent, then $\hat{\mathbf{k}}_b = (\theta_b, \phi_a + N\pi)$ (N integer). In this case the product of the phase-factor of the spherical harmonics in (4.19),

$$e^{iM\phi_a} e^{-iM(\phi_a + N\pi)} = e^{-iMN\pi} = (-1)^{MN},$$

is real. From this, it results that $B_{10}^{LL}(\hat{\mathbf{k}}_a, \hat{\mathbf{k}}_b)$ are real which is in contrast with property (i).

(vi) The circular dichroism vanishes if we integrate over one of the directions $\hat{\mathbf{k}}_a$, $\hat{\mathbf{k}}_b$. This follows from the orthogonality of the spherical harmonics. This is a very important property because it means that the circular dichroism can be observed only in coincidence experiments. The chirality is a property of the emitted electron-pair, and it cannot be revealed if one of the two electrons is not detected.

Circular dichroism (CD) is defined as the normalised difference between right and left circular polarisation TDCS. Being a physical observable, it must be invariant under the exchange of the two photoemitted particles;

$$\mathrm{CD}(\mathbf{k}_a, \mathbf{k}_b) = \frac{\sigma^+(\mathbf{k}_a, \mathbf{k}_b) - \sigma^-(\mathbf{k}_a, \mathbf{k}_b)}{\sigma^+(\mathbf{k}_a, \mathbf{k}_b) + \sigma^-(\mathbf{k}_a, \mathbf{k}_b)} = \mathrm{CD}(\mathbf{k}_b, \mathbf{k}_a). \tag{4.20}$$

This property, added to (4.18) and BSH property (iii), implies that the γ_{LL} functions must be even under the electrons exchange, i.e.

$$\gamma_{LL}(k_a, k_b) = -\gamma_{LL}(k_b, k_a).$$

This leads to a vanishing CD for electrons of equal kinetic energy.

4.2 Circular dichroism and chirality

The properties listed in the previous section state that, in order to observe CD, the three vectors of interest $\mathbf{k}$, $\mathbf{k}_a$ and $\mathbf{k}_b$, must be mutually independent. Thus, they must form an oriented coordinate system, $\mathcal{S}$. In this sense a polarisation inversion corresponds to invert the orientation of $\mathcal{S}$. Assume that we are in the situation depicted in Fig.4.1 where the photon beam is perpendicular to the plane defined by $\hat{\mathbf{k}}_a$ and $\hat{\mathbf{k}}_b$. The DPE cross-section depends on the electrons' kinetic energies and on the angle between them θ_{ab}. For this reason we can choose the situation in which the photon direction is perpendicular to the plane of the drawing and the x-axis is the bisector of θ_{ab}.

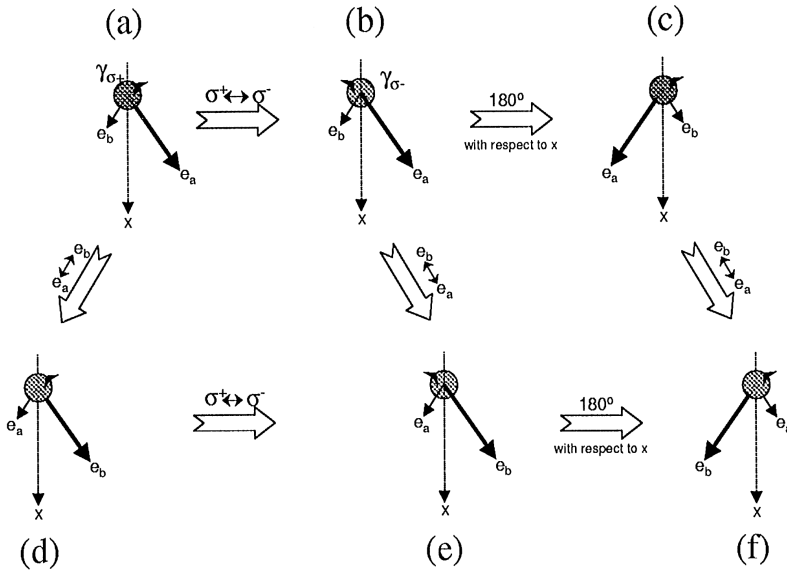

Figure 4.1: Schematic illustration of the chirality in the final-state of a DPE process. The propagation direction of the photon is perpendicular to the sheet and right (clockwise) and left (anticlockwise) circular polarisation are indicated by $\gamma_{\sigma+}$ and $\gamma_{\sigma-}$, respectively. The emitted electrons are indicated by the arrows labelled as e_a and e_b. The length of the arrows is proportional to the electron kinetic energy. Image from [81].

Fig.4.1(a) and Fig.4.1(b) represent the experimental set-up with right and left circular polarisation, respectively. The difference in the coincidence rates of these two cases gives the CD. The Pauli principle requires that the results of the experiment must be the same if we exchange the role of the two electrons, Fig.4.1(d) and Fig.4.1(e) respectively. It is clear that all these cases are characterised by the fact that the fast electron, indicated by the long arrow, is always on the right side of the x-axis. As a consequence, the operation of reversing the light helicity does not correspond to any rotation in the space, e.g. it is not possible to obtain the set-up in Fig.4.1(a) by any rotation of the one in Fig.4.1(b). If we perform a 180° rotation around the x-axis we can reverse the light helicity but in the final state the fast electron is on the left side of the x-axis, see Fig.4.1(c) and Fig.4.1(f). All of this points out that the CD in DPE can be considered as an effect of this left-right asymmetry. If the electrons are ejected in the same direction, $\theta_{ab} = 0$, or in back-to-back configuration, $\theta_{ab} = \pi$, the asymmetry disappears and no CD is observed. Analogous considerations can be drawn if the two electrons escape with the same kinetic energy. In this case it is not possible to distinguish between the fast and slow electron and CD disappears.
In the considered case the initial atom has no preferred direction. This means that the chirality in the initial state is carried by the photon. After the photon has been absorbed its chirality might be transferred either to the electron-pair or to the electrons in the residual ion. In the first case, the detected electron-pair becomes chiral and circular dichroism is observed in the DPE spectrum. In the second one the chirality is carried away by the residual ion and the circular dichroism in the DPE cross section vanishes.

4.3 Circular dichroism in He double-photoionisation

The results shown in the previous pages have been used by Berakdar *et al.* [25] to obtain numerical results for the size and shape of the CD in the double-photoionisation of He atoms. He is the simplest two-electron system and, since there are no electrons in the doubly-ionised final ion, the chirality of the photon is always transferred to the electron-pairs. In order to calculate the TDCS for left and right circular polarisation we have to define the wave-functions for the initial Φ_i and final $\psi_{\mathbf{k}_a\mathbf{k}_b}$ many-electron states. We have seen, in the first pages of this chapter, that in order to have a non-vanishing DPE intensity we cannot use independent particle wave-functions to describe the initial or final state of the process. In this case we will describe the initial two-electron state by a two-parameter Hylleraas wave-function given by

$$\Phi_i = Ne^{-\alpha(r_a+r_b)+\beta r_{ab}},$$

where r_a (r_b) is the distance between the electron a (b) and the nucleus and r_{ab} is the distance between the two electrons. For He the parameters have values,

$$N = 1.474 \quad \alpha = 1.858 \quad \beta = 0.255.$$

The final state is defined starting from a wave-function describing two outgoing electrons and satisfying the Coulomb boundary conditions,

$$\begin{aligned}\psi_{\mathbf{k}_a\mathbf{k}_b}(\mathbf{r}_a,\mathbf{r}_b) &= \frac{1}{(2\pi)^{3/2}}e^{i\mathbf{k}_a\cdot\mathbf{r}_a}e^{\pi\alpha_a/2}\Gamma(1+i\alpha_a)\,{}_1F_1(-i\alpha_a;1;-i(k_a r_a+\mathbf{k}_a\cdot\mathbf{r}_a))\\ &\times\frac{1}{(2\pi)^{3/2}}e^{i\mathbf{k}_b\cdot\mathbf{r}_b}e^{\pi\alpha_b/2}\Gamma(1+i\alpha_b)\,{}_1F_1(-i\alpha_b;1;-i(k_b r_b+\mathbf{k}_b\cdot\mathbf{r}_b))\\ &\times e^{-\pi\alpha_{ab}/2}\Gamma(1-i\alpha_{ab})\,{}_1F_1(i\alpha_{ab};1;-i(\mathbf{k}_{ab}r_{ab}+\mathbf{k}_{ab}\cdot\mathbf{r}_{ab}))\end{aligned} \tag{4.21}$$

with

$$\alpha_a = \frac{Z}{k_a} \qquad \alpha_b = \frac{Z}{k_b} \qquad \alpha_{ab} = \frac{1}{2k_{ab}} \qquad \mathbf{k}_{ab} = \frac{1}{2}(\mathbf{k}_a-\mathbf{k}_b) \qquad \mathbf{r}_{ab} = \mathbf{r}_a-\mathbf{r}_b$$

where $Z = 2$ is the nuclear charge. In what follows we will use the symmetrized part of this function,

$$\psi^S_{\mathbf{k}_a\mathbf{k}_b} = \sqrt{\frac{1}{2}}\left[\psi_{\mathbf{k}_a\mathbf{k}_b}(\mathbf{r}_a,\mathbf{r}_b)+\psi_{\mathbf{k}_a\mathbf{k}_b}(\mathbf{r}_b,\mathbf{r}_a)\right].$$

The investigated experimental set-up is shown in Fig.4.2. The circularly polarised light hits the sample along the vertical direction $\hat{\mathbf{z}}$. The emitted electrons are detected in the plane $\hat{\mathbf{x}}-\hat{\mathbf{y}}$ perpendicular to the light direction. The emission direction of one of the two electrons is fixed and coincides with $\hat{x}$. The second electron, indicated with the subscript a, is detected at an angle ϕ with respect to the first one labelled as b. Fig.4.3(a) shows the DPE TDCS calculated for right (R) and left (L) circularly polarised light as a function of a-electron kinetic energy E_a. In this case the emission directions of the photoelectrons are mutually perpendicular, i.e. $\varphi = 90^\circ$ and their sum energy has been chosen to be $E_a + E_b = 50$ eV.

The two TDCS curves have the same value when the energy of both electrons is the same and equal to 25 eV. This is in agreement with the properties of CD, affirming that it must vanish for equal electron energies. In this configuration, the sign of the CD changes under the reflection at $E_a = E_b$ and its maxima correspond to $E_>/E_< \sim 9$ eV, where we indicated with $E_>$ ($E_<$) the highest (lowest) between the two photoelectrons' kinetic energies. As stated in the previous section,

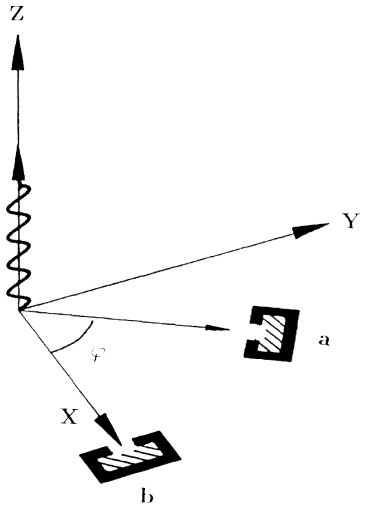

Figure 4.2: Coordinate frame and experimental set-up taken from [25]. Circular polarised light hits the sample in the $\hat{\mathbf{z}}$ direction. One electron analyzer (b) is in the $\hat{\mathbf{x}}$ direction, whereas the other one (a) can be rotated in the $\hat{\mathbf{x}} - \hat{\mathbf{y}}$ plane, orthogonal to the light direction.

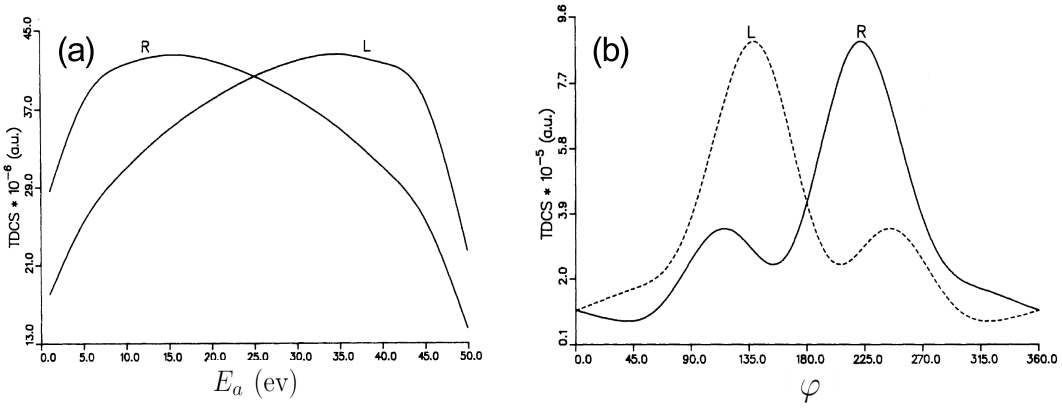

Figure 4.3: (a) The TDCS for He as a function of the kinetic energy E_a of the electron emitted in $\hat{\mathbf{y}}$ direction, see Fig.4.2. The sum energy of the electron-pair is $E_a + E_b = 50$ eV. R and L stand for right and left circular polarisation. See [25] for details.

the CD is the consequence of a geometrical asymmetry in the electron-pair as a whole. Despite this, a reduced symmetry is still visible in the two curves which are identical under a reflection at the energy $E_a = E_b = 25$ eV.
The angular dependence of the CD is shown in Fig.4.3(b). In this case the electron b is fixed in the $\hat{\mathbf{x}}$ direction while the electron a is detected at an angle φ relative to electron b. The energies of the electrons are fixed with $E_a = 5$ eV and $E_b = 45$ eV, in order to be on the maximum of the CD. The continuous (dashed) line in Fig.4.3(b) represents the TDCS for right (left) circular polarisation. The two curves intersect, leading to a vanishing CD, when the photoelectrons are emitted in parallel or anti-parallel direction, at $\varphi = 0^\circ$ and $\varphi = 180^\circ$, respectively. As already seen in Fig.4.3(a) the electron-pair shows some symmetry. Indeed, the two TDCS have the same shape under the transformation $\varphi \to 360^\circ - \varphi$.

4.4 Circular dichroism in core-resonant DPE

In this section we will treat the circular dichroism in the case of core-resonant DPE. Since we are interested in highlighting the differences between direct and core resonant DPE we will consider the case in which the lifetime of the intermediate state (core-hole) is long enough to treat the Auger process in a two-step picture. In these conditions the presence of the intermediate state involves additional conditions for the CD to exist. The following results are taken from the works of Kabachnik and Schmidt [82].
The first step to obtain a formula for the CD in the case of two-step core resonant DPE corresponds to rewrite the expression for CD in direct DPE [eq. (4.18)] by means of the formalism used by Kabachnik (see [83] and references therein for further details),

$$\Delta = \sqrt{2}\sum_L A(L,L,1) B_{10}^{LL}(\mathbf{k}_a, \mathbf{k}_b). \tag{4.22}$$

Here $B_{10}^{LL}(\mathbf{k}_a, \mathbf{k}_b)$ represents the formerly defined bipolar spherical harmonics and

$$\begin{aligned} A(L,L,1) \;=\; & C \sum_{JJ'J_rJ'_r} \sum_{j_1 j'_1 j_2 j'_2} \frac{(\hat{L}\hat{J}\hat{J}')^2 \hat{J}_r \hat{J}'_r}{\hat{J}_i^2} (-1)^{1+j'_2+J_r+J_f+J+J_i+k} \\ & \times \begin{Bmatrix} 1 & J & J_i \\ J' & 1 & 1 \end{Bmatrix} \begin{Bmatrix} j_2 & J_r & J_f \\ J'_r & j'_2 & L \end{Bmatrix} \begin{Bmatrix} J_r & j_i & J \\ J'_r & j'_1 & J' \\ L & L & 1 \end{Bmatrix} \\ & \times c_{L0}(l_1 j_1, l'_1 j'_1) c_{L0}(l_2 j_2, l'_2 j'_2) T^J_{\beta\alpha}(E_a, E_b) T^{J'*}_{\beta'\alpha'}(E_a, E_b). \end{aligned} \tag{4.23}$$

J (J') represents the total (ion + free electrons) angular momentum, J_f (J'_f) the angular momentum of the residual ion, j_a, j_b (j'_a, j'_b) the total angular momenta of the emitted electrons. Here the differences between the one- or two-step processes are ascribable to the presence of the intermediate core-hole state with a well-defined angular momentum, J_r. This implies that the rules for angular momentum (and parity) conservation must be satisfied in both the first (photoemission) and second (Auger decay) step of the DPE process, as stated by the Wigner 6-j and 9-j symbols.
In this case we considered a momentum coupling scheme in which J_f and j_2 are first coupled to get the angular momentum of the core-hole, J_r, and later J_r and j_1 are coupled to get the total angular momentum J, $(J_f + j_2 = J_r) + j_1 = J$. We indicated with $\hat{j} = (2j+1)^{1/2}$ the square root of the multiplicity of the angular momentum.

The radiative parameters $C_{L0}(jl, j'l')$, defined as

$$C_{L0}(jl, j'l') = \frac{1}{4\pi}\hat{l}\hat{l}'\hat{j}\hat{j}'(-1)^{j'+1/2}\langle l0, l'0\,|L0\rangle \begin{Bmatrix} j & l & 1/2 \\ j' & l' & L \end{Bmatrix}, \tag{4.24}$$

describe the photoelectrons angular distribution, which depends on the alignment of the intermediate core-hole state with the quantization axis of the system corresponding to the incident direction of the photon.
$T^J_{\beta\alpha}(E_a, E_b)$ represents the matrix element for the transition from the initial (photon + atom) to the final state (ion + two electrons in continuum) with electrons kinetic energies E_a and E_b, respectively. α and β represent the set of quantum numbers to describe these states. In core-resonant DPE the transition amplitude, from (3.21), can be written as

$$T^J_{\beta\alpha}(E_a, E_b) = \frac{\langle \psi_{\beta E_a}\,|V\,|\Phi_r\rangle\langle\Phi_{rE_b}|\,D\,|\Phi_i\rangle}{E_b - \varepsilon_r + i\Gamma}, \tag{4.25}$$

where V is the Coulomb potential. The final state $\psi_{\beta E_a}$ is the anti-symmetric product of the ion- and Auger electron- wavefunctions as well as the intermediate state Φ_{rE_b} is the product of singly-charged ion and photoelectron states. The resonance energy corresponds to the photoemission energy $\varepsilon_r = E_0 + \hbar\omega - E^{N-1}$. Substituting the amplitude in (4.25) in (4.22), after some mathematics (see [82] for the details) we can write

$$\Delta = -\sigma_{J_r}(\hbar\omega)\frac{\omega_A}{4\pi}c(E_b)\sum_L \alpha_L \bar{\Delta}_L B^{LL}_{10}(\mathbf{k}_a, \mathbf{k}_b), \tag{4.26}$$

where

$$c(E_b) = \frac{\Gamma/\pi}{(E_b - \varepsilon_r)^2 + \Gamma^2} \tag{4.27}$$

is a standard Lorentz factor, which describes the line shape of the photo-ionisation process independently from the subsequent Auger decay. The photoelectrons emission rate is accounted by the photoionisation cross section,

$$\sigma_{J_r}(\hbar\omega) = \frac{4\pi^2\alpha\hbar\omega}{3(2J_i+1)}\sum_{l_1 j_1 J}\left|\langle J_r(l_1\ 1/2)j_1 : J\,||D||\,J_i\rangle\right|^2, \tag{4.28}$$

describing the process in which one electron of angular momentum $j_i = l_i + 1/2$ is emitted leaving the residual ion in a state of angular momentum J_r which is related to j_i by the fact that their sum must be equal to the angular momentum of the total system J.

$$\omega_A = \frac{\Gamma_{J_r \to J_f}}{\Gamma} \tag{4.29}$$

is the partial Auger decay rate to the final state with angular momentum J_f and

$$\begin{aligned} \alpha_L &= \frac{1}{N}(-1)^{J+J_f-\frac{1}{2}\hat{J}}\sum_{l_2 j_2 l_2' j_2'}\hat{l}_2\hat{j}_2\hat{l}_2'\hat{j}_2'\langle l_2 0, l_2' 0\,|L0\rangle \begin{Bmatrix} J & J & L \\ j_2 & j_2' & J_f \end{Bmatrix} \\ &\quad\times \begin{Bmatrix} j_2 & j_2' & L \\ l_2' & l_2 & \frac{1}{2} \end{Bmatrix}\langle J_f(l_2\ 1/2)j_2; J\,||V||\,J\rangle\langle J_f(l_2'\ 1/2)j_2'; J\,||V||\,J\rangle^* \\ N &= \sum_{l_2 j_2}\left|\langle J_f(l_2\ 1/2)j_2; J\,||V||\,J\rangle\right|^2 \end{aligned} \tag{4.30}$$

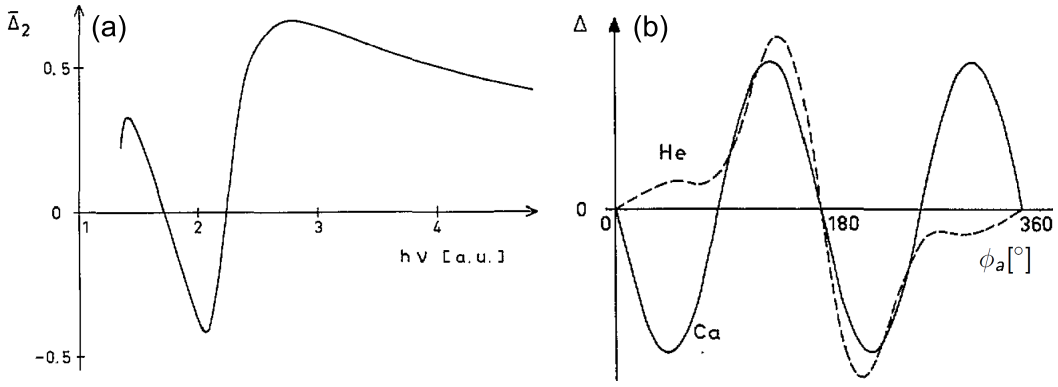

Figure 4.4: (a) Photon energy dependence of the parameter $\hat{\Delta}_2$ for the two-step Auger decay of Ca ($3p_{3/2}$ photoemission followed by $M_3N_1N_1$ Auger decay) [82]. (b) Angular dependence of circular dichroism Δ for Ca $M_3N_1N_1$ Auger decay (solid line), and the corresponding curve for He direct DPE (dashed line) as calculated by Berakdar & Klar [25]. Image from [82]

is the Auger decay anisotropy coefficient [84], which depends on the Auger matrix elements and describes the angular anisotropy of the Auger transition.
The quantity

$$\bar{\Delta}_L = \frac{-\sqrt{6}}{2L+1}\frac{B(L,L,1)}{B(0,0,0)} \tag{4.31}$$

with

$$\begin{aligned} B(L,L,1) &= 3\sum_{JJ'l_1l_1'j_1j_1'} \hat{J}\hat{J}'\hat{l}_1\hat{l}_1'\hat{j}_1\hat{j}_1'(-1)^{j_1'-1/2+J+J_i+1}\left\langle l_1 0 l_1' \,|L0\right\rangle \\ &\times \left\{ \begin{array}{ccc} j_1 & l_1 & 1/2 \\ l_1' & j_1' & L \end{array} \right\} \left\{ \begin{array}{ccc} 1 & J & J_i \\ J' & 1 & 1 \end{array} \right\} \left\{ \begin{array}{ccc} J_r & j_i & J \\ J_r & j_1' & J' \\ L & L & 1 \end{array} \right\} \\ &\times \left\langle J_r(l_1\ 1/2)j_1;J\,||D||\,J_i\right\rangle \left\langle J_r(l_1'\ 1/2)j_1';J'\,||D||\,J_i\right\rangle^*, \end{aligned} \tag{4.32}$$

is related to the inner-shell photoionisation step. It is separated from the parameters describing the Auger decay and and the ones describing the geometrical properties, represented by the bipolar spherical harmonics (BSH).
Since in core-resonant DPE the intermediate state (core-hole) has well defined parity and angular momentum, the angular pattern of the CD has additional constraints with respect to the direct DPE case. The symmetry properties of the 9−j symbol imply that the angular momenta on the same row or column must satisfy a triangular relation. For example considering the first column of the 9−j symbol in (4.32), $|J_r - J_r| \leq L \leq |J_r + J_r|$. This implies that the sum index L in (4.22) assumes integer values, $0 \leq L \leq 2J_r$. In addition, the definite parity of the ionic-state leads to the further condition $L =$ even because, oppositely to direct DPE, in two-step core-resonant DPE the parity is conserved in both photoemission and subsequent Auger decay. This has a consequence also in the geometrical conditions because the BSH with odd index disappear from the sum.

In order to highlight the differences between one- or two-step core-resonant DPE we will show the example of the $3p_{3/2}$ photoemission from Ca and the subsequent $M_3 - N_1N_1$ Auger decay

proposed by Kabachnik and Schmidt [82]. We consider the transition towards the $^1S_0$ configuration of the final ion for which the asymmetry parameter α_2 is known and equal to -1. Being the only possible transition for the decay from the M_3 core-hole state we have $\omega_A = 1$. The angular momentum of the vacancy is $J_r = 3/2$, therefore the only term contributing to the CD is the one with $L = 2$. In the dipole approximation, the electrons photoemitted from $3p_{3/2}$ level can have s or d symmetry, so the transition is described by the two matrix elements D_s and D_d whose relative phase is $\delta = \delta_s - \delta_d$. Under these conditions equation (4.31) can be calculated to give

$$\hat{\Delta}_2 = -\frac{3}{\sqrt{5}} \frac{D_s D_d \sin\delta}{D_s^2 + D_d^2} = -\sqrt{\frac{8}{5}} \eta_{3/2} \tag{4.33}$$

where $\eta_{3/2}$ is the photoelectron spin-polarisation parameter. By means of the spherical harmonics definition we can now obtain the circular dichroism,

$$\begin{aligned} \Delta &= -\sigma_{3/2}(\hbar\omega) \frac{1}{4\pi} c(E_b) \alpha_2 \hat{\Delta}_2 B_{10}^{22}(\mathbf{k_a}, \mathbf{k}_b) \\ &= \sigma_{3/2}(\hbar\omega) \frac{1}{(4\pi)^2} c(E_b) 6\eta_{3/2} [\frac{1}{2}(1-\cos^2\theta_a)(1-\cos^2\theta_b)\sin 2(\phi_a - \phi_b) \\ &\quad + \cos\theta_a \cos\theta_b \sin\theta_a \sin\theta_b \sin(\phi_a - \phi_b)], \end{aligned} \tag{4.34}$$

as a function of the polar θ_i and azimuthal ϕ_i ($i = a, b$) angle of the electrons in the continuum. The photon energy dependence of the CD, depending on the spin-polarisation parameter $\eta_{3/2}(\hbar\omega)$ obtained from the RRPAE (Relativistic Random Phase Approximation with Exchange) calculations performed by Deshmukh and Johnson [85], is shown in Fig.4.4(a). The two zeros of $\hat{\Delta}_2$ falling at $\hbar\omega = 1.75$ a.u. $= 47.6$ eV and $\hbar\omega = 2.25$ a.u. $= 62.1$ eV, correspond to a destructive interference between the final s and d channels, $\sin\delta = 0$, and to a zero crossing of the dipole matrix element D_d (Cooper minimum), respectively. So in this particular cases the vanishing of CD is purely an effect of the photoionisation from Ca $3p_{3/2}$.

Fig.4.4(b) shows the angular dependence of the CD, calculated in a configuration analogous to the one considered in He double-photoionisation, Fig.4.2. The two electrons are detected in the plane perpendicular to the light direction ($\theta_a = \theta_b = 90^\circ$), the direction of the photoelectron is kept fixed at $\phi_b = 0^\circ$ and the Auger electron direction ϕ_a is variable. The photon energy has been chosen to be $\hbar\omega = 2.75$ a.u. $= 74.8$ eV corresponding to the maximum of the CD. In order to highlight the differences between one- or two-step DPE the dashed line in Fig.4.4(b) represents the CD in He case obtained subtracting the two curves calculated by Berakdar and Klar [25] and shown in Fig.4.3(b). It is clear how the presence of the stationary well defined intermediate (core-hole) state brings additional restrictions on the CD. Indeed, in the two-step case the angular distribution of the CD is proportional to $\sin 2(\phi_a - \phi_b)$. It has a higher symmetry with respect to the one-step picture which shows a proportionality to $\sin(\phi_a - \phi_b)$. This dependence adds further conditions to parity conservation which only requires zeros at $(\phi_a - \phi_b) = 0^\circ$ and $(\phi_a - \phi_b) = 180^\circ$.

Chapter 5

Experimental details

In the following pages we will introduce electron-electron coincidence spectroscopy paying particular attention to the description of the experimental apparatus used in the experiments performed in this thesis.
The specificity of DPE experiments lies in the fact that, oppositely to common single-particle spectroscopies, one has to deal with the detection of correlated electron-pairs. In a DPE process two electrons are emitted upon the absorption of a single photon so the need to develop a spectroscopic technique that is able to simultaneously detect both the emitted particles and to disentangle correlated from uncorrelated electron-pairs. The former are made up of electrons produced in the same physical event, while the latter correspond to electrons produced in independent physical events, e.g. two photon absorptions leading to two independent electron emissions.
The prototypical scheme of 1-photon IN 2-electrons OUT, $(\gamma, 2e)$, processes,

$$h\nu + A \rightarrow e_1^- + e_2^- + A^{++}(v^{-1}v^{-1}),$$

clarifies the characteristic observables of a DPE experiment, i.e. the kinetic energies (E_1, E_2) and momenta ($\mathbf{k}_1, \mathbf{k}_2$) distribution of correlated electron-pairs. These distributions can be recorded by means of *electron-electron coincidence spectroscopy* in which one measures the kinetic energy and momentum (emission angle) of those electrons that are correlated in time and hence originate from the same double-ionisation event.
The schematic of such an experiment is given in Fig. 5.1. The main components are:

- A primary photon source (X-Ray lamps, discharge lamps, synchrotron radiation sources).
- Two independently tunable electron-analysers.
- A coincidence electronics.

The electrons emitted upon the absorption of a photon of energy $h\nu$ impinging on the neutral target A are selected with respect to their energy and momentum by the two electron-analysers and arrive to the detectors D_1 and D_2. The signals produced by the detectors are then analysed by a coincidence electronics, which acts as a logic AND gate, and allows the detection of those electrons that are emitted within a well defined time window (usually of the order of hundreds of nanoseconds). Through the coincidence electronics it is possible to record, in addition to the energies and emission angles, the arrival times of the electrons at the detectors. In this way one can construct the time coincidence spectrum of the experiment, i.e. the distribution of the differences in the arrival times of the two detected electrons $\Delta t = t_1 - t_2$. From the time distribution one can in

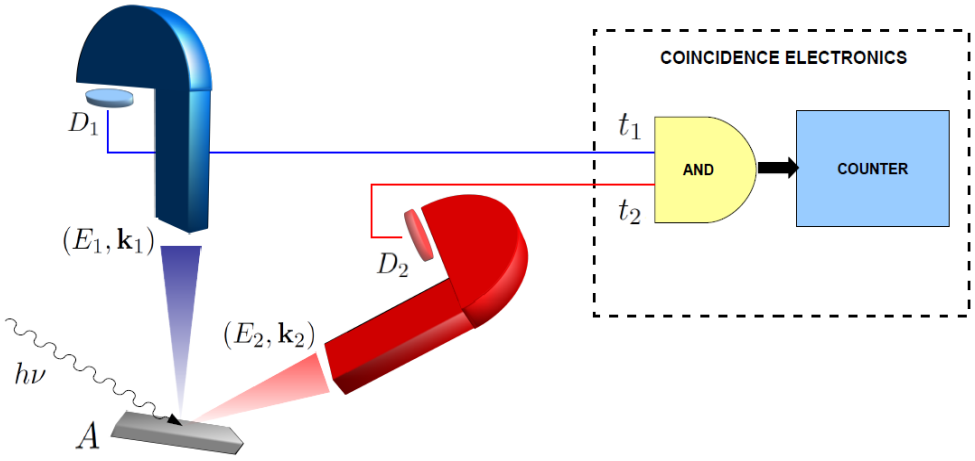

Figure 5.1: Scheme of an electron-electron coincidence set-up.

principle distinguish those electron-pairs that have been emitted in the same physical event from those that have not. Indeed, if two electrons are emitted in the same process (e.g. DPE), they have to reach their respective detectors at the same time within the experimental resolution. So the detection of correlated electron-pairs will result in events always delayed by the same amount which give rise, in the time spectrum, to a peak centered at $\Delta t = 0$.
However, it is also possible to detect events in which two incident photons are absorbed within the time window of the experiment and cause the detection of two uncorrelated electrons. These events (accidental coincidences) manifest themselves by a background continuously distributed over all the possible time differences. By removing the background of accidental coincidences one is able to determine the number of correlated electron-pairs emitted by the sample.
Several time spectra are measured by varying the energies or the angles accepted by the analysers, thus one can extract the number of true coincidences, i.e. the intensity of correlated electron-pairs, as a function of the electrons kinetic energies and emission angles and determine the triple differential cross section (TDCS) of the process.

In the following part of the chapter we will present a detailed description of the experimental apparatus used in this thesis, paying particular attention to the description of the synchrotron radiation source, the electron analysers and the coincidence electronics. In the last part the optimisation of the experimental conditions is discussed.

5.1 Photon source: synchrotron radiation

When electrons, moving with relativistic speed, are forced by the action of electric and magnetic fields to follow circular trajectories, they emit electromagnetic radiation in a narrow cone around their direction of motion, Fig. 5.2. This highly-collimated light is called synchrotron radiation [33, 86].
Common synchrotron radiation sources are high-energy, circular electron accelerators (storage rings) and consist of evacuated pipes in which the electrons are forced to follow circular paths under the action of (bending) magnets placed along the circumference. The synchrotron radiation is emitted along the curved orbit in a bending magnet. One can increase the light emission by

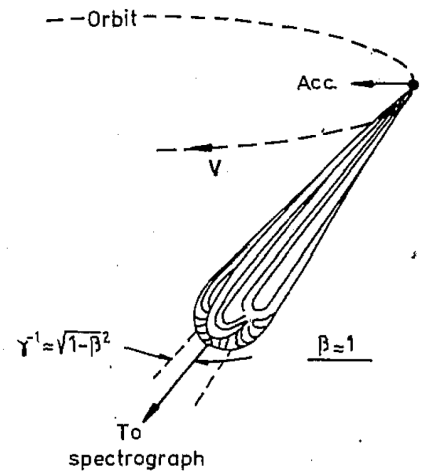

Figure 5.2: Radiation characteristic of an electron moving in a circular orbit at relativistic speed ($v/c \sim 1$). The angular distribution of the radiation peaks strongly in the forward direction. Image from [64].

placing combinations of magnets (insertion devices) into straight sections in the storage rings. These bend the electron beam back and forth, each bend producing radiation but with the overall direction of the beam remaining unchanged.

There are three different types of insertion devices. The wavelength shifter is a three pole arrangement, where the central magnet operates at very high magnetic field and reduces the critical wavelength[1] of the radiation. This device is used to produce, even in low energy synchrotrons, a beam of high energy radiation.

The second type of insertion device is the multipole wiggler, which consists of a series of magnets with changing polarity along the length of the device. This device will act a N independent bending magnets and increase the radiation intensity N-fold.

Finally the undulator (used in this thesis) is a multipole wiggler with many (up to 100) magnets, which work in a the low field regime and confine the radiation of the device to a small angular range. This results in intense radiation, which, for a narrow wavelength range (harmonic), yields up to 10^4 times the intensity obtained with a single bending magnet [64, p. 24-27]

The measures presented in this thesis have been performed at the beam-line UE56/2-PGM2 installed at the synchrotron radiation source BESSY II in Berlin, Germany.

5.2 Light production: the UE56 undulator

The UE56 planar double undulator, depicted in Fig. 5.3(a), is an insertion device that is able to provide linearly and circularly polarised light within the energy range $89 - 1938$ eV. The undulator is made up of two identical modules, indicated as U_1 and U_2 in Fig. 5.3(a), placed at a distance of 2 m and separated by a magnetic chicane, Ch. Each module consists of 31 periods with a period length of 56 mm. Normally, the two modules are set to produce light of opposite helicity of the circular polarisation. With the help of three magnets D_1, Ch, D_2 the electron beam can be steered

[1] $\lambda_c = 5.8\frac{R}{E^3}$, where E is the electron energy and R the radius of the storage ring. λ_c corresponds to the wavelength that divides the total synchrotron power spectrum into two equal parts.

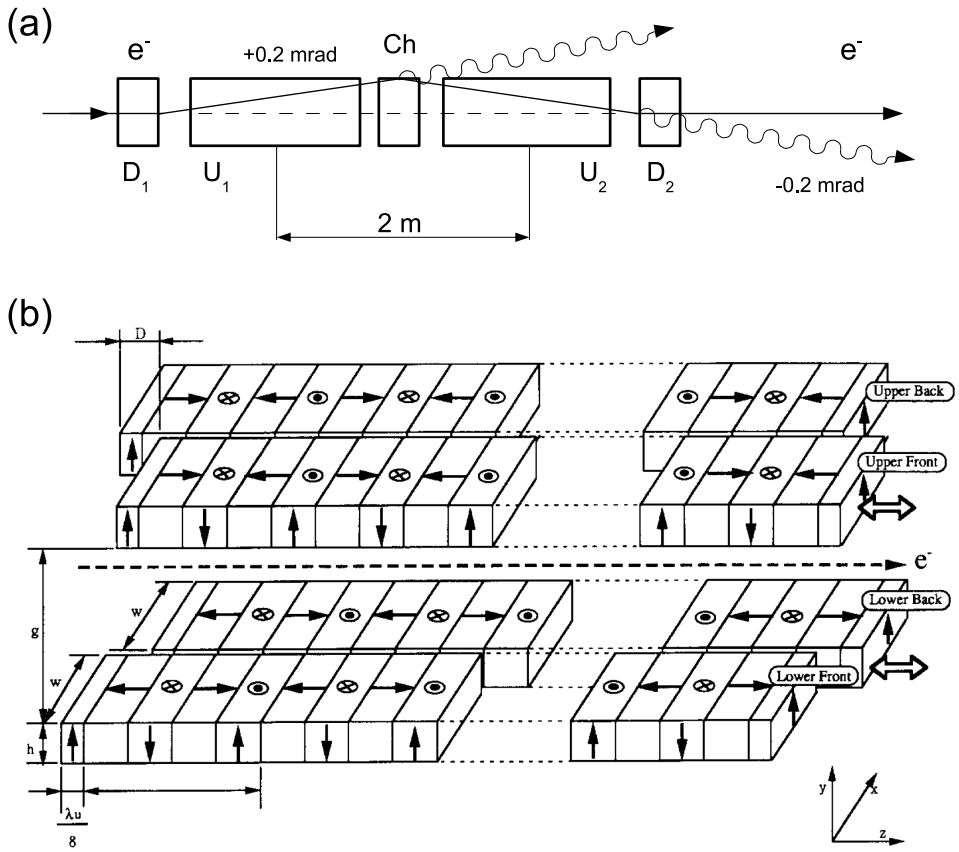

Figure 5.3: (a) Schematic of the radiation emission geometry of the UE56 planar undulator. U_1 and U_2 are the two APPLE modules, D_1 and D_2 the deflecting magnets and Ch the magnetic chicane [87]. (b) Schematic drawing of the APPLE module. The black arrow in each block represents the magnetisation direction, the dashed arrow the flight direction of the electrons. The coordinate system used in the text is also shown [88].

horizontally, in the plane of the ring, by 0.2 mrad in U_1 and -0.2 mrad in U_2. In this way the two produced light beams radiate in different directions and the light polarisation can be quickly switched by means of a light chopper that blocks one of the two beams. If the two modules are set on the same polarisation, the magnets D_1 and D_2 are switched off and the magnetic chicane Ch is used to adjust the phase of the two beams, the device acts as one undulator whose total length is the sum of the two modules lengths.
Fig. 5.3(b) shows a schematic drawing of one of the two single modules. Each module, denoted as APPLE (Advanced Planar Polarised Light Emitter), consists of two plains of planar permanent-magnet rows placed above and below the electron orbit plane, dashed line in Fig. 5.3(b). Two of the four rows (say upper front and lower back) are phase adjustable, i.e. can be moved together with respect to the fixed rows allowing the polarisation state to be changed. The arrow in each block represents the direction of the magnetisation. In Fig. 5.3(b), g is the gap between the upper and lower jaw, λ_μ is the magnetic period length, h and w represents the height and width of each magnetic block, and D is the phase shift between moving and fixed rows.
In order to calculate the magnetic field inside the device we can consider it as composed by two undulators [88]. The first (undulator a), is formed of the lower back row and upper front row, while the second (undulator b) corresponds to a set of the lower front row and upper back row. The magnetic field in one point of the space can be calculated as the sum of the contribution from each block. Therefore, the total field is calculated by adding the contribution from undulator a and b. The components of the magnetic filed generated by the first undulator are

$$B_{ax} = \alpha \sin\left(\frac{2\pi}{\lambda_\mu} z\right) \tag{5.1}$$

and

$$B_{ay} = \beta \sin\left(\frac{2\pi}{\lambda_\mu} z\right). \tag{5.2}$$

If undulator b is shifted by D with respect to a, its contribution is given by

$$B_{bx} = \alpha \sin\left[\frac{2\pi}{\lambda_\mu}(z+D)+\pi\right], \tag{5.3}$$

and

$$B_{by} = \beta \sin\left[\frac{2\pi}{\lambda_\mu}(z+D)\right]. \tag{5.4}$$

Here α and β are the height of horizontal and vertical peak magnetic field, respectively. The on-axis magnetic filed of the whole APPLE undulator is given by adding equations (5.1),(5.3) and (5.2), (5.4), so that

$$B_x = B_{ax} + B_{by} = 2\alpha \cos\left(\frac{\pi}{2} + \pi\frac{D}{\lambda_\mu}\right) \sin\left[\frac{2\pi}{\lambda_\mu}\left(z+\frac{D}{2}\right)+\frac{\pi}{2}\right], \tag{5.5}$$

and

$$B_y = B_{ay} + B_{by} = 2\beta \cos\left(\pi\frac{D}{\lambda_\mu}\right) \sin\left[\frac{2\pi}{\lambda_\mu}\left(z+\frac{D}{2}\right)\right]. \tag{5.6}$$

It is clear from equations (5.5) and (5.6) that the x and y components of the magnetic field are always shifted by $\pi/2$ independently of the phase shift D of the magnet rows. This leads to two appreciable advantages; first, a principal axis of the projected electron beam trajectory does not tilt from the horizontal axis, i.e. the principal axis of the elliptical polarisation does not tilt. Second,

Table 5.1: Parameters of BESSY II and the UE56 undulator, as listed in [87].

Nominal electron energy, E	1.7 GeV
Stored current	300 mA
Horizontal source size, σ_h	0.31 mm
Vertical source size, σ_v	0.022 mm
Undulator period, λ_μ	56 mm
Number of period, N	31
Horizontal peak magnetic field, α	0.38 T
Vertical peak magnetic field, β	0.63 T
Total length	1890 mm
Photon energy	
First harmonic	$89-436$ eV
Third harmonic	$357-981$ eV
Fifth harmonic	$594-1328$ eV

with the right choice of the phase shift it is possible to obtain radiation with horizontal or vertical polarisation. The main parameters of BESSY II and UE56 undulator are listed in Tab.5.1.

Fig. 5.4 shows the on-axis magnetic field generated by the device for different values of the phase shift D, as calculated in [89]. The solid line represents the variation of the vertical component of the magnetic field B_y, while the dashed line the horizontal field component B_x. For $D = 0$ the horizontal component in (5.5) vanishes and one obtains a vertically sinusoidal field. The opposite situation is obtained for $D = 1/2\lambda_\mu$. In this case the vertical component in (5.6) vanishes and the magnetic field sinusoidally oscillates in the horizontal plane. Intermediate cases, with a helical field or a distorted helical field can be obtained for $D = 3/8\lambda_\mu$ and $D = 2/8\lambda_\mu$, respectively.

The electronic orbit can be calculated by the integration along the $z-$axis of the Lorentz force. Fig. 5.5 shows the projection on the *x*-*y* plane of an electron orbit, as obtained from the simulations of Sasaki *et al.* [89]. The part of the orbit represented by the lighter line indicates the path followed by the electrons in entering and exiting the undulator. These parts of the orbit can be neglected as they do not describe the polarisation of the light. In the calculation the electron energy is assumed to be $E = 1$ GeV. For the phase shift $D = 0$ the undulator generates a sinusoidal electron orbit in the horizontal plane, i.e. the electron oscillates in the x direction and the projection of its orbit is an horizontal line. For $D = 4/8\lambda_\mu$ a vertical sinusoidal orbit is generated. Perfectly helical orbit are generated for $D = 3/8\lambda_\mu$, $D = 5/8\lambda_\mu$. The difference in the two cases is given by the electron travel direction, clockwise in the first case and anticlockwise in the second. Distorted helical orbits are obtained in all the other cases ($D = 1/8\lambda_\mu, D = 2/8\lambda_\mu, D = 6/8\lambda_\mu, D = 7/8\lambda_\mu$). Since the state of the polarisation is essentially the same as the projected electron motion on the *x*-*y* plane, horizontal and vertical polarisation is obtained at $D = 0$, $D = 1/2\lambda_\mu$, respectively. Right-handed and left-handed circular polarisation is obtained at $D = 3/8\lambda_\mu$, $D = 5/8\lambda_\mu$. Elliptical polarisation is obtained in all the other cases.

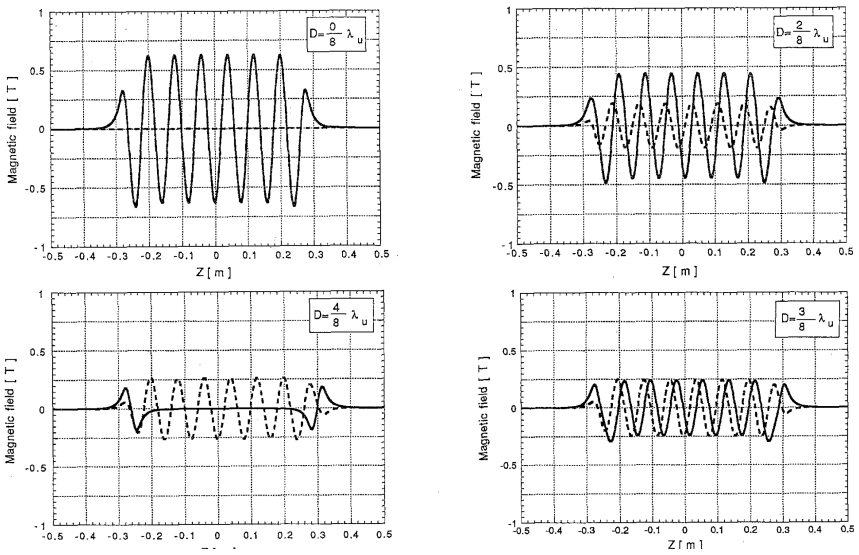

Figure 5.4: On-axis magnetic field generated by the APPLE module with different values of the adjustable phase shift D. Solid and broken lines corresponds to vertical (y) and horizontal (x) component of the magnetic field, respectively [89].

5.3 Light transportation: UE56/2-PGM2 beam-line.

The beam-line UE56/2-PGM2 at BESSY II is a device capable to transport the light produced by the UE56 undulator to the sample in the experimental chamber. It has been designed in such a way that it employs a single set of optical elements for steering and monochromatising the two beams with opposite polarisation. This allows the polarisation to be switched at a high rate (> 100 Hz) with no effect on the beam position, energy and energy resolution.

The beam-line schematic is shown in Fig. 5.6 and the various parameters of the optical elements are listed in Tab.5.2. The beam-line acceptance is 0.8 mrad $\times$ 0.4 mrad ($h \times v$) and is defined by an aperture kept at about 10 m from the source (undulator). The horizontal acceptance is kept as the double of the vertical one in order to transport the two angularly separated beams produced

Table 5.2: Parameters of the optical elements of the beam-line taken from [87].

Optical element Shape	M_1 toroidal	M_2 plane	M_3 cylindrical	M_4 conic	Grating 1 plane	Grating 2 plane
Deflection	Horizontal	Vertical	Horizontal	Horizontal	Vertical	Vertical
Optical active surf. (cm^2)	280×10	300×20	200×25	60×10	90×15	90×15
Coating	Pt	Pt	Pt	Pt	Au	Au
Incidence angle	87^o	Variable	87^o	87^o	Variable	Variable
Source distance (mm)	17000	-	∞	1000	-	-
Radius, R (mm)	334105	-	∞	∞	-	-
Radius, ρ (mm)	1779	-	942	$52.8 - 56.8$	-	-
Groove density (n/mm)	-	-	-	-	400	1200
Groove width to period ratio, c	-	-	-	-	0.70	0.65

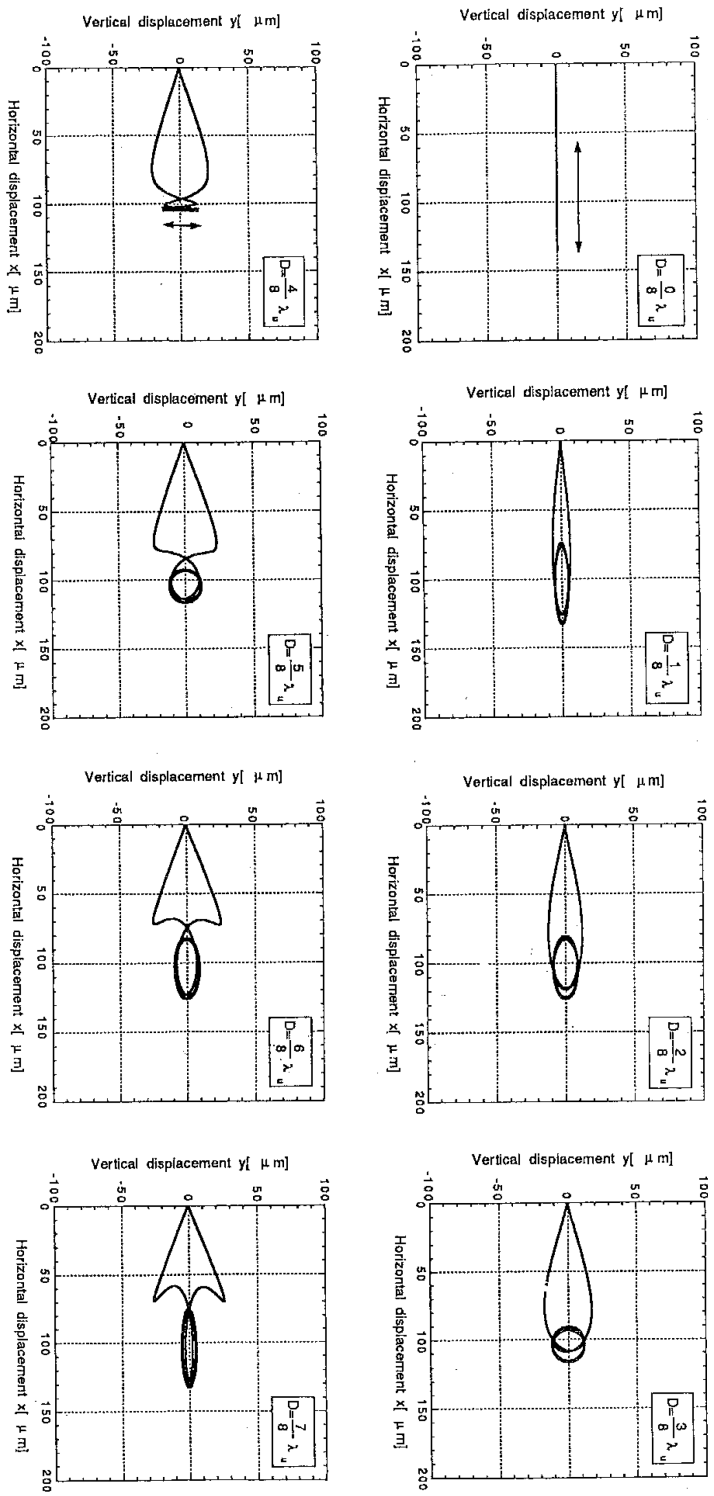

Figure 5.5: Electron trajectories inside the APPLE module projected in the $x-y$ plane at different phase shift D [89].

by the two modules of the undulator. For this reason the horizontal focusing is performed, by means of the mirror M_1, right ahead of the monochromator G. M_1 is the first optical element of the beam-line. Due to its toroidal shape, with different horizontal and vertical radii, it has two different roles. It horizontally focuses the radiation onto the sample with an almost unity linear magnification ($m = 17 : 18$), while the sagittal radius R collimates the beam in the vertical direction. The light from M_1 is vertically diffracted by a plane-grating monochromator (PGM) in SX700 design working with parallel light beams. The SX700 design consists of a rotating plane mirror (M_2) installed before the grating G. During an energy scanning both M_2 and G are rotated in order to change the incidence α and diffraction angle β. The major advantage in working with collimated light is that the focusing condition for a plane grating ($c_f = \cos\alpha/\cos\beta = C = \text{const.}$), which must be kept constant in common SX700 design [90], can be varied freely without the need to rearrange the optical elements behind the grating [91]. In this way the monochromator can be operated in the high-resolution mode (high c_f) or in the higher-order suppression mode (low c_f). In addition, the flux throughput can be maximised by choosing the proper deflection angle at the grating to keep it at high efficiency. In order to cover the whole undulator spectral range ($89 - 1328$ eV) two gratings of 400 l/mm and 1200 l/mm are employed.
The cylindrical mirror M_3 kept behind the monochromator focuses the synchrotron radiation vertically onto the exit slit. In order to have the highest vertical overlapping between the beams produced by U_1 and U_2, the exit slit is placed 4 mm ahead of the nominal position obtained assuming that the source is at the centre of the UE56 undulator. The defocussing of the two beams leads to some loss in brightness but in this way the vertical overlap of the two spots at the sample is optimal, see Fig. 5.7(b). The two beams are vertically refocused onto the sample by an horizontally deflecting conical mirror M_4 with a $1 : 1$ magnification. The mirror is placed behind the exit slit, in this way its presence does not affect the spectral resolution and its peculiar shape allows a better overlapping of the two beams at the the sample position.
Fig. 5.7 shows the intensity distribution, at the sample position, of the light produced by U_1 (dotted line) and U_2 modules (continuous line) in the horizontal (a) and vertical (b) direction, as measured in [87]. In both the directions the overlap is quite good. The point by point difference of the intensity of the two beams distribution, shown in the bottom panel of each figure, shows that maximum deviations are less than 2% of the total intensity. The spot size on the sample can be calculated considering the full width at half maximum (FWHM) of the horizontal and vertical intensity distributions. The 1 mm FWHM of the horizontal and the 2 mm FWHM of the vertical distribution lead to a spot area of $1 \times 2 = 2$ mm^2 on the sample. A UHV-compatible chopper allows for the fast (> 100 Hz) switching of the light polarisation by blocking one of the two beams. The chopper is placed 1 m behind the M_3 mirror, see Fig. 5.6.
The beam-line is able to provide circularly polarised light with a high energy resolution, $E/\Delta E$, ranging from 6000 to 13000, depending on the photon energy and slit width. A photon flux between $10^{10} - 10^{13}$ photons/s can be achieved, with a degree of circular polarisation of 100% above 116 eV [87].

5.4 Electron detection: hemispherical electron-energy analysers

The energy selection of the electrons in our experiments is made by 180° hemispherical analysers, Fig. 5.8. They consist of two concentric hemispherical electrodes of mean radius R_0 mounted on a base plate in which the entrance and exit slits of width W_i and W_o are located. The working principle of the analysers is quite simple; the electrodes are polarised in such a way that electrons arriving to the centre of the entrance slit with a kinetic energy equal to a selected energy, E_p

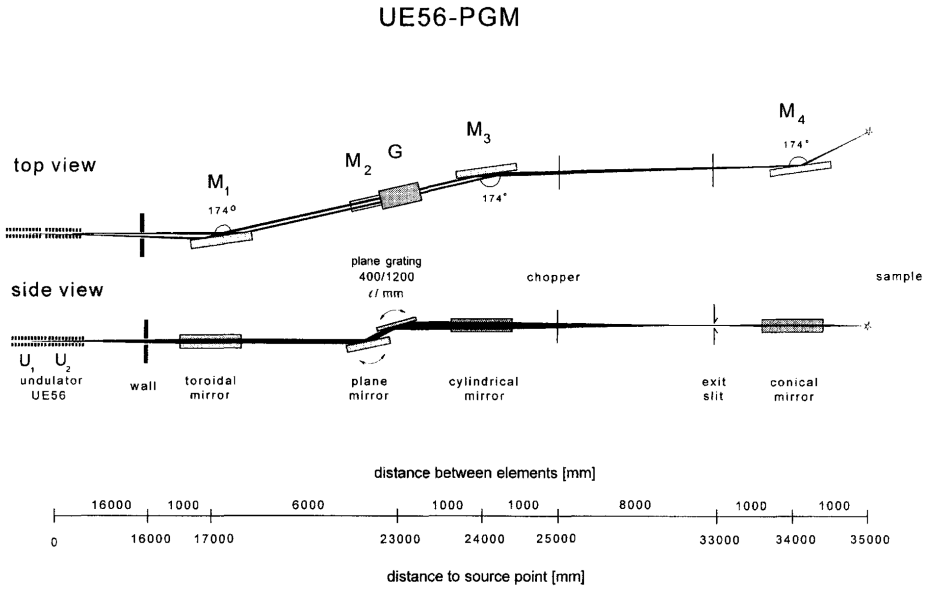

Figure 5.6: Top and side view of the UE56/2-PGM2 beam-line [87]. The distance of the different optical elements from the undulator is also shown.

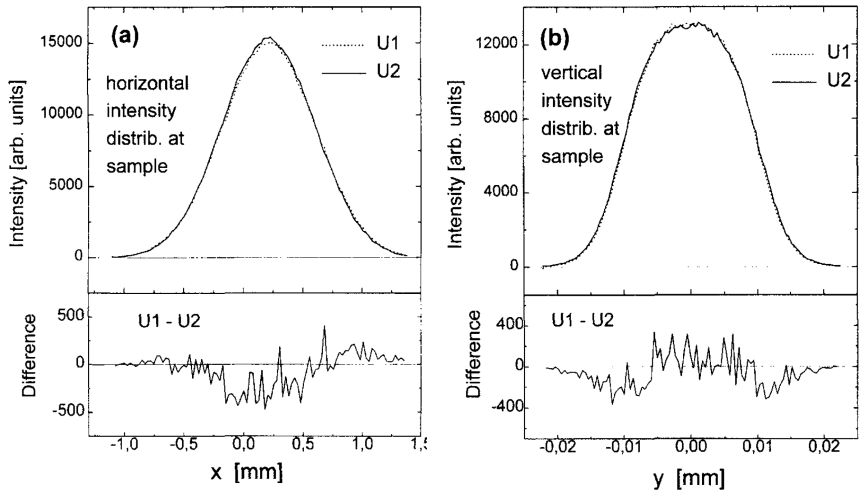

Figure 5.7: Intensity distribution at the sample derived by ray tracing at 425 eV photon energy, (a) horizontal distribution at 20 μm exit slit, (b) vertical distribution. Images from [87].

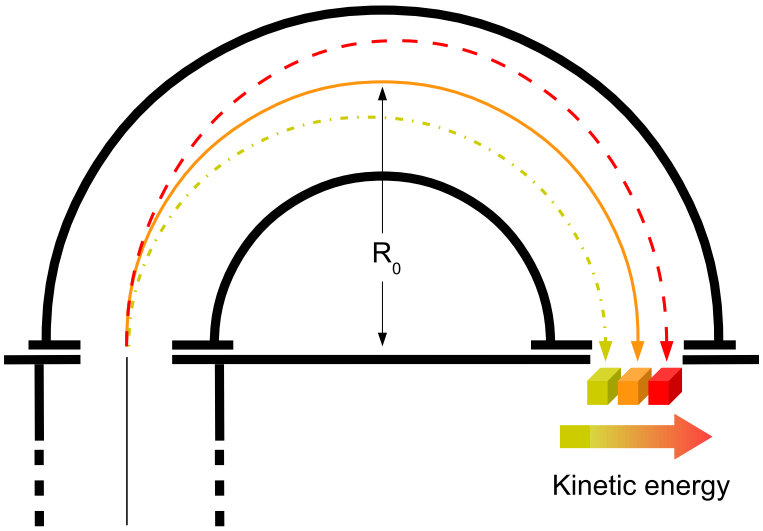

Figure 5.8: A side view of an hemispherical analyser. The continuous line represents the orbit of electrons arriving at the entrance slit with a kinetic energy equal to the selected pass-energy. The dashed and dashed dotted lines are the distorted orbits of electrons whose kinetic energies are higher or lower with respect to the pass-energy, respectively. The arrow indicates the direction of electron-energy dispersion.

(pass-energy), go through a circular path of radius R_0 and come out of the analyser at the middle point of the exit slit (continuous line in Fig.5.8). Electrons whose kinetic energy is lower (dashed dotted line) or higher (dashed line) than the pass energy go through distorted orbit and leave the analyser at different points of the exit slit. A position sensitive detector is used to determine the exit positions of the charged particles. They can be associated to the kinetic energy inside the hemispheres and energy discrimination is achieved.
In order to determine the potentials of the inner V_{in} and outer V_{out} electrodes we must consider energy conservation along the electrons' path inside the hemispheres. The intensity $\mathcal{E}$ of the electric field inside the analyser is given by,

$$\mathcal{E}(r) = \frac{\Delta V}{r^2}\left(\frac{1}{R_{in}} - \frac{1}{R_{out}}\right)^{-1}, \tag{5.7}$$

where ΔV is the potential difference applied to the hemispheres and the radial coordinate r runs from the inner-sphere, R_{in}, to the outer-sphere, R_{out}, radius. Centrifugal and electrostatic force must be equal for electrons travelling along a circular path of radius $R_0 = (R_{in} + R_{out})/2$ with energy E_p,

$$\frac{mv_0^2}{R_0} = \frac{2E_p}{R_0} = e\frac{\Delta V}{R_0^2}\left(\frac{1}{R_{in}} - \frac{1}{R_{out}}\right)^{-1}. \tag{5.8}$$

Solving (5.8) with respect to ΔV we obtain that the potential difference applied to the spheres,

$$\Delta V = \frac{2E_p R_0}{e}\left(\frac{1}{R_i} - \frac{1}{R_{out}}\right) = \frac{E_p}{e}\left(\frac{R_{out}}{R_{in}} - \frac{R_{in}}{R_{out}}\right), \tag{5.9}$$

is proportional to the pass-energy and depends on the ratio between the inner and outer radius. The shift in the radial position ΔR for electrons reaching the entrance slit with an angle $\pm\delta\theta$ with respect to the tangential direction and within an energy window ΔE around the pass energy can be written as

$$\Delta R = 2R_0\frac{\Delta E}{E_p} - 2R_0(\delta\theta)^2. \tag{5.10}$$

Considering that only electrons whose initial and final positions fall into W_i and W_o can be detected, inverting (5.10), we can express the amplitude of the energy window accepted by the analyser as

$$\Delta E = E_p\left[\frac{W}{2R_0} + (\delta\theta)^2\right], \tag{5.11}$$

where $W = (W_i + W_o)/2$ is the half-width of entrance and exit slit convolution. It is clear from this expression that an increase in the pass-energy results in a larger accepted energy window but this is accompanied by the drawback of a worst energy resolution. This is due to the fact that the electrons' dispersion inside the analyser decreases for higher kinetic energies. When performing an experiment one has to deal with these two conflicting needs and find a compromise in order to detect energy in a wide region with an acceptable resolution. In the measurements of this thesis we used two electrostatic analysers with $R_0 = 200$ mm and $W_i = W_o = 1$mm. Working at a fixed pass energy of $E_p = 300$ eV we were able to detect electrons within an energy range of $\Delta E = 27$ eV with an energy resolution $\delta E = 0.8$ eV.

Transport optics

The electrons emitted from the sample are driven to the electrostatic analyser by means of a pre-retardation stage consisting of a transport optics made by a series of cylindrical electrostatic lenses. The electron optics has a double function. It focuses the electron beam to the middle of the analyser entrance slit and accelerates (or decelerates) the electrons in order to make them reach the analyser with a kinetic energy equal to the pass-energy. In fact, a standard way to operate with hemispherical analysers is to keep the pass-energy fixed and select the lens potentials in such a way that the electrons of selected kinetic energy, E_k, are accelerated or decelerated to the pass-energy (E_p).
In general, the first element of the optics is kept at sample potential ($V = 0$) in order to avoid the introduction of distorting electric fields between the sample and the analyser. The last electrode potential V_p is instead defined by the chosen pass-energy. This is because the kinetic energy of the electron in the i-th electrode,

$$E_i = E_k + eV_i, \tag{5.12}$$

implies

$$E_p = E_k + eV_p \Longrightarrow V_p = \frac{E_p - E_k}{e}. \tag{5.13}$$

The focusing properties of the optics are defined by the electron refraction through regions of different potential. Suppose we have a point-like charge moving from a region of potential V_1 to a region of potential V_2. Energy conservation at the interface gives

$$\frac{1}{2}mv_1^2 + eV_1 = \frac{1}{2}mv_2^2 + eV_2, \tag{5.14}$$

where we indicated with v_1 (v_2) the velocity of the electron in region 1 (2). We assume that the potential changes abruptly at the interface which is parallel to the x direction. The component of

the momentum parallel to the interface is conserved and we have,

$$mv_1 \sin\alpha_1 = mv_2 \sin\alpha_2, \tag{5.15}$$

where we α_1 and α_2 are the electron angles with respect to the normal to the surface in region 1 and 2, respectively. If the zero point of the potential corresponds to those points in space where the electrons have zero kinetic energy we can write,

$$\frac{1}{2}mv^2 = eV \Longrightarrow v = \left(\frac{2e}{m}V\right)^{1/2}. \tag{5.16}$$

Inserting (5.16) in (5.15) we obtain,

$$\sqrt{V_1} sin\alpha_1 = \sqrt{V_2}\sin\alpha_2. \tag{5.17}$$

This means that an electron beam is broadened in angle when the electrons move from a higher to a lower potential region ($V_1 > V_2$) and is squeezed in the opposite case ($V_1 < V_2$).
For an electron beam of size d and angular divergence α equation (5.17) can be rewritten using the Helmoltz-Lagrange relationship [92],

$$d_1\alpha_1\sqrt{E_1} = d_2\alpha_2\sqrt{E_2}. \tag{5.18}$$

To our purposes, point 1 is at the sample position and point 2 corresponds to the entrance slit of the analyser where electrons kinetic energies are $E_1 = E_k$ and $E_2 = E_p$. Equation (5.18) becomes

$$\sqrt{\frac{E_k}{E_p}} = \sqrt{R} = \left(\frac{d_2}{d_1}\right)\left(\frac{\alpha_2}{\alpha_1}\right) = mM \tag{5.19}$$

where the retard R corresponds to the ratio between the initial and final electron kinetic energy and $m = d_2/d_1$and $M = \alpha_2/\alpha_1$ represent the linear and angular magnification of the optics, respectively.
The transmission t of the whole system is proportional to the solid angle of the electrons emitted at the sample position. In an axially symmetric lens system the solid angle is proportional to the square of the angular acceptance at the sample, α_1^2, thus

$$t \sim \alpha_1^2 = (\alpha_2)^2\left(\frac{d_2}{d_1}\right)^2\left(\frac{E_p}{E_k}\right). \tag{5.20}$$

As we will show in section (5.6) t must be as large as possible. Unfortunately, the requirement for high-transmission is in contrast to the one for high-energy resolution. The first requires high values of α_2 and E_p. High resolution requires exactly the reverse [see equation (5.11)]. This conflicting requirements are at the heart of the difficulties in performing coincidence experiments.

Micro-channel plates detectors

Micro-channel plate (MCP from now on) detectors are position-sensitive electron detectors. They consist of $10^4 - 10^7$ miniature electron multipliers oriented parallel to one another, Fig. 5.9. Typical channel diameters are of the order of $10 - 100$ μm with length-to-diameter ratios α around 40. The channel matrix is in general fabricated from a lead glass, treated in such a way to reduce channel work function and to optimise the secondary electron emission. The walls of each multiplier

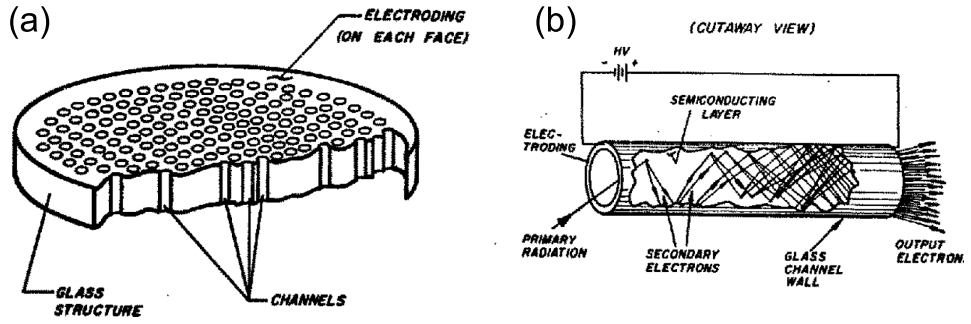

Figure 5.9: (a) A section of a micro-channel plate. (b) A straight-channel electron multiplier. Images from [93].

are made semiconducting in order to allow charge from an external voltage source to flow and refill the channels. Parallel electrical contact between the channels is obtained by the deposition of a metallic coating (Nichrome or Inconel) in the front and back face of the MCP, having the function of contact electrodes. The typical resistance between channels is of the order of 10^9 Ω. MCP, used singly or in cascade, allow electron-multiplication factors of the order of $10^4 - 10^7$ with ultra-high time resolution (~ 0.1 ns) and optimal spatial resolution which is determined by channel dimensions and spacings [93]; typically 12 μm diameters and 15 μm centre-to-centre distance.
Each channel, shown in Fig. 5.9(b), constitutes a straight single-electron multiplier. Electron multiplication occurs by means of a simple mechanism in which one incident electron, hitting the channel walls, produces g secondary electrons. In the second stage g^2 secondary electrons are produced, so that the total gain, G, after n stages is given by $G = g^n$. For sake of simplicity, we consider the case in which the secondary electrons are emitted normally to the walls for which it can be demonstrated that [94, p.1 - 18]

$$G = \left(\frac{AV}{2\alpha V_0^{1/2}} \right)^{4V_0\alpha^{1/2}/V}, \tag{5.21}$$

where V is the total voltage applied to the channel, V_0 the energy of one emitted secondary electron (~ 1 eV), α the length-to-diameter ratio and A is a proportionality constant obtained assuming that the number of secondary electrons, δ, produced in a collision with impact energy V_c is described by the relation

$$\delta = AV_c^{1/2}. \tag{5.22}$$

Qualitatively speaking, as long as the potential V applied to the channel is increased δ increases because each collision happens at higher V_c. The increase in the secondary emission production is compensated by a reduced number of collisions leading to a maximum in the G vs V characteristics. Equation (5.21) also presents a critical point with respect to α. This means that the there is a particular gain which is independent from the length-to-diameter ratio of the channels. This point can be calculated from the condition $d(\ln G)/d\alpha = 0$ which gives

$$\begin{aligned} \alpha_M &= \frac{AV}{3.3V_0^{1/2}} \sim \frac{V}{16.5}, \\ G_M &= \exp(0.184A^2V) \sim \exp(0.0074V), \end{aligned} \tag{5.23}$$

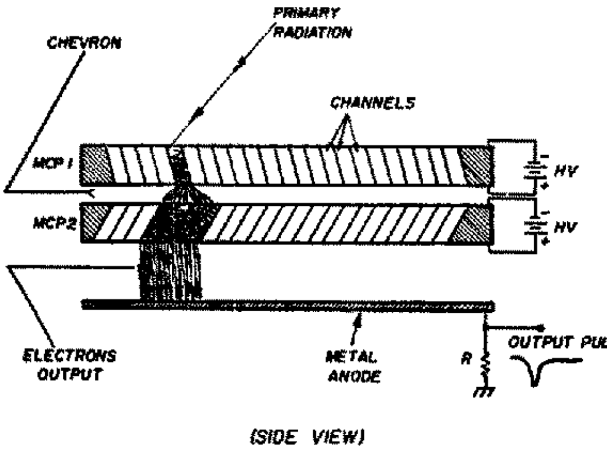

Figure 5.10: Two MCP detectors in Chevron configuration. One electron of the primary radiation enters the front plate whose channels are tilted by 8° with respect to the detectors normal. The electron beam generated in the first MCP is accelerated towards a second plate whose channels have a tilt angle of $-8°$, thus preventing ion feedback. The position of the electron beam coming out from the last MCP is recorded by a resistive metal anode. Image from [93].

where G_M and α_M are the values of G and A in the extremal point, respectively. If we assume an applied potential of $V = 1$ kV, then we obtain $G_M = 1635$ and $\alpha_M = 60$. More detailed simulations [95], taking into account secondary-electron emission not orthogonal to the channel walls, predict $\alpha_M = V/22$ so that $\alpha_M = 45$. In any case, α is usually kept between 40 and 60 to gain more signal intensity.
The gain of a straight channel MCP is limited by ion production. Indeed, as the gain increases, the probability to produce positively charged ions at the high charge density region at the exit of the channel increases too. These ions are produced by the impact of the electrons with the gas desorbed from the channel walls under electron-bombardment. The positive charges can go back to the channel input and produce spurious pulses.

Ion feedback suppression can be achieved by using MCP detectors in Chevron configuration. This configuration, schematically depicted in Fig. 5.10, allows high-gain (10^7) space-charge saturated pulses. Two (or more) plates are arranged in a series in such a way that the bias angles of the plates channels (typically around 8°) have opposite direction and provide a large directional change to prevent the ions to fly back to the front plate entrance. The different plates have typical distances of about $50-150$ μm and operate at 10^4 gain. The Chevron can reach high saturation gains ($> 10^7$) because, due to the broadening of the electron cloud in passing between one plate to the other, more than one channel is excited in the rear plate. This of course results in a degradation of the spatial resolution, but this drawback can be overcome by applying an accelerating potential between front and rear plates. In this way, the effect on the electron-velocity component parallel to the plates is reduced and spatial resolution is increased.

The electron-cloud emanating from the last MCP travels in a uniform electric field and is deposited onto a resistive anode encoder (RAE). The produced charge packet then diffuses in the uniform resistive sheet surface of the RAE towards the collection electrodes located on its periphery and is conducted to four metallic electrodes (A,B,C,D) at the four corners of the anode. The relative charge reaching each of the corners is a linear function of the impact position along

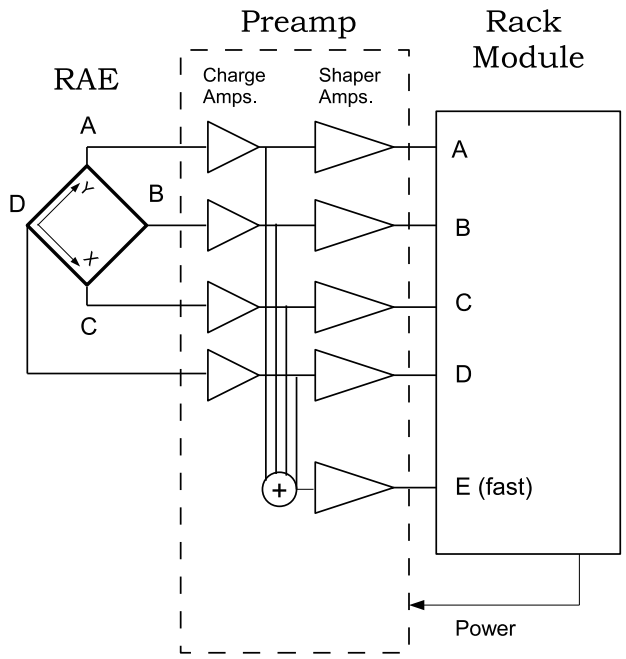

Figure 5.11: Schematic view of the complete detector system consisting of a resistive anode encoder (RAE), charge and shaper amplifiers, and a position analyser encoder.

the X and Y orthogonal axis of the RAE and thus the position can be encoded by arithmetic processes. Fig. 5.11 shows the scheme of the complete detector system, which is composed by three components:

(i) the resistive anode encoder.

(ii) the charge-sensitive/shaper amplifiers that convert the low-level charge pulses coming from the RAE into higher level shaped bipolar pulses suitable for input to the position analyser encoder.

(iii) the position analyser encoder that generates an analog voltage output proportional to pulse position according to the formulas,

$$X = \frac{A+B}{A+B+C+D}, \qquad Y = \frac{B+C}{A+B+C+D}.$$

The position analyser logic selects acceptable pulses and stores the selected events for a short time. Once a signal has been analysed and its X and Y positions are available, a strobe pulse is generated. Our analysers are equipped with 40 mm micro-channel plates detector [2] whose spatial resolution is about $1/100$ of the active area, $\Delta r = 400$ μm.

Energy calibration

The energy calibration of the analysers is an essential operation due to the fact that the spectrometers energy scale is not the same as the sample energy scale. This is because, due to the electron emission processes, an electrical connection is made between the specimen and the analysers. Thermodynamic equilibrium requires their chemical potentials (Fermi levels) to be aligned and

[2] Quantar Technology Incorporated, Model 3300 SERIES MCP

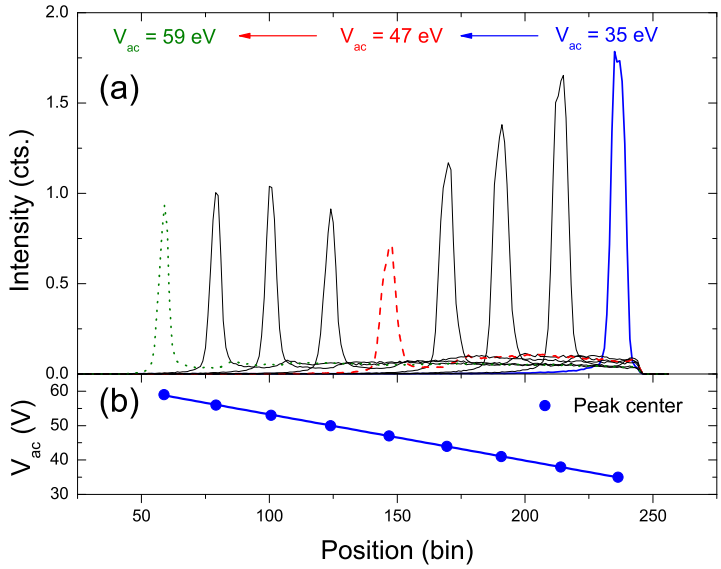

Figure 5.12: (a) Energy calibration curves for the electron analyser. The intense and sharp elastic peak is moved through the whole energy window accepted by the analyser by changing the acceleration voltage, V_{ac} of the primary electron beam. Differences in the elastic peak intensities are ascribable to variation of the incident current when V_{ac} is changed. (b) Variation of the elastic peak position on the detector when V_{ac} is moved (dots). The solid line represents a linear fit to the experimental data.

this results in different vacuum levels for sample and spectrometers. Two important goals must be fulfilled in order to have an exact energy calibration. First, we need to verify the linearity between the impact position of the electrons on the detector and their kinetic energy. Second, we need to quote the electronic energies with respect to the vacuum level of the considered sample.
The linearity of the detectors is verified through the use of an electron-gun. The sample is shined with an electron-beam of known accelerating voltage (V_{ac}). The peak of elastically scattered electrons (elastic peak), for fixed analyser settings, is recorded at different V_{ac} values. By measuring the position of the primary peak on the detector as a function of the accelerating voltage the linearity can be easily verified.

Fig. 5.12(a) represents energy-calibration spectra obtained for one of the two analysers used in this thesis. Each spectrum is characterised by a very sharp and intense peak due to the elastically scattered electrons and a less intense tail in the low-kinetic-energy region ascribable to electrons that have lost part of their energy in the interaction with the sample surface (energy-loss events). The electron-beam accelerating voltage was moved by 3 eV steps from $V_{ac} = 35$ eV (solid, blue line) to $V_{ac} = 59$ eV (dotted, green line) in order to cover the whole energy window accepted by the analyser. Each peak can be fitted by means of a Gaussian function. This allows to measure the relation between the acceleration voltage and hitting position of the electrons on the detector. This is represented by the circles in panel (b) of Fig. 5.12, where the linearity is tested by performing a fit to the experimental data using a linear function (straight line). Once the linearity of the detectors has been verified the energy scale is fixed in absolute terms. To do this a single measurement is required, where we identify a signal whose kinetic energy with respect to the sample vacuum level is known (e.g. a photoemission peak) and look at its position on the spectrometer scale. The

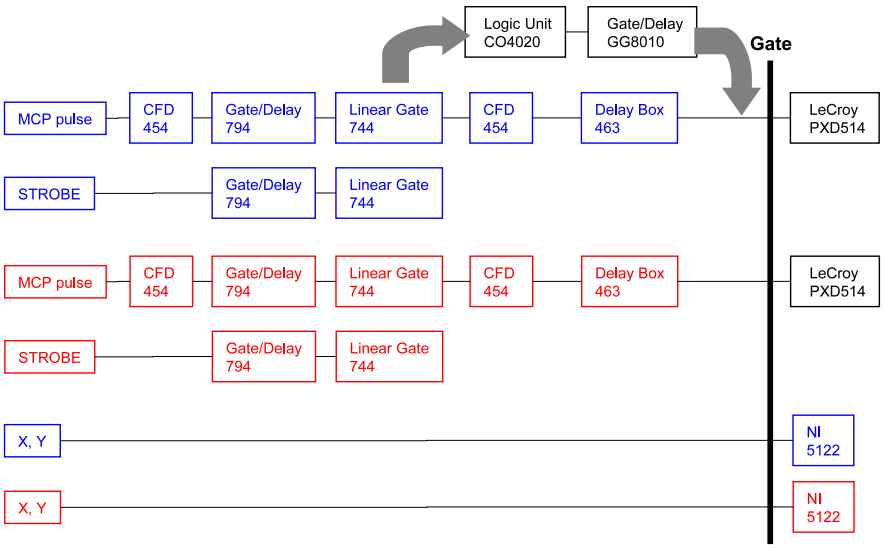

Figure 5.13: Block diagram of the coincidence electronics used in this thesis.

difference between the measured and the expected value is the offset we need to know to have an absolute energy calibration.

5.5 Coincidence electronics

The electronics required for the coincidence experiment performed in this thesis is represented in Fig. 5.13. The acquisition line in each channel (blue or red) consists of a preamplifier, a constant fraction discriminator (CFD), a gate/delay generator, a linear gate and a high resolution digitiser. The use of fast preamplifiers is essential to achieve the required time resolution (see section 5.7). The CFD are used to discriminate against the noise or spurious pulses coming from the MCP detectors. They provide a standard height pulse at a time determined by a constant fraction of the input pulse height. Oppositely to threshold discriminator CFD are not subjected to problem of *time walk* and the time information is less sensitive to the pulse height and rising time variations. The gate/delay generator and the linear gate are used to convert the bipolar signal coming from the CFD in a unipolar signal to be converted in a digital pulse.
The coincidence measurement is performed by a four-way coincidence circuit CO4020. In order to be accepted, the channel-plate pulses originating from the two spectrometers have to be within a time interval of 170 ns while the strobe pulses generated by the electronics of the resistive anodes indicate successful impact position determinations. The latter condition is required to determine the kinetic energy of the coincident electrons. If the condition for one valid coincidence event is satisfied, the circuit provides a signal which is set to trigger on the leading edge of a pulse determined by the overlap of the two MCP pulses. At this point, the arrival times (t_1 and t_2) of the two pulses with respect to the trigger are recorded by means of an Analog-to-Digital-Converter (ADC) Lecroy PXD514.
In this way it is straightforward to determine, for each kinetic energy pair (E_1, E_2), the distribution of the differences in the arrival time $\Delta t = t_1 - t_2$ of the electrons, and construct the time spectra of

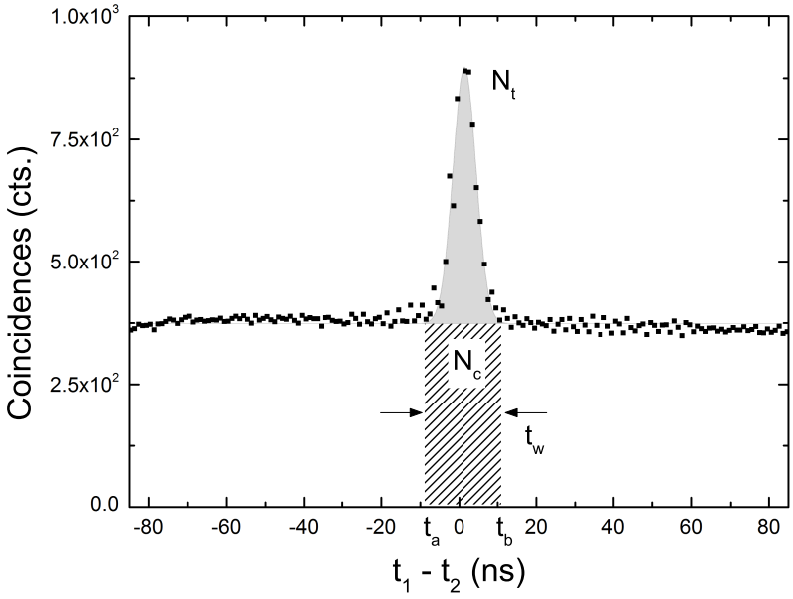

Figure 5.14: Example of time spectrum acquired in a coincident experiment performed in this thesis. The grey region indicates the number of true coincidences N_t which is given by the area between the central peak and the background of accidental coincidences, N_c (dashed region).

the experiment.
Through the high-resolution digitisers (NI 5122) located in each line it is possible to visualise the x and y electron-impact coordinates, hence to record the energy spectra acquired by each analyser independently.

5.6 Coincidence time spectrum

A measured coincidence time spectrum, in which we reported the number of coincidences as a function of the delay time between two detected electrons, is presented in Fig. 5.14. Correlated electrons result in events always delayed by the same amount and give rise to the peak located at $\Delta t = 0$ ns. The peak width ($dt \sim 8$ ns) is mainly due to a different time-of-flight of the particles from the sample to the detectors (see section 5.7 for details). Electrons emitted in uncorrelated events can possess, in principle, any delay time and result in the continuous background distributed through the whole accepted energy window of 170 ns. The shape of the background reflects the properties of the photon source, e.g. it is constant for a common x-ray laboratory lamp and it represents the self convolution of the ring fill pattern in the case of synchrotron radiation sources [96].
There are of course many way to subtract the accidental background from the true coincidences; the simplest one consists in performing a fit of the time spectrum using a Gaussian peak superimposed on an appropriately chosen background. This method is very appealing but presents some problems when the true to accidental coincidences ratio is low. In this conditions the results of the fitting procedure are not completely reliable and this might lead to a wrong determination of the coincidence rate. When the background can be considered constant on the whole time window an-

other subtraction method is available. It consists in computing the area under the true coincidences peak including the background and then subtracting to it the background area (N_c) indicated by the dashed region in Fig. 5.14. In order to estimate N_c it is very convenient to use the whole recorded background and then normalise it to the time window t_w considered in the calculation of the area under the main peak. If we indicate with c_i the counts corresponding to the i-th delay time $t_i = -85, \ldots, 85$ ns, then we can write the total (peak plus background) area as,

$$N_{tot} = \sum_{t_a}^{t_b} c_i, \tag{5.24}$$

where $t_a < 0$ and $t_b > 0$ define the peak window $t_w = t_b - t_a$, see Fig. 5.14. The error, following Poisson statistics, is given by

$$\delta N_{tot} = \sqrt{\sum_{t_a}^{t_b} c_i}. \tag{5.25}$$

The background, N_c, can be estimated considering the counts outside the peak window,

$$\overline{N}_c = \sum_{t_i=-85}^{t_a} c_i + \sum_{t_i=t_b}^{85} c_i. \tag{5.26}$$

They are normalised taking into consideration the difference in the peak and background, $T = (85 - |t_a|) + (85 - t_b)$, time windows,

$$N_c = \frac{t_w}{T}\overline{N}_c = \frac{t_w}{T}\left[\sum_{t_i=-85}^{t_a} c_i + \sum_{t_i=t_b}^{85} c_i\right], \tag{5.27}$$

with error,

$$\delta N_c = \frac{t_w}{T}\sqrt{\sum_{t_i=-85}^{t_a} c_i + \sum_{t_i=t_b}^{85} c_i}. \tag{5.28}$$

The true counts are defined as

$$N_t = N_{tot} - N_c = \sum_{t_i=t_a}^{t_b} c_i - \frac{t_w}{T}\left[\sum_{t_i=-85}^{t_a} c_i + \sum_{t_i=t_b}^{85} c_i\right], \tag{5.29}$$

and the true coincidences error corresponds to the square sum of the errors in (5.25) and (5.28)

$$\delta N_t = \sqrt{\sum_{t_i=t_a}^{t_b} c_i + \left(\frac{t_w}{T}\right)^2 \sum_{t_i=-85}^{t_a} c_i + \sum_{t_i=t_b}^{85} c_i}. \tag{5.30}$$

Equation (5.30) shows that the error can be made smaller by decreasing the value t_w/T. This can be achieved by minimising the resolving time t_w and by increasing the time window of the spectrometer. This is the reason why a time window of hundreds of ns is accepted up to a peak width of few ns.

Further considerations can reveal which experimental parameters can be optimised in order to decrease the acquisition time. Suppose that we make use of two electron analysers to record the electron-electron coincidence spectrum. Each analyser, from now on indicated by the subscript 1 (2), is characterised by its accepted energy window δE_1 (δE_2), solid angle $\delta\Omega_1$ ($\delta\Omega_2$) and efficiency

α_1 (α_2). The true coincidence rate, R_t, is proportional to the incident current, I_0, and is related to the cross section of the two-electron process, $\sigma_t = d^2\sigma/d\Omega_1 d\Omega_2 dE$, by

$$R_t = I_0 \frac{d^2\sigma}{d\Omega_1 d\Omega_2 dE} dl \delta E_c \delta\Omega_1 \delta\Omega_2 \alpha_1 \alpha_2. \tag{5.31}$$

Here dl is the density of scattering points in the sample and δE_c represents the coincidence energy resolution. For analysers with Gaussian response functions

$$\delta E_c = \left[(\delta E_1)^2 + (\delta E_2)^2\right]^{1/2}.$$

The rate of chance coincidence, R_c, is the probability of two events detected by the analysers to be coincident within the time window t_w and is given by

$$R_c = R_1 R_2 t_w, \tag{5.32}$$

where the single-rate of each analyser,

$$R_{1,2} = I_0 \frac{d^2\sigma}{d\Omega_{1,2} dE_{1,2}} dl \delta\Omega_{1,2} \delta E_{1,2} \alpha_{1,2},$$

is proportional to the cross section for single emission, $\sigma_{1,2} = d^2\sigma/d\Omega_{1,2} dE_{1,2}$. A key parameter for a coincidence experiment is represented by the ratio between the rate of true and accidental coincidences (true to accidental ratio),

$$\Gamma = \frac{R_t}{R_c} = \frac{\sigma_t}{\sigma_1 \cdot \sigma_2} \frac{1}{I_0 \cdot dl \cdot t_w} \frac{\delta E_c}{\delta E_1 \cdot \delta E_2}. \tag{5.33}$$

The minimisation of this parameter leads to a coincidence error reduction. It is clear from (5.33) that the true to accidental ratio is maximum at low incident current.
In planning a coincidence experiment one must consider the time ($t\%$) required to obtain a certain statistical error expressed in terms of true coincidences percentage ($\delta\%$). This can be calculated considering the subtraction procedure shown before. Using a trivial relation the number of true coincidences [eq. (5.29)] can be rewritten as

$$N_t = N_{tot} - N_c = (N_t + N_c) - N_c \tag{5.34}$$

whose error is given by

$$\delta N_t = \sqrt{(N_t + N_c) + N_c} = \sqrt{N_t + 2N_c}. \tag{5.35}$$

If we now express the number of true (accidental) events in terms of the acquisition rate R_t (R_c) multiplied by an integration time t we get for the relative error,

$$\frac{\delta N_t}{N_t} = \frac{\sqrt{(R_t + 2R_c)t}}{R_t t} = \frac{\sqrt{R_t + 2R_c}}{R_t} t^{-1/2}. \tag{5.36}$$

Equation (5.36) can be solved with respect to the time t to obtain the definition of the percentage time, $t\%$,

$$t\% = \frac{1}{(\delta\%)^2} \left[\frac{1}{R_t} + 2\frac{R_c}{R_t^2}\right]. \tag{5.37}$$

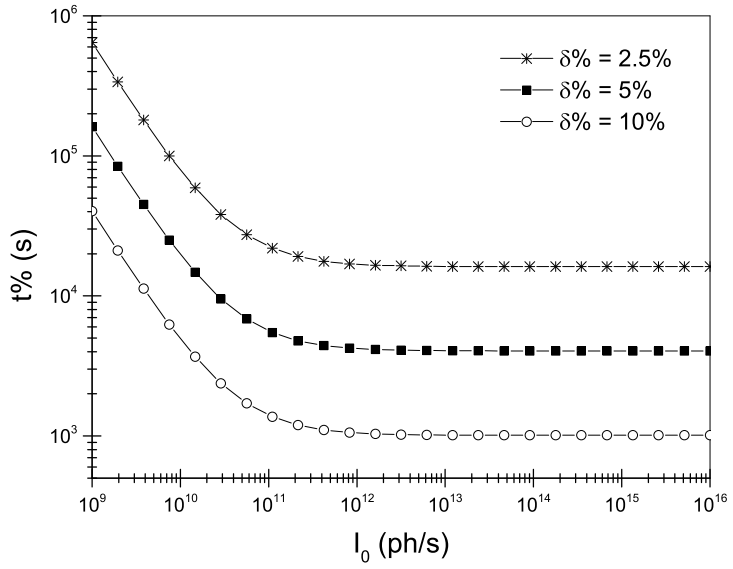

Figure 5.15: Example of the variation with the photon flux of the acquisition time $t\%$ required to obtain a given statistical uncertainty $\delta\%$ in the coincidence rate (see text for details).

The substitution of R_t and R_c with their expressions in (5.31), (5.32) gives,

$$t\% = (\delta\%)^{-2}(\sigma_t\alpha_1\alpha_2\delta\Omega_1\delta\Omega_2)^{-1}\left[\frac{1}{I_0 dl\delta E_c} + 2t_w\frac{\sigma_1\sigma_2}{\sigma_t}\frac{\delta E_1\delta E_2}{\delta E_c^2}\right]. \tag{5.38}$$

The behaviour of the acquisition time $t\%$ as a function of the incident photon flux is shown in Fig. 5.15. We took into consideration three different values of the relative error: $\delta\% = 10\%$ (stars), $\delta\% = 5\%$ (black squares) and $\delta\% = 2.5\%$ (open circles). We can artificially divide the graph in two regions. In region 1 ($I_0 \leq 10^{12}$ ph/s) the acquisition time rapidly decreases when the photon flux increases, $t\%$ diminishes by more than one order of magnitude when I_0 varies from 10^9 to 10^{11} ph/s. In region 2 ($I_0 > 10^{12}$) the decreasing term in (5.38) becomes negligible with respect to the additional constant,

$$C = \lim_{I_0\to\infty} t\% = (\delta\%)^{-2}(\sigma_t\alpha_1\alpha_2\delta\Omega_1\delta\Omega_2)^{-1}\left[2t_w\frac{\sigma_1\sigma_2}{\sigma_t}\frac{\delta E_1\delta E_2}{\delta E_c^2}\right],$$

and a further increase in the photon flux does not bring any reduction in the acquisition time. In addition, an increase in the photon flux has the side effect to reduce the true to accidental ratio, thus indicating that in a coincidence experiment is better to work with the lowest current in the saturation region, $I_0 \sim 10^{12}$ ph/s. In these conditions a further decrease in the accumulation time can be obtained by reducing the multiplying constant in (5.38). This can be only done by increasing the solid angles accepted by the analysers $\delta\Omega_1$, $\delta\Omega_2$. Unfortunately, maximising the solid angle and, at the same time minimising the resolving time are conflicting requests in an electron-spectrometer so the better choice must be a compromise between large solid angle and small resolving time.

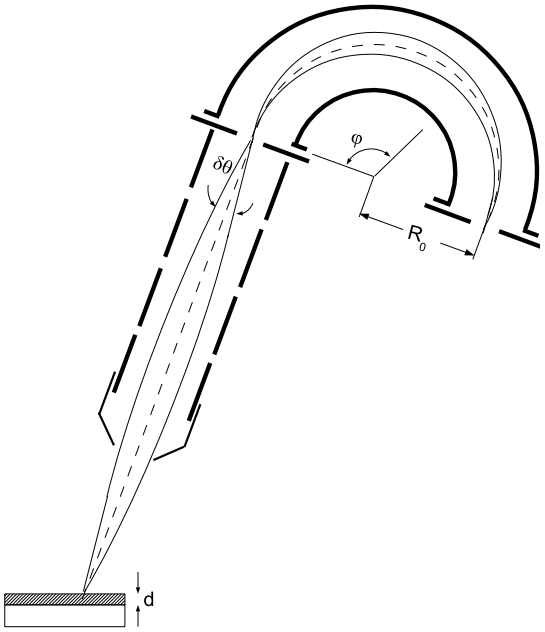

Figure 5.16: General set-up for the detection of one electron in an electron-electron coincidence experiment. The time resolution of the experiment is determined by the length of the interaction volume d, by the angular acceptance $\delta\theta$ and the energy resolution of the hemispherical analyser of mean radius R_0, and by the detector and electronics.

5.7 The resolving time

In this section a detailed analysis of the coincidence spectrometer resolving time will be given following the work by Volkel and Sandner [97]. The total resolving time t_w is given by the sum of the variation in the travelling time, from the sample to the detector, of the emitted electrons

$$t_w = \Delta t_1 + \Delta t_2. \tag{5.39}$$

Following reference [97] we can write Δt_i, in channel 1 and 2, as the sum of different contributions

$$\Delta t_i = \Delta t_i^{vol} + \Delta t_i^{energy} + \Delta t_i^{geometric} + \Delta t_i^{detector} + \Delta t_i^{electronic}, \tag{5.40}$$

where each contribution to the time spread can be treated separately.

(i) Δt^{vol} is the time spread arising due to the finite extension d of the interaction volume of the particles inside the sample. If E represents the kinetic energy of the electron, m its mass and v its velocity we can write

$$\Delta t^{vol} = \frac{d}{v} = \frac{d}{\sqrt{2E/m}}. \tag{5.41}$$

In a solid the typical interaction volume extension is given by the electron escape depth (~ 10Å) and for 20 eV electrons results $\Delta t^{vol} \sim 3.7 \cdot 10^{-6}$ ns, which is absolutely negligible.

(ii) Δt^{energy} is the time interval ascribable to the finite energy window of the spectrometer. In a hemispherical analyser if we consider only the electrons arriving with a fixed incidence angle, θ_0,

Table 5.3: Calculated values of the geometrical time spread, $\Delta t^{geometric}$ for hemispherical analysers of mean radius equal to $R_0 = 500$ mm and $R_0 = 50$ mm, respectively. $\Delta t^{geometric}$ has been calculated for two different electron energies of 20 eV and 200 eV, and two values for the acceptance angle $\delta\theta = \pm 1^\circ$ and $\delta\theta = \pm 4^\circ$ [97].

R_0 (mm)	$\delta\theta(^\circ)$	E (eV)	$\Delta t^{geometric}$ (ns)
500	± 4	20	11.3
	± 4	200	3.6
	± 1	20	2.8
	± 1	200	0.9
50	± 4	20	5.3
	± 4	200	2.7
	± 1	20	1.3
	± 1	200	0.4

to the entrance slit, there will be a certain bandwidth of energies being transmitted and this leads to,

$$\Delta t^{energy} = D\left(\frac{1}{v_{min}} - \frac{1}{v_{max}}\right) \sim D\frac{\Delta v}{\hat{v}^2}, \tag{5.42}$$

where D is the path length inside the analyser, v_{max} and v_{min} the maximum and minimum electrons' velocities and $\hat{v} = \frac{v_{max}-v_{min}}{2}$ is their mean value. The above equation can be written in terms of the mean kinetic energy E and of the time window accepted by the analyser, ΔE,

$$\Delta t^{energy} \sim \frac{D}{2}\sqrt{\frac{m}{2E}}\frac{\Delta E}{E}. \tag{5.43}$$

For $D = \pi R_0 = 625$ mm ($R_0 = 200$ mm), $E = 50$ eV and $\Delta E/E = 3\%$ we get $\Delta t^{energy} \sim 2ns$.

(iii) $\Delta t^{geometric}$ is the time spread due to the possible different paths that mono-energetic electrons can cover inside the analyser. Electrons entering the analyser with the same energy but at different entrance angles can experience different paths length before they are focused onto the exit slit. The time difference depends on the type of analyser and on its angular divergence $\delta\theta$. For a hemispherical analyser the transit time t_{trans} inside the hemisphere can be calculated applying angular momentum, j, conservation (see [98] for details),

$$t_{trans}(E,\theta) = \frac{m}{j(E,\theta)}\int_0^{\phi} r^2(E,\mathcal{E},\theta,\phi)d\phi, \tag{5.44}$$

where $r(E,\mathcal{E},\theta,\phi)$ is the radial distance of the electron from the centre of the hemisphere with E and $\mathcal{E}$ electron kinetic energy and electric field strength, respectively. Electrons trajectories and transit times can be calculated by means of dedicated simulation programs, e.g. [99]. The geometric time spread for hemispherical analysers with mean radius $R_0 = 500$ mm and $R_0 = 50$ mm, respectively, have been obtained by Volkel and Sandner [97] and are listed in Table 5.3. They considered configurations with 20 or 200 eV electrons and analysers accepted angles of $\delta\theta = \pm 1^\circ$ and $\delta\theta = \pm 4^\circ$ The extremal values in table (5.3) show that the geometric time ranges

from $\Delta t \sim 1$ ns to $\Delta t \sim 10$ ns. In order to obtain reliable estimates in different experimental conditions, we can use the approximate scaling relationship [51],

$$\Delta t^{geometric} \propto \text{size} \cdot \delta\theta \cdot E^{-1/2},$$

where "size" stands for the characteristic dimensions, W_0 and R_0, respectively. This means that we can estimate a mean value of $\Delta t^{geometric} = 5$ ns for our $R_0 = 200$ mm analyser.

(iv) $\Delta t^{detector}$ takes into account any transit time variation of the electronic cloud inside the electron multiplier. For a single-channel detector (channeltron) this time reaches values of about $2-3$ ns and produces a significant contribution to the resolving time t_w. For multi-channel detectors (MCP) this contribution can be significantly reduced to the values $\Delta t^{detector} \leq 0.5$ ns [100, 101].

(v) $\Delta t^{electronics}$ is the time jitter of all the electronic components driving the signals from the detectors to the coincidence devices. With fast amplifiers and discriminator one can keep the jitter below 1 ns, typically $\Delta t^{electronics} \leq 0.5$ ns.

It is clear from above considerations that, provided that we are using multi-channel detectors, the largest contribution to the time resolution is due to the different geometrical paths inside the spectrometer (iii). To minimise the time spread one can reduce the accepted angles of the analysers. This operation is not advisable for what concern the accumulation time ($t\%$), since any reduction in $\delta\theta$ leads to a reduction in the true coincidence count rate. Once again one must find the best compromise between acceptable time resolution and acquisition time.

Chapter 6

Direct and core resonant DPE on Cu(001)

In this chapter we present the measurements obtained from a clean Cu(001) surface. We measured the DPE spectrum from the valence band of Cu(001) upon the absorption of linearly and circularly polarised light. In both cases the photon energy, 125 eV, was far above the Cu $3p$ ionisation threshold ($\sim$ 75 eV) so that we have been able to simultaneously measure direct and core-resonant ($M_{23}M_{45}M_{45}$) DPE.
As expected in the description of the single-step direct DPE mediated by electron-electron interaction, the particles belonging to the emitted electron-pairs continuously share the excess energy of the process. The same behaviour is also observed in the core-resonant process, thus demonstrating that Cu $M_{23}M_{45}M_{45}$ super Coster-Kronig transition can be only described within a single-step picture.

With the use of linearly polarised light we have been able to observe differences in the core-resonant DPE line shape when measured using different relative orientations of the light polarisation and the emission directions of each detected electron in the pair. Taking into consideration the $M_{23}M_{45}M_{45}$ Auger spectrum measured in coincidence with $3p_{3/2}$ photoelectrons, i.e. considering the $M_3M_{45}M_{45}$ APECS (Auger-photoelectron coincidence spectroscopy) spectrum, we have been able to increase or decrease the relative intensities of the two-hole final state multiplet terms (^1G, ^3F, ^1D) by considering two different geometries. This demonstrated the ability of the APECS to disentangle the contributions to the Auger spectrum form electronic sub-levels characterised by different magnetic quantum numbers.

Acquiring the DPE spectrum with right- and left-hand circularly polarised light we have been able to observe circular dichroism (CD) in both direct and core-resonant DPE. The lack or presence of CD in the electron-pair intensity is connected to the symmetry of the two-hole final state, thus demonstrating that the chirality of the incident photon can be transferred to either the electron-pair or the residual ion. The presence of a non-vanishing CD for the core-resonant DPE can be considered a second proof of the breakdown of two-step description of the photoinduced Auger decay [82].

6.1 The Cu(001) sample

The sample studied in this experience is a copper mono-crystal cut along the (001) surface. This choice has been made for two reasons: first, the Cu(001) electronic structure is well established

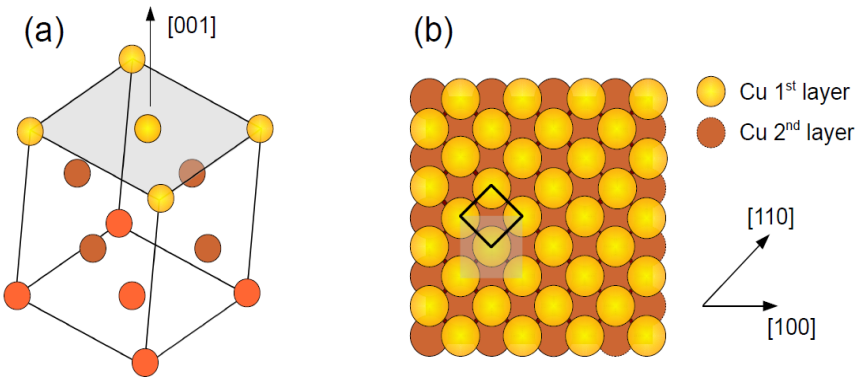

Figure 6.1: FCC unit cell (a) and corresponding (001) surface (b) obtained by cutting the solid orthogonally to the [001] direction. The circles represent the Cu atoms in first (light orange), second (dark orange) and third (orange) layer, respectively. The black square defines the surface unit cell.

[102] and this represents a substantial advantage in the interpretation of the data. Second, copper belongs to the transition metals whose valence band structure is strongly influenced by electron-electron correlations. Since the DPE cross section is non-vanishing only for correlated systems, Cu represents an ideal candidate for such an experiment.

Atomic structure

Copper crystallizes in a face-centered cubic (FCC) crystal structure in which the atomic nuclei are arranged on the vertices and face center of a cube of edge $a = 3.6147$ Å. Fig. 6.1 represents the unit cell of a Cu crystal (a) with the corresponding (001) surface structure obtained by cutting the solid orthogonally to the [001] direction (b). The surface unit cell, indicated by the black lines in Fig. 6.1(b), corresponds to a square whose edge a_s is equal to the half-diagonal of the cube face, $a_s = 2.55$ Å.

Electronic structure

The electronic configuration of atomic copper is $[Ar]3d^{10}4s^1$ showing its belonging to the 3d-transition metals. In the metallic state the closed-shell electronic levels, typical of the Ar configuration ($1s^2 2s^2 2p^6 3s^2 3p^6$), give rise to tightly bound bands lying well below the characteristics energies of any of the remaining electronic levels in the metal. For most purposes, the electrons in the low-lying levels can be considered as a part of the inert ion-cores and the valence-band structure can be calculated by considering an FCC Bravais lattice of Cu^{11+} ions to which are added 11 electrons ($3d^{10}4s^1$) per primitive cell. Six bands are needed in order to arrange the 11 additional electrons and their structure is shown in the right panel of Fig. 6.2. The continuous lines show the band structure for copper along the high symmetry directions calculated by Eckardt *et al.* [103] compared to the measurements performed by various authors represented by the dots and collectively regrouped in [104]. For almost all the wave-vectors, $\mathbf{k}$, the six bands can be seen to separate in five relatively localised bands lying in a small region between 2 and 5 eV below the Fermi level (E_F) and a sixth band spanning a large energy region from 7 eV above to 9 eV below E_F. It is common to call the five narrow bands as the d-bands and the remaining the s-band. This definition

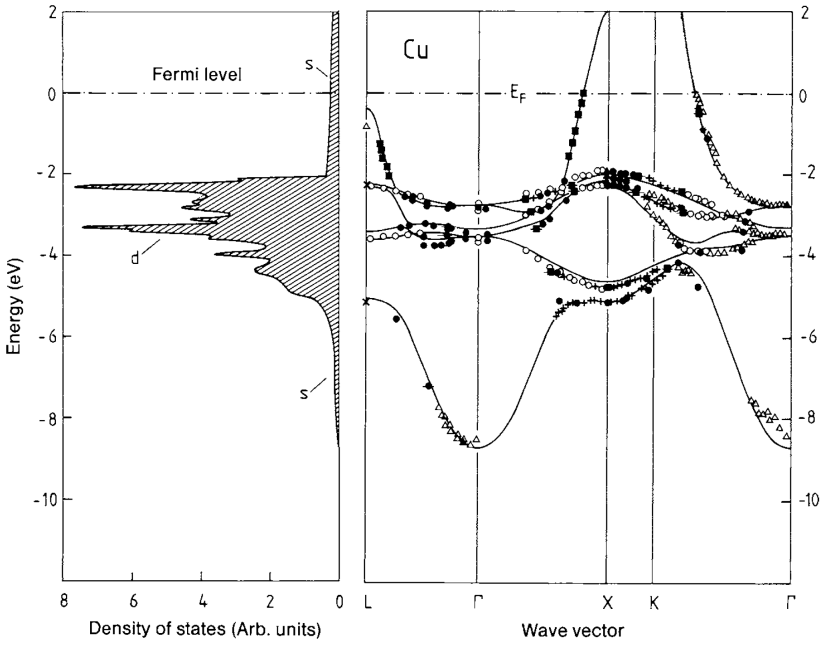

Figure 6.2: Cu valence band structure, $E(\mathbf{k})$, along the high-symmetry directions (right panel). The continuous line represents the calculations performed by Eckardt *et al.* [103] while the experimental dots have been measured by several authors and have been collectively regrouped by Courths and Hüfner [104]. The valence band single-particle density of states (left panel) has been calculated by Heckardt, Fritsche and Noffke [105].

might be misleading since at some k values all the six levels are very closed spaced and no distinction is possible. This nomenclature reflects the fact that at the points where the distinction is clear, the five bands are derived from electrons occupying the atomic 3d levels while the sixth band is occupied by the electron in the 4s level. It has to be noticed that the s-band levels, except for those points where they approach the d levels, bears a k dispersion similar to the parabolic dispersion of a free electron band.
The left panel in Fig. 6.2 represents the density of states obtained from the calculated band structure [105]. It is clear that the majority of the spectral weight of the DOS is contained in the energy region included between 2 and 5 eV below the Fermi level and is essentially given by the d-bands. The two maxima, located around 2 and 3 eV below E_F respectively, corresponds to the regions of maximum superposition between the d-levels. The DOS ascribable to the s-band is negligible with respect to the d-levels contributions and is represented by the low background spanning from a few eV above to 9 eV below the Fermi level.

6.2 Linearly polarised light

The experimental setup used to acquire the Cu(001) DPE spectrum with linearly polarised light is schematically depicted in Fig. 6.3. The light produced by the UE56 planar undulator impinges on the sample with a grazing angle of 10°. The optical axis of the left (vertical) and of the right (horizontal) analyser are mutually perpendicular and they both lie in the plane perpendicular to the

incident light direction, with the right analyser aligned to the [100] direction of the sample surface. Each analyser accepts an angle about $\pm 15^\circ$ around the optical axis. Since the light electric field oscillates in the plane of the ring (horizontal polarisation) the two analysers collect electrons in different geometries. The electrons detected by the right analyser have escape direction, i.e. wave-vector, parallel to the light polarisation (aligned configuration, "A"), while the ones detected by the left analyser escape orthogonally to the light polarisation (not-aligned configuration, "N"). The sample was tilted in such a way that the mean take-off angles for right and left analyser with respect to the surface normal were 15° and 75°, respectively.
The two spectrometers were set to detect kinetic energies in a range of 27 eV around a mean kinetic energy of 50 eV, with a resolution of 0.8 eV.
The incident radiation energy was $h\nu = 125$ eV; at this photon energy the analysers were able to detect, within their energy windows, both the photoelectrons coming from copper $3p$ levels ($41 \text{ eV} \leq E_k \leq 48$ eV) and Auger electrons from $M_{23}M_{45}M_{45}$ super Coster-Kronig decay ($50 \text{ eV} \leq E_k \leq 61$ eV).

6.2.1 Single photoemisssion spectra

Fig. 6.4 represents the single photoemission spectra measured with the right [panel (a)] and left [panel (b)] analyser, respectively. In each spectrum the number of electrons emitted upon the absorption of linearly polarised photons of energy $h\nu = 125$ eV has been reported as a function of their kinetic energy. Single photoemission measurements were performed for multiple reasons. First, to verify the cleanness of the Cu(001) surface by looking for the presence of photoemission signals relative to surface contaminants. Second, to determine the characteristic kinetic energies of Cu(001) photo- and Auger electrons to be used in the analysis of the coincidence spectra.
The two analysers were set to detect electrons in the same energy window going from 37.5 eV to 62.5 eV. The low-kinetic-energy portion ($38 < E < 50$ eV) of the photoemission spectra can be associated to the emission of electrons from Cu $3p$ levels. It can be fitted by means of two Voigt functions, corresponding to the two spin-orbit components $3p_{1/2}$ and $3p_{3/2}$, superimposed on a polynomial background which takes into account electrons inelastic scattering and analysers' transmission effects. The two contributions are represented by the full ($3p_{3/2}$) and shaded area ($3p_{1/2}$), respectively. In the fitting procedure the Gaussian broadening of the peaks has been forced to be the same and equal to the experimental (photon + analysers) energy resolution, $W_G = 0.8$ eV. The Lorentzian full width at half maximum, W_L, has been constrained to be the same for both peaks because it essentially depends on the lifetime of the $3p$ core-hole states which can be supposed to be the same for $j = 1/2$ and $j = 3/2$ state. The kinetic energies and Lorentzian line widths of the photoemission peaks measured with the different analysers are listed in Tab. 6.1. The fitting parameters are almost identical for both the detectors; the kinetic energies of the spin-orbit doublet are $E_k(3p_{1/2}) = 45.7$ eV and $E_k(3p_{3/2}) = 43.0$ eV. The resulting binding energies (BE) corresponding to BE $= 77.40 \pm 0.1$ eV and BE$= 74.72 \pm 0.02$ eV for Cu $3p_{1/2}$ and $3p_{3/2}$ levels lead to a measured spin-orbit splitting of 2.68 ± 0.10 eV which is consistent with previous results [14]. The same is for measured Lorentzian widths, which are $W_L = 1.95 \pm 0.10$ eV and $W_L = 1.99 \pm 0.12$ eV for left and right analyser, respectively. The large width of the photoemission line shape reflects the fact that the created core-hole state is very short-lived due to the strong coupling between the 3p hole and the 3d valence electrons resulting in a very rapid $M_{23}M_{45}M_{45}$ Auger decay of the hole.
The electrons emitted in the Auger decay are responsible for the broad structure visible in the high-kinetic energy part ($E_k > 50$ eV) of both single spectra.

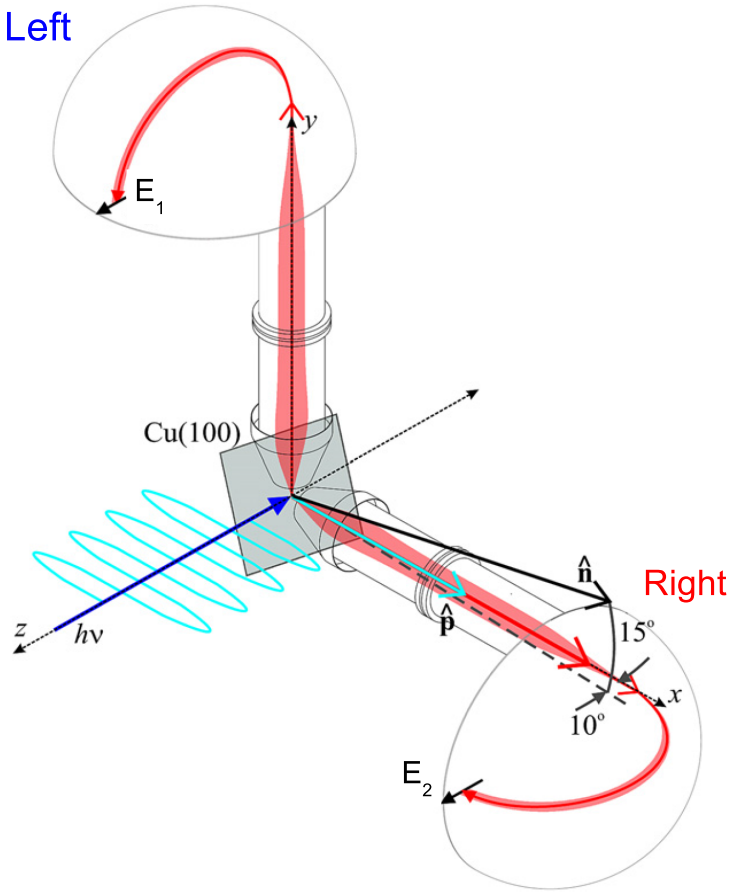

Figure 6.3: Schematic view of the experimental set-up to measure the DPE spectrum from Cu(001). The light is incident on the sample at a grazing angle of 10°. The axis of the analysers transfer lenses lie in the plane orthogonal to the light direction and form an angle of 90° to each other. The energy dispersion directions are marked as E_1 and E_2 for left and right analyser, respectively. $\hat{\mathbf{n}}$ is the normal to the Cu(001) crystal surface while $\hat{\mathbf{p}}$ gives the direction of light polarisation. Image from [15].

Table 6.1: Experimental values of $3p_{1/2}$, $3p_{3/2}$ energies and Lorentzian line-widths (in eV) obtained with left and right analyser.

analyser	Energy. $3p_{1/2}$	FWHM $3p_{1/2}$	Energy $3p_{3/2}$	FWHM $3p_{3/2}$
Left	43.00 (0.15)	1.95 (0.10)	45.68 (0.02)	1.95 (0.10)
Right	43.04 (0.10)	1.99 (0.12)	45.68 (0.03)	1.99 (0.12)

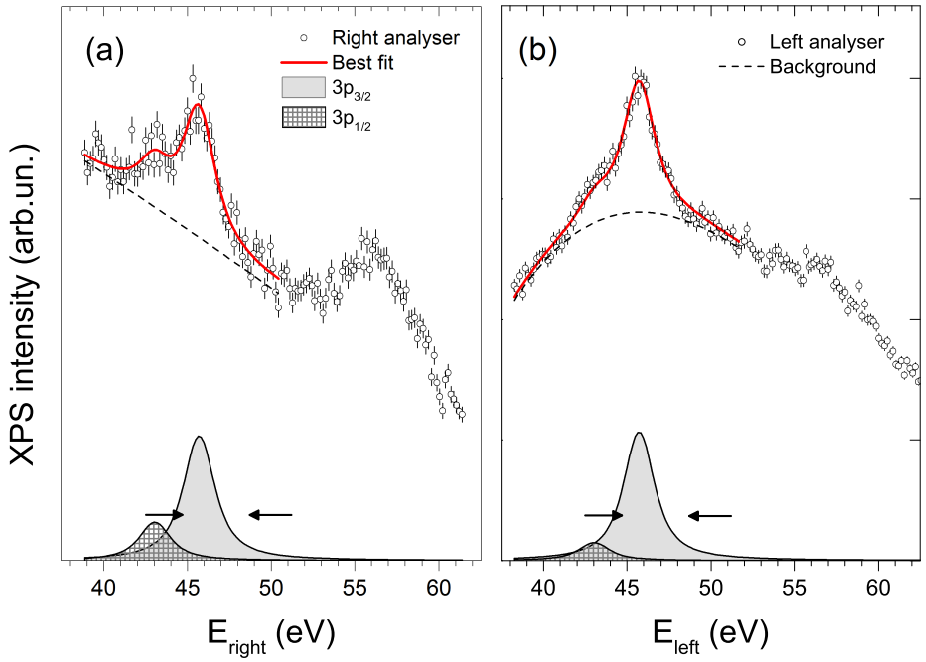

Figure 6.4: Cu(001) $3p$ photoemission (PE) and $M_{23}M_{45}M_{45}$ spectrum (open dots) for $h\nu = 125$ eV measured with right (a) and left (b) analyser; the PE curves were fitted with two Voigt profiles accounting for $3p_{3/2}$ (full area) and $3p_{1/2}$ photoelectrons (shaded area) and a polynomial background (dashed line). The best fit curve (thick red line) is given by the sum of the different contributions. The arrows indicate the energy windows selected for APECS measurements of $M_3M_{45}M_{45}$ Auger lines.

6.2.2 Double photoemission spectrum

Figure 6.5 represents the 2-dimensional DPE spectrum obtained from Cu(001) upon excitation of 125 eV radiation. We reported the number of correlated electron-pairs detected by the coincidence spectrometer as a function of the electrons kinetic energies (E_{right}, E_{left}). Several spectral features are clearly observable in the spectrum. The high energy diagonal structure, located at $E_{sum} = E_{left} + E_{right} \approx 112$ eV, below which the electron-pair intensity is non-vanishing is related to the onset of DPE, i.e. to the maximum sum energy accessible to the electron-pairs. Considering energy conservation in a non-interacting picture, the electron-pair sum energy is given by

$$E_{sum} = h\nu - (\varepsilon_1 + \varepsilon_2) - 2\phi,$$

where ε_1 and ε_2 are the electrons binding energies and the work function ϕ is equal to 4.6 eV for Cu(001) [69]. The maximum sum energy should correspond to the emission of two electrons located at the Fermi edge ($\varepsilon_1 = \varepsilon_2 = 0$), which implies $E_{sum} = 125 - 2\phi = 115.8$ eV as indicated by the straight diagonal line in Fig. 6.5. The onset of the DPE appears to be located ~ 4 eV below the expected value. This is easily explained considering that Cu single-particle density of states at Fermi level (Fig. 6.2), ascribable to sp states, is negligible with respect to the 3d levels density of states located approximately 2 eV below E_F. The condition $E_{sum} = 112$ eV corresponds to the emission of electron-pairs characterised by $\varepsilon_1 = \varepsilon_2 = 1.9$ eV which is consistent with electrons located at the top of the d-bands.
Below the DPE onset there are two intense structures, labelled as AN and NA, characterised by $(E_{right}, E_{left}) = (45 \text{ eV}, 56 \text{ eV})$ and $(56 \text{ eV}, 45 \text{ eV})$, respectively. These energies correspond to the nominal kinetic energies of the 3p photoelectrons (see Tab. 6.1) in coincidence with the $M_{23}M_{45}M_{45}$ Auger electrons, i.e. to core-resonant DPE. Accordingly to this, the structure labelled as AN can be attributed to 3p photoelectrons detected by the right analyser and Auger electrons by the left analyser. In the same way the region labelled as NA corresponds to exchanging the role of the analysers; the photoelectrons are detected by the left analyser and the Auger electrons by the right. The nomenclature AN or NA reflects the geometry of the coincidence experiment. The AN geometry corresponds to a condition in which the photoelectrons are collected in a direction which is aligned to the direction of the polarisation $\hat{\mathbf{p}}$, while the Auger electrons are collected in the direction perpendicular to $\hat{\mathbf{p}}$ (not aligned). The NA configuration corresponds to the condition in which the photoelectrons are not aligned with $\hat{\mathbf{p}}$ while the Auger electrons are aligned.
The two core-resonant DPE structures have a diagonally oriented structure which is characteristic of electrons sharing their kinetic energies while keeping their sum energy constant. As explained in the description of core-resonant DPE (section 3.1), energy sharing between photo- and Auger electrons is a fingerprint of the fact that the Cu $M_{23}M_{45}M_{45}$ Auger decay can only be described within a single-step picture as verified by G. van Riessen *et al* [15].
Besides the intense core-resonant DPE structures, two other intensity regions are visible. The two structures, parallel to either E_{left} or E_{right}, are characterised by the energy of one of the two electrons to be constant and equal to the Cu 3p photoelectron energy. Thus, they origin from the coincident detection of the photoelectrons with *inelastic* Auger electrons, i.e. those Auger electrons that have lost part of their energy by inelastic scattering inside the solid [106].

6.2.3 Sum energy spectrum

Further informations on the DPE process can be obtained by constructing a *sum energy spectrum*, in which we report the number of correlated electron-pairs as a function of their sum energy,

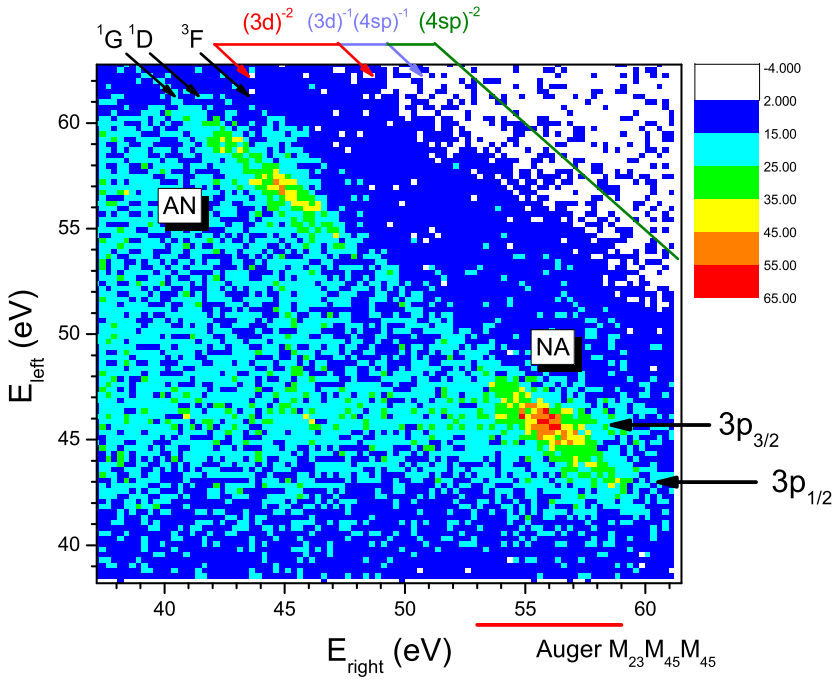

Figure 6.5: 2D energy distribution of correlated electron-pairs.

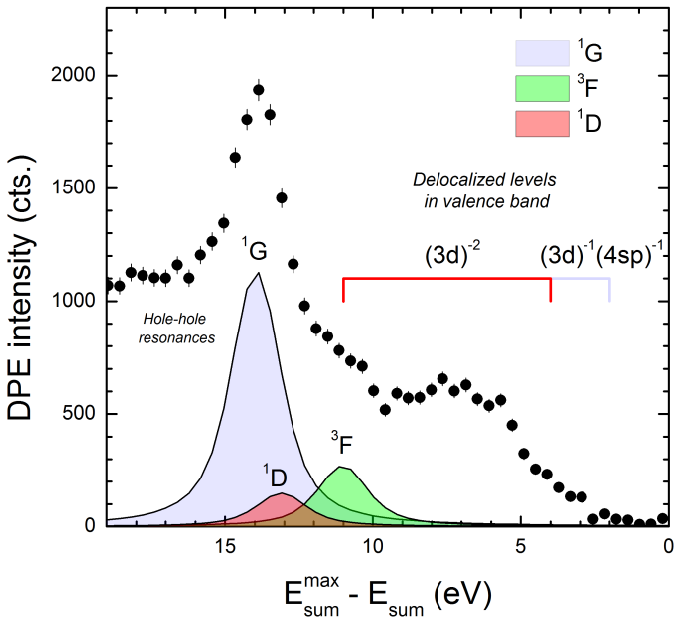

Figure 6.6: Sum energy spectrum.

$E_{sum} = E_{left} + E_{right}$, Fig. 6.6. In order to assign each feature of the spectrum to the specific two-electron state from which emission took place, it is more convenient to consider, as independent variable, the difference between the sum energy of the pairs and the two-particle Fermi edge, $E_{sum}^{max} = h\nu - 2\phi$. In analogy to single photoemission, this operation corresponds to construct a DPE spectrum as a function of the binding energy of the electron-pairs.
For sake of simplicity, the sum energy spectrum in Fig. 6.6 can be artificially divided into two regions. The first one, $0 \leq E_{sum}^{max} - E_{sum} \leq 11$ eV, is dominated by double-ionisation processes leaving the system with two holes located on different atomic sites. A first, very weak onset in the coincidence intensity is observed ~ 2 eV below the maximum sum energy. In accord to Cu band structure, it corresponds to the emission of one electron from 3d bands and one electron from sp bands, $(3d)^{-1}(4sp)^{-1}$. A second, more visible, onset is observable at 4 eV and it is associated to DPE processes in which the system is left with two holes in the 3d bands, ($3d^{-2}$). In a Cini-Sawatzky description [18, 19], the line shape of this portion of the spectrum is described by the self-convolution of the single particle density of states. The maximum DPE intensity is reached at ~ 7 eV below the Fermi edge. This energy corresponds to twice the nominal binding energy of Cu 3d bands.
The second region, $E_{sum}^{max} - E_{sum} > 11$ eV, can be associated to final states in which the valence band holes are localised on the same atomic site. The resulting DPE pairs possess higher binding energies than the inter-atomic case. The energy difference is due to the hole-hole interaction in the final state and corresponds to the Coulomb energy cost to place two positively charged particles on the same atomic site. In this case, the interaction between the holes gives rise to the appearance of atomic-like multiplet terms analogous to the ones observed in Cu $L_{23}VV$ Auger spectrum presented in Sec. 1.8. The 2-hole final states have a $3d^8$ electronic configuration and, since the hole-hole Coulomb interaction is dominant, $U \sim 8$ eV, they can be described in the L-S representation as singlet ^{1}S, ^{1}D, ^1G or triplet ^{3}P, ^{3}F ionic-states. The energies and intensities of the three most intense contributions to the DPE spectrum, given by ^{1}D, ^1G and ^{3}F states, are represented by the three peaks shown in Fig.6.6. In ($M_{23}VV$) core-resonant DPE, the electron-pairs emission occurs through the formation of a (3p) core-hole. The matrix element of the process, presented in (3.28), implies that the dominant Auger reactions are the ones ending with two holes localised on the same atomic site. This is not the case for direct DPE due to the absence of the localised intermediate state. Thus, it is possible to ascribe the low-binding-energy portion of the sum energy spectrum to electron-pairs ejected by direct DPE and the high-binding-energy to the ones produced in core-resonant reactions.

6.2.4 Angular dependence of the Auger spectrum

In order to study the angular dependence of the Auger electron distribution when detected in coincidence with the correlated photoelectron (APECS), cuts have been performed in the 2-dimensional DPE spectrum. We selected those events that can be associated to the coincident detection of $3p_{3/2}$ photoelectrons and of the corresponding Auger electrons.
The M_3VV APECS spectrum in AN configuration has been constructed by reporting the number of coincidences in the region 44.7 eV $\leq E_{left} \leq$ 48.7 eV as function of the energy of the right analyser E_{right}. This corresponds to tune the kinetic energy of the left analyser on the high kinetic energy side of the $3p_{3/2}$ photoemission peak, see arrows in Fig. 6.4, while the right analyser is scanned on the whole Auger spectrum. In this way one is able to record the intrinsic line shape of the M_3VV transition with no contributions due to the decay of the $3p_{1/2}$ core-hole, whose photoemission peak is located at a lower kinetic energy, see Tab. 6.1.

Config.	Linewidth (eV)	${}^1D - {}^1G$ splitting (eV)	${}^3F - {}^1G$ splitting (eV)	${}^1G/{}^3F$	${}^1D/{}^3F$
NA	1.37 (0.08)	0.70 (0.18)	3.0 (0.1)	4.5 (0.6)	1.8 (0.6)
AN	1.37 (0.08)	0.70 (0.18)	3.0 (0.1)	3.2 (0.2)	0.6 (0.15)

Table 6.2: Experimental values of ${}^1G$, ${}^1D$ and ${}^3F$ relative splitting and intensities as obtained in the two geometrical configurations used for measurements.

The spectrum in NA configuration has been obtained applying the aforementioned procedure and by exchanging the role of the two analysers, i.e. the right analyser is fixed on the high kinetic energy side of the M_3 photoemission peak while the left one detects the corresponding Auger electrons. The Auger spectra measured in coincidence with $3p_{3/2}$ photoelectrons in NA and AN configurations are presented as full circles in Figs. 6.7(a) and (b), respectively. Statistical error bars are reported together with the data.
According to the analysis performed by Gotter *et al.* on Cu(111) [14] coincidence experimental data have been fitted with a trial function (solid thick line) made up by the sum of three Voigt profiles, accounting for ^{1}G, ^{3}F and ${}^1D$ final-state transitions, and of a Shirley-type integral background (dashed dotted line) accounting for inelastically scattered electrons [107]. The FWHM of the Gaussian broadening of the Voigt profiles has been set to be equal to the experimental resolution of the apparatus ($W_G = 0.8$ eV), while the Lorentzian width, left as a free parameter, has been forced to be equal for all the peaks. Peak energies and intensities have been left free to vary during the fit, exception done for ^{1}D term in the AN configuration, whose energy splitting with respect to the most intense transition ${}^1G$, has been forced to be equal to the one obtained in the fit of the NA spectrum.
The results of the fitting procedure, relative intensities and energy difference between the different multiplet components, are listed in Table 6.2 . The energy separation between ^{1}G and ^{3}F components of 3.0 ± 0.1 eV, as well as the one between the ^{1}G and ^{1}D components, equal to 0.70 ± 0.18 eV are comparable to the values obtained in previous works [14, 108].
It is clear that the coincidence Auger spectra in NA configuration differs considerably from the one in AN. In particular, the contribution of the triplet component, represented by the shoulder in the high kinetic energy side of the main peak, is considerably reduced in NA configuration with respect to AN. The inverse behaviour is observed for the singlet term, ^{1}D, whose intensity, negligible in AN configuration, is larger than the one of the triplet state in NA configuration.

The angular dependence of the APECS line shape can be understood by means of a simplified two-step description of the entire process. First, emissions from the atomic site (photoemission and Auger electron emission) take place, second the emitted electron-couple is diffracted by the crystal lattice. In this picture the final state of the atomic Auger decay acts as a "source wave" for the diffraction.
Anisotropies in the source wave are dictated by the presence of a quantization axis, i.e. the light polarisation vector $\hat{\mathbf{p}}$, and by the presence of the core-hole intermediate state [83, 57]. These result in selction rules governing the photoionisation and the subsequent decay. The photoionisation process is governed by the optical dipole selection rules [79, p. 429], $\Delta l = \pm 1$, which reduce

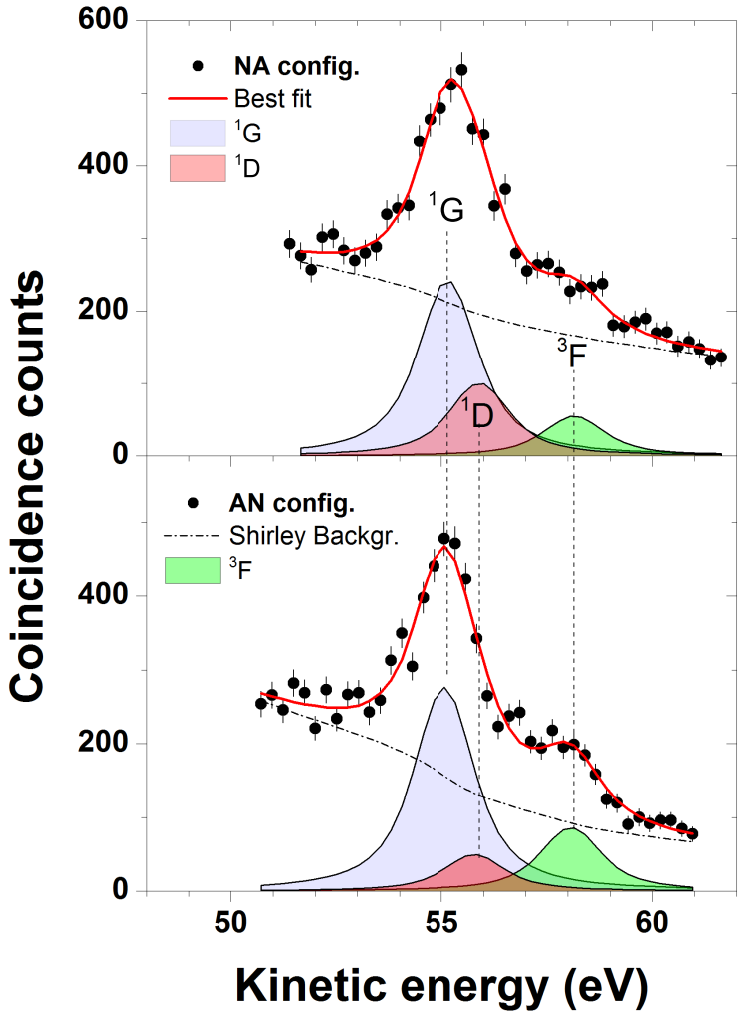

Figure 6.7: Cu core-resonant DPE ($M_3M_{45}M_{45}$) spectra measured in configurations NA (top) and AN (bottom). The thick solid line is the best fit to the data obtained by using the multiplet terms (shaded peaks) describing the most intense Auger transitions. The dashed dotted line represents a Shirley-type integral background.

the possible partial waves of the photoelectrons to the ones whose angular momentum quantum number l differs by one from the angular momentum of the core-hole. In addition, since in this case the light is linearly polarised, the magnetic quantum number of the photoelectrons must be identical to that of the core-hole, $\Delta m = 0$. For what concerns the Auger electron, its quantum numbers are connected to the ones of the core-hole by the selection rules for the Auger decay [57]:

$$\begin{aligned} l_c + l_1 + k &= \text{even integer}, && (6.1)\\ l_A + l_2 + k &= \text{even integer}, && (6.2)\\ \beta &= m_1 - m_c = m_A - m_2, && (6.3)\\ |l_c - k| &\leq l_1 \leq l_c + k && (6.4)\\ |l_A - k| &\leq l_2 \leq l_A + k, && (6.5) \end{aligned}$$

where l_c, l_A, l_1 and l_2 are the orbital quantum numbers of the core hole, the emitted Auger electron, and of the two holes left in the final state, respectively. In the same way, m_c, m_A, m_1, and m_2 are the corresponding magnetic quantum numbers. k and β are the orbital and magnetic quantum numbers of the expansion of the Coulomb potential in spherical harmonics $Y_{k\beta}(\Omega)$ [57],

$$\frac{1}{|\mathbf{r}_1 - \mathbf{r}_2|} = 4\pi \sum_{k=0}^{\infty} \sum_{\beta=-k}^{k} \frac{1}{2k+1} \frac{r_<^k}{r_>^{k+1}} Y^*_{k\beta}(\Omega_1) Y_{k\beta}(\Omega_2).$$

Here $r^>$ is the greater and $r^<$ is the lesser of r_1 and r_2.
In $M_3M_{45}M_{45}$ Auger decay the first ionisation is from a 3p level so that $l_c = 1$. Thus, the photoelectron can only be emitted as an s- ($l_p = 0$) or d-wave ($l_p = 2$). Due to the dipole selection rule on the magnetic number $m_c = m_p = 0, \pm 1$. The considered transition ends with two holes in the d-levels so that $l_1 = l_2 = 2$. Earlier works, studying the Auger and photoelectron diffraction patterns [56, 55] have established that the Auger electron predominantly emerges as an f-wave so that $l_A = 3$ and $m_A = 0, \pm 1, \pm 2, \pm 3$.

If only the first order terms are considered in the expansion of the Coulomb potential, i.e. if $\beta = 0$, the selection rule (6.3) implies that the magnetic quantum numbers of the two final holes, m_1 and m_2, are equal to the ones of the photoelectron ($m_1 = m_c = m_p$) and of the Auger electron ($m_2 = m_A$), respectively. Hence the difference of the two holes magnetic quantum numbers corresponds to the difference in the magnetic numbers of the two detected electrons, $\Delta m = m_1 - m_2 = m_p - m_A$. In order to better understand the multiplet selectivity in the core-resonant DPE spectra it is useful to observe that in LS coupling, which is appropriate for these transitions [52], it is possible to write the two-hole wavefunction of the residual ion as the superposition of two-particle states given by the product of single-particle wavefunctions:

$$|LM\rangle = \sum_{\substack{l_1 + l_2 = L \\ m_1 + m_2 = M}} C^{LM}_{l_1 m_1 l_2 m_2} |l_1 m_1\rangle |l_2 m_2\rangle , \qquad (6.6)$$

where L and M are the two-hole angular momentum and its projection along the $z-$axis, respectively, and $C^{LM}_{l_1 m_1 l_2 m_2}$ are the Clebsch-Gordan coefficients. Equation (6.6) allows to calculate the relative weight of each final-state multiplet term. This can be done considering all the possible microstates, $|l_1 m_1\rangle |l_2 m_2\rangle$ giving rise to the triplet (^3F) and singlet (^1D, ^1G) states, and by calculating the respective Clebsch-Gordan coefficients. The results of this simple calculation are shown in Fig. 6.8 in which the relative weight of each multiplet term is represented as a function of the difference

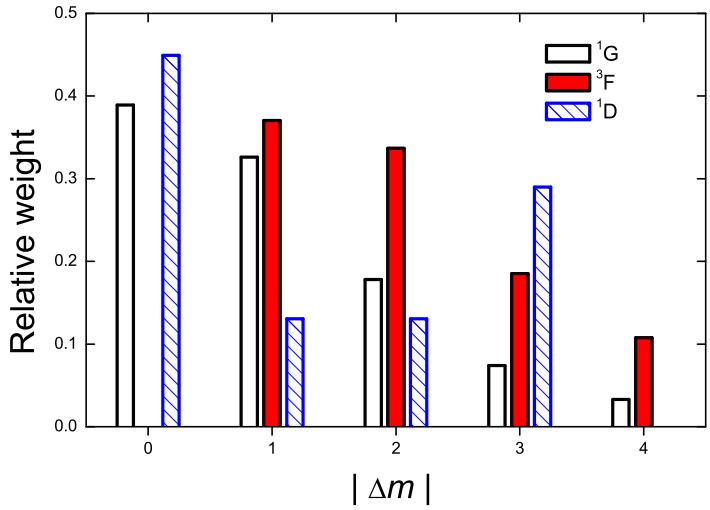

Figure 6.8: Predicted contributions to the ${}^1G$, ${}^1D$ and ${}^3F$ multiplets as a function of the difference in the magnetic quantum numbers, $|\Delta m| = |m_1 - m_2|$, of the two holes in the DPE final state.

in the magnetic quantum numbers, $|\Delta m| = |m_1 - m_2|$, of the two holes. Clearly, the wave functions of triplet final states are weighted towards higher $|\Delta m|$ values, while the singlet states tend to favour smaller $|\Delta m|$. This is a consequence of the exchange interaction among the electrons. The singlet states are characterised by a spin wavefunction antisymmetric with respect to the exchange of the two holes that can be coupled to a symmetric spatial wavefunction. This means that the two holes can possess the same spatial quantum numbers and the states with $m_1 = m_2$ are favourite. On the other hand, the triplet states are characterised by a symmetric spin wavefunction and as a consequence only holes with different magnetic numbers, $|\Delta m| \neq 0$, can give contributions to the total two-hole wavefunction. It has been observed in previous works [14, 59] that collecting electrons ejected close to the direction of the linear polarisation vector, $\hat{\mathbf{p}}$, favours $m = 0$ components of the emitted electrons partial waves, while the contributions of the $m \geq 1$ waves start to dominate for ejection angles larger than 55°. This means that in the NA configuration the dominant contributions to the coincidence spectrum are given by $m_2 = m_A = 0$ and $m_1 = m_p = 0, \pm 1$, so that $|\Delta m| = 0, 1$. In the opposite configuration, AN, a selection is applied on the photoelectron ($m_p = 0$) while all the partial waves of the Auger electron are detected, $m_A = 0, \pm 1, \pm 2, \pm 3$, so that the possible values of the difference in the magnetic numbers of the electron-pair are $|\Delta m| = 0, 1, 2, 3$. According to the reconstructed $|\Delta m|$ values, the results obtained in the fitting procedure of the coincidence spectra can be qualitatively explained. In NA configuration, where low $|\Delta m|$ values are favourite, the contribution to the line shape of the singlet terms is dominant with respect to triplet. Indeed for ${}^1G$ and ${}^1D$ states more than 60% of the total contribution is ascribable to $|\Delta m| = 0, 1$ components, while it is less than 40% for the ${}^3F$. When moving to the opposite configuration, AN, all the possible differences in the electrons magnetic numbers are selected and the contribution of the ${}^3F$ multiplet is enhanced with respect to the one of the ${}^1G$ and ${}^1D$. This leads to a ${}^1G/{}^3F$ and ${}^1D/{}^3F$ ratios that are smaller in AN configuration than in NA and give rise to dichroic effect in angle-resolved core-resonant DPE.

It only has to be explained why the dichroic effect, DE[1], for the ^1D ($\sim 50\%$) is more than doubled with respect to the ^1G ($\sim 17\%$). This can be understood by considering that the $|\Delta m| = 0$ contribution to the G state is only given by the combination of terms with $m_1 = m_2 = \pm 2$. These terms are not accessible in the $M_{23}M_{45}M_{45}$ decay because dipole selection rules require $m_1 = m_p = 0, \pm 1$. This means that the most intense contribution to the ^1G state can not be accessed in this experimental conditions, thus resulting in a reduced dichroic effect with respect to the ^1D term for which all the $|\Delta m|$ contributions can be accessed.

The results of this experiment have shown that core-resonant DPE measurements are selective to the spin-coupling in the two-hole final state. In the considered case, dichroism effects arise from the multiplet nature of the two-hole final state due to the high hole-hole correlation energy in Cu d-bands.
Analogous experiments on $(\sqrt{3} \times \sqrt{3})R30^\circ$ -Sn/Ge(111) and Cu(111) surfaces were already performed [58, 14]. In those cases the authors observed differences in the coincidence spectra acquired in AN and NN configurations. They highlighted the possibility to observe decays originating from different sub-levels of the intermediate core-hole state, whose alignments with respect to the quantization axis (the light polarisation vector) can be controlled by varying the detection angle of the photoelectron. In this case we demonstrated that the selection of a particular sub-level can be also achieved by applying a selection on the Auger electron detection angle. This is because the quantum numbers of the Auger electron are related to the ones of the core-hole via the selection rules for the Auger decay listed in (6.1)-(6.5).

The spin-selectivity of APECS can be very helpful in resolving the multiplet contributions to the Auger spectra of complex materials by considering peculiar geometries in which the contribution of a particular multiplet term is enhanced or suppressed. In recent years APECS spin-selectivity have been exploited to study the local valence-spin configuration of ferromagnetic [63] and anti-ferromagnetic systems [62, 61].

6.3 Circularly polarised light

Unique informations regarding the electron correlation can also be achieved by studying how the DPE triple differential cross section (TDCS) varies as a function of the helicity of the incident circularly polarised light. In this case the exchange interaction acting between the electrons, i.e. the fact that the two emitted electrons are indistinguishable, together with parity conservation in the complete two-electron emission process can give rise to differences between the DPE spectra acquired with left (σ^-) and right (σ^+) circularly polarised light. Circular dichroism, CD, is essential to characterise the dynamics of the DPE process and is a footprint of the correlated behaviour of the emitted electron-pairs which can only be described as single quantum states.
Most works on this subject are focused to the study of unpolarised atomic targets [25, 26, 40, 81, 82]. This is because of the difficulties in handling CD to describe the obtained data. Indeed, since the DPE processes only occur due to the electron correlation, the size and sign of the calculated CD depend sensibly from the approximated wave functions used to describe the two-electron states.
It has been already shown (see chapter 4 and references therein) that a non-vanishing CD in the DPE spectrum can be observed provided that:

(i) the two emitted electrons are detected in coincidence

[1] $\mathrm{DE} = \frac{\mathrm{NA}-\mathrm{AN}}{\mathrm{NA}+\mathrm{AN}}$,
where we indicated with NA and NA the intensity of one of the singlet peaks as relative to the triplet in NA and AN configuration, respectively.

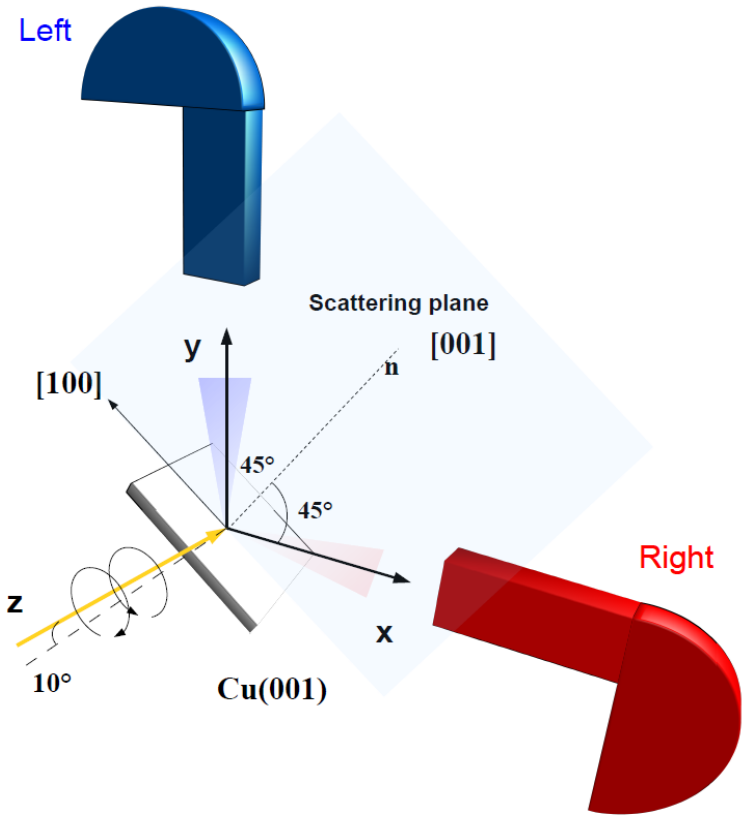

Figure 6.9: Schematic view of the experimental setup to detect DPE pairs with right and left circularly polarised light.

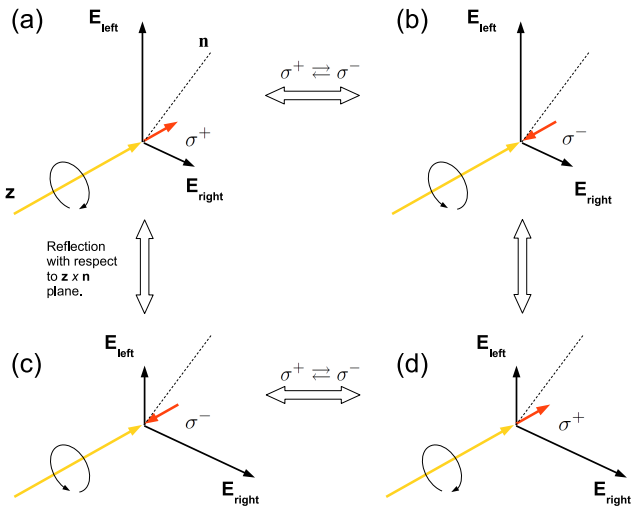

Figure 6.10: Schematic illustration of the chirality in the final state of the DPE process. The propagation direction of the light is indicated by the yellow line and right and left circular polarisations are indicated by σ^+ and σ^-, respectively. The emitted electrons energies are indicated by E_{left} and E_{right}. The length of the arrows is proportional to the electron kinetic energy.

(ii) the two electrons have different kinetic energy

(iii) the two electrons are not emitted in the same direction or in back-to-back configuration

(iv) the direction of incident light and the escape directions of the electrons do not lie in the same plane.

These propensity rules have been verified by Viefhaus *et al.* [40] by performing an electron-electron coincidence experiment on free He atoms using left and right circularly polarised light. In the mentioned case, no electrons are left in the residual ion, so the chirality of the incident photon is necessarily transferred to the emitted electron-pairs. In the case of atoms with $Z > 2$ it is possible that the chirality of the photon, after its absorption, is transferred to the electrons in the residual ion. If this is the case the electron-pairs are not chiral and this results in a vanishing CD intensity. By measuring the direct and core-resonant DPE spectrum on a Cu(001) we observed that the DPE pairs from ^1G final states show non-vanishing CD, oppositely to the pairs from the triplet ionic states. This demonstrates that the chirality of the DPE pairs is strongly correlated to the spatial symmetry of the corresponding final ionic state.

Fig. 6.9 represents the experimental set-up to acquire the Cu(001) DPE spectrum with circularly polarised light. The characteristics of the experimental apparatus are identical to the case of linearly polarised light with the exception that in this case we chose a symmetric geometry with the normal of the Cu(001) surface forming the same angle of 45° with respect to both analysers. In this way we excluded any contribution to the chirality ascribable to geometrical reasons.

6.3.1 Circular dichroism in DPE spectrum

A schematic of the investigated process is shown in Fig. 6.10. The photon beam, travelling along the $\hat{\mathbf{z}}$ direction, is represented by the thick yellow arrow. Left and right circular polarisation are indicated as σ^- and σ^+, respectively. The electrons are emitted with a mutual angle $\theta_{lr} = 90°$ and

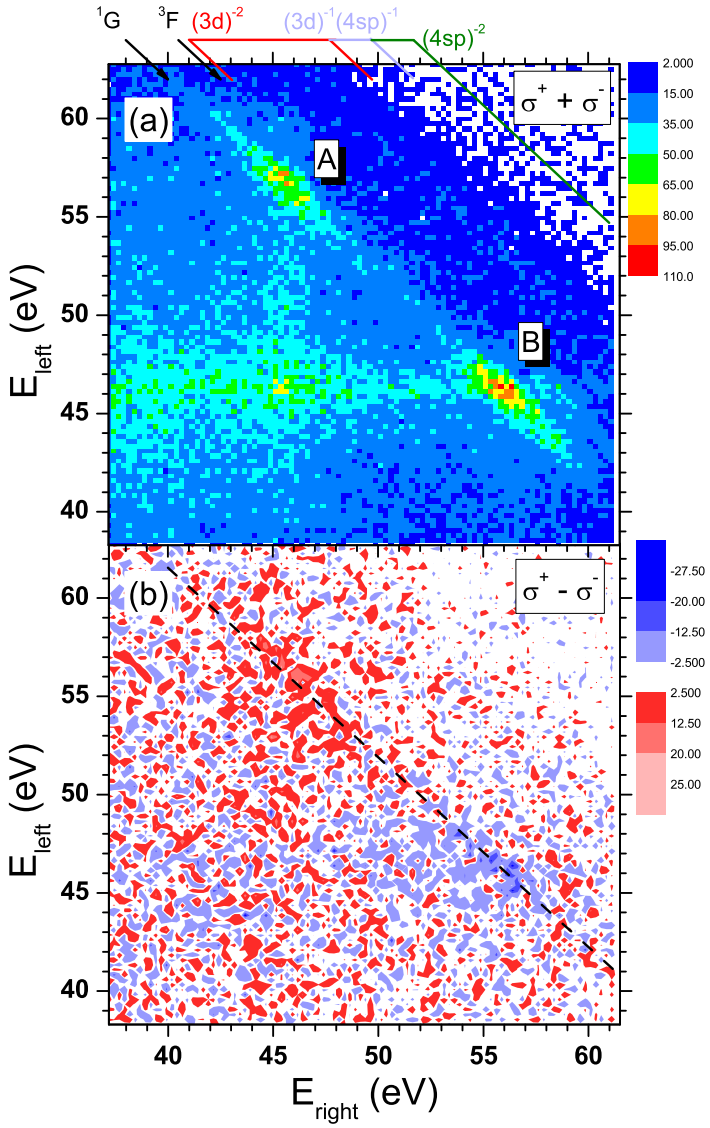

Figure 6.11: Sum (a) and difference (b) of the 2D energy distribution of correlated electron-pairs emitted upon the absorption of 125 eV photons with different helicity, $\sigma^{\pm}$. The final states of the most intense transitions are indicated in panel (a), according to energy conservation. See the text for further details.

are indicated by the black arrows labelled as E_{left} and E_{right}. The normal to the sample surface, $\hat{\mathbf{n}}$, represents the bisector of θ_{lr}.
As already mentioned in section 4.2, CD corresponds to a left-right asymmetry with respect to the $(\hat{\mathbf{z}} \times \hat{\mathbf{n}})$ plane. If the energy of the two electrons is different, for both helicities, the system is characterised by the fact that the faster electron, indicated by the longer arrow, is always detected by the left analyser, see Fig. 6.10(a) and (b). On the contrary, if we perform a reflection with respect to the $(\hat{\mathbf{z}} \times \hat{\mathbf{n}})$ plane, e.g. e.g. Fig. 6.10(a) $\rightarrow$ Fig. 6.10 (c), we obtain an helicity inversion but in this case the faster electron is detected by the right analyser.

Fig. 6.11(a) and (b) show the sum and difference of the DPE pairs two-dimensional energy distribution from Cu(001) excited by circularly polarised 125 eV photons with different helicity, $\sigma^{\pm}$, respectively. The main features of the sum 2D distribution in Fig. 6.11(a) have been already explained in section 6.2.2. As in the case of linear polarisation, the coincidence distribution shows a broad diagonal structure due to direct DPE from Cu 3d valence bands, indicated as $3d^{-2}$, and two sharp structures ascribable to core-resonant DPE pairs, indicated as ^1G and ^3F, respectively.
Additional informations can be obtained by considering the CD of the DPE pairs which is presented as the difference 2D distribution of Fig. 6.11(b). In this spectrum the intensity of CD vanishes in those regions where positive (blue) and negative (red) values are randomly distributed. However, two intense structures are observable along the diagonal structure ascribable to ^1G core-resonant DPE pairs. In this case the ^1G pairs show a degree of CD which is antisymmetric with respect to the line $E_{left} = E_{right}$, i.e. with respect to the exchange of the two emitted electrons. This reflects the chiral properties of the experimental set-up shown before. With right-handed circular polarisation the condition in which the faster electron is detected by the left analyser is favoured with respect to the left-handed circular polarisation case. Opposite effects occur when the fast electron is detected by the right analyser.

In order to get further informations on the dichroic properties of the electron-pairs emitted in both direct and core-resonant DPE we calculated the sum energy spectra associated to the sum and difference 2D spectra of Fig.6.11. Sum energy spectra are obtained by reporting the number of coincidence counts as a function of the sum energy of the electron-pairs ($E_{sum} = E_{left} + E_{right}$) measured with respect to the maximum energy accessible to them ($E_{sum}^{max} = h\nu - 2\phi$). The sum energy spectrum for $(\sigma^+ + \sigma^-)$ is shown in Fig. 6.12 (a). As in the case of linearly polarised light we can distinguish the direct from core-resonant DPE pairs according to their sum energy. The low binding energy region ($0 \leq E_{sum}^{max} - E_{sum} \leq 11$ eV) is dominated by electron-pairs emitted in the direct DPE process from the valence band. The major contribution to this region is ascribable to pairs emitted from the Cu 3d bands. In the high-binding energy region, $E_{sum}^{max} - E_{sum} > 11$ eV, the three peaks ascribable to the multiplet splitting of the two-hole final state in core resonant DPE (^1G, ^1D, ^3F) are visible.
The sum energy plot of the difference 2D distribution is reported in Fig.6.12 (b). In this case the spectrum (black dots with error bars) has been calculated as,

$$(N_{>}^{\sigma^+} - N_{>}^{\sigma^-}) + (N_{<}^{\sigma^-} - N_{<}^{\sigma^+}),$$

where N^{σ^+} (N^{σ^-}) indicates the number of coincidences for right (left) circularly polarised light and the subscripts $>$ and $<$ stand for the conditions $E_{left} > E_{right}$ and $E_{left} < E_{right}$, respectively. The so constructed spectrum, showing the CD as a function of the sum energy of the DPE pairs, allows to discriminate the chiral from achiral pairs. In the core-resonant region the CD distribution presents a very intense peak centred around 13.5 eV, corresponding to the binding energy of the singlet ^1G final state. The absence of a clearly distinguishable peak at the nominal energy of the triplet ^3F final state, ~ 10.7 eV, leads to the conclusion that the ^3F pairs are not chiral. In direct

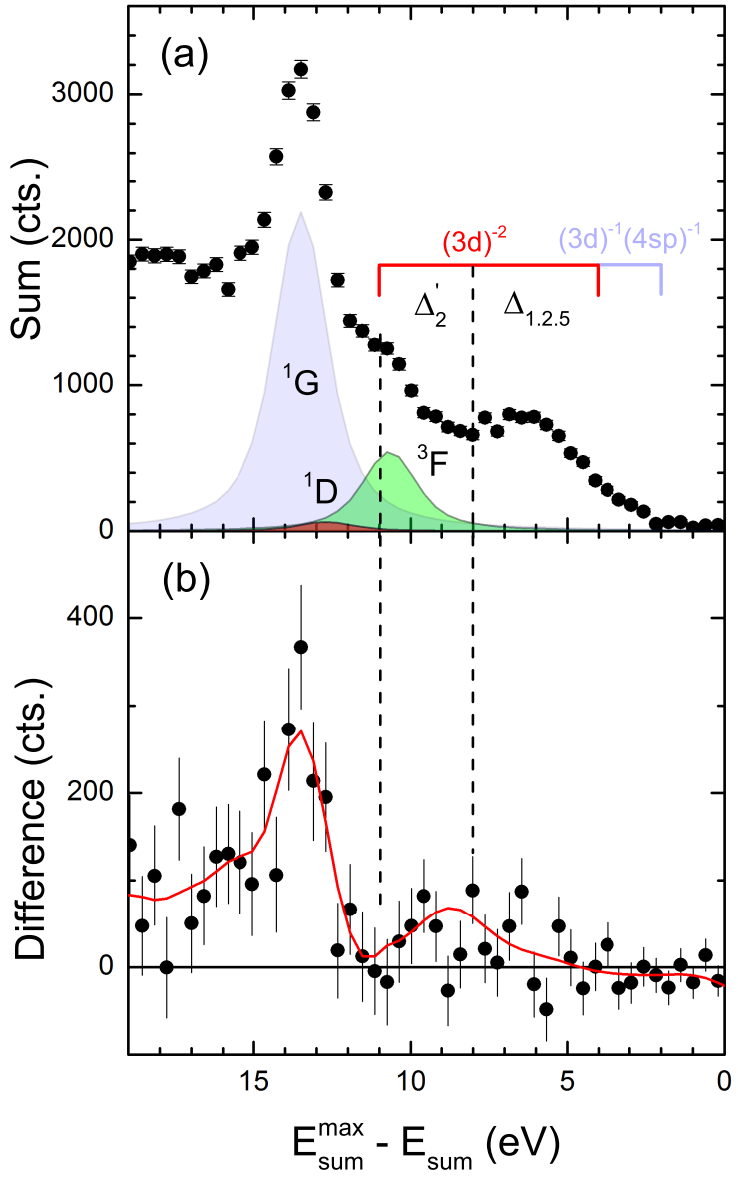

Figure 6.12: Sum (a) and difference (b) of the sum energy spectra of the DPE pairs obtained with different helicity of the circularly polarised light. The three peaks in the sum spectrum represent the most intense core-resonant DPE transitions, labelled as ^1G, ^3F, ^1D according to the LS coupling scheme. The final states of the direct DPE have been assigned according to the electrons binding energies.

DPE non-zero CD is observed for $7.5 \leq E_{sum}^{max} - E_{sum} \leq 10.5$ eV. This energy region corresponds to the emission of two electrons from the bottom of Cu 3d bands with binding energies between 3.25 and 5.25 eV.

Results presented so far are a clear evidence that we can observe circular dichroism in both direct and core-resonant DPE. The presence of CD in the core-resonant case confirms that the Cu $M_{23}M_{45}M_{45}$ Auger transition can be only described in a single-step picture. Indeed, according to the theories developed by Kabachnik and Schmidt [82, 109] and Berakdar and Klar [81, 25] (see chapter 4), the presence of a well defined intermediate (core-hole) state brings additional restrictions to the CD with respect to the direct DPE. If we indicate with θ_{lr} the angle between the two electrons, in a single-step process parity conservation forces the CD to go as $\sin\theta_{lr}$ (see section 4.4 for further details and examples). In a two-step process parity conservation must be fulfilled in both first and second step independently and this causes an higher symmetry with CD proportional to $\sin 2\theta_{lr}$. In our case, where $\theta_{lr} = 90°$, the observation of CD in core-resonant DPE indicates the breakdown of the two-step description.

Results point out that the localisation of the process to a single atom is not a necessary condition to have chiral DPE electron-pairs. So, what are the differences between chiral or achiral pairs? In core-resonant DPE, only the electron-pairs leaving the system in the singlet ^1G ionic state are chiral. The spin wave function of a singlet two-particle state is antisymmetric with respect to the exchange of the two particles. This means that the two holes must be in a symmetric spatial state, even with respect to the mirror plane defined by the light incident direction and the normal to the Cu(001) surface (see Fig. 6.9). In addition, by decomposing the ionic state into single-particle microstates, $|l_1 m_1\rangle\,|l_2 m_2\rangle$, it can be demonstrated that the major contribution to the ^1G state is given by two 3d electrons with the same magnetic number $m_1 = m_2 = \pm 2$.
For direct DPE electron-pairs the maximum of the CD is located around $E_{sum}^{max} - E_{sum} = 9$ eV corresponding to the emission of two electrons from the middle of the Δ_2' band, according to the binding energy region reported in [110]. The Δ_2' band corresponds to electronic states symmetric to the mirror plane characterised by magnetic quantum number $m = \pm 2$. In analogy to the core-resonant case the emitted electrons arise from the same spatial state and, as a consequence, they must have antiparallel spins and be in a singlet state.
Thus, it can be concluded from our experiment that chiral DPE pairs can only origin from electrons with initial magnetic quantum numbers $m = \pm 2$, which leave the residual ion in a spatial state symmetric with respect to the mirror plane.
The results shown so far supply a further evidence of the analogy between direct and core-resonant DPE processes, when the latter can be described in a single-step picture. In this case the presence of a short-lived intermediate core-hole state has the only effect to influence the locality of the indirect double-photoionisation process which is more likely to take place on one atomic site.

We can now focus on the core-resonant case, in particular to the study of the influence of the intermediate core-hole state on the chirality of the DPE pairs. This can be done by constructing the helicity-dependent energy sharing curves for the ^1G state. The sharing curves can be obtained selecting the coincidences satisfying the constraint $E_{sum}^{max} - E_{sum} = 13.5 \pm 1$ eV and by reporting them as a function of the energy difference, $E_{left} - E_{right}$, of the two electrons. The results of this procedure, for right (triangles) and left (circles) circular polarisation, are shown in Fig.6.13 (a). The corresponding asymmetry curve,

$$\mathrm{Asy} = \frac{N^{\sigma^+} - N^{\sigma^-}}{N^{\sigma^+} + N^{\sigma^-}},$$

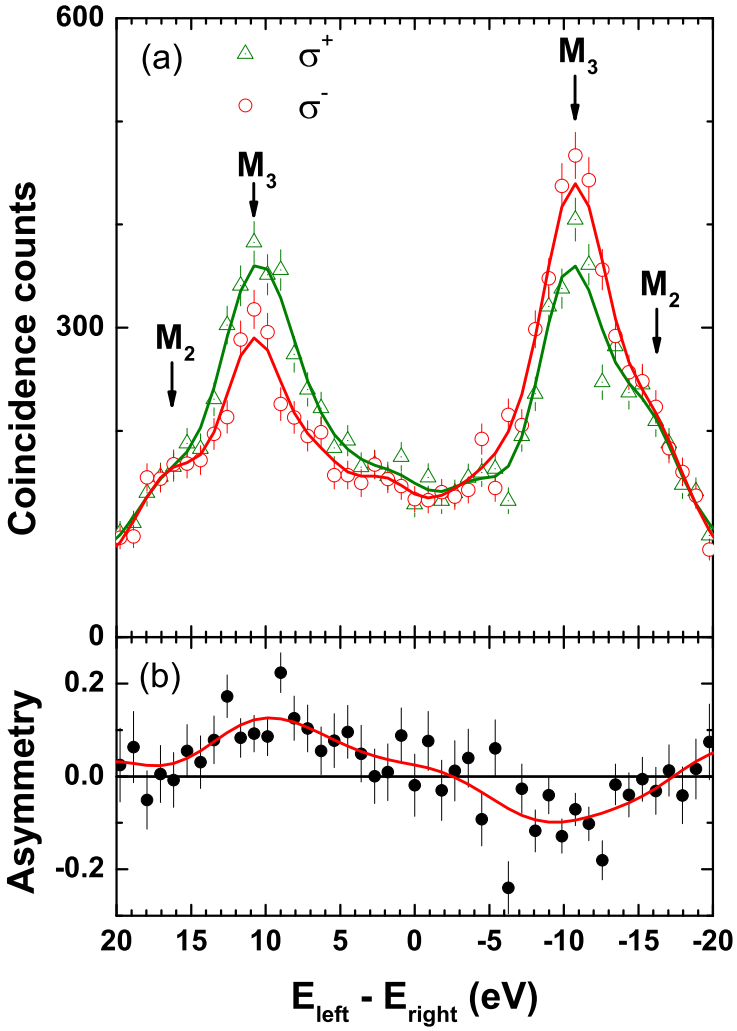

Figure 6.13: (a) Energy sharing curves for the core-resonant DPE pairs from ^1G final state, defined by $E_{sum}^{max} - E_{sum} = 13.5 \pm 1$ eV. Triangles and circles are obtained with right (σ^+) and left (σ^-) circular polarisation, respectively. (b) Corresponding asymmetry curve, given by the difference of the energy sharing curves normalised to their sum.

is presented in Fig. 6.13(b). The sharing curves show maximum intensity at energy difference $E_{left} - E_{right} = \pm 10.8$ eV, with two shoulders at $E_{left} - E_{right} \sim \pm 16$ eV. These sets of energies correspond to the measured energy difference of the $3p_{3/2}$ and $3p_{1/2}$ photoelectrons with respect to the corresponding $M_{23}M_{45}M_{45}$ Auger electrons. This is the reason why they have been marked as M_3 and M_2 in Fig.6.13 (a).
The asymmetry curve in Fig.6.13 (b) is antisymmetric with respect to the origin of the x-axis and shows extreme values of $\pm 11\%$ for M_3 and zero for M_2 DPE pairs. It has to be noticed that the CD is zero also for equal energy sharing, $E_{left} = E_{right}$. This is not surprising because two electrons with the same kinetic energy are not distinguishable and the chirality in the experimental set-up is no longer visible. This is related to the properties of the bipolar spherical harmonics describing the angular dependence of the two-electron wavefunction in the continuum, which are odd with respect to the exchange of the two particles (see section 4.1 for further details). From the shape of this curve we can deduce that only the DPE pairs involving the decay of the $3p_{3/2}$ hole are chiral. This can be understood considering the theory for the CD in core-resonant DPE [82] exposed in section 4.4. The CD intensity, Δ, is given by:

$$\Delta = -\sigma_{J_r}(\hbar\omega)\frac{\omega_A}{4\pi}c(E_a)\sum_L \alpha_L \bar{\Delta}_L B_{10}^{LL}(\mathbf{k}_a, \mathbf{k}_b), \tag{6.7}$$

where all the terms of the above expression have been defined in equations (4.27) – (4.32). In the presence of an intermediate core-hole state of total angular momentum J_r the above sum is restricted to $0 < L \leq 2J_r$, with L even. In the case $J_r = 1/2$ ($3p_{1/2}$) no term contributes to the dichroism. Indeed, CD in core-resonant DPE reveals the non-isotropic angular distribution of the Auger transition, which is the consequence of the non-uniform population of the magnetic sub-levels of the intermediate state. The $3p_{1/2}$ magnetic sub-levels, $m_j = \pm 1/2$, are either parallel or anti-parallel to the quantization axis, which in this case is given by the photon (spin) direction and is perpendicular to the scattering plane. This means that the population of the $J_r = 1/2$ core-hole state is isotropic within the scattering plane and leads to a vanishing CD. On the contrary, the populations of the $3p_{3/2}$ magnetic sub-levels are not isotropically distributed within the scattering plane and this is the source of the CD observed in $M_3M_{45}M_{45}$ decay.

In conclusion, we have mapped out the helicity-dependent angular resolved energy distribution of both direct and core-resonant DPE electron-pairs from a Cu(001) surface. Results show that both kind of pairs can be sensitive to the switching of the light helicity depending on the symmetry of the ionic state they leave behind. Furthermore, the detection of chiral core-resonant electron-pairs with mutual angle between the electrons of 90° and the energy sharing between them demonstrate the breakdown of the two-step description for the $M_3M_{45}M_{45}$ Auger decay in spin and energy space, respectively.

Chapter 7

DPE on Cu(001)-$p(2\times2)$S

In this chapter we will present the process of double photoemission of Cu(001) surface covered with sulphur, Cu(001)-$p(2\times2)$S.
The increasing interest in sulphur-transition-metal interfaces is mainly due to catalysis processes. Sulphur species are poisons for all catalytic processes involving noble and transition metals as catalyst [111, 112]. This is because a sulphur compound is strongly chemisorbed onto and reacts with the active catalytic sites, thus altering the surface structure. The specific S/interface interaction is quite complex and depends upon the oxidation state of the sulphur impurity, i.e. how many sulphur s-p electron-pairs are available for bonding with the d-electrons of the metal and whether they are screened or not by the other electrons. There is a considerable amount of literature devoted to the study of the electronic properties of S/Cu interface from both theoretical and experimental [113, 114, 115, 116, 117, 118] point of view, but in no case the authors focussed on the study of the two-particle properties of the system. Two-particle properties can influence the most of the ground-state properties of materials, and are essential for the description of dynamical processes, e.g. dynamic electron screening and many-particle scattering.

In this experiment we have measured the direct and core-resonant DPE spectrum of sulphur adsorbed on Cu(001) following the absorption of left (σ^-) and right (σ^+) circularly polarised photons. We chose a photon energy sufficiently high to excite a S 2p core-electron into the vacuum in order to observe, together with direct DPE pairs, also core-resonant DPE pairs coming from the decay of the 2p core-hole via an Auger process leaving the system with two holes in the valence band ($L_{23}VV$). This type of decay is supposed to take longer to proceed with respect to the Cu(001) $M_{23}VV$ Auger transition. This is because the valence levels participating in Cu(001) MVV Auger decay are mainly from 3d-bands and have the same principal quantum number of the initial core-hole. This type of transitions, called super Coster-Kronig, are supposed to occur on a time scale of ~ 500 attoseconds [17, 119]. For this reason a meaningful temporal separation between photoelectron emission and Auger decay becomes questionable. This is the reason why this "fast" decay can be only described in a single-step picture, as verified in chapter 6. On the other hand, the S LVV transition, having the sulphur valence electrons 3s or 3p character, involves electrons with different principal quantum number and is supposed to occur in few femtoseconds. The longer time of the decay would, in principle, make the two-step approximation appropriate. This conjecture has been tested by acquiring the energy and helicity dependent DPE spectrum of Cu(001)$p(2\times2)$-S. The acquired energy distribution of the DPE pairs as well as the observed lack of circular dichroism can be considered a proof of the validity of the two-step description for the considered decay.

The study of the L3VV coincidence line-shape also gave the opportunity to determine the two-

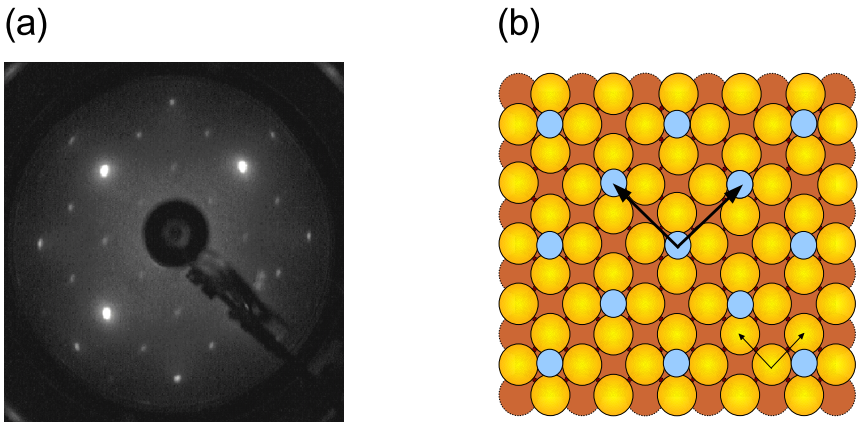

Figure 7.1: (a) LEED image for Cu(001)-$p(2\times2)$S at a primary energy $E_p = 124$ eV. (b) Schematic top view of Cu(001)-$p(2\times2)$S surface reconstruction. The small circles represent the S adatoms, the big circles the Cu atoms in first (light orange) and second (dark orange) layer. Thin and thick arrows stand for Cu(001) and S/Cu(001) surface lattice vectors respectively.

particle properties and to measure the valence band hole-hole correlation energy of the system.

7.1 The Cu(001)-$p(2\times2)$S sample

There is a vast amount of literature on the preparation of sulphur overlayers on metal surfaces and their properties in particular on Cu(001) and Ni(001) surfaces [120, 121, 122, 123]. The preparation of the Cu(001) surface followed standard procedures consisting in Ar^+ sputtering and annealing cycles. We prepared S overlayers onto the surface via H_2S exposure. In order to establish the conditions to give saturation S coverages we performed ancillary studies in a separate apparatus equipped with Low Energy Electron Diffraction optics and Auger spectrometer. The S/Cu(001) film was prepared by exposing the Cu(001) surface to H_2S gas for 20 L at room temperature as laid out in the literature [120]. In order to increase the dosing efficiency, the exposure was carried out using a mechanical doser [124]. This increased the dosing efficiency by ~ 12. The sample was kept about 5 cm away from the doser end during the exposure. The sample was subsequently annealed at 300°. Fig. 7.1(a) shows an exemplary LEED image of the sample. The appearance of half-spots in both the horizontal and vertical direction are characteristic of the expected $p(2\times2)$ reconstruction observed at 0.25 monolayer of sulphur coverage in which the sulphur atoms are chemisorbed above a fourfold hollow site [see Fig. ref2x2.reconstruction(b)], with a S-Cu bond of about 2.26($\pm$0.06) Å[123].

Electronic properties

Numerical simulations within the density-functional theory (DFT) have been performed [125] to determine the electronic properties of the system with the Perdew-Burke-Ernzerhof (PBE) functional for exchange and correlation [126]. A 9-layer thick Cu slab with S adsorbed on one side has been considered, and its coordinate has been relaxed together with 3 Cu layers underneath in a $p(2\times2)$ structure as depicted in Fig. 7.1(b). The plane-wave, ultrasoft pseudopotential method was used as implemented in the QUANTUMESPRESSO simulation package [127]. Results for

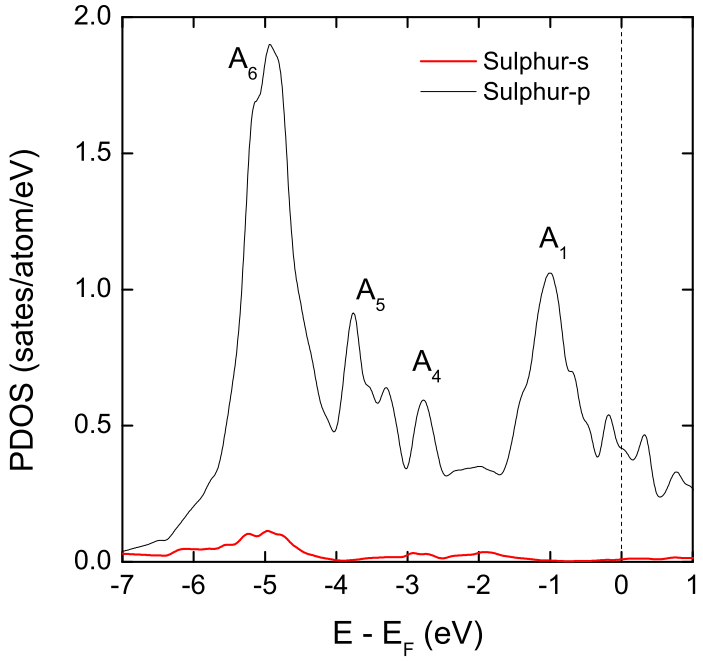

Figure 7.2: Cu(001)-$p(2\times2)$S DFT single-particle density of states projected on the atomic orbitals of the sulfur atom.

the density of states (DOS), shown in Fig. 7.2, are analogous to those reported in the literature with full potentials and the local density approximation [113].

The most important contribution to the DOS has p symmetry around the nucleus (thin black line), with the occupied portion having an overall width $W \approx 6$ eV. The main features of the DOS have been labelled as A_i, following the literature [113]. The curves in Fig. 7.2 clearly point to the formation of S-Cu hybrid orbitals. Indeed, the A_1 state at ≈ -1 eV indicates a strong hybridization between S-p orbitals and Cu-d bands with antibonding character. At higher binding energies the superposition between S-p orbitals and Cu-s and Cu-d bands gives rise to the bonding states labelled as A_5 (≈ -4 eV) and A_6 (≈ -5 eV). Sulfur orbitals with s-symmetry around the nucleus give a minimal contribution to the total DOS as indicated by the thick red line in Fig. 7.2.

7.2 Single photoemission spectrum

The geometry of the experimental set-up is identical to the one used to measure the Cu(001) DPE spectrum, Fig. 6.9. The circularly polarised light impinges on the sample with a grazing angle of 10°. The optical axis of the left (vertical) and of the right (horizontal) analyser are mutually perpendicular and lie in the plane perpendicular to the incident light direction, with the right analyser aligned to the [100] direction of the sample surface. The optical axis of both the analysers form angles of 45° with respect to the surface normal.

In Fig. 7.3 we present a typical single electron spectrum obtained from Cu(001)-$p(2\times2)$S sample by measuring the kinetic energy distribution of the electrons emitted upon the absorption of 301 eV photons. The settings for the left (a) and right (b) spectrometer are the same used for the

Table 7.1: Experimental values of $3p_{1/2}$, $3p_{3/2}$ energies and Lorentzian line-widths (in eV) obtained with left and right analyser.

Analyser	Energy $2p_{1/2}$	FWHM $2p_{1/2}$	Energy $2p_{3/2}$	FWHM $2p_{3/2}$
Left	131.59 (0.02)	0.19 (0.05)	132.77 (0.02)	0.08 (0.02)
Right	131.59 (0.01)	0.16 (0.03)	132.73 (0.02)	0.05 (0.01)

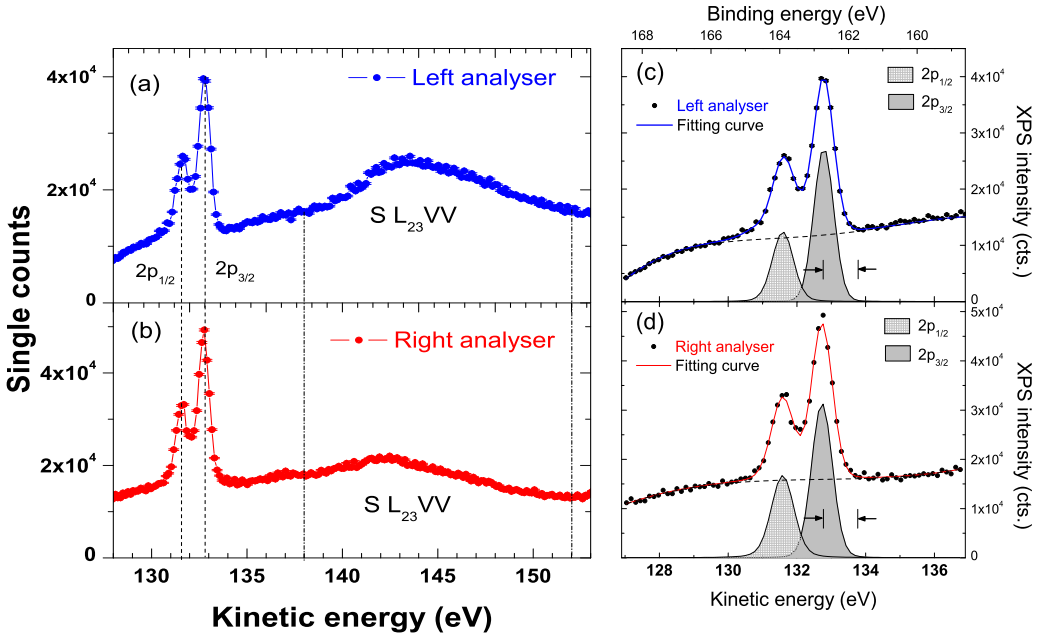

Figure 7.3: (a) and (b) Single electron spectra obtained from a Cu(001)-$p(2\times2)$S structure by means of left (a) and (right) spectrometer. The incident energy was $h\nu = 301$ eV. The dashed vertical lines defines the kinetic energy of the spin-orbit split photoelectron lines which are clearly resolved. The broad peak included between the two vertical dashed dotted lines is due to Auger electrons emitted in the decay of $2p_{1/2}$ and $2p_{3/2}$ core-holes. (c) and (d) Fitting to the photoemission S $2p$ lines using trial functions made up by two Voigt profiles, accounting for the S $2p_{1/2}$ (shaded area) and $2p_{3/2}$ (full area), superimposed on polynomial background. The arrows indicate the energy window for APECS measurements of the L_3VV line.

coincidence measurements and the field of view of each spectrometer includes S 2p photoelectrons, located in the low kinetic energy side of the spectrum ($130 \leq E_k \leq 134$ eV), and Auger electrons responsible for the broad structure around ~ 142 eV. Single channel measurements were performed in order to verify the cleanliness of the adsorbate-substrate system and to determine the kinetic energies of electrons emitted from S $2p$ levels, that will be used in the coincidence experiment. To this end, the low kinetic energy part of each measured spectrum, Fig. 7.3 (c) and (d), was fitted by means of two Voigt profiles, accounting for $2p_{3/2}$ and $2p_{1/2}$ photoemission peaks, superimposed on a polynomial background which takes into account the inelastic scattering. The shape of the background is also determined by analysers transmission effects. The results of the fitting procedure are listed in Tab. 7.1. The Gaussian full-width at half maximum was forced to be the same for both peaks and equal to the experimental resolution, $W_G = 0.8$ eV, while the Lorentzian full-width at half maximum, W_L, which is essentially due to the core-hole lifetime was left as a free parameter. The obtained parameters are similar for both analysers; the kinetic energies of the spin-orbit split peaks are $E_k(2p_{3/2}) = 132.75$ eV and $E_k(2p_{1/2}) = 131.6$ eV, with a spin-orbit splitting for S $2p$ levels of $\Delta E_{SO} = 1.15 \pm 0.03$ eV, in agreement with previous results [117]. Results show a Lorentzian width $W_L < 0.1$ eV for the L_3 peak, while the one of the L_2 is larger, $0.1 \text{ eV} \leq W_L \leq 0.2$ eV. This means that the $2p_{3/2}$ core-hole lifetime is longer than the $2p_{1/2}$ one showing that there could be additional decay channels for the latter level with respect to the former one, for example radiative decays or Coster-Kronig preceded Auger transitions.

7.3 Double photoemission spectrum

We display in Fig. 7.4 2D energy spectra, i.e. the number of coincident electron-pairs as a function of the electrons kinetic energies (E_{left}, E_{right}), measured on the S/Cu(001) sample with a photon energy of $h\nu = 301$ eV. Panel (a) shows the results obtained by summing the spectra acquired with σ^+ and σ^- helicity. The coincidence distribution is described by intensity bands which are parallel either to the vertical or horizontal axis. These intensity bands are further subdivided into two smaller regions. If we extend the vertical intensity features to the x-axis we found that they intercept it at $E_{right} = 131.6$ and 132.7 eV, respectively. Recalling the results of the fitting procedure on the single spectra in Tab. 7.1 and Fig. 7.3 we can identify these high intensity features with coincidence events in which the electron detected by the right spectrometer is a photoelectron. In addition, the energy of the electron detected by the left analyser falls within the energy region dominated by the emission of Auger electrons (centered around $E_{left} = 142$ eV), so we can ascribe the high intensity bands to the coincident detection of one Auger electron with the correlated photoelectron, i.e. APECS events. We observe a non-vanishing coincidence rate on the whole energy range detected by the left analyser and this is a sign that a broad Auger spectrum is correlated to each one of the two photoemission peaks. The horizontal intensity bands correspond to photoelectron-Auger electron coincidence events, analogous to the ones of the vertical bands, but in which the role of the two analysers is exchanged.
The intensity distribution presented in Fig. 7.4(a) is expected if the two-step model is appropriate to describe the sulphur L_{23}VV Auger decay. In particular there is no diagonal band connecting the high intensity regions centred at (132 eV, 142 eV) and (142 eV, 132 eV). This means that there is no evidence for a one-step process as observed on Cu 3p Auger decay shown in previous chapter. In this case the initial photoemission process and the subsequent Auger decay can be considered as independent events and energy conservation can be applied separately to the two processes. Thus,

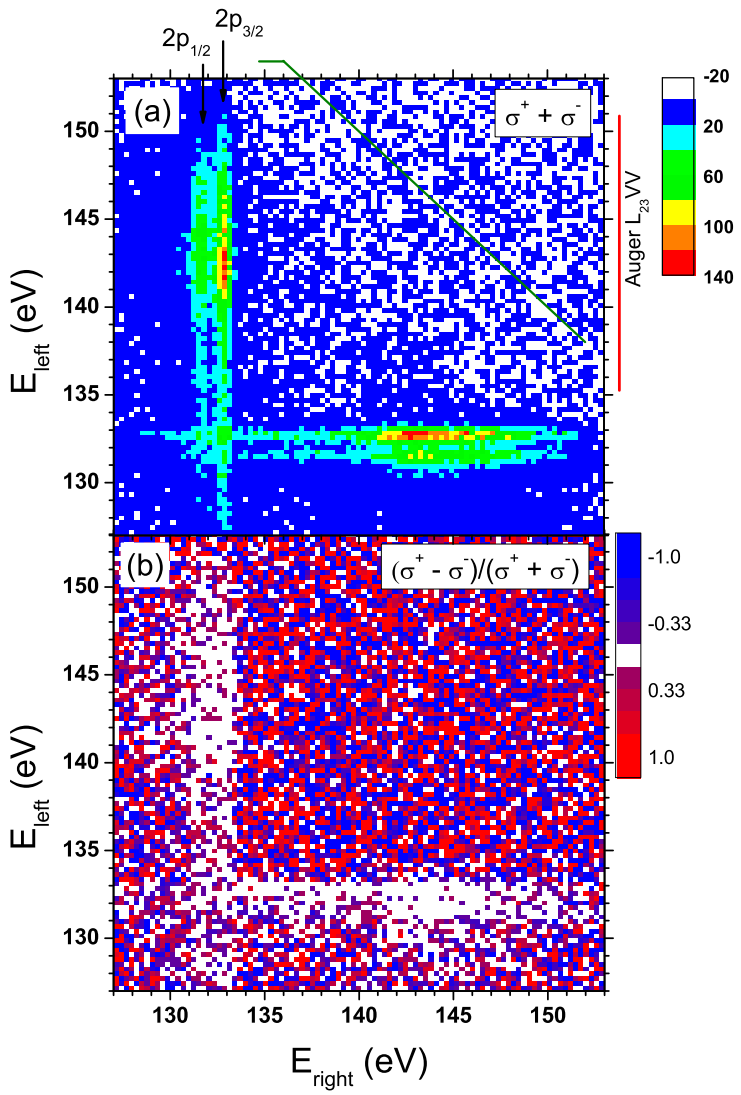

Figure 7.4: (a) 2D DPE energy spectrum of S/Cu(001) at $h\nu = 301$ eV, obtained by summing the DPE distributions acquired with σ^+ and σ^- helicity, $\sigma^+ + \sigma^-$. The solid diagonal line marks the position of the maximum sum energy, E_{sum}^{max}, accessible to the pairs. (b) Asymmetry between σ^+ and σ^- 2D spectra.

the kinetic energy of the photoelectron,

$$E_p = h\nu - \varepsilon_c - \phi,$$

is obtained by the difference of the incident photon energy, $h\nu$, and the binding energy of the core-level involved in the transition, ε_c, measured with respect to the vacuum level, ϕ. In the same framework the kinetic energy of the Auger electron emitted in the decay of the core-hole,

$$E_A = \varepsilon_c - \varepsilon_i - \varepsilon_j - U_{eff},$$

depends on the binding energies of the levels involved in the transition up to a correction term, U_{eff}, accounting for relaxation effects and hole-hole interaction in the final state (see chapter 3.2). Indeed, no energy sharing is expected between photo- and Auger electron.
Finally, we have added a diagonal line in Fig. 7.4(a) which corresponds to the position of the two-particle Fermi level $E_{sum}^{max} = h\nu - 2\phi$. This marks the position at which two electrons from the top of the valence band would be emitted. The absence of a clear cut-off in the intensity in the vicinity of this line clearly shows that direct DPE processes from the valence states yields no detectable intensity. This could be a consequence of the photon energy dependence of the direct DPE cross section (see chapter 2.1). The DPE intensity is expected to decrease upon increasing the photon energy and so it is not unexpected to see a large loss in the transition amplitude when moving from $h\nu = 125$ eV, in the case of Cu(001), to $h\nu = 301$ eV.

We report in Fig. 7.4(b) the asymmetry between the DPE spectra acquired with opposite helicity, defined as the difference between the two spectra normalised to their sum,

$$\text{Asy} = \frac{N^{\sigma^+} - N^{\sigma^-}}{N^{\sigma^+} + N^{\sigma^-}}.$$

In the region where the coincidence intensity is high the measured asymmetry is zero, which according to the color coding corresponds to a white region. Outside the high intensity regions the asymmetry fluctuates around positive (red) and negative (blue) values due to the few counts in this region. This means that no dichroic effect is observed in core-resonant DPE of S/Cu(001).

7.4 The $L_{23}VV$ Auger spectrum

One of the main advantages of the used coincidence spectrometer lies in the fact that we can measure coincidences at different electronic energies in parallel, remarkably reducing the acquisition time. Once the 2D distribution is acquired one can perform cuts at given energies and isolate specific coincidence events.
In our case two different cuts were performed in order to obtain the APECS spectra for the L_3VV ($2p_{3/2}$-valence-valence) and L_2VV ($2p_{1/2}$-valence-valence) Auger decays. A first spectrum, L_3VV, was built by reporting the number of coincidences in the region 132.8 eV $\leq E_{\text{left}} \leq$ 133.8 eV as a function of the energy of the right analyser, Fig. 7.5(a). This means that the vertical analyser is tuned on the high kinetic energy side of the $2p_{3/2}$ photoemission peak, see arrows in Fig. 7.3(c), while the horizontal analyser captures the whole Auger spectrum. Similar spectra, obtained by exchanging the role of the two analysers, are shown in Fig. 7.5(b).
The L_2VV coincidence spectra, not shown, were built in an analogous way, by tuning the fixed energy analyser on the low kinetic energy side of the $2p_{1/2}$ peak, 130.6 eV $\leq E_{\text{left}} \leq$ 131.6 eV.

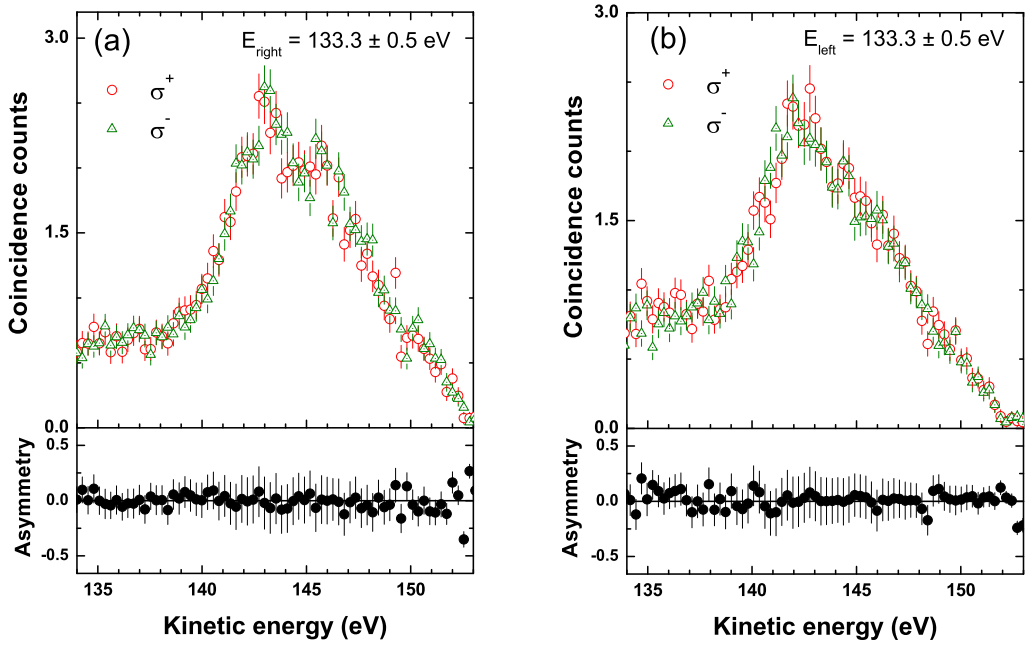

Figure 7.5: (a) Top panel, L_3VV Auger spectra measured by the left analyser in coincidence with $2p_{3/2}$ photoelectrons, for right (open circles) and left (open triangles) circularly polarised light. Bottom panel, point by point asymmetry calculated as the difference between the spectra in top panel divided by their sum. (b) The same as panel (a) for the right analyser.

7.4.1 Circular dichroism in core-resonant DPE spectrum

We report in the top panel of Fig. 7.5(a) the L_3VV Auger spectrum measured by the left analyser in coincidence with $2p_{3/2}$ photoelectrons The open circles with statistical error bars represent the coincidence spectrum with σ^+ helicity and is compared with the same spectrum acquired with σ^- helicity (open triangles). The point by point asymmetry between the two spectra, shown in the bottom panel, is randomly distributed around zero, thus indicating the lack of circular dichroism in the core-resonant DPE spectrum. Identical results, Fig. 7.5(b), are obtained in the configuration in which the Auger spectrum is measured by the right analyser in coincidence with the photoelectrons detected by the left one.
The lack of circular dichroism in the $L_{23}VV$ APECS spectrum is not unexpected, according to the two-step nature of the process. In the two-step description of the core-resonant DPE process conservation rules (e.g. energy, parity) must be independently satisfied in both stages of the process, initial photoionisation and subsequent Auger decay. In this case the expression for the dichroism ($\Delta = \mathrm{TDCS}_{\sigma^+} - \mathrm{TDCS}_{\sigma^-}$) can be obtained using the theory developed by Kabachnik and Schmidt [82], already presented in section 4.4,

$$\Delta = -\sigma_{J_r}(\hbar\omega)\frac{\omega_A}{4\pi}c(E_b)\sum_L \alpha_L \bar{\Delta}_L B_{10}^{LL}(\mathbf{k}_a,\mathbf{k}_b), \qquad L = 2,4,\cdots,2J_r \qquad L = \text{ even} \tag{7.1}$$

where the terms contained in the above expression have been already discussed in equations (4.27) - (4.32). $\sigma_{J_r}(\hbar\omega)$ and $C(E_b)$ describe the cross section for the initial photoionisation from a core-level of total angular momentum J_r and photoelectrons energy distribution, respectively. $\hat{\Delta}_L$ is related to the transition matrix elements for the photoemission process. ω_A and α_L represent the partial Auger decay rate and the Auger anisotropy coefficient, respectively. The aforementioned terms describe the dynamical part of dichroism in the core-resonant DPE process and are separated from the geometrical one which is described by the bipolar spherical harmonics $B_{10}^{LL}(\mathbf{k}_a,\mathbf{k}_b)$ [see (4.19)], which originate from the partial waves expansion of the two-electron final state and describe the dependence of the CD with respect to the emission angles of the electrons. The sum index L runs over the possible orientations of the core-hole sub-levels with respect to the quantization axis. The presence of a well-defined intermediate state implies that parity conservation must be independently fulfilled in first and second step of the process, leading to the condition that L must be even. Hence, no term contributes to the circular dichroism in the decay of the $2p_{1/2}$ core-hole because $2J_r = 1$.
The circular dichroism for L_3VV transition can be written has,

$$\Delta = \sigma_{3/2}(\hbar\omega)\frac{1}{4\pi}C(E_b)\alpha_2\hat{\Delta}_2 B_{10}^{22}(\mathbf{k}_a,\mathbf{k}_b), \tag{7.2}$$

where the angular dependence of Δ is given by the bipolar spherical harmonics (BSH),

$$B_{10}^{22}(\hat{\mathbf{k}}_a,\hat{\mathbf{k}}_b) = \sum_{M=-2}^{2}\langle 2M2-M\,|\,10\rangle\, C_{2M}(\hat{\mathbf{k}}_a)C_{2-M}(\hat{\mathbf{k}}_b). \tag{7.3}$$

Substituting the values of the Clebsch-Gordan coefficients $\langle 2M2-M\,|\,10\rangle$ and the definition of the spherical harmonics we obtain,

$$B_{10}^{22}(\hat{\mathbf{k}}_a,\hat{\mathbf{k}}_b) \sim \frac{1}{2}(1-\cos^2\theta_a)(1-\cos^2\theta_b)\sin 2(\phi_a-\phi_b) + \cos\theta_a\cos\theta_b\sin\theta_a\sin\theta_b\sin(\phi_a-\phi_b), \tag{7.4}$$

where $\theta_{a,b}$ and $\phi_{a,b}$ are the polar and azimuthal angles of the electrons with respect to the photon beam. In the considered experimental set-up, with the light incident direction orthogonal to the scattering plane (Fig. 6.9), $\theta_a = \theta_b = 90°$, the second term in (7.4) vanishes and,

$$\Delta \sim \sin 2(\phi_a - \phi_b). \tag{7.5}$$

Since we collect electrons in orthogonal directions, $\phi_a - \phi_b = 90°$, we are not able to see CD in the two-step Auger decay. The presented results point out how the presence of an intermediate state with well defined parity and symmetry affects the emission of correlated electrons. Indeed, parity conservation in single-step DPE process requires the CD to be zero when the two electrons of the pair are emitted in parallel, $\phi_a - \phi_b = 0°$, or back-to-back configuration, $\phi_a - \phi_b = 180°$. Due to the lack of dichroism we will present in the following helicity averaged Auger spectra.

7.4.2 Determination of Cu(001)-$p(2\times2)$S hole-hole correlation energy

The line shape of core-valence-valence (CVV) Auger spectra has been subject of analysis since the early '50s [128]. In particular, the most important issue was to understand why some materials show band-like line shapes while others show CVV Auger spectra with atomic-like multiplet structures. This peculiar behaviour was explained by the Cini-Sawatzky (CS) theory developed in 1977 [18, 19] and already presented in section 1.8. The atomic-like vs band-like character of the Auger spectrum is driven by the on-site particle-particle interaction energy U which describes how strongly the two valence band holes in the final state interact with each other and the effect of the valence band electrons in screening such interaction.
As the value of U, relative to the valence band width W, increases from negligible ($U/2W \ll 1$) to sizeable amounts ($U/2W \gtrsim 1$), the Auger line shape evolves from simple self-convolution of the single particle density of states to a more complex atomic-like appearance reflecting the presence of two holes resonances. This makes the Auger spectroscopy an ideal candidate for studying electronic correlations. In fact by the comparison of the measured CVV Auger spectrum with the predictions of the CS theory it is possible to determine the intensity of the interaction between two valence holes.

We now present in detail the results for the L_3VV Auger line measured in coincidence, shown in Fig. 7.6. The black dots in panel (a) represent the helicity averaged Auger spectrum recorded by the left analyser when the right analyser is fixed on the $2p_{3/2}$ photoelectron, while the open circles represent the same spectrum measured when the role of the analysers is exchanged. The curves were normalised to the same maximum intensity, in order to account for the different efficiency of the detectors. The point by point difference of the measured line shapes, panel (b), shows values randomly distributed around zero, as expected. This confirms that the two independent measurements of the L_3VV line shape are comparable and allows us to add the two spectra. The result is shown in panel (c) of Fig. 7.6, which represents the Cu(001)-$p(2\times2)$S L_3VV Auger line shape measured with an excellent statistics.
Notice, as a comparison, that the APECS spectrum is much more resolved than the single one [continuous line in Fig. 7.6(c)], owing to the remarkable decrease of the background. This is due to the fact that most of the secondary electrons have no time correlation with the photoelectron of the primary ionisation and do not contribute to the coincidence signal, beyond the selection of a core-hole state that allows to isolate overlapping structures in the electron energy distribution. In addition, the increased surface sensitivity in the coincidence experiment reduces the energy loss contributions that are responsible for the low energy tails in conventional Auger spectra.

The same analysis was performed for the Cu(001)-$p(2\times2)$S LVV Auger spectrum in coincidence with the $2p_{1/2}$ photoelectron. The L_2VV Auger spectrum, not shown, is shifted by about

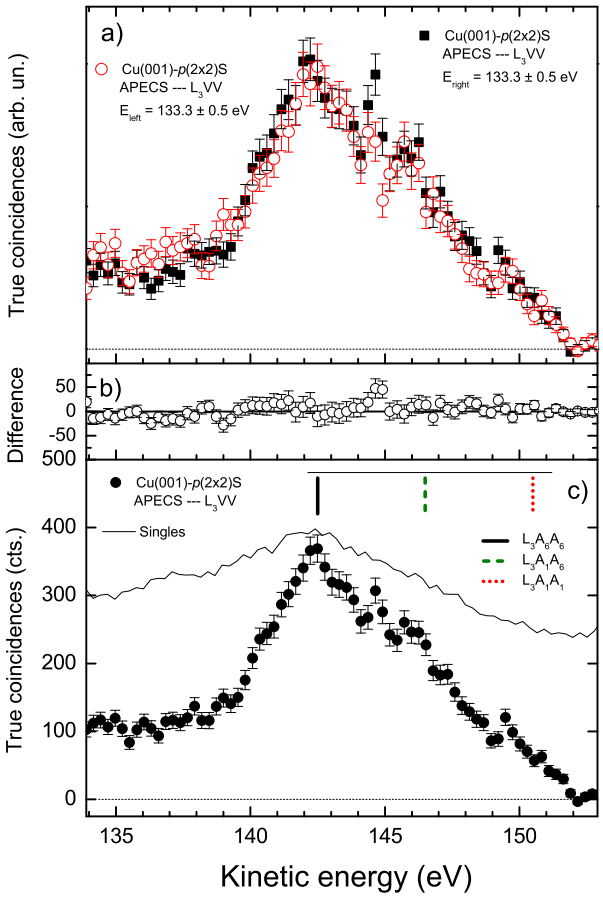

Figure 7.6: (a) S L_3VV Auger spectrum in coincidence with $2p_{3/2}$ photoelectrons. The black squares represent the Auger spectrum recorded by the left analyser with the right one fixed on the photoelectron, the open circles depict the APECS spectrum recorded with the right analyser when the left detects photoelectrons. The curves have been rescaled in order to have the same maximum intensity. (b) Point by point difference of the curves shown in panel (a). Points randomly distributed around zero indicate no differences between the two independent measures of the same APECS spectrum. (c) Cu(001)-$p(2\times2)$S L_3VV APECS spectrum obtained by summing the curves in panel (a). The bar plot shows the energies of the most intense transitions ending with two holes in Cu-S interface states. The continuous line represents the single Auger spectrum.

1 eV towards higher kinetic energies with respect to the L_3VV one, reflecting the spin-orbit energy splitting. This is due to the fact that, according to energy conservation (3.33), Auger electrons coming from the decay of a deeper core-hole ($2p_{1/2}$) escape with higher kinetic energies. The $2p_{1/2}$ decay spectrum is also less intense than the $2p_{3/2}$ one and this is a consequence of the reduced number of holes one can create in a $j = 1/2$ state with respect to a $j = 3/2$. An accurate comparison of L_2VV and L_3VV spectra points out that there are no detectable differences between the two measured line shapes.

In an independent particle picture, the CVV spectrum is proportional to the self-convolution of the single particle density of occupied states, apart from matrix element effects and a shift corresponding to the core energy. Hence, we start by analysing the DOS projected on the sulfur atomic orbitals, as computed by DFT, which is shown in Fig. 7.2. Taking two non-interacting electrons within the valence band [see the $U = 0$ curve in Fig. 7.7] it is possible to explain the main features observed in the L_3VV (L_2VV) spectrum: the linewidth of about 12 eV is twice the single-particle DOS width, W, as expected for noninteracting systems; the three structures at about 142.5, 146.5, and 150.5 eV kinetic energy [indicated by vertical bars in Fig. 7.6(c)] correspond to transitions with two holes left in the A_6 (A_6A_6), one hole left in the A_1 and one in the A_6 (A_1A_6) and two holes left in the A_1 (A_1A_1) single particle states, respectively. We can conclude that in this system U is significantly smaller than W.

We now consider the effect of the hole-hole interaction and evaluate the two-particle interacting DOS in the atomic region. The interaction between the two holes in the valence shell is treated by the CS theory [18, 19]. That allows for a formal solution of a many-body Hamiltonian in the case of closed bands, but its results have been tentatively applied here also in the case of S/Cu(001) whose p states are not completely filled and which would in principle require the evaluation of higher-order propagators [20, 129]. In practice, from the non-interacting DOS of the two particles, which is evaluated as the convolution of the single-particle (DFT) ones, one constructs the non-interacting Green function G^0. Eventually, a Dyson equation with kernel U allows to determine the interacting Green function G:

$$G(E) = G_0(E) + G_0(E)UG(E). \tag{7.6}$$

While for atomic-like spectra the full dependence of U on the specific two-particle states has to be taken into account to correctly reproduce the observed multiplets [130], here a scalar form of Eq. (7.6) will be used with the DFT DOS averaged over the quantum numbers and with an effective value of U to be determined phenomenologically. It is interesting to address the dependence of the results on the value of U. This is shown in Fig. 7.7. As U increases, spectral weight is progressively transferred to more strongly bound states, thus enhancing the A_6A_6 peak as in the experiment.

A quantitative analysis was then performed by fitting the line shape using the calculated two-particle DOS with different U values as trial functions, and U as a fitting parameter. The theoretical functions were convoluted with a Gaussian function of 0.8 eV FWHM in order to take into account the energy resolution of the experimental apparatus. The Auger spectrum is superimposed on a background, due to inelastically scattered electrons, whose intensity increases at lower kinetic energies. This background was reproduced by means of a Shirley-type function [dashed line in Fig. 7.8(a)], and is summed to theoretical results (yielding the solid line) to facilitate the comparison to experimental findings. An additional contribution (at about 140.5 eV) was added to take into account further emissions which are visible at the low-kinetic energy side of the spectrum. These extra contributions to the line shape can be ascribed to either satellite Auger transitions, e.g. involving more than two electrons, or to energy loss features in which the elastic photoelectron is

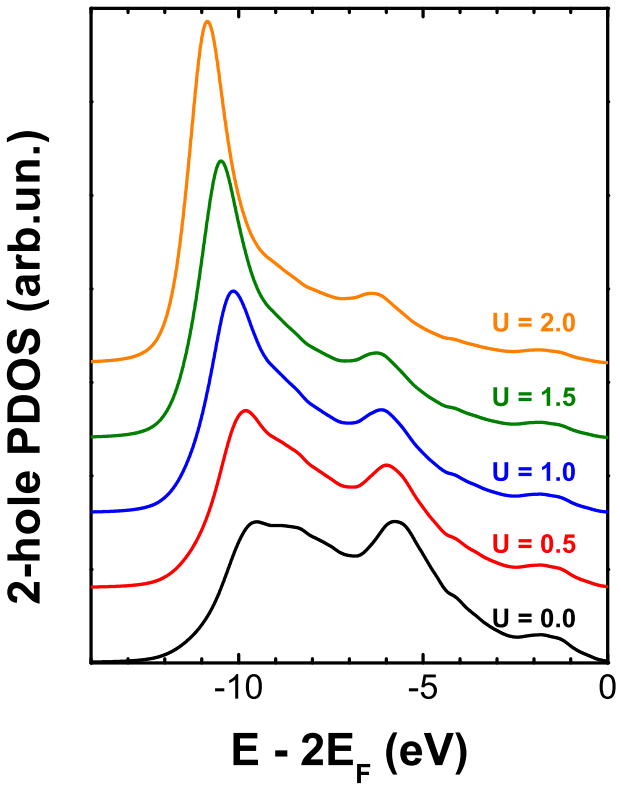

Figure 7.7: Two-particle density of states around the sulphur atom as evaluated by the Cini-Sawatzky theory, see Eq. (7.6), for different values of the hole-hole interaction energy, U.

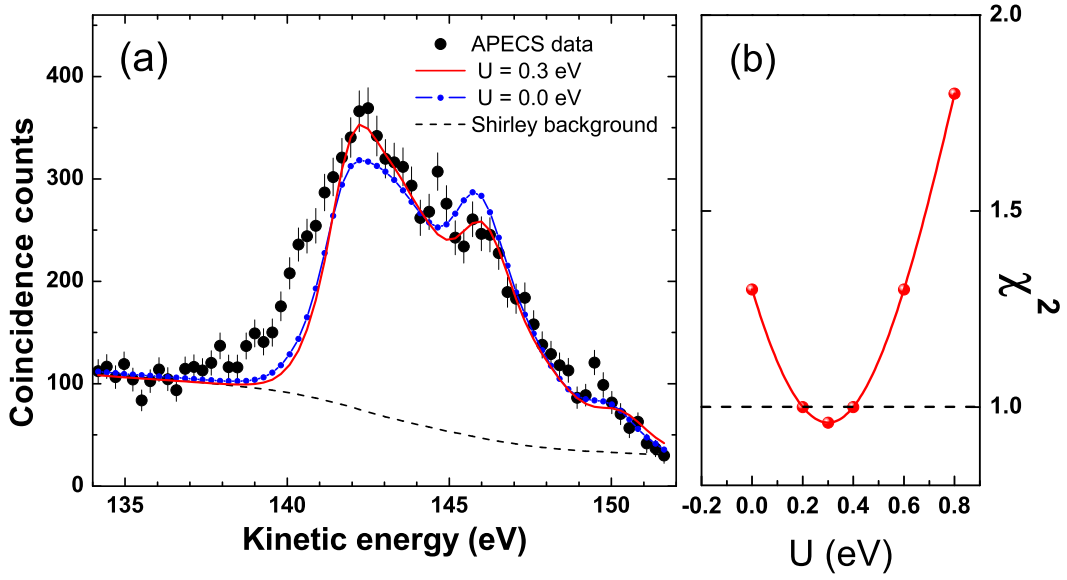

Figure 7.8: (a) Fits to the Cu(001)-$p(2\times2)$S L_3VV Auger line shape generated by the sum of a Shirley-type integral background (dashed line) and the Cini-Sawatzky equation calculated for the best fit value of $U = 0.3$ eV (solid line) and non-interacting particles ($U = 0.0$ eV) (dotted line). (b) chi-square distribution as a function of hole-hole correlation energy U.

detected in coincidence with the inelastic Auger electron. The energy loss of the additional peak, located 2 eV below the most intense ($L_3A_6A_6$) Auger transition at 142.5 eV, is comparable to the energy separation between the occupied A_1 levels (binding energy ~ 1 eV) and the sulphur-induced unoccupied states, u_1, located between 1 and 2 eV above the Fermi level [118]. This suggests that the low kinetic energy portion of the APECS spectrum is dominated by Auger transitions accompanied by the creation of an additional $u_1 - A_1$ electron-hole pair. These transitions, involving more than two electrons and leaving the system in a excited state, were not taken into account in the theory.

The goodness-of-fit was tested by performing a statistical test using a χ^2-variable defined as,

$$\chi^2_U = \frac{1}{dof}\sum_{k=1}^{n}\left(\frac{y_k - f_U(E_k)}{\sigma_k}\right)^2, \tag{7.7}$$

where y_k are the experimental values measured with statistical error σ_k, and $f_U(E_k)$ represents the theoretical function (parametrically depending on U) used to fit the spectrum and dof defines the number of degrees of freedom. We report in Fig. 7.8(b) the χ^2 distribution as a function of the hole-hole correlation energy. The value of the hole-hole correlation energy was obtained by selecting those U values for which the corresponding χ^2_U was acceptable within a confidence level of 95%. The best fit was obtained with $U = 0.3 \pm 0.1$ eV. The relative intensities of the three main features are in excellent agreement with measurements. Conversely, the independent-particle results ($U = 0$, dotted line) underestimate the intensity of the peaks at lower kinetic energy and are not appropriate for the description of the electronic properties of the system.

In conclusion we have measured the direct and core-resonant DPE spectrum of a sulphur overlayer on Cu(001) surface upon the absorption of circularly polarised light. We observed that the direct DPE transition probability is negligible at the considered photon energy, so we focused on the study of the Auger decay following the excitation of the S $2p$ levels. The energy distribution of core-resonant DPE processes, with the absence of energy sharing between correlated electrons, follows the predictions of a two-step approximation for the decay. This is a consequence of the long lifetime of $2p$ intermediate core-hole states, whose photoemission lines have a width around 0.2 eV corresponding to a decay time of few femtoseconds. This allowed us to obtain informations on how the presence of a well-definite core-hole intermediate state influences the dynamics of two-electron emission. We observed that, oppositely to the cases in which the Auger decay acts as a single-step process, no circular dichroism is observed in the electron-pair emission. This results have been explained by means of an atomic description of the process. The dynamics of the indirect double-photoionisation process in the presence of an intermediate state of well-defined parity restricts the possible values of the angular momentum accessible to the electron-pairs in the final state. This restriction results in the absence of circular dichroism when the electrons of the core-resonant DPE pairs are emitted with relative angles of 90°.
Complementary informations have been obtained by studying the energy distribution of the core-resonant DPE pairs. We performed APECS experiments by measuring the $L_{23}VV$ line shape in coincidence with $2p_{1/2}$ and $2p_{3/2}$ photoelectrons, respectively. In this way we determined the L_3VV and L_2VV Auger intrinsic line shapes. The main features of the measured APECS spectra can be explained by the self-convolution of single particle density of states, pointing out that the hole-hole interaction is small. However, the description of experimental data is improved when taking such interaction into account within the CS theory, and a value of $U = 0.3 \pm 0.1$ eV, best fits the coincidence measurements.

Chapter 8

Double photoemission from Ag(001)

In this chapter we will show the DPE spectrum of Ag(001). We mapped out 2-dimensional coincidence spectra at different photon energy, $h\nu = 118$ eV and $h\nu = 739$ eV, in order to measure, together with direct DPE pairs, also core-resonant DPE pairs due to $4p$ and $3d$ photoelectrons in coincidence with $M_{45}VV$ and $N_{23}VV$ Auger electrons, respectively. Our experiments demonstrate that the two-step model is able to describe the shape of the Ag $M_{45}VV$ spectrum but fails to describe the $N_{23}VV$ transition. In the second case an extensive energy sharing between the Ag $4p$ photoelectrons and the correlated Auger electrons is observed, as a consequence of the dynamic fluctuations in which the core-hole makes a transition from the $4p$ to the $4d$ level together with the excitation of additional electron-hole pairs, $4p^{-1} \rightleftharpoons 4d^{-2}mf$. These fluctuations, whose states of interest fall in the very region of the $4p$ hole state, lead to a situation in which the system may no longer be stable in the $4p^{-1}$ configuration, thus destroying the quasi-particle nature of the single-hole state.

The core-level X-ray photoemission spectroscopy is one of the most useful tools in the elemental analysis of surface atoms, based on the observed sharp photoelectron peaks which are the experimental proof of well defined core-hole states in the quasi-particle picture. When a photoelectron leaves an atom bound in a solid or molecule, the electrons in the neighbourhood will relax around the localised charge that has been generated. Thus, the created core-hole turn on a local potential that is responsible for a series of dynamic electron screening processes, e.g. shake-up of the outer shell electrons, plasmon excitations and the emission of Auger electrons. These electronic dynamics, driven by electron-hole interactions, take place on the few femtoseconds or even attoseconds time-scale and can be revealed by means of attosecond time-resolved spectroscopy [16, 17] or by studying the line shape of resonant core-electron spectra [131, 132].

Core-resonant DPE represents another way to probe the electron dynamics around a core-hole in the attosecond time-scale. In this sense the photoelectron can be considered as a "pump" signal while the second ejected (Auger) electron is the "probe" signal. The characteristic time-scale τ of this process can be estimated by Heisenberg uncertainty relation, $\Delta E \cdot \tau \approx \hbar = 0.66$ eV $\cdot$ fs, where ΔE is the energy uncertainty within the DPE pair.

Direct DPE technique has been already employed to reveal and completely map the exchange-correlation hole, i.e. the zone of reduced electronic charge around each electron of a system ascribable to the fact that electrons tend to stay away from each other as a consequence of Coulomb and exchange interactions. The exchange-correlation hole is of fundamental interest in solid state physics as it constitutes an integral part in local density approximation [133] and it is a key concept to understand dynamic screening effects in condensed matter.

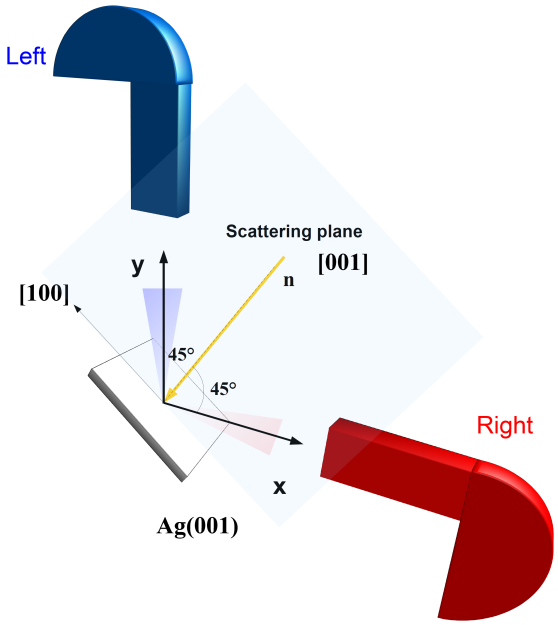

Figure 8.1: Schematic of the experimental set-up to detect the DPE pairs emitted from Ag(001) surface upon the absorption of 739 and 118 eV photons. A coplanar geometry was chosen with the propagation direction of the light (yellow arrow) in the same plane of the escape directions of the electrons, respectively **x** and **y**.

In this case we exploited the exceptional capability of core-resonant DPE to get an insight into the early stages of photo-excitation processes, where the generated core-hole has not been fully screened. Of course, in order to get this kind of informations we have to consider those cases in which the quasi-particle picture of the core-hole states is no longer valid and the two-step model for the Auger decay breaks down. This is because the high-velocity of the decay does not allow the singly ionised state to relax and all the excitations made together with the primary ionisation can be adsorbed and carried away by the probe Auger electron (see chapter 3.1).
The nature of the core-resonant DPE processes depends on the amplitude of the photoelectron linewidth, Γ_{1h}, as relative to the inverse of the singly ionised state relaxation time, described by the two-hole line width Γ_{2h}: one-step holds for $\Gamma_{1h} \gg \Gamma_{2h}$ while two-step is valid for $\Gamma_{1h} \ll \Gamma_{2h}$.

With this experiment we demonstrated the importance of Γ_{1h} in determining the nature of the core-resonant DPE. We observed, by studying the energy distribution of the DPE pairs, that the two-step model is adequate to describe the $M_{45}VV$ transitions but it breaks down in the $N_{23}VV$ ones. This second transitions are expected to take shorter to proceed due to the fact that all the electronic levels involved in the super Coster-Kronig decay have the same principal quantum number, this assuring maximum superposition between the electronic orbitals. The effects of the shake-up inter-band transitions induced in the core ionisation are identified by comparing this coincidence spectrum with the one obtained for the two-step $M_{45}VV$ Auger transition.

8.1 Experimental aspects

The experimental set-up used to acquire the Ag(001) DPE spectra is presented in Fig. 8.1. The coincidence spectrometer for surfaces is made up by two electrostatic analysers, left and right, having the electro-optical axis perpendicular to each other. In this case we chose a coplanar geometry, with the normal incidence photon beam and the two outgoing electrons all lying within the scattering plane defined by the [001] and [100] directions of the Ag(001) surface. Each analyser was able to detect electrons within an accpeted angle of $\pm 15^{\circ}$ around its optical axis. The pass energy and mean kinetic energy of each analyser were set to detect a 27 eV energy window around the central energy. The measured kinetic energies are quoted with respect to the Ag(001) vacuum level and the energy resolution for single and coincidence spectra are 0.8 and 1.2 eV, respectively. The experiments were performed at room temperature in a ultra-high vacuum chamber with a base pressure of 8×10^{-11} mbar.

8.2 Double photoemission spectra

The DPE experiments were performed at different photon energies, 739 eV and 118 eV, in order to assure the $3d$ ($4p$) photoelectrons to be in the same energy window with $M_{45}VV$ ($N_{23}VV$) Auger electrons. The energy distribution of core-resonant DPE electron-pairs is different in the case of two- or one-step description of the double-photoionisation process. In a two-step model (section 3.2), the photoelectrons from core-levels possess discrete energies and the Auger electrons can be distributed in energy over a maximum range of about two times the valence-band width ($\sim$ 10 eV). Core-resonant DPE events result, in a two-dimensional spectrum, as isolated spots whose shape is given by the superposition of the photoemission line shape, in one direction, with the line shape of the Auger spectrum in the other direction. Thus, core-resonant intensity bands are centered at the nominal kinetic energies of the electrons emitted in the indirect double-photoionisation process and their dimensions depend on the line widths of Auger and photoelectron spectra, respectively [see Fig. 8.2(a)]. If the photoionisation and the Auger decay happen in an single step the distinction between photo- and Auger electron becomes meaningless. In this picture (section 3.1), the excess energy of the process is shared between the emitted electrons and this results in an intense diagonal structure at constant sum energy with maxima of intensity when the kinetic energy of one of the two electrons is equal to the photoelectrons expected energies, Fig. 8.2(b).

Figure 8.3(a) presents the 2D intensity distribution of the DPE pairs excited by a single 739 eV photon. The spectrum has the characteristic shape of a two-step Auger decay. The coincidence distribution is dominated by intensity bands parallel either to the x- or y-axis. As in the case of Cu(001)-$p(2 \times 2)$S (section 7.3) if we extend the vertical (horizontal) features to the x (y) axis we find that they intersect it at E_{right} (E_{left}) = 366.6 eV and E_{right} (E_{left}) = 360.9 eV, that correspond to the nominal energies of Ag $3d_{5/2}$ and $3d_{3/2}$ photoelectrons, respectively. So the vertical intensity bands observed in Fig. 8.3(a) correspond to the $3d$ photoelectrons detected by the right analyser in coincidence with the corresponding $M_{45}VV$ Auger electron detected by the left analyser. The horizontal bands are described by analogous events in which the role of the analysers is exchanged. Since the natural line widths of the Ag $3d$ photoelectrons are only 0.3 eV [134], the width of the intensity bands of 0.8 eV reflects the energy resolution of the experimental apparatus. The coincidence lines have maximum intensity at 347.3 eV and 353 eV, corresponding to the nominal energy of M_5VV and M_4VV Auger electrons [53], respectively. Thus both kinds of core-resonant DPE pairs have the same sum energy, $E_{left} + E_{right} = 713.9$ eV, which is 16.4 eV

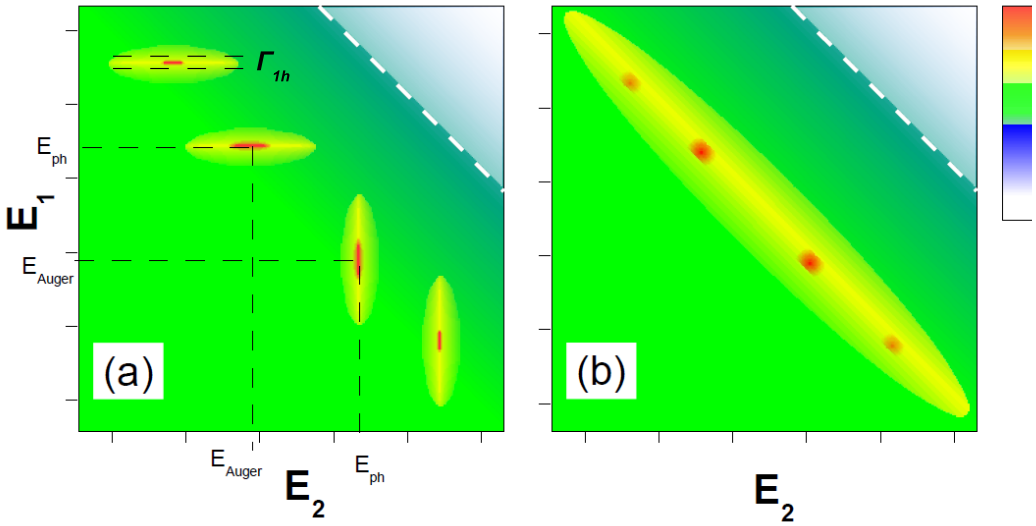

Figure 8.2: Schematic view of typical 2-dimensional (2D) energy distributions of the direct and core-resonant DPE pairs originating from different core-hole states but resulting in the same Auger final state. (a) for the validity ($\Gamma_{1h} \ll \Gamma_{2h}$ and (b) for the break down ($\Gamma_{1h} \gg \Gamma_{2h}$) of the two step model.

below the maximum sum energy accessible to the electron-couples, $E_{sum}^{max} = h\nu - 2\phi = 730.3$ eV, that is indicated by the dashed line in Fig. 8.3(a). Most of the intensity is concentrated in the region corresponding to the emission of electron-pairs whose sum energy is included between 13 eV and 20 eV below the maximum energy accessible to the pairs, $13 < E_{sum}^{max} - E_{sum} < 20$ eV, that is delimited by the two black lines in Fig. 8.3(a). From now on we denote this region as region II. The region characterised by $E_{sum}^{max} - E_{sum} > 20$ eV, denoted as region III, is characteristic of electron-pairs which have lost part of their sum energy to excite some degrees of freedom of the system. Region III is then dominated by the energy loss contributions of the DPE pairs produced in region II. The structures observed in this region, indicated by the arrows **P**, are ascribed to the elastic photoelectrons (Auger electrons) in coincidence with the corresponding inelastically scattered Auger electrons (photoelectrons). The overlap of these features gives rise to the high intensity regions indicated by the ellipses/rectangles **S**.

Fig. 8.3(b) shows the 2D energy distribution of the DPE-pairs upon absorption of 118 eV photons. Oppositely to the case of $M_{45}VV$ Auger transition, the coincidence distribution is described by one prominent diagonal structure characterised by $13 < E_{sum}^{max} - E_{sum} < 20$ eV. Both $M_{45}VV$ and $N_{23}VV$ transitions show their maximum intensity at the same value $E_{sum}^{max} - E_{sum} = 16.4$ eV, this demonstrating that the two transitions are characterised by the same two-hole final state. It is clear that core-resonant DPE transitions towards the same final state have different characters in the energy sharing within the DPE-pairs. In the $N_{23}VV$ transitions the continuous energy sharing is characteristic of a single-step Auger decay. In this case the Auger process takes place from a non-stationary singly-ionised ($4p^{-1}$) state. This state spans all the possible ionised configurations that are embedded in the double-photoionisation continuum, so that there is no constraint in the kinetic energies of the emitted electrons which can share the energy available in the final state of the process. On the other hand, in the $M_{45}VV$ transitions the energy exchange between $3d$

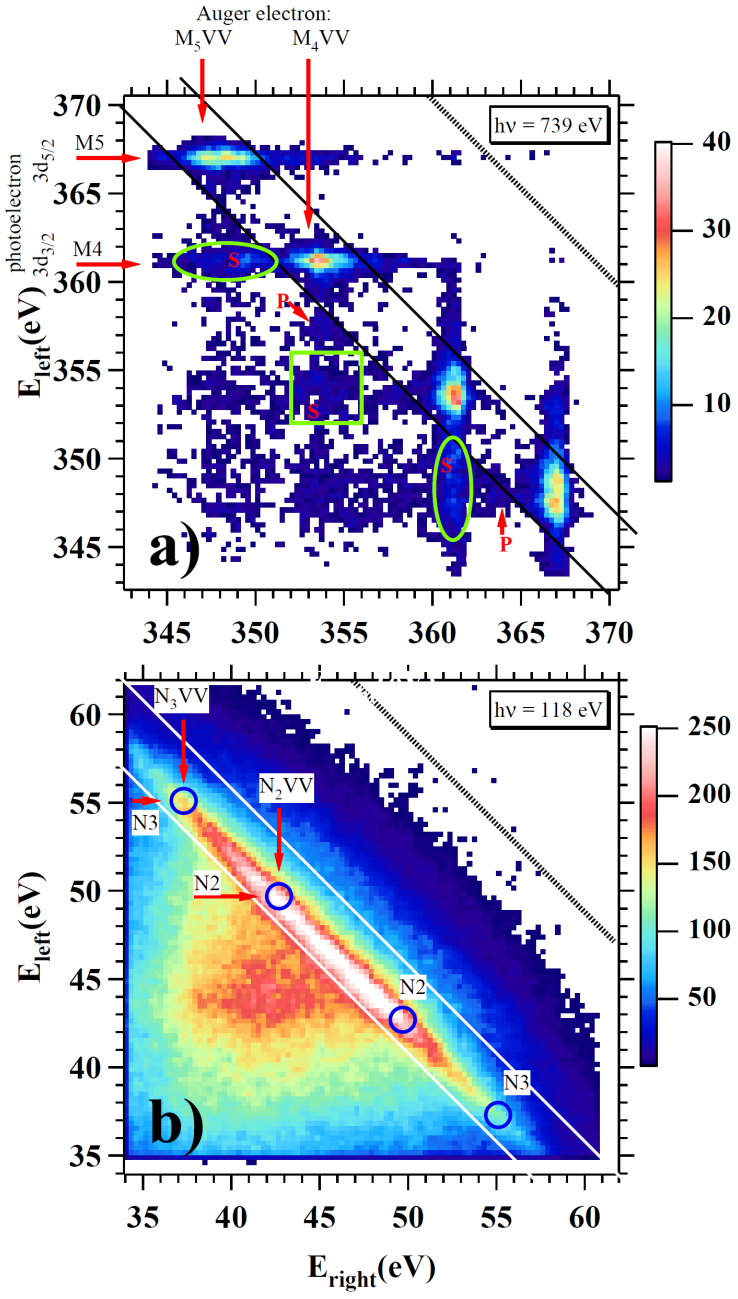

Figure 8.3: 2D distribution of correlated electron-pairs emitted upon the impact of 739 eV (a) and 118 eV (b), respectively. The core-resonant DPE pairs are concentrated between the solid lines at $13 < E_{sum}^{max} - E_{sum} < 20$ eV. The dashed lines indicate the maximum sum energy accessible to the DPE pairs.

photoelectrons and the corresponding Auger electrons is very unlikely and this results in intense localised lobes in the 2D distribution. The mentioned differences arise from the reduced life-time of the $4p$ holes with respect to the $3d$ ones. The Ag $4p$ photoelectron lines have natural line width of 11 eV [135], much bigger than the $3d$ one of 0.3 eV. In the time-domain, the long life-time $3d$ core-hole state (with small Γ_{1h}), indicates the large delayed time of Auger electron emission with respect to the photoemission process. In principle, it possible to distinguish the photoelectron with respect to the Auger emission by means of fs-time-resolved spectroscopy [71, 72]. In the case of the short-lived $4p$ core-hole states, the time distinction between photo- and Auger emission is no longer valid and the whole process must be described in a single-step picture. This clearly demonstrates that, for transitions resulting in the same final state (same line width of the DPE pairs Γ_{2h}), it is the life-time of the intermediate core-hole state that decides whether the core-resonant DPE process can be described by a two-step model or not.

8.3 Sum energy spectra: probing electron dynamic screening

As already mentioned in chapter 3 the line shape of the core-resonant DPE processes depends on the overlap between the wavefunctions of the intermediate core-hole state and the two-hole Auger final state. This means that core-hole effects are also visible in the line shape of the sum energy spectra, obtained by reporting the DPE pairs intensity as a function of their sum energy, $E_{sum} = E_{left} + E_{right}$, as relative to the maximum accessible sum energy E_{sum}^{max}. Fig. 8.4(a) compares the sum energy spectrum of $M_{45}VV$ (circles) and the $N_{23}VV$ (solid line) core-resonant DPE pairs. Both spectra are presented as relative intensity, with the area of each spectrum unit. The line shapes differ significantly in region II and III: $13 < E_{sum}^{max} - E_{sum} < 30$ eV, as observable in the difference spectrum of Fig. 8.4(b). No differences are observed in region I, included between $0 \leq E_{sum}^{max} - E_{sum} \leq 13$ eV.

Region II corresponds to transitions with $4d^{-2}$ final state configuration and in which the two left holes are mainly located within the same atomic site. The strong correlation between the two holes, $U \sim 4.5$ eV [53], leads to the appearance of atomic-like multiplet terms peak, indicated as ^1G, ^3F, ^1D, ^3P and ^1S according to Arena *et al.* [53].

Region III is ascribable to energy loss contributions of the DPE pairs in region II. In the $M_{45}VV$ line shape (dotted line) a broad peak **S**, is clearly resolved. With respect to the main peak (16.4 eV) in region II, the **S** structure has energy loss around $6-8$ eV and is superimposed on the shoulder **P** of the main peak starting at 3.7 eV energy loss. The characteristic energy losses of these two structures correspond to collective plasmon excitations [137, 138], which mainly origin from bulk atoms just underneath the topmost surface atoms [139]. In contrast, the **S** peak cannot be resolved in the $N_{23}VV$ sum energy spectrum (solid line).

The difference between the $N_{23}VV$ and the $M_{45}VV$ coincidence spectra is presented in panel (b) of Fig. 8.4. It has to be noticed that the subtraction procedure removes the contributions of inelastic scattering of the DPE pairs during their escape from the surface, since extrinsic inelastic contributions are not sensitive to the kinetic energy of electrons above ~ 50 eV [106, 140]. Fig. 8.4(b) demonstrates a spectral-weight transfer from the main peak in region II to the energy loss region III in the $N_{23}VV$ pairs. Two peaks, centred at energy loss of 5.2 eV (IB) and 10.4 eV (2IB), can be assigned to single and double inter-band transitions, respectively. The peak labelled as 2IB has a width of 4.8 eV, equal to $\sqrt{2}$ times the IB peak width of 3.5 eV, further indicating itself as a double inter-band transition. As it was theoretically predicted, they result from the coupling of electron-hole pairs with equal and opposite momentum due to the vacuum fluctuation [141]. This predictions still lack of an experimental evidence due to the short lifetime of the electron-hole pair

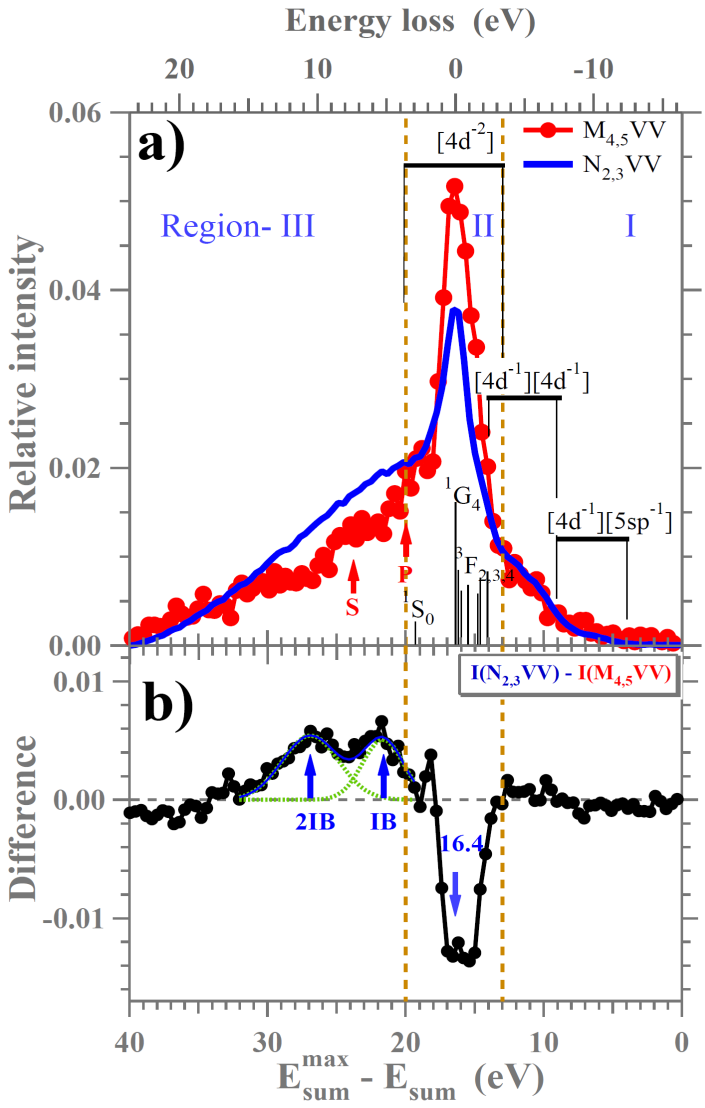

Figure 8.4: The sum energy spectra of the DPE pairs intensity from the $M_{45}VV$ (red dots) and the $N_{23}VV$ Auger transitions with impact photo energy of 739 eV and 118 eV, respectively. The intensities are normalised to the corresponding total counts. The relative intensities and energy positions of the different Auger final state multiplets, as obtained by theoretical calculations [136], are indicated by the vertical bars. (b) Point by point difference of the spectra presented in panel (a). It clearly shows a spectral-weight-transfer from the region II ($13 < E_{sum}^{max} - E_{sum} < 20$ eV) to region III ($E_{sum}^{max} - E_{sum} > 20$ eV) in the case of $N_{23}VV$ transition.

and to the strong mixing with collective plasmon excitations.

Region I corresponds to final states with two holes in the valence band that are not localised within the same atomic site, as indicated by the formalism $[4d^{-1}][4d^{-1}]$ and $[4d^{-1}][5sp^{-1}]$, where each set of square brackets includes the electron configuration localised to one atomic site. These DPE pairs correspond to the emission from the surface valence band, are not observable in isolated atoms and can also be generated in direct DPE without involving the core electrons [24]. However, if we observe the 2D distribution at $h\nu = 739$ eV, we can state that the direct DPE contribution to the total intensity is negligible. Direct DPE should result in electron-pairs characterised by a strong energy sharing between the electrons, thus in coincidences distributed along the directions of constant sum energy. The intensities in region I of Fig. 8.3(a) concentrate only along the $3d$ photoelectron lines and are clearly ascribable to core-resonant processes. Thus the broad peak in region I corresponds to the band-like part of the core-resonant DPE spectrum [18, 19]. This portion of the spectrum is proportional to the self convolution of the single-particle valence band density of states and corresponds to those final states in which the two holes are on different atomic sites [142].

Our results are in agreement with the ones reported by Bartynski *et al.* [143]. In their work the authors measured the Ag $N_{23}VV$ Auger spectrum in coincidence with $4p_{1/2}$ and $4p_{3/2}$ photoelectrons, respectively. Due to a value of the on-site hole-hole correlation energy that is comparable to the Ag d valence band width they found that the measured spectra exhibit both atomic-like and band-like structures. With respect to the $M_{45}VV$ decay [53], a larger contribution of the two-hole decay spectral weight was observed in the band-like part of the spectrum. An enhancement of the low energy tails of the Auger spectra was also observed and tentatively attributed to non-radiative decays involving more than two electrons. Effectively, what we have observed in our 2D distributions is a spectral-weight transfer from the atomic-like portion of the Auger spectrum to the low energy tails, while the intensity in the band-like region remains unchanged. This observation is crucial to determine the nature of the transitions in region III. If the intensity increase in the low energy region of the $N_{23}VV$ spectrum was due to an increased energy loss probability at lower kinetic energies, then we would observe a decrease in the intensity of the band-like part of the spectrum, too. Since we do not observe this intensity reduction we can exclude this hypothesis and conclude that the low energy excess emissions are ascribed to single or double inter-band transitions, which are local excitations produced in the universal attosecond response to the creation of the core-hole [17], before the build-up of collective plasmon excitations in the extended system [16].

8.4 One- or two-step core resonant DPE?

In previous sections we have experimentally verified that the relative line-widths of photoelectrons, Γ_{1h}, and DPE pairs, Γ_{2h}, are responsible for the one- or two-step nature of the core-resonant processes. However, why shall the line-width of the DPE pairs act as a benchmark for the nature of the core-resonant DPE? Or, in other words, how can the future (Auger electron emission) influence the past (photoemission) in a classical picture? This can be only explained in a quantum mechanical approach. According to Heisenberg uncertainty principle, the line-widths (Γ) observed in the emission spectra reflect the lifetime (τ) of the remaining excited states, $\Gamma \cdot \tau \lesssim \hbar$. This means that, after the photon absorption, the electronic state can fluctuate back and forth over the intermediate core-hole and final two-hole states. The time spent by the system in each configuration is dictated by the lifetime of the state. In most cases the residual time on the Auger final state is much shorter than the one on the intermediate core-hole state ($\Gamma_{1h} \ll \Gamma_{2h}$), thus the quasi-particle picture for the

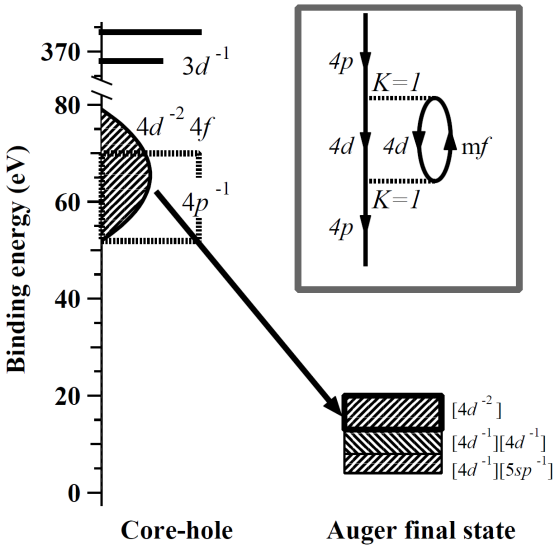

Figure 8.5: Energy level diagram for the intermediate core-hole (left) and the Auger (right) final states. The energies of the $4p^{-1}$ (thick, dashed box) and $4d^{-2}mf$ (shaded area) overlap significantly in the energy region $53 \sim 70$ eV. The inset shows the self energy contribution corresponding to the $4p \rightarrow 4d$ fluctuation of the core-hole made together with the excitation of an electron-hole pair $4d - mf$. In this process the hole has a change in quantum number associated to the angular momentum, $K = 1$. The conservation rules for the Coulomb matrix element demand that the same change appears in the corresponding electron-hole pair excitation [57, 144].

single-hole state as well as the two-step model for the Auger decay are valid. On the contrary, in the transitions characterised by $\Gamma_{1h} \gg \Gamma_{2h}$ the system will spend more time in the Auger final state. This implies the breakdown of the quasi-particle picture for the core-hole state and the two-step model fails to describe the core-resonant DPE process.

In silver the dynamic fluctuations $4p^{-1} \rightleftharpoons 4d^{-2}mf$ dominate the N_{23} photoemission and is responsible for the enlargement of the corresponding photoemission line, as first suggested by Wendin *et al.* [144]. This is a consequence of the large overlap in the wavefunctions corresponding to $4p$ and $4d$ electrons within the same shell. In addition, the kinetic energy of the $N_{23}VV$ Auger electrons is around $30 - 50$ eV, region in which the $4f$ unoccupied states are dominant in the Ag(001) crystal potential [145]. In consequence, the energy of the $4p^{-1}$ and $4d^{-2}4f$ 2-hole-1-electron state overlap strongly, as shown in Fig. 8.5. This explains the velocity of the $N_{23}VV$ Auger transition, oppositely to the $M_{45}VV$ ones in which the less overlap between $3d$ and $4d$ orbitals does not allow this kind of fluctuations.

The distinction between $M_{45}VV$ and $N_{23}VV$ Auger transitions can be made more clear by the use of Feynmann diagrams. Fig. 8.6(b) describes the $M_{45}VV$ decay; the time scale increases as we move from the bottom to the top of the diagram and the origin is set at the time of the core ionisation. The diagram clearly shows that the Auger transition has not yet started when the $3d$ electron, emitted as a p- (εp) or f-wave (εf), escapes from the screened Coulomb potential of the $3d^{-1}$ core-hole state, which can be considered a quasi-stationary state within its lifetime of 2 fs. In contrast, in the $N_{23}VV$ processes described in Fig. 8.6(a) the photoelectron coming from

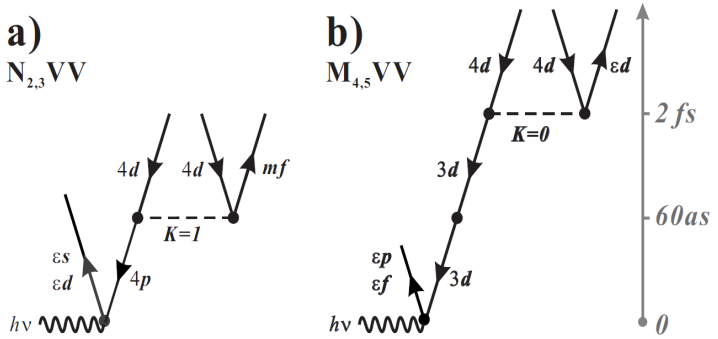

Figure 8.6: Diagrammatic picture of the $N_{23}VV$, panel (a), and $M_{45}VV$ (b) Auger transitions. The time increases moving from the bottom to the top of the picture with the origin of the time scale corresponding to the photoemission process. The $3d$ photoelectron in (b) only interacts with the $3d^{-1}$ state due to the long lifetime of the core-hole state which couples very weakly with the monopole transitions of the other electrons, $4d \rightarrow \varepsilon d$. On the contrary, the $4p$ photoelectron in (a) experiences the field of both the $4p^{-1}$ and $4d^{-2}$ states, due to the fast $4p^{-1} \rightleftharpoons 4d^{-2}mf$ dipole fluctuations.

the $4p$ level experiences, before leaving the system, the Coulomb field of both the $4p^{-1}$ core-hole state and the $4d^{-2}$ two-hole state arising from the $4p^{-1} \rightleftharpoons 4d^{-2}mf$ fluctuations. Both states are characterised by a very short lifetime of 60 attoseconds. Due to the velocity of the decay and the overlapping in energy, the photoelectron has to share its energy with the mf Auger electron and this results in the extended diagonal structure in region II, as observed in Fig. 8.3(b). In addition, since the transition of the $4p$-hole corresponds to a change in its angular momentum quantum number, $K = \Delta l = 1$, we have a dipolar fluctuation around the intermediate hole. This interacts with dipolar fluctuations around the other electrons corresponding to the creation of electron-hole pairs having dipolar symmetry, e.g. $4d \rightarrow 5p$. The two sets of fluctuations, i.e. the ones of the hole and the ones of the other electrons, strongly couple through Coulomb interactions [144]. This gives rise to an higher probability to shake-up additional electron-hole pairs in the valence band with respect to the monopole transition $3d \rightarrow 4d$, thus contributing to the spectral-weight-transfer from region II to region III in the sum energy spectra of Fig. 8.4.

In conclusion, we have demonstrated that the nature of the core-resonant DPE from a Ag(001) surface depends on the lifetime of the intermediate core-hole state. The comparison between the 2-dimensional and sum energy spectra of the $M_{45}VV$ and $N_{23}VV$ Auger transitions showed a spectral-weight transfer from the quasi-atomic part of the spectrum, in which the hole-hole interaction is dominant, to its low sum energy tail in the decay of the $4p$ core-holes. This is due to shake-up processes occurring during the photo-excitation which create extra electron-hole pairs. The presented results clearly demonstrated that core-resonant DPE can be considered a powerful tool to investigate the ultra-fast dynamic screening processes occurring at attosecond time-scale in the very beginning of the photoemission.

Conclusions

In this thesis we have performed direct and core-resonant Double-PhotoEmission (DPE) experiments on Cu(001), Cu(001)$p(2 \times 2)$-S and Ag(001) surfaces. The motivation to experimentally study this kind of processes can be found in understanding how the two-electron dynamics is influenced by the correlated motion of the electrons in both the initial and final state of the double-photoionisation process. Indeed, until now the understanding of the DPE processes from systems more complicated than simple atomic targets is far from being completely understood. This, from the theoretical side, is due due to the fact that the treatment of electronic systems with a large number of electrons rapidly becomes more complex than the atomic case. From the experimental point of view, the low cross section of the process and the need to detect both the emitted electrons to complete determine its kinematics, constituted the major difficulties to obtain a complete experimental characterisation of the DPE in the latest years.

The study of different systems in different experimental conditions gave us the opportunity to highlight many properties of double-photoionisation processes and to study how they relate to electron-electron correlations. We now present the main results achieved and presented in this thesis.

The direct and core-resonant DPE spectrum of Cu(001) surface was presented in chapter 6. By the use of linearly and circularly polarised light we studied how the angular distribution of the DPE pairs is influenced by the introduction of a preferred direction in the experimental set-up. In the first case (linear polarisation) we studied the angular dependence of the Cu $M_{45}VV$ core-resonant process by means of Auger-PhotoElectron Coincidence Spectroscopy (APECS). We took into consideration two different geometries. In the first one (AN) the escape direction of the photoelectron is aligned with the light polarisation vector while the corresponding Auger electron is emitted orthogonally to it. In the second one (NA) the emission angles of the two electrons were exchanged, with the Auger electron emitted in the same direction of the light polarisation and the photoelectron in the orthogonal direction. Differences are visible in the line shapes of the APECS spectra acquired at different geometries. In particular, we observed an enhancement of the coincidence yield due to spin-symmetric (triplet) two-hole final states with respect to the spin-antisymmetric (singlet) ones when passing from NA to AN geometry. This final-state spin selectivity is a consequence of the presence of an intermediate core-hole state in the indirect double-photoionisation process. The unbalance in the population of the hole magnetic sub-levels results in a different degree of alignment with the quantization axis of the system. As a consequence of dipole and Coulomb selection rules the alignment of the intermediate state can be controlled by applying a selection on the emission direction of the Auger and photoelectron.
In the second case (circular polarisation) we mapped out the helicity-dependent energy distribution of the direct and core-resonant DPE pairs. We observed that the emission intensity of both kind of pairs can be sensitive to the switching of the light helicity. In particular chiral or achiral behaviour of the pairs strictly depends on the symmetry of the two-hole final state they leave behind in the

residual doubly-ionised system. Circular dichroism, CD, is observed in those transition leaving the system in spin-antisymmetric, space-symmetric two-hole final states. Indeed, when the residual ion is left in a spatial state symmetric with respect to the exchange of the two holes, it has no chirality. This means that the chirality carried by the photon in the initial stage of the DPE process, is carried away by the emitted electron-pairs. This results in the appearance of circular dichroism in the DPE spectrum.

In chapter 7 we have measured the direct and core-resonant DPE spectrum of a sulphur overlayer on Cu(001) surface upon the absorption of circularly polarised light, focussing on the study of the Auger decay following the excitation of the S $2p$ levels. The energy distribution of core-resonant DPE processes, with the absence of energy sharing between correlated electrons, follow the predictions of a two-step approximation for the decay. This is a consequence of the long lifetime of $2p$ intermediate core-hole states, whose photoemission lines have a width around 0.2 eV corresponding to a decay time of few femtoseconds. Oppositely to the cases in which the Auger decay acts as a single-step process, no circular dichroism is observed in the electron-pair emission. This is because the dynamics of the indirect double-photoionisation process in the presence of an intermediate state of well-defined parity restricts the possible angular momentum values accessible to the electron-pairs in the final state. This restriction results in the absence of circular dichroism when the electrons of the core-resonant DPE pairs are emitted with a mutual angle of 90°.
The study of the $L_{23}VV$ line shape in coincidence with $2p_{1/2}$ and $2p_{3/2}$ photoelectrons allowed to study the effects of hole-hole correlations in the doubly-ionised system on the energy distribution of the core-resonant DPE pairs. We observed that the valence band two-particle density of states of S/Cu interface cannot be described by the self-convolution of the single-particle density of states also in this system where the hole-hole correlation energy ($U = 0.3 \pm 0.1$ eV) is negligible with respect to the holes kinetic energy ($W = 6$ eV).

We presented, in chapter 8, DPE spectra from Ag(001) surface measured at different photon energies, $h\nu = 118$ eV and $h\nu = 739$ eV. These two energies allowed to measure, together with direct double-photoionisation from the valence band of the system, also core-resonant events due to the decay of $4p$ ($h\nu = 118$ eV) and $3d$ ($h\nu = 739$ eV) core-hole via an Auger transition leaving the system with two holes in the valence band, i.e. $M_{45}VV$ and $N_{23}VV$ Auger decays. We have demonstrated that the nature of the core-resonant DPE from a Ag(001) surface depends on the lifetime of the intermediate core-hole state. In particular, we observed that a two-step model is able to describe the Auger decay of the long-lived ($\tau \sim 2$ fs) $3d$ holes, but fails to describe the $N_{23}VV$ Auger decay due to the short lifetime ($\tau \sim 60$ as) of the $4p$ core-hole states. The comparison between the 2-dimensional and sum energy spectra of the $M_{45}VV$ and $N_{23}VV$ Auger transitions showed a spectral-weight transfer from the quasi-atomic part of the spectrum, in which the hole-hole interaction is dominant, to its low sum energy tail in the decay of the $4p$ core-holes. This is a consequence of shake-up processes occurring during the photo-excitation which create extra electron-hole pairs and, due to the high rate of the decay, are reabsorbed in the Auger emission. The presented results clearly demonstrated that core-resonant DPE can be considered a powerful tool to investigate the ultra-fast dynamic screening processes occurring at attosecond time-scale in the very beginning of the photoemission.

In conclusion, we obtained a vast experimental characterisation of the DPE from solids surfaces. The obtained results are very interesting and furnish a description of how the dynamics of two-electron emission can be studied to obtain informations on the electronic correlations in system more complicated than atomic ones. Unfortunately, a unified theory capable of describing

specific behaviours of double-ionisation processes in different systems and experimental conditions is very hard to obtain and this prevents to achieve a further inside into the mechanisms of many-electron emission.

In the latest years K.A. Kouzakov and J. Berakdar [146, 147] have highlighted the possibility to use two-electron emission spectroscopy to provide novel informations on the mechanisms of superconductivity. In their works the authors calculated the DPE current of a superconductive system as the sum of one uncorrelated and one correlated term. The first one describes the incoherent emission of two uncorrelated electrons and constitutes part of the background for the coincidence experiment. The second term describes the DPE photocurrent associated with the emission of condensed Cooper-pairs (CPs). It depends on the wave function of the CPs in the momentum space and vanishes above the transition temperature, T_c. It has been shown that the latter term directly depends on the energy gap of the superconductive state, hence on the pairing potential and can give access to important informations about the condensation mechanism. Additional informations can be obtained by measuring the circular dichroism that has been demonstrated to be related to the (complex) gap phase.
Numerical simulations predicted the appearance, below T_c, of a pronounced peak around the two-electron Fermi energy in the DPE photocurrent. The position and intensity of the peak being related to condensation dynamics and the number of CPs, respectively. The corresponding uncorrelated current, above and below T_c, is distorted by the appearance of the superconductive gap in the single-particle density of states.

The experimental study of these processes will consist in measuring the DPE spectra of a system in its metallic and superconductive state. A comparison between the two spectra is expected to highlight the effects of CPs emission to the DPE process. For example we expect, below T_c, a drastic increase in the two-electron photocurrent for those geometries corresponding to the emission of electron-pairs with zero momentum. This is a consequence of the condensation of the electrons in Cooper-pair states with zero sum momentum.
Unfortunately, these experiments are made extremely difficult by the small value of the supercondctive gap ($\sim 1-3$ meV) in conventional superconductors. This means that, in order to extract all the informations contained in the DPE signal, the energy resolution of the coincidence spectrometer must be improved by more than two order of magnitude with respect to conventional ones. High temperature superconductors (HTSC) are instead more accessible experimentally having a typical energy gap of ~ 10 meV and higher. In this case, with a huge effort in developing high-resolution electron spectrometers covering nearly 2π of the solid angle above the sample (to increase the coincidence rate to detectable values), DPE experiments to detect CPs emission can be made feasible. In addition, the mechanisms of how CPs are generated in HTSC are still under discussion. DPE from these systems has the potential for providing a novel insight into pair correlations, gap energy, symmetries of the two-electron wavefunctions, and into the temperature dependence of these quantities [146, 147].

Bibliography

[1] Hubbard, J., Proceedings of the Royal Society of London. Series A. Mathematical and Physical Sciences **276** (1963) 238.

[2] Anisimov, V. I., Zaanen, J., and Andersen, O. K., Phys. Rev. B **44** (1991) 943.

[3] Anisimov, V. I., Solovyev, I. V., Korotin, M. A., Czyżyk, M. T., and Sawatzky, G. A., Phys. Rev. B **48** (1993) 16929.

[4] Anisimov, V. I., Aryasetiawan, F., and Lichtenstein, A. I., Journal of Physics: Condensed Matter **9** (1997) 767.

[5] Georges, A., Kotliar, G., Krauth, W., and Rozenberg, M. J., Rev. Mod. Phys. **68** (1996) 13.

[6] Kotliar, G. and Vollhardt, D., Physics Today **57** (2004) 53.

[7] Berakdar, J., Phys. Rev. B **58** (1998) 9808.

[8] Gunnarsson, O. and Schönhammer, K., Phys. Rev. B **22** (1980) 3710.

[9] Gunnarsson, O. and Schönhammer, K., Phys. Rev. Lett. **46** (1981) 859.

[10] Mahan, G. D., *Many Particle Physics series: Physics of solids and liquids*, Springer, 3rd edition.

[11] Bardeen, J., Cooper, L. N., and Schrieffer, J. R., Phys. Rev. **108** (1957) 1175.

[12] Chandra, N. and Ghosh, R., Phys. Rev. A **70** (2004) 060306.

[13] Parida, S. and Chandra, N., Physics Letters A **373** (2009) 1852 .

[14] Gotter, R. et al., Phys. Rev. B **79** (2009) 075108.

[15] van Riessen, G. et al., Journal of Physics: Condensed Matter **22** (2010) 092201.

[16] Borisov, A., Sanchez-Portal, D., Muino, R. D., and Echenique, P., Chemical Physics Letters **387** (2004) 95 .

[17] Breidbach, J. and Cederbaum, L. S., Phys. Rev. Lett. **94** (2005) 033901.

[18] Cini, M., Solid State Communications **24** (1977) 681 .

[19] Sawatzky, G. A., Phys. Rev. Lett. **39** (1977) 504.

[20] Cini, M. and Verdozzi, C., Journal of Physics: Condensed Matter **1** (1989) 7457.

[21] Verdozzi, C., Cini, M., and Marini, A., Journal of Electron Spectroscopy and Related Phenomena **117 - 118** (2001) 41 .

[22] Gonis, A., Journal of Electron Spectroscopy and Related Phenomena **161** (2007) 207 .

[23] Schumann, F. O., Winkler, C., Kerherve, G., and Kirschner, J., Phys. Rev. B **73** (2006) 041404.

[24] Schumann, F. O., Winkler, C., and Kirschner, J., Phys. Rev. Lett. **98** (2007) 257604.

[25] Berakdar, J. and Klar, H., Phys. Rev. Lett. **69** (1992) 1175.

[26] Berakdar, J., Klar, H., Huetz, A., and Selles, P., Journal of Physics B: Atomic, Molecular and Optical Physics **26** (1993) 1463.

[27] Jacobs, V. L., Journal of Physics B: Atomic and Molecular Physics **5** (1972) 2257.

[28] Carlson, T. A., Phys. Rev. **156** (1967) 142.

[29] Carlson, T. A. and Krause, M. O., Phys. Rev. **140** (1965) A1057.

[30] Salpeter, E. E. and Zaidi, M. H., Phys. Rev. **125** (1962) 248.

[31] Haak, H. W., Sawatzky, G. A., and Thomas, T. D., Phys. Rev. Lett. **41** (1978) 1825.

[32] Haak, H. W., *Auger-Photoelectron Coincidence Spectroscopy. A study of correlations effects in solids*, PhD thesis, University of Groningen, Groningen, Netherlands, 1983.

[33] Mobilio, S. and Balerna, A., Introduction to the main properties of Synchrotron Radiation, in *Synchrotron Radiation: Fundamentals, Methodologies and Applications*, edited by Mobilio, S. and Vlaic, G., Conference proceedings. Vol. 82, pages 1–23, Italian Physical Society, 2003.

[34] Mazeau, J., Selles, P., Waymel, D., and Huetz, A., Phys. Rev. Lett. **67** (1991) 820.

[35] Huetz, A., Selles, P., Waymel, D., and Mazeau, J., Journal of Physics B: Atomic, Molecular and Optical Physics **24** (1991) 1917.

[36] Wannier, G. H., Phys. Rev. **90** (1953) 817.

[37] Schwarzkopf, O., Krässig, B., Elmiger, J., and Schmidt, V., Phys. Rev. Lett. **70** (1993) 3008.

[38] Avaldi, L. and Huetz, A., Journal of Physics B: Atomic, Molecular and Optical Physics **38** (2005) S861 .

[39] Avaldi, L. and Stefani., G., Direct and resonant double photoionization: from atoms to solids, in *Fragmentation Processes*, Cambridge University Press, 2012.

[40] Viefhaus, J. et al., Phys. Rev. Lett. **77** (1996) 3975.

[41] Biester, H. W., Besnard, M. J., Dujardin, G., Hellner, L., and Koch, E. E., Phys. Rev. Lett. **59** (1987) 1277.

[42] Herrmann, R., Samarin, S., Schwabe, H., and Kirschner, J., Phys. Rev. Lett. **81** (1998) 2148.

[43] Stefani, G., Iacobucci, S., Ruocco, A., and Gotter, R., Journal of Electron Spectroscopy and Related Phenomena **127** (2002) 1 .

[44] Wigner, E. and Seitz, F., Phys. Rev. **43** (1933) 804.

[45] Slater, J. C., Rev. Mod. Phys. **6** (1934) 209.

[46] Fominykh, N. et al., Solid State Communications **113** (2000) 665 .

[47] Fominykh, N., Berakdar, J., Henk, J., and Bruno, P., Phys. Rev. Lett. **89** (2002) 086402.

[48] Gollisch, H., Schwartzenberg, N. v., and Feder, R., Phys. Rev. B **74** (2006) 075407.

[49] Ohno, M. and Wendin, G., Journal of Physics B: Atomic and Molecular Physics **12** (1979) 1305.

[50] Bartynski, R., Jensen, E., Hulbert, S., and Kao, C.-C., Progress in Surface Science **53** (1996) 155 .

[51] Sawatzky, G. A., Auger Photoelectron Coincidence Spectroscopy, in *Auger electron spectroscopy*, edited by Briant, C. L. and Messmer, R. P., pages 167 – 243, Academic Press, Boston, 1988.

[52] Jensen, E., Bartynski, R. A., Hulbert, S. L., Johnson, E. D., and Garrett, R., Phys. Rev. Lett. **62** (1989) 71.

[53] Arena, D. A., Bartynski, R. A., Nayak, R. A., Weiss, A. H., and Hulbert, S. L., Phys. Rev. B **63** (2001) 155102.

[54] Butterfield, M. T., Bartynski, R. A., and Hulbert, S. L., Phys. Rev. B **66** (2002) 115115.

[55] Ramaker, D., Yang, H., and Idzerda, Y., Journal of Electron Spectroscopy and Related Phenomena **68** (1994) 63 .

[56] Idzerda, Y. U., Surface Review and Letters **04** (1997) 161.

[57] Feibelman, P. J., McGuire, E. J., and Pandey, K. C., Phys. Rev. B **15** (1977) 2202.

[58] Gotter, R. et al., Phys. Rev. B **72** (2005) 235409.

[59] Stefani, G. et al., Journal of Electron Spectroscopy and Related Phenomena **141** (2004) 149 .

[60] Stefani, G. et al., Relevance of the Core Hole alignment to Auger-Photoelectron Pair Angular Distributions in Solids, in *Correlation Spectroscopy of Surfaces, Thin Films, and Nanostructures*, edited by Berakdar, J. and Kirschner, J., Wyley, 2004.

[61] Gotter, R. et al., Phys. Rev. B **88** (2013) 094403.

[62] Gotter, R. et al., EPL (Europhysics Letters) **94** (2011) 37008.

[63] Gotter, R. et al., Phys. Rev. Lett. **109** (2012) 126401.

[64] Hüfner, S., *Photoelectron Spectroscopy: Principles and Applications*, Springer, Berlin, 3rd edition, 2003.

[65] Ibach, H. and Lüth, H., *Solid-State Physics. An Introduction to Principles of Materials Science*, Springer, Berlin, 4th edition, 2009.

[66] Courths, R. and Hüfner, S., Physics Reports **112** (1984) 53 .

[67] Sakurai, J. J., *Modern Quantum Mechanics (Revised Edition)*, Addison Wesley, 1 edition, 1993.

[68] Taylor, J. R., *Scattering Theory: The quantum Theory on Nonrelativistic Collisions*, Wiley, New York, 1972.

[69] Weinelt, M., Journal of Physics: Condensed Matter **14** (2002) R1099.

[70] Gunnarsson, O. and Schonhammer, K., Surface Science **89** (1979) 575 .

[71] Drescher, M. et al., Nature **419** (2002) 803.

[72] Miaja-Avila, L. et al., Phys. Rev. Lett. **101** (2008) 046101.

[73] Matthew, J. and Komninos, Y., Surface Science **53** (1975) 716 .

[74] Jennison, D. R., Phys. Rev. Lett. **40** (1978) 807.

[75] Cherepkov, N. A., Physics Letters A **40** (1972) 119 .

[76] Cherepkov, N. A., Spin polarization of atomic and molecular photoelectrons, volume 19 of *Advances in Atomic and Molecular Physics*, pages 395 – 447, Academic Press, 1983.

[77] Lee, C. M., Phys. Rev. A **10** (1974) 1598.

[78] Baumgarten, L., Schneider, C. M., Petersen, H., Schäfers, F., and Kirschner, J., Phys. Rev. Lett. **65** (1990) 492.

[79] Bransden, B. H. and Joachain, C. J., *Physics of atoms and molecules*, Longman, Harlow, 2nd edition, 2003.

[80] Brink, D. M. and R., S. G., *Angular Momentum*, Clarendon Press, Oxford, second edition, 1968.

[81] Berakdar, J. and Klar, H., Physics Reports **340** (2001) 473 .

[82] Kabachnik, N. M. and Schmidt, V., Journal of Physics B: Atomic, Molecular and Optical Physics **28** (1995) 233.

[83] Kabachnik, N. M., Journal of Physics B: Atomic, Molecular and Optical Physics **25** (1992) L389.

[84] Berezhko, E. G., Kabachnik, N. M., and Sizov, V. V., Journal of Physics B: Atomic and Molecular Physics **11** (1978) 1819.

[85] Deshmukh, P. C. and Johnson, W. R., Phys. Rev. A **27** (1983) 326.

[86] Koch, E. E., editor, *Handbook on Synchrotron Radiation*, volume 1a, North-Holland, Amsterdam, 1983.

[87] Sawhney, K. et al., Nuclear Instruments and Methods in Physics Research Section A: Accelerators, Spectrometers, Detectors and Associated Equipment **390** (1997) 395 .

[88] Sasaki, S., Nuclear Instruments and Methods in Physics Research Section A: Accelerators, Spectrometers, Detectors and Associated Equipment **347** (1994) 83 .

[89] Sasaki, S. et al., Nuclear Instruments and Methods in Physics Research Section A: Accelerators, Spectrometers, Detectors and Associated Equipment **331** (1993) 763 .

[90] Domke, M. et al., Review of Scientific Instruments **63** (1992) 80.

[91] Follath, R. and Senf, F., Nuclear Instruments and Methods in Physics Research Section A: Accelerators, Spectrometers, Detectors and Associated Equipment **390** (1997) 388 .

[92] Moore, J. H., Davis, C. C., and Coplan, M. A., *Building scientific apparatus*, Cambridge University Press, fourth edition, 2009.

[93] Wiza, J. L., Nuclear Instruments and Methods **162** (1979) 587 .

[94] Schagen, P., *Advances in image pick-up and display*, volume 1, Academic Press, New York, 1974.

[95] Guest, A. J., Acta electronica **14** (1971) 79.

[96] Gotter, R. et al., Nucl. Instrum. Methods Phys. Res. A **467-468, Part 2** (2001) 1468.

[97] Volkel, M. and W., S., Journal of Physics E: Scientific Instruments **16** (1983) 456.

[98] Roy, D. and Carette, J.-D., Review of Scientific Instruments **42** (1971) 1122.

[99] SIMION sold by Scientific Instruments Services Inc.

[100] Green, M., Kenealy, P., and Beard, G., Nuclear Instruments and Methods **99** (1972) 445.

[101] Hink, W., Brunner, K., and Wolf, A., Journal of Physics E: Scientific Instruments **13** (1980) 882.

[102] Burdick, G. A., Phys. Rev. **129** (1963) 138.

[103] Eckardt, H., Fritsche, L., and Noffke, J., Journal of Physics F: Metal Physics **14** (1984) 97.

[104] Courths, R. and H Physics Reports **112** (1984) 53 .

[105] Eckardt, H., Fritsche, L., and Noffke, J., Journal of Physics F: Metal Physics **14** (1984) 97.

[106] Werner, W., Störi, H., and Winter, H., Surface Science **518** (2002) L569 .

[107] Shirley, D. A., Phys. Rev. B **5** (1972) 4709.

[108] Antonides, E., Janse, E. C., and Sawatzky, G. A., Phys. Rev. B **15** (1977) 1669.

[109] Schmidt, V., Nuclear Instruments and Methods in Physics Research Section B: Beam Interactions with Materials and Atoms **87** (1994) 241 .

[110] Rücker, U., Gollisch, H., and Feder, R., Phys. Rev. B **72** (2005) 214424.

[111] Arabczyk, W., Moszynski, D., Narkiewicz, U., Pelka, R., and Podsiadly, M., Catalysis Today **124** (2007) 43 .

[112] Tiancun, X., Lidun, A., Weimin, Z., Shishan, S., and Guoxin, X., Catalysis Letters **12** (1992) 287.

[113] Monachesi, P., Chiodo, L., and Del Sole, R., Phys. Rev. B **69** (2004) 165404.

[114] Tibbetts, G. G., Burkstrand, J. M., and Tracy, J. C., Phys. Rev. B **15** (1977) 3652.

[115] Menyhard, M., Surface Science **258** (1991) L683 .

[116] Salmerón, M., Baró, A. M., and Rojo, J. M., Phys. Rev. B **13** (1976) 4348.

[117] Ma, Y. et al., Phys. Rev. B **41** (1990) 5424.

[118] Leschik, G., Courths, R., and Wern, H., Surface Science **294** (1993) 355 .

[119] Wickenhauser, M. and Burgdörfer, J., Laser Physics **14** (2004) 492 .

[120] Colaianni, M. L. and Chorkendorff, I., Phys. Rev. B **50** (1994) 8798.

[121] Colaianni, M. L., Syhler, P., and Chorkendorff, I., Phys. Rev. B **52** (1995) 2076.

[122] Rosenblatt, D. H. et al., Phys. Rev. B **23** (1981) 3828.

[123] Schach von Wittenau, A. E. et al., Phys. Rev. B **45** (1992) 13614.

[124] Kuhl, D. E. and Tobin, R. G., Review of Scientific Instruments **66** (1995) 3016.

[125] Fratesi, G. and Trioni, M. I., Private communications.

[126] Perdew, J. P., Burke, K., and Ernzerhof, M., Phys. Rev. Lett. **77** (1996) 3865.

[127] Giannozzi, P. et al., J. Phys.: Condens. Matter **21** (2009) 395502.

[128] Lander, J. J., Phys. Rev. **91** (1953) 1382.

[129] Marini, A. and Cini, M., Phys. Rev. B **60** (1999) 11391.

[130] Antonides, E., Janse, E. C., and Sawatzky, G. A., Phys. Rev. B **15** (1977) 1669.

[131] Fohlisch, A. et al., Nature **436** (2005) 373 .

[132] Brühwiler, P. A., Karis, O., and Mårtensson, N., Rev. Mod. Phys. **74** (2002) 703.

[133] Kohn, W., Rev. Mod. Phys. **71** (1999) 1253.

[134] Mårtensson, N. and Nyholm, R., Phys. Rev. B **24** (1981) 7121.

[135] Ohno, M., Mariot, J.-M., and Hague, C., Journal of Electron Spectroscopy and Related Phenomena **36** (1985) 17 .

[136] Parry-Jones, A. C., Weightman, P., and Andrews, P. T., Journal of Physics C: Solid State Physics **12** (1979) 1587.

[137] Matthew, J., Netzer, F., and Astl, G., Surface Science **259** (1991) L757 .

[138] Rocca, M., Surface Science Reports **22** (1995) 1 .

[139] Werner, W. S. M. et al., Phys. Rev. Lett. **94** (2005) 038302.

[140] Werner, W. S. M., Surface and Interface Analysis **31** (2001) 141.

[141] Single particle versus collective electronic excitations, volume 477 of *Lecture Notes in Physics*, pages 125 – 141, Springer.

[142] Sawatzky, G. A. and Lenselink, A., Phys. Rev. B **21** (1980) 1790.

[143] Bartynski, R. A., Qian, Q., and Hulbert, S. L., J. Phys. IV France **09** (1999) 157 .

[144] Wendin, G., Ohno, M., and Lundqvist, S., Solid State Communications **19** (1976) 165 .

[145] Muller, J. E., Jepsen, O., Andersen, O. K., and Wilkins, J. W., Phys. Rev. Lett. **40** (1978) 720.

[146] Kouzakov, K. A. and Berakdar, J., Phys. Rev. Lett. **91** (2003) 257007.

[147] Kouzakov, K. and Berakdar, J., Journal of Electron Spectroscopy and Related Phenomena **161** (2007) 121 .